DESIGN OF Si/SiC HYBRID STRUCTURES FOR ELEVATED TEMPERATURE MICRO-TURBOMACHINERY

by

Hyung-Soo Moon

B.S., Mechanical Engineering, Seoul National University, Korea, (1992)
M.S., Mechanical Engineering, Seoul National University, Korea, (1995)

Submitted to the Department of Mechanical Engineering
in Partial Fulfillment of the Requirements for the Degree of

Doctor of Philosophy

at the

Massachusetts Institute of Technology

June 2002

Signature of Author_____
Department of mechanical Engineering
May 24, 2002

Certified by_____
Professor S. Mark Spearing
Associate Professor of Aeronautics and Astronautics, Thesis Supervisor

Certified by_____
Professor Lallit Anand
Professor of Mechanical Engineering, Committee Chairman

Certified by_____
Professor Alan H. Epstein
R. C. Maclaurin Professor of Aeronautics and Astronautics

Certified by_____
Professor Martin A. Schmidt
Professor of Electrical Engineering and Computer Science

Accepted by_____
Professor Ain A. Sonin
Chairman, Department Committee on Graduate Students

Design of Si/SiC Hybrid Structures for Elevated Temperature Micro-Turbomachinery

by

Hyung-Soo Moon

Submitted to the Department of Mechanical Engineering on May 24, 2002, in partial fulfillment of the Requirements for the Degree of Doctor of Philosophy

Abstract

Silicon, the material of choice of the first (demonstration) microengine, exhibits strong thermal softening behavior at temperatures above 900 K. This thermal softening behavior limits the turbine inlet temperature, which in turn significantly degrades the overall engine efficiency. Previous studies have shown that hybrid structures of silicon and silicon carbide have good potential for improved engine performance. Detailed design of Si/SiC hybrid structures for high temperature micro-turbomachinery, however, has been hampered by the relatively poor performance of single crystal Si at elevated temperatures and high stresses and by the unavailability of accurate material properties data for both Si and SiC at the temperatures of interest. From previous work, the critical structures and materials issues to be resolved, in order to proceed with the design of high temperature Si/SiC hybrid structures, were identified as follows:

1. the safety margin of the Si/SiC hybrid structures based on the upper yield strength of Si
2. reliable estimation of the service life of the Si/SiC hybrid structures
3. structural instabilities caused by the combination of stress concentrations and strain softening.

In the course of this thesis, these issues provided the key motivations of the work, and have been substantially resolved.

As a first step, it is critical to obtain a better understanding of the mechanical behavior of this material at elevated temperatures in order to properly exploit its capabilities as a structural material. Creep tests in simple compression with n-type single crystal silicon, with low initial dislocation density, were conducted over a temperature range of 900 K to 1200 K and a stress range of 10 MPa to 120 MPa. The compression specimens were machined such that the multi-slip <100> or <111> orientations were coincident with the compression axis. The creep tests reveal that the response can be delineated into two broad regimes: (a) in the first regime rapid dislocation multiplication is responsible for accelerating creep rates, and (b) in the second regime an increasing resistance to dislocation motion is responsible for the decelerating creep rates, as is typically observed for creep in metals. An isotropic elasto-viscoplastic constitutive model that accounts for these two mechanisms has been developed in support of the design of the high temperature turbine structure of the MIT microengine.

From the experimental observations and model validation, basic guidelines for the design of Si/SiC hot structures have been provided. First, the use of the upper yield strength of single crystal Si for design purpose is non-conservative. Also from the perspective of the design of Si hot structures, the lower yield strength is insufficient, particularly for micro-turbomachinery operating at elevated temperatures and high stresses. The recommended approach to the design of Si hot structures is to use the Si model for extracting appropriate operating conditions, and to reinforce the Si structures with SiC in strategic locations. Second, at high temperatures, the effect of stress concentrations is not crucial. Unlike the low temperature Si structures, the plasticity present adjacent to the sharp corners reduces the effect of stress concentrations. Third, the Si/SiC hybrid structures concept was verified. The considerable increase in the load carrying capability of the Si/SiC hybrid specimens encourages the development of Si/SiC hybrid structures for elevated temperature micro-turbomachinery in order to extend the available design space. Finally, the FE results for the creep life estimation of the Si/SiC hybrid turbine rotor identified the limit of the all-Si turbine rotor of the current microengine as well as the superior performance of the Si/SiC hybrid rotor in terms of creep life.

Thesis Supervisor: S. Mark Spearing
Title: Associate Professor, Department of Aeronautics and Astronautics

Acknowledgments

This thesis would not have been possible without the support and encouragement of a number of people.

First of all, I would like to thank my family: my parents and sisters for their endless support and belief in me, my wife, Yoonjung, for her dedicated love, and my daughter, Soyoon, for giving me the boundless joy and a huge motivation to become a better father.

I would like to thank my advisor, Prof. S. Mark Spearing, for providing me with the opportunity to work on the microengine project, and his consistent support and encouragement in the course of thesis work. I would also like to thank the other members of my thesis committee, Prof. Lallit Anand, Prof. Alan H. Epstein, and Prof. Martin A. Schimdt for sharing their invaluable insight and advice. Particularly, I would like to express my deepest thank to Prof. Anand, my former advisor, for keeping me interested in the academic career at the MIT even after leaving his research group.

My life at the MIT began at the Mechanics and Materials Group in Bldg. 1, full of wonderful colleagues such as Brian Gearing, Prakash Thamburaja, Mike Kim, C. Gu, Steve Xia, Jin Yi, and more. Raymond G. Hardin also helped me a lot for the administrative assistance. The members of Materials, Structures, and Packaging (MS & P), a subgroup of the microengine project, have also enriched my life at the MIT: Dongwon Choi, Erin Noonan, Dr. V. T. Srikar, Christine H. Tsau, Carissa Tudryn, Kevin Turner, and Dr. Norihisa Miki. I would like to thank them all. Particularly, Dongwon Choi, my co-worker in the development of Si/SiC hybrid structures, was a great partner to work with. I would like to wish the best of luck to him for the successful completion of his thesis.

I would also like to thank John Kane for helping me conduct the mechanical testing in the basement of Bldg. 37, and Paul E. Warren for providing me with the secure computational environment. I also owe a lot to my UROP's, Vanessa Marquez, Anna Mracek, Leah R. Soffer, Mattew D. Neave, particularly as my defense date drew near. I cannot also miss my thanks to all the members of GTL and microengine; Dr. Yifang Gong, Dr. Yoav Peles, Chris Spadaccini, Chris Protz, Nick Savoulides, Boris Sirakov, Vai Man Lei, Chian-Juay Teo, Jinwook Lee, Jhongwoo Peck, Anthony Chobot, Dr. Duc Vo, Taek Choi, and so on. I would also like to thank Lori Martinez, Diana Park, Holly Anderson, Julie Finn, and Mary McDavitt for their administrative assistance.

Finally, many thanks to my friends for making my life at Cambridge enjoyable: Seungkil Son, Kisok Song, Jinpyung Chung, Dr. Taejung Kim, Dohyoung Kim, Hyungsuk Lee, Joonil Seog, Dr. Moonsoo Jin, Dr. Jaehyun Kim, Taesik Lee, and so on.

This work was supported by the United States Army Research Office, Dr. R. Paur and Dr. T. Doligalski, technical managers. This support is gratefully acknowledged.

Contents

List of Figures

List of Tables

Chapter 1

1 Introduction

1.1 Overview

Microelectromechanical systems (MEMS)-based engines are under development at the Gas Turbine Lab (GTL) and the Microsystems Technology Laboratory (MTL) at the Massachusetts Institute of Technology (MIT). Preliminary design studies have shown that such devices for use in Micro Aerial Vehicles (MAV) or portable power applications could produce 50 W of electric power or 0.2 N of thrust [1]. Initial efforts have focused on developing all-silicon engines fueled by hydrogen to demonstrate the overall concept. This all-silicon demonstration microengine is made out of six silicon layers to yield a device 21 mm in diameter and 3.7 mm in thickness. A cross-sectional diagram of the microengine is shown in Figure 1.1.

The current design of the all-silicon engine fueled by hydrogen does not have a sufficient power density to achieve the desired power or thrust levels because the engine design is driven by the limitations of current fabrication technology. Silicon, the material selected for the entire engine structure, exhibits strong thermal softening behavior at temperatures above 900K, as shown in Figure 1.2. The strategy employed in the all-silicon engine is to design the rotor so that there is a high heat flux from the turbine rotor to the compressor to keep the wall temperature of the turbine rotor below 950K. This strategy, while yielding a workable demonstration device, has a severe negative impact on the engine efficiency and power output.

In order to increase the turbine inlet temperature to improve the overall engine efficiency, high temperature materials for turbine blades and blade cooling methods have been developed in parallel in macroscale gas turbine engines. Figure 1.3 demonstrates how developments in high temperature materials and blade cooling methods have increased

the maximum temperature limit in conventional macroscale turbine blades over the past five decades and indicates anticipated future trends. The same strategies employed in the macroscale need to be conducted in parallel for micro-turbomachinery to increase the maximum turbine inlet temperature from the current baseline design.

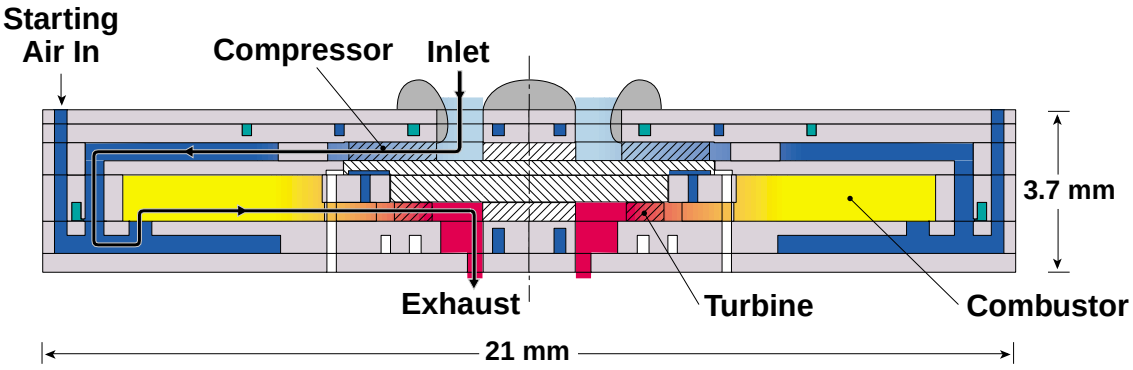

(a)

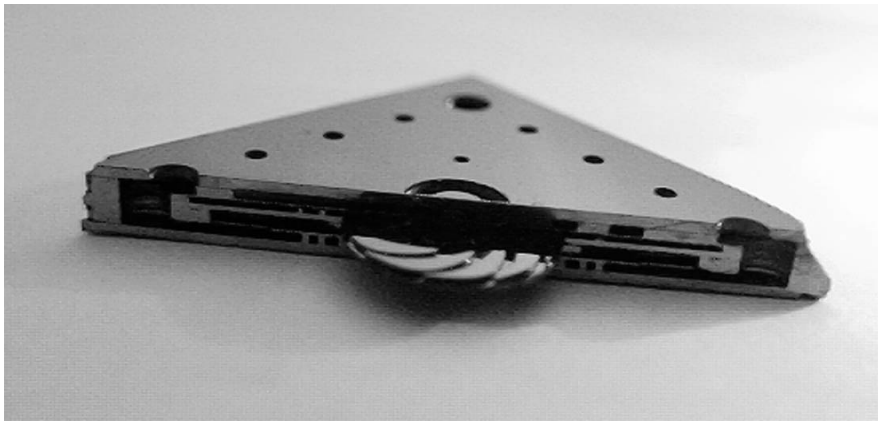

(b)

Figure 1.1 (a) Cross-sectional diagram of the demonstration microengine turbojet. The device is axisymmetric about the centerline, (b) Micro-fabricated turbocharger die [J. Protz, Ph. D. Thesis, Dept. of Aero & Astro, MIT, 2000]

The strategy of developing elevated temperature structures strongly depends on developing appropriate fabrication technologies. SiC in single crystal form is a very attractive material for MEMS applications because of its high stiffness, hardness, toughness, and strength at elevated temperatures. However, the use of SiC in single crystal form is unlikely to be feasible because the low chemical reactivity and the extremely high melting temperature of SiC hamper the development of the necessary micro-fabrication processes, particularly etching and bonding. Instead, this material could be placed in strategic locations to reinforce locally the structure by means of chemical vapor deposition (CVD) of SiC into silicon molds. This hybrid structure concept has been explored in various ways, as illustrated in Figure 1.4. Previous studies have concluded that considering the micro-fabrication difficulties Si/SiC hybrid structures are more feasible than monolithic SiC structures, and that the design of high temperature structures and the development of micro-fabrication processes should be conducted simultaneously [2, 3].

This thesis focuses on the design of Si/SiC hybrid structures for elevated temperature micro-turbomachinery which exploit the superior properties of SiC at high temperatures, but which are also feasible to micro-fabricate, given the constraints imposed by the microfabrication processes. Section 1.2 briefly reviews the status of the development of the high temperature Si/SiC hybrid structures in terms of the design requirements and constraints associated with the materials and hybrid structures. In Section 1.3, the thesis objectives are given along with a list of key tasks to perform. Finally, Section 1.4 outlines the overall structure of this thesis.

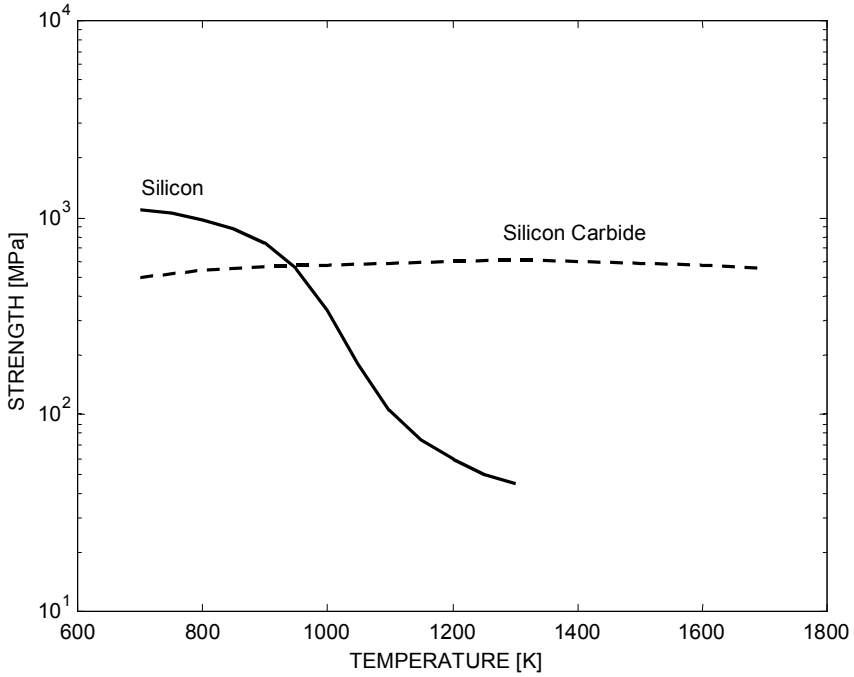

Figure 1.2 Strength of silicon and silicon carbide vs. temperature (Trends based on literature data from Pearson 1957, Mura 1996, Castaing 1981, Patel 1963, Huff 1993, Pickering 1990, Hirai & Sasaki 1991, Chen 1999, Reprinted from B. Miller, S. M Thesis, MIT, 2000)

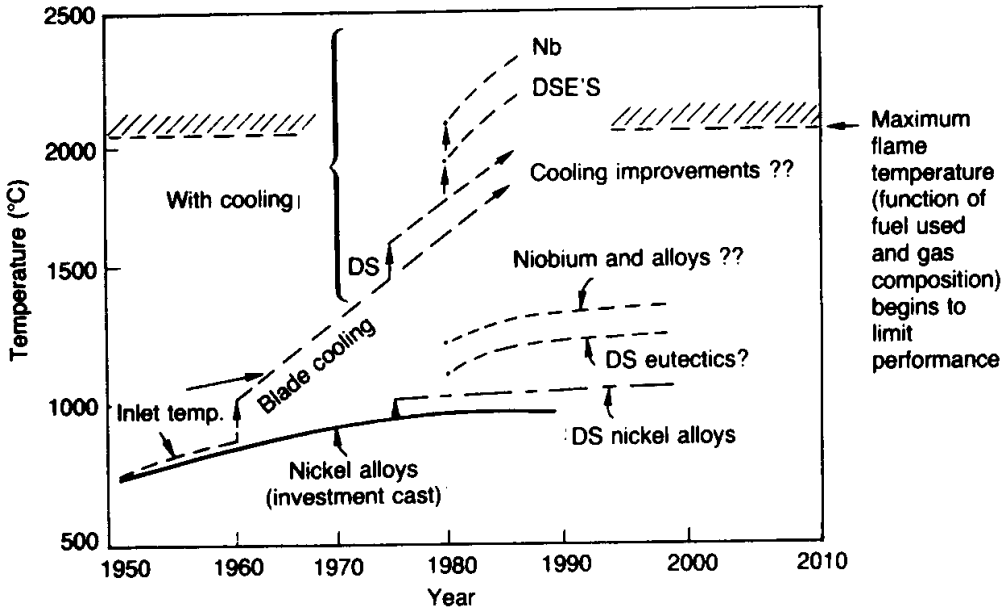

Figure 1.3 Temperature evolution and future materials trends in turbine blades [M. F. Ashby and D. R. H. Jones, Engineering Materials 1--An introduction to their properties & application, 2nd ed, Butterworth Heinmann, 1996]

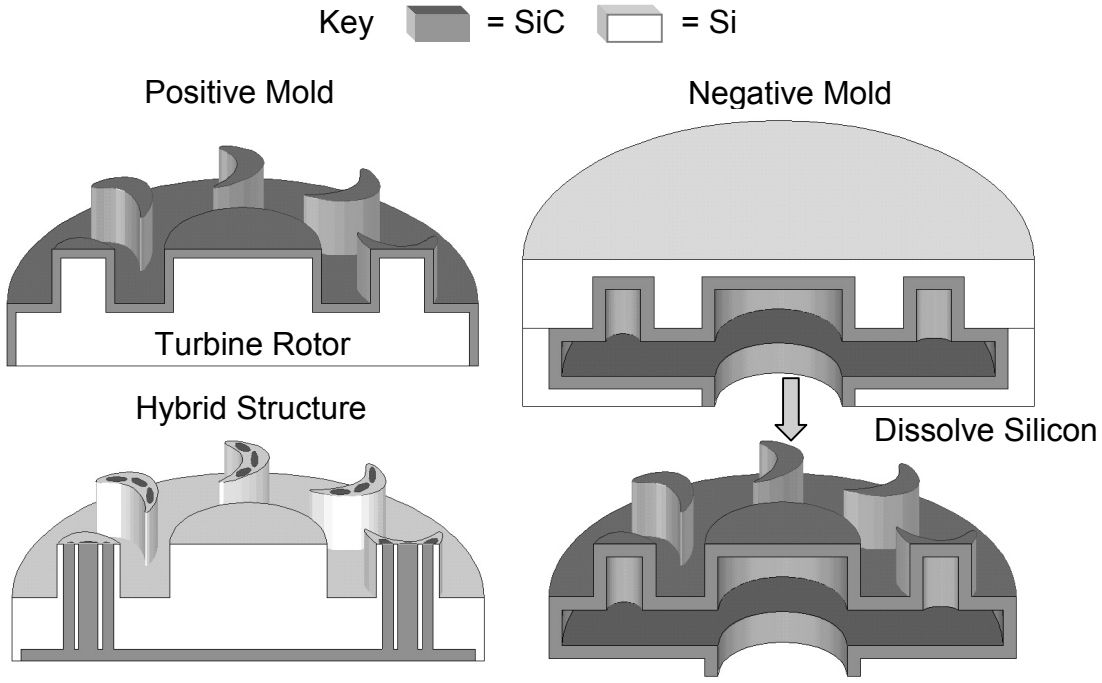

Figure 1.4 Si/SiC hybrid concepts [K. Lohner, S. M. Thesis, Dept. of Aero & Astro, MIT, 1999]

1.2 Background

The overall microengine development requires a multi-disciplinary approach. Thus, it is important to understand the requirements and constraints of the engine before undertaking any redesign of a particular component or inserting a new technology. Before discussing the specific tasks to be performed in the course of this research, it is worth reviewing the status of the development of the microengine rotor in terms of high temperature materials and Si/SiC hybrid structures.

1.2.1 Background of Materials

1.2.1.1 Silicon

In the first generation microengine, silicon is the material of choice for the overall engine structure in order to ensure compatibility with currently available micro-fabrication technology. Obviously, the pronounced thermal softening material behavior of silicon, as shown in Figure 1.2, makes silicon a sub-optimal material for high temperature structures. The turbine rotor of the microengine is exposed to a severe operating environment with peak gas temperatures around 1600 K for hydrogen and 2500 K for hydrocarbon fuels. A high centrifugal loading results from the high rotational speed (1.2 million rpm), which leads to primary stress levels in the range of 250 to 400 MPa.

1.2.1.2 Silicon Carbide

In general, conventional turbine blade materials should satisfy the following criteria: resistance to creep, resistance to high-temperature oxidation, toughness, thermal fatigue resistance, thermal stability, and low density. This is also true for the turbine materials in microengines. Covalently-bonded SiC is a potential material candidate for high temperature MEMS structural applications which satisfies the above criteria. Its creep resistance is outstanding up to 1600 K. Its low expansion and high thermal conductivity also allow it to resist thermal shock well in spite of its relatively low toughness. However, viable micro-fabrication processes for SiC in single crystal form that are as precise as those for silicon have not yet been established. Instead, chemical vapor deposition (CVD) of SiC into silicon molds has been identified as a viable option, together with post-processing steps such as planarization and bonding. Hyper-Therm, Inc., a partner in the MIT microengine project, has explored CVD SiC process technology to assess the viability in terms of material properties and compatibility with microelectronics fabrication processes necessary for MEMS device fabrication [4].

1.2.2 Design constraints of the Microengine Rotor

The extreme operating conditions of the microengine rotor create major design problems. The rotor design requires the following structural considerations: deflection-limited design, fracture design, strength-limited design, and temperature limits.

1.2.2.1 Deflection-limited Design and Brittle Fracture Design

The geometric integrity imposed by the tight tolerance of a few microns requires structures with high specific stiffness. For instance, the journal bearing gap is only a few microns in its designed operating condition. High centrifugal stress and the asymmetric geometrical shape of the blades and rotor induce axial deflection and blade distortion as well as radial expansion, which may deteriorate the bearing operation. Room temperature material characterization has been performed, and probabilistic stress analysis using the resulting material properties reveals that the blade root regions are the locations with the highest probability of failure. The effect of fillet radii determined from the fabrication routes on the stress field has also been accounted for. Weibull statistics has been used to predict the failure probability of the silicon turbomachinery structures using NASA CARES/LIFE [5, 6].

1.2.2.2 Strength-limited Design and Temperature Limits

As the temperature rises from 900 K to 1000 K, the yield strength of silicon drastically decreases from approximately 1 GPa to 100 MPa. This thermal softening behavior has to be taken into consideration in the design stage. As a result, the wall temperature of the all-silicon engine must be kept below 950 K. This temperature limit, however, may not be sufficient because the creep behavior of silicon at temperatures above 900 K may cause a catastrophic failure once yield begins under constant loading. As the temperature is raised, loads that give no permanent deformation at room temperature cause creep. In the case of ceramics, creep starts when the temperature is greater than approximately 40 % of the homologous melting temperature [7]. Preliminary creep characterization of single crystal silicon has been performed by Walters [8]. In Figure 1.5(a), a silicon

specimen after a four-point bend test at high temperature clearly indicates localized deformation resulting from creep and plasticity. The density of active slip bands shown in Figure 1.5(b) is far greater at the loading point than anywhere else in the specimen, consistent with the macroscopic observations of localized deformation.

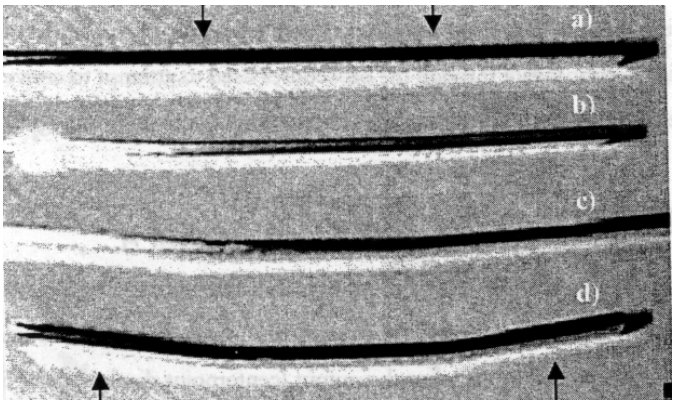

(a)

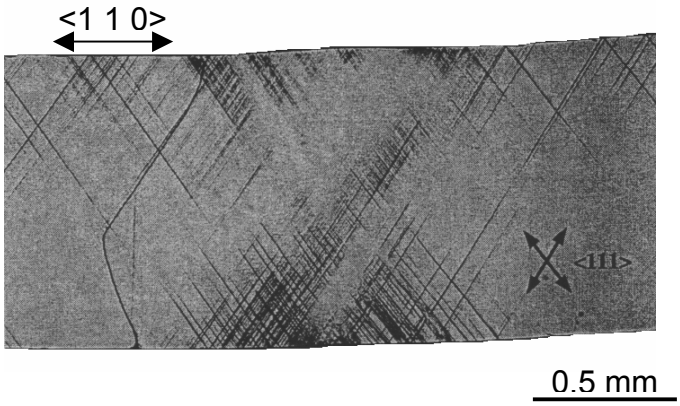

(b)

Figure 1.5 (a) Silicon incremental test specimens sideviews. Center point deflections prior to unload are a) -0.50mm, b) -0.70mm, c) -1.21mm, and d) 1.88mm, (b)Magnified view of the specimen cross-section [D. S. Walters, S. M. Thesis, MIT, 1999]

1.2.3 Si/SiC Mirco-fabrication Processes

The use of SiC in single crystal form is not possible because viable micro-fabrication processes, as precise as those for silicon, have not yet been established. Instead of single crystal SiC, chemical vapor deposition (CVD) of SiC on silicon molds is a promising process candidate. However, post-processing of CVD SiC is still challenging because of the chemical inertness and hardness of SiC, which is second only to diamond.

1.2.3.1 Planarization

The planarization of surfaces plays a key role in the fabrication of Si/SiC hybrid structures. Surface roughness of less than 20 nm with good surface flatness is required for a reliable bond [9]. In order to create the sufficiently flat surfaces required for high reliability bonding, chemical-mechanical polishing (CMP), in which the wafer is polished in an abrasive slurry on a polishing pad, may be used. However, due to the chemical inertness of SiC, the current planarization process relies only on mechanical polishing (lapping), which is a tedious process and currently suffers from low yields.

1.2.3.2 Bonding

Wafer bonding techniques rely on achieving sufficiently flat, planar surfaces (wafer bow on the order of a few micrometers) and carefully controlling the surface chemistry. Initial efforts to bond silicon and SiC at the die level have been made under elevated temperatures and pressures in order to utilize the plasticity and diffusional flow of the silicon [9]. The bond strength of tested samples has yet to be measured, and the physics controlling the bond strength is not clearly understood. Developments of techniques for bonding dissimilar materials at the wafer level and controlling the residual stresses that can arise in these structures are under way [10].

1.2.4 Preliminary FE Analysis of Si/SiC Hybrid Structure

In order to improve the microengine's performance, the heat flux from the turbine into the compressor must be reduced by introducing a thermal barrier structure between the two rotors. Decreasing the heat flux, however, implies that the turbine wall temperature may increase higher than the silicon can withstand. Thus, it is critical for the development of the next generation engine that a high temperature structure with a thermal barrier be built. The structural analysis has focused on predicting the maximum operating temperature that the proposed hybrid structures can withstand and assessing the benefits from the spool design from the point of view of the overall engine efficiency. Miller

demonstrated the potential of Si/SiC hybrid structures for increasing the operating temperature of the microengine spool by a series of finite element (FE) analyses [3].

Two design candidates were compared with the baseline engine and a breakeven case in terms of the overall engine efficiency: first, a combination of a disc with 30 % SiC reinforcement and blades with 60 % SiC core and second, a combination of a disc with 30 % SiC reinforcement and all-silicon blades with 60 % core together with a thermal barrier. The engine performance and the corresponding configuration of the thermal barrier were estimated by a 1-D cycle analysis [11]. The comparison among these cases is summarized in Table 1.1. Considering the complications such as filling SiC into a narrow channel, the second design candidate is the preferred one. Thus, the second candidate was proposed as a baseline design for the next generation engine. Figure 1.6 illustrates the proposed conceptual design.

Table 1.1 Contribution of a Si/SiC hybrid spool to the engine performance [B. Miller, MS Thesis, Dept. of Aero & Astro, MIT, 2000]

Configuration	Max. Temp. [K]	A/A*	Cycle Press. Ratio	Compressor Efficiency	Shaft Power (W)	Engine Efficiency
Baseline : all Si	950	100 %	1.7	0.36	-	-
0 Net power	960	25 %	1.7	0.38	0	0 %
30% SiC disc 300um SiC core	1200	2.5 %	2.125	0.53	16.8	3.1 %
30% SiC disc 300um Si core	1160	3.0 %	1.93	0.52	13.6	2.5 %

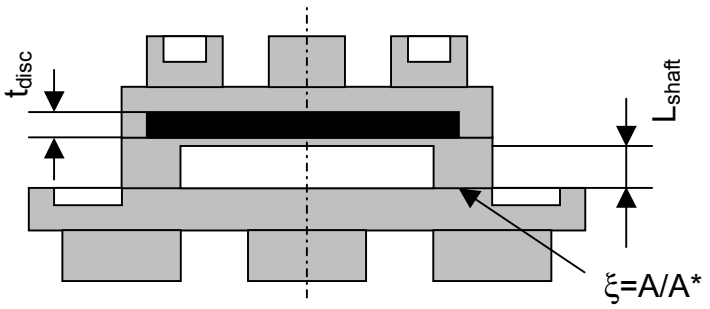

Figure 1.6 Proposed conceptual design of a Si/SiC hybrid rotor [B. Miller, MS Thesis, Dept. of Aero & Astro, MIT, 2000]

1.3 Objectives

As a part of the MIT microengine project, the primary goal of this research is to design a high temperature Si/SiC hybrid rotor that improves the overall engine efficiency while maintaining structural integrity. While successful in yielding the proposed Si/SiC hybrid rotor from the previous work [2, 3, 5, 8], the detailed design of the hybrid rotor has been limited by the lack of understanding of the mechanical behavior of Si and Si/SiC hybrid structures at elevated temperatures. The materials and structures issues associated with the microengine rotor and the overall system considerations result in two main objectives for this thesis, namely:

1) To develop a self-consistent design for Si/SiC hybrid structures for elevated temperature micro-turbomachinery, power MEMS, given the constraints imposed by the micro-fabrication processes and system considerations.
2) To obtain elevated temperature mechanical property data for Si and Si/SiC structures and to extract constitutive models to support the design process.

In order to achieve these objectives, tasks to be performed include mechanical testing at elevated temperatures, mathematical modeling of silicon and SiC constitutive behavior revealed by the experiments, and implementation of the constitutive model in a finite element code. With this material model implemented, the FE analysis will enable design iterations of Si/SiC hybrid structures for elevated temperature operation. The development of the micro-fabrication processes required to create Si/SiC hybrid structures is under way in a parallel effort. Figure 1.7 describes the flow chart for the design of high temperature Si/SiC hybrid micro-turbomachinery, where the required tasks are organized toward the overall goal of this work.

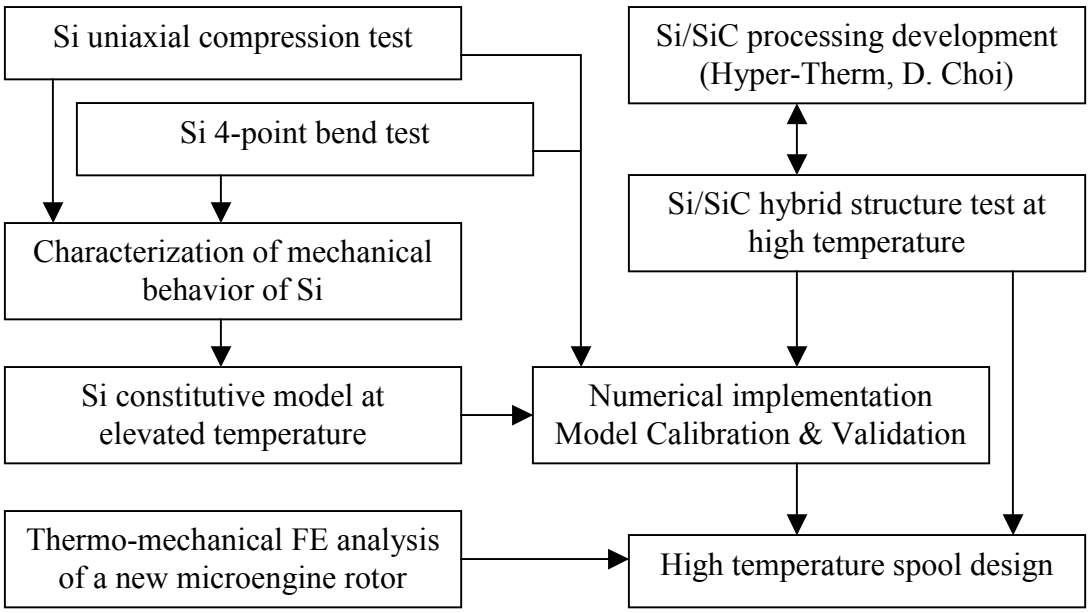

Figure 1.7 Flow chart for the design of high temperature Si/SiC hybrid micro-turbomachinery

1.4 Thesis Outline

The chapters of this thesis are arranged as a series of coherent steps towards achieving the objectives stated in Section 1.3.

Chapter 2 describes the initial structural design of the Si/SiC hybrid turbine rotor. This chapter presents the initial design efforts made in parallel with the overall microengine development, given the constraints imposed by the micro-fabrication and system considerations. The initial structural design includes a series of thermo-mechanical FE analyses to obtain temperature and stress fields of Si/SiC hybrid structures to assess the advantage of the hybrid structure, and to provide structural design criteria and fabrication requirements. However, limitations due to the unavailability of an accurate material model that accounts for creep and strain softening behavior of single crystal silicon call for a better material model for Si based on more rigorous mechanical testing at high temperatures. Chapter 3 provides a review of the material characterization of single crystal silicon at high temperatures. A general description of creep and creep

mechanisms for various classes of materials is given, followed by a review of previous work pertaining to the experimental studies on Si creep. A brief review on various types of constitutive models and material testing methods suggests the appropriate direction to take for the development of a new constitutive model for single crystal silicon at elevated temperature. In Chapter 4, the experimental methods are proposed to investigate the mechanical behavior of Si at the temperatures and stresses of interest and to assess the feasibility of Si/SiC hybrid structures. Separate subsets of the experimental methods are designed to allow for both the calibration and validation of the Si material model. Further, a Si/SiC hybrid flexural specimen is also described as a simple means to verify the hybrid structural concept for the microengine. Details are given with regard to specimen fabrication, test methods, and test apparatus. Chapter 5 presents the efforts carried out to understand the mechanisms active in the mechanical behavior of single crystal silicon at high temperatures and high stresses and to model its constitutive behavior at the macro scale. This chapter describes a constitutive model for silicon, necessary to predict accurately the deformation of Si/SiC hybrid structures, that accounts for its creep and strain softening as well as the micro mechanisms governing the elevated temperature mechanical behavior. This constitutive model for silicon implemented in the ABAQUS^{TM} user subroutine, VUMAT [12], is calibrated and then validated against the various experimental results. In Chapter 6, the structural design of the Si/SiC hybrid rotor is revisited with the advanced design tool, a constitutive model for Si at elevated temperature. The appropriate design guidelines are extracted based on the better knowledge and the experimental observations of the deformation mechanisms of Si and Si/SiC hybrid structures, together with the advanced constitutive model for Si. Finally, Chapter 7 gives overall recommendations and conclusions regarding the design of high temperature Si/SiC hybrid micro-turbomachinery.

References

1. A. H. Epstein, S. D. Sentura, Macro Power from Micro Machinery, SCIENCE Magazine, Vol. 276, 23 May 1997.
2. K. A. Lohner, Microfabricated Refractory Ceramic Structures for Micro Turbomachinery, S. M. Thesis, Dept. of Aeronautics and Astronautics, MIT, Cambridge, MA, 1999.
3. B. Miller, Hybrid Silicon/Silicon Carbide Microstructures and Silicon Bond Strength Tests for the MIT Microengine, S. M. Thesis, Dept. of Aeronautics and Astronautics, MIT, Cambridge, MA, 2000.
4. R. J. Shinavski, W. S. Steffier, Enhanced Strength, Nanolayered SiC for Micro-Gas Turbine Portable power Generation, ARO report by Hyper-Therm Inc., 1999.
5. K.-S. Chen, Materials Characterization and Structural Design of Ceramic Micro Turbomachinery, Ph. D. Thesis, Dept. of Mechanical Engineering, MIT, Cambridge, MA, 1999.
6. S. M. Spearing, K.-S. Chen, Micro-Gas Turbine Materials and Structures, 21st Annual Cocoa Beach Conference and Exposition on Composite, Advanced Ceramics, Materials and Structures, Jan., 1997.
7. M. F. Ashby, D. R. H. Jones, Engineering Materials 1, 2nd ed, Butterworth Heinemann,1996.
8. D. S. Walters, Creep Characterization of Single Crystal Silicon in Support of the MIT Microengine, S. M. Thesis, Dept. of Mechanical Engineering, MIT, Cambridge, MA, 1999.
9. D. Choi, A. A. Arturo, personal communication, GTL, MT, 2000.
10. D. Choi, R. J. Shinavski, S. M. Spearing, Process Development of Silicon-Silicon Carbide Hybrid Micro-Engine Structures, Mat. Res. Soc. Symp. Proc., Vol. 687, B5.44, Fall 2001.
11. J. Protz, An Assessment of the Aerodynamics, Thermodynamics, and Manufacturing issues for the Design, Development, and Micro-fabrication of a Demonstration Micro Engine, Ph. D. Thesis, Dept. of Aero & Astro, MIT, 2000.
12. ABAQUS/Standard v5.8, Hibbitt, Karsson, & Sorrencen, Inc., 2001.

Chapter 2

Initial Structural Design of Si/SiC Hybrid Rotor

2.1 Overview

Silicon, the material of choice for the first (demonstration) microengine, exhibits strong thermal softening behavior at temperatures above 900 K. This thermal softening behavior limits the turbine inlet temperature, which in turn significantly degrades the overall engine efficiency. Thus, the strategy employed in the all-silicon demonstration engine was to design the rotor so that there is a high heat flux from the turbine rotor to the compressor to keep the wall temperature of the turbine rotor below 950 K, at which temperature the Si yield strength is on the order of 250 MPa. This strategy, while permitting a workable demonstration device, has a severe negative impact on the engine efficiency and power output.

In order to improve the microengine's performance, the heat flux from the turbine into the compressor must be reduced by introducing a thermal barrier structure between the turbine and compressor. Decreasing the heat flux, however, implies that the turbine wall temperature may increase higher than the silicon can withstand. Thus, it is critical for the development of the next generation engine that a high temperature structure with a thermal barrier be built allowing for the micro-fabrication constraints. The proposed conceptual design of a Si/SiC hybrid rotor structure, which exploits the superior mechanical properties of SiC at high temperatures, but is feasible to micro-fabricate, is shown schematically in Figure 2.1. The rationale that led to this structural design has been discussed in more detail together with preliminary structural analyses and its contributions to the overall engine performance in reference [1].

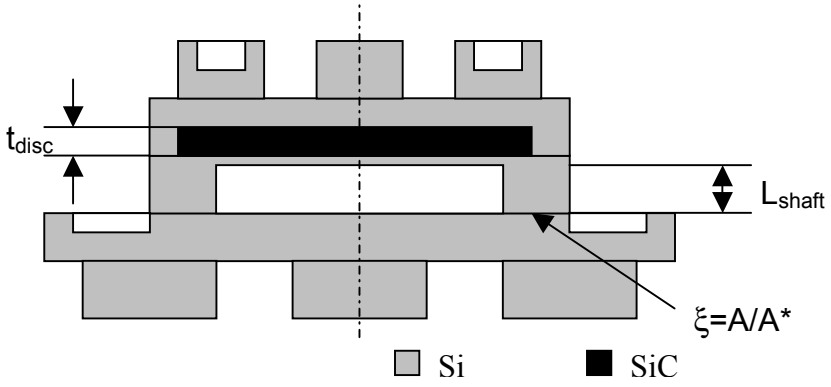

Figure 2.1 Proposed conceptual design of a Si/SiC hybrid rotor

In this chapter, the structural analysis for the microengine rotor is focused on predicting the maximum operating temperature that the proposed hybrid structures can withstand and assessing the benefits from the spool design from the point of view of the overall engine efficiency. A full 3-D thermo-mechanical FE analysis enabled the identification of hot spots that may cause a catastrophic failure when combined with high stress concentrations. Structural concerns that arise from the thermal barrier/insulation between the turbine and compressor rotors have also been accounted for using axisymmetric thermo-mechanical FE analysis with a simplified blade shape. The following results demonstrate the potential of Si/SiC hybrid structures to improve the engine performance. This chapter concludes with an assessment of the conceivable problems associated with the mechanical behavior of Si at elevated temperatures which have not previously been considered in detail.

2.2 Material Properties

This section summarizes the values of the material properties of Si and CVD SiC necessary for the following structural analysis to be performed. While most of the values of the material parameters used in the previous studies by Chen [2] and Miller [1] were adopted in the current work, additional comprehensive material data for Si are available in reference [3]. By comparison, material data for CVD SiC are rather limited. Recently

the elastic material properties of the CVD SiC were reported by Jackson [4] and Hyper-Therm, Inc. [5]. These values will be used in the following analysis.

2.2.1 Mechanical properties

2.2.1.1 Single crystal silicon

As the melting temperature of Si is relatively low ($T_{melt\ Si}$ = 1396-1444 °C, ASTM), most of the mechanical material properties of Si are temperature-dependent at the temperatures of interest. Furthermore, the anisotropic material parameters associated with the cubic symmetry of single crystal silicon also add more complexity to the structural analysis. Table 2.1 summarizes the elastic material properties of Si. In view of the difficulties of performing exact calculations in anisotropic media, the isotropic approximation is often preferred. From the comparison of the isotropic 2-D FE results and 3-D FE results with cubic material parameters for the biaxial fracture strength testing, Chen justified the use of isotropic approximation of the material parameters in the subsequent analyses [2]. In the current study, the isotropic approximation of the elastic material properties were used together with the linear temperature-dependence. The density of 2330 kg/m^3 was used for silicon throughout.

Table 2.1 Elastic material properties of silicon

Elastic material properties	Values
Elastic stiffness at room temperature and atmospheric pressure[1]	C_{11} = 165.6 GPa C_{12} = 63.9 GPa C_{44} = 79.5 GPa
Temperature-dependence of the elastic stiffness[2]	$(1/C_{11})dC_{11}/dT$ = -9.4E-5 K^{-1} $(1/C_{12})dC_{12}/dT$ = -9.8E-5 K^{-1} $(1/C_{44})dC_{44}/dT$ = -8.3E-5 K^{-1}
Average Young's modulus[3]	E_{ave} = 165.6 GPa
Poisson's ratio[3]	ν = 0.218

1. The values were reported by Hall [6].
2. The temperature-dependence of Cij was investigated by Hall [6] in the range 4.2-310 K, and Burenkov and Nikanorov [7] up to 1273 K. In the temperature range of 150 to 1000 K, the decrease rate of the Cij with increasing temperature is fairly linear.
3. The isotropic approximation was obtained by Voigt averaging [3].

The softening behavior of Si at elevated temperatures was accounted for by using the yield strength of Si at the given temperatures in the following analyses. To be consistent with Miller in the previous work [1], the same linear fit of the Si yield strength against Chen's experiments [2] in the temperature range of 600 to 1220 K was used. The structural analysis presented in this chapter does not take the post-yielding behavior of Si (softening or hardening) into consideration. ABAQUS^{TM} PLASTICITY [8] was used, in which silicon was defined as an elastic-perfectly plastic material in the simulations. Section 2.5 further discusses the yield strength of Si.

2.2.1.2 CVD SiC

The preliminary study on the Si/SiC hybrid turbine rotor used bulk material properties of SiC. Recently the elastic material properties of CVD SiC processed at Hyper-Therm were measured by Jackson at room temperature [4]. The high melting temperature of SiC (3110 K in a bulk form) justifies the use of the material properties of CVD SiC measured at room temperature for the structural analysis at the temperatures of interest. The material data for SiC are summarized in Table 2.2.

Table 2.2 Material properties of SiC

Material properties	Values
Young's modulus	470 GPa in a bulk form 430 GPa, CVD SiC film
Poisson's ratio	0.21
Density	3200 kg/m^3

2.2.2 Thermal properties

The analysis presented in this chapter considered only the thermal steady-states. The temperature field calculated by the heat transfer analysis was then taken as a boundary condition for the stress analysis (sequentially coupled thermal-stress analysis). This sequentially coupled thermal-stress analysis requires two thermal properties: thermal conductivity and thermal expansion coefficient. At the temperatures of interest, these parameters are temperature-dependent as shown in Figure 2.2 and Figure 2.3. The

thermal properties of CVD SiC were taken from the Morton^{TM} CVD SiC data sheet [9]. As the temperature gradient within the SiC layer is negligibly small, the average thermal conductivity of 80 W/mK was used for SiC in the heat transfer analysis.

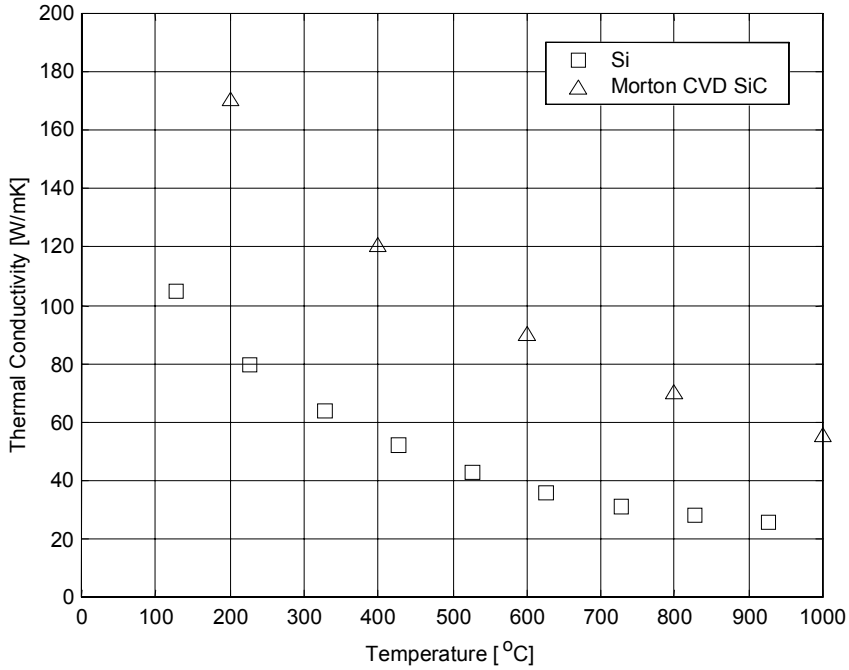

Figure 2.2 Thermal Conductivity of Si and CVD SiC [3, 9].

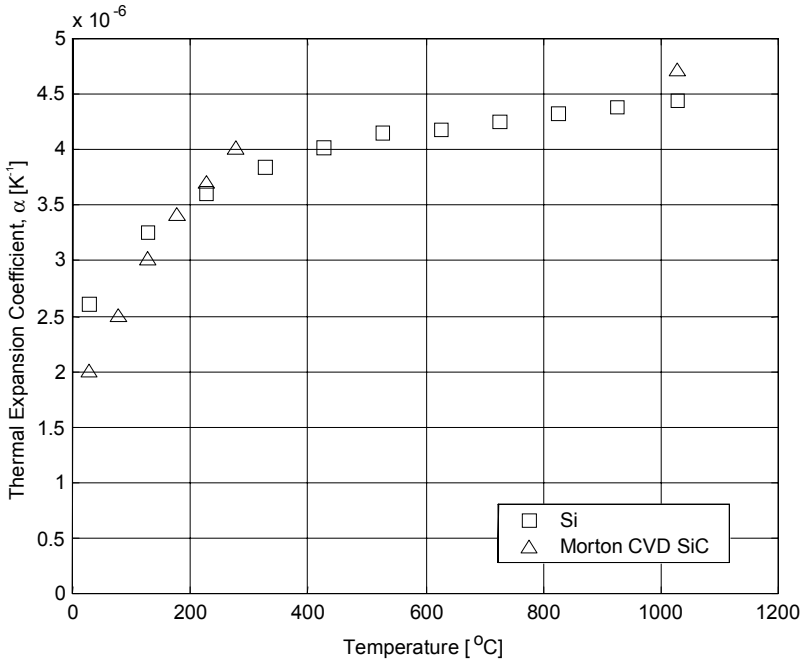

Figure 2.3 Thermal Expansion Coefficient of Si and CVD SiC [3, 9]

2.3 Structural Analysis of Hybrid Turbine Rotor

2.3.1 Preliminary FE analysis of Hybrid Turbine Rotor

3-D FE simulations for a hybrid turbine rotor have been performed with a refined model combining the turbine disc and blade as shown in Figure 2.4 in order to verify the previous structural analysis by Miller [1], where the hybrid turbine blade and disc were considered as separate bodies. The FE mesh was created using a commercial pre-/ post-processing package, MSC/NASTRAN^{TM} [10], and analyzed using ABAQUS^{TM} STANDARD [8], a commercially available finite element package. A relative SiC thickness of 30 % was incorporated in the turbine rotor disc in between Si disc layers. While SiC, whose melting point is 3300 K, was assumed to behave elastically throughout the temperature range (up to 1200 K), the material model for Si was assumed to be elasto-plastic as modeled by ABAQUS^{TM} STANDARD PLASTICITY with no strain-hardening/softening behavior. The thermal softening behavior of Si was described with the yield strength decreasing with increasing wall temperature according to:

$$\sigma_Y = -A*T + B, \quad (1)$$

where A and B are the linear fit coefficients. Assuming that the periodic boundary condition has little influence on the overall deformation and stress fields of the rotor, only one twentieth of the turbine rotor is modeled. For simplicity, the thermal barrier (hollow shaft) is modeled as a linear spring.

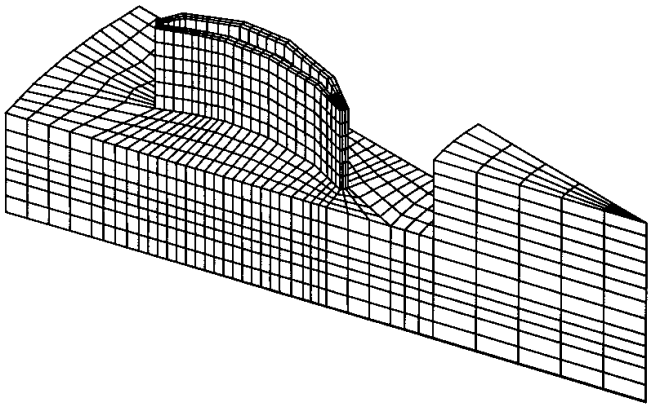

(a)

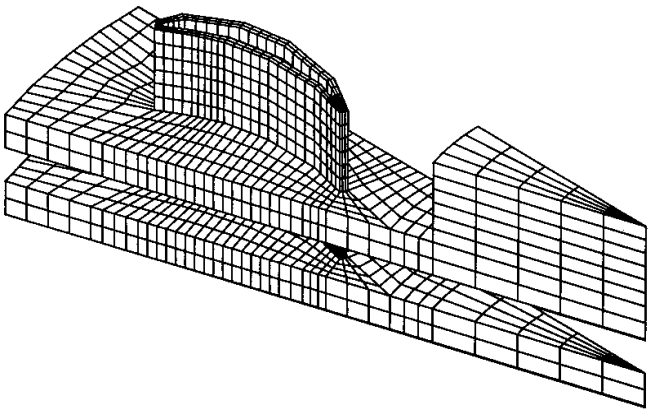

(b)

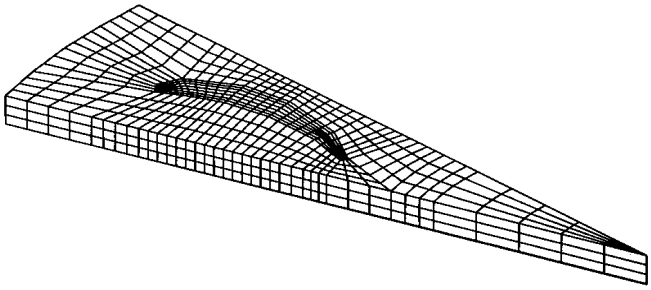

(c)

Figure 2.4 Refined FE model for blade and disc (a) total FE mesh, (b) FE mesh for the silicon, and (c) FE mesh for the SiC

As illustrated in Figure 2.5, the geometrical configurations considered here are as follows:

(1) Solid silicon blade and disc reinforcement with 30% SiC
(2) All-silicon hollow blade with a half-height inner core and disc reinforcement with 30% SiC
(3) Hybrid Si/SiC hollow blade with a half-height SiC inner core and disc reinforcement with 30% SiC
(4) All-silicon hollow blade with a half-height inner core and SiC post up to blade roots and disc reinforcement with 30% SiC

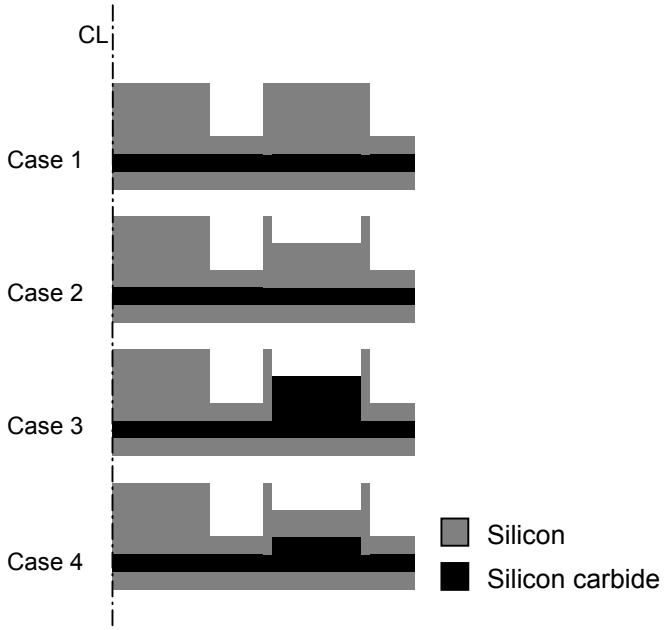

Figure 2.5 Geometrical configurations considered in the analysis

Figure 2.6 shows how the maximum stresses and deflections for each case vary as the temperature increases. The results are summarized in Table 2.3. This refined 3-D FE simulation correlates well with the previous hybrid disc and blade analysis in terms of the prediction of the maximum turbine wall temperature that the hybrid structure can withstand. In conclusion, the FE simulation results confirm the potential of the hybrid structure concept for improving engine efficiency, and although there is little difference in achievable maximum operating temperature among the four cases, Case 2 (all-silicon hollow blade and disc reinforced with SiC) stands out as a prospective candidate for the hybrid turbine rotor when micro-fabrication difficulties are taken into account.

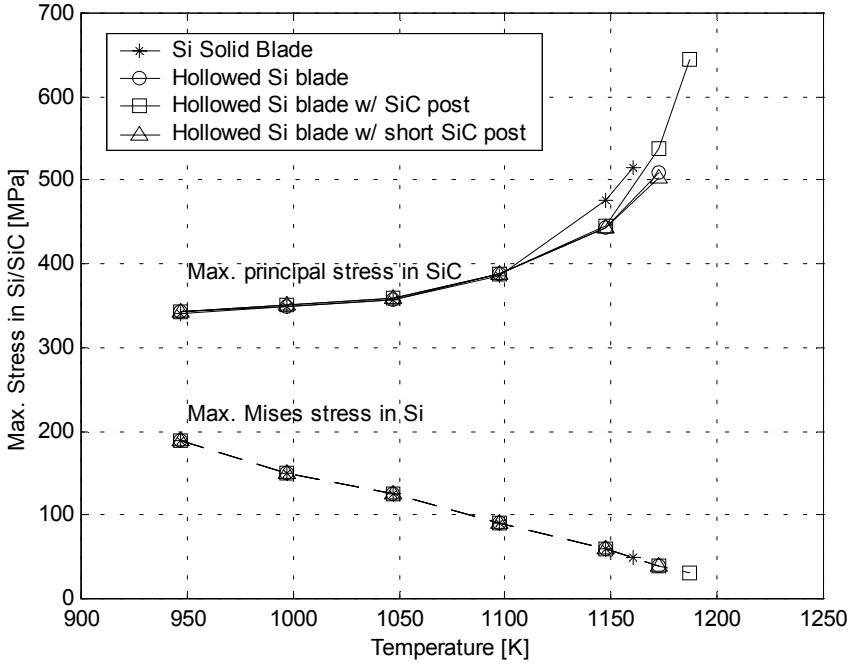

(a)

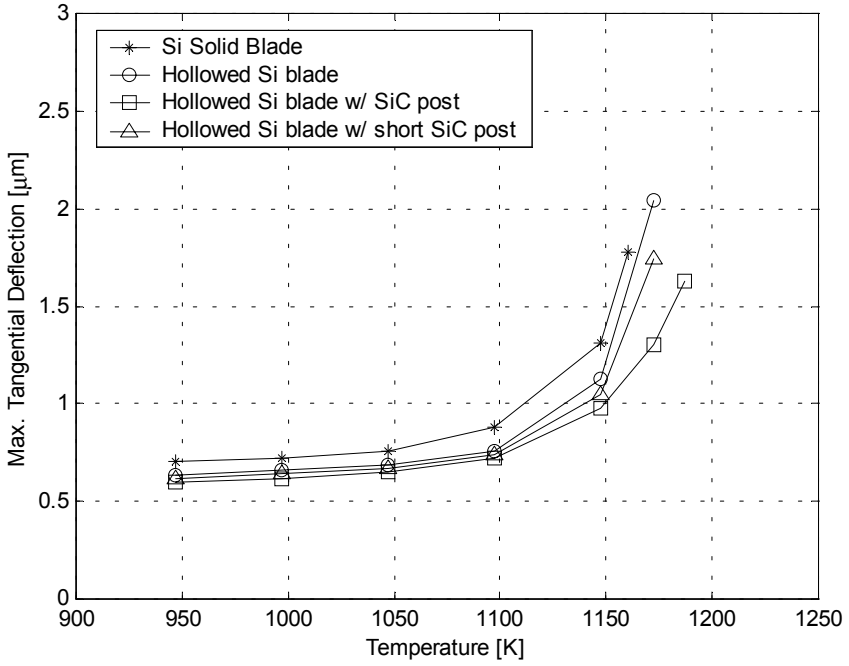

(b)

Figure 2.6 Key maximum stresses and deflections in the Si/SiC hybrid turbine rotor of four design configurations (a) Maximum stress in silicon and silicon carbide (b) Maximum radial expansion (c) Maximum tangential deflection (d) Maximum vertical deflection

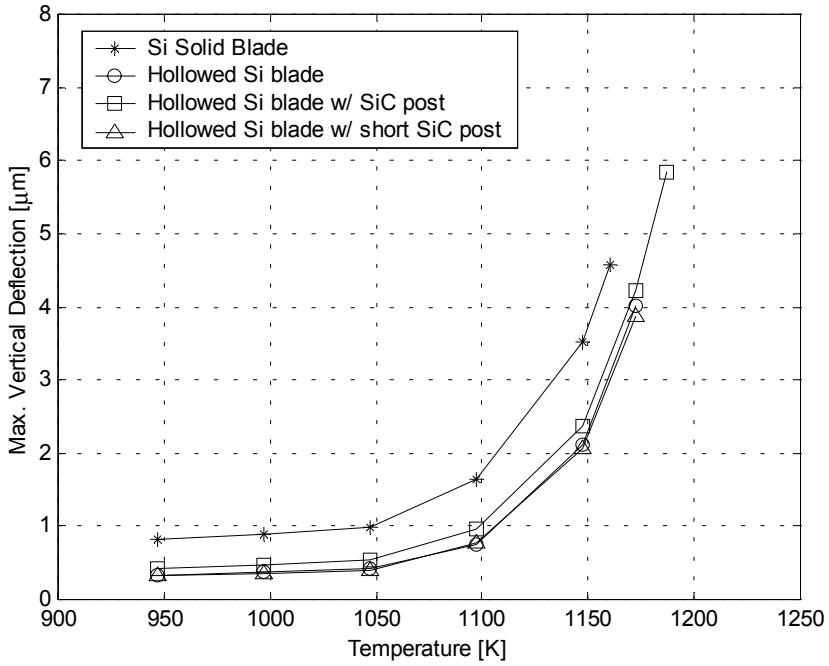

(c)

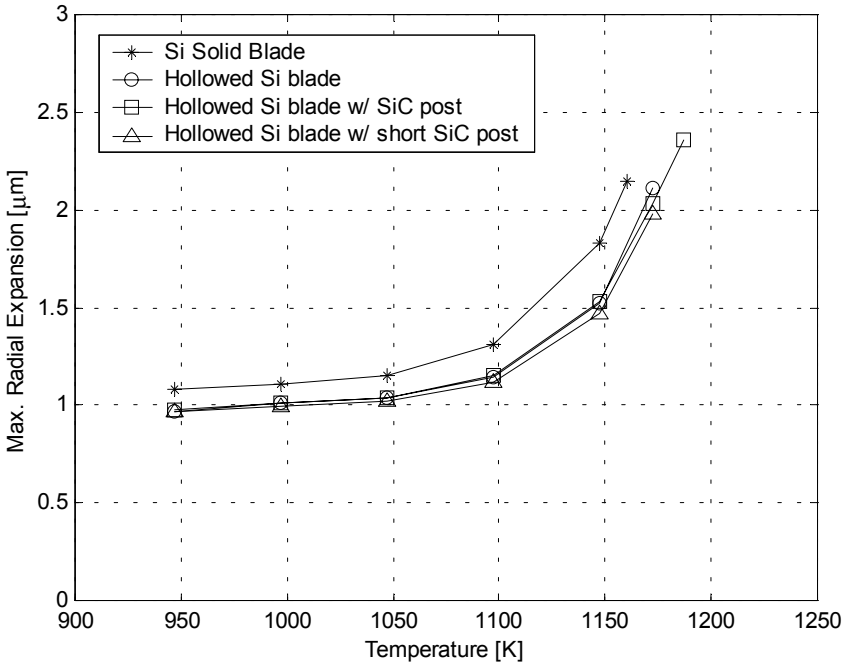

(d)

Figure 2.6 (continued) Key maximum stresses and deflections in the Si/SiC hybrid turbine rotor of four design configurations (a) Maximum stress in silicon and silicon carbide (b) Maximum radial expansion (c) Maximum tangential deflection (d) Maximum vertical deflection

Table 2.3 Summary of FE calculations of the Si/SiC hybrid turbine rotor

Case	Max. Temp. [K]	Max. stress in SiC [MPa]	Max. radial expansion [μm]	Max. tangential deflection [μm]	Max. vertical deflection [μm]
Solid Si blade + 30% SiC disc	1160	514	2.2	1.8	4.6
All Si hollow blade + 30% SiC disc	1175	509	2.1	2.0	4.0
Hollow Si blade w/ 50% SiC core + 30% SiC disc	1190	644	2.4	1.6	5.8
All Si hollow blade w/ SiC post up to blade root + 30% SiC disc	1175	510	2.0	1.7	3.9

* Stress and deflection values are obtained at the corresponding maximum temperature.

2.3.2 Thermo-mechanical FE Analysis of Turbine Rotor

The structural analysis results in the previous section were obtained assuming uniform temperature in the turbine rotor, which is a reasonable assumption, given the Biot number of approximately 0.02. The isothermal assumption, however, may not be valid when there is a heat sink (i.e., the compressor) that gives rise to a high thermal gradient. Thus, in order to identify any hot spots in the structure that may cause a catastrophic failure when combined with high local stresses, a 3-D thermo-mechanical FE analysis has been performed using the same FE mesh. It is critical that accurate thermal boundary conditions, which are not always readily available, be applied in the analysis. The thermal boundary conditions shown in Figure 2.7 were based on the previous analysis [2] and the CFD results [11]. For simplicity, the thermal barrier structure (hollow shaft) is again modeled structurally as a linear spring.

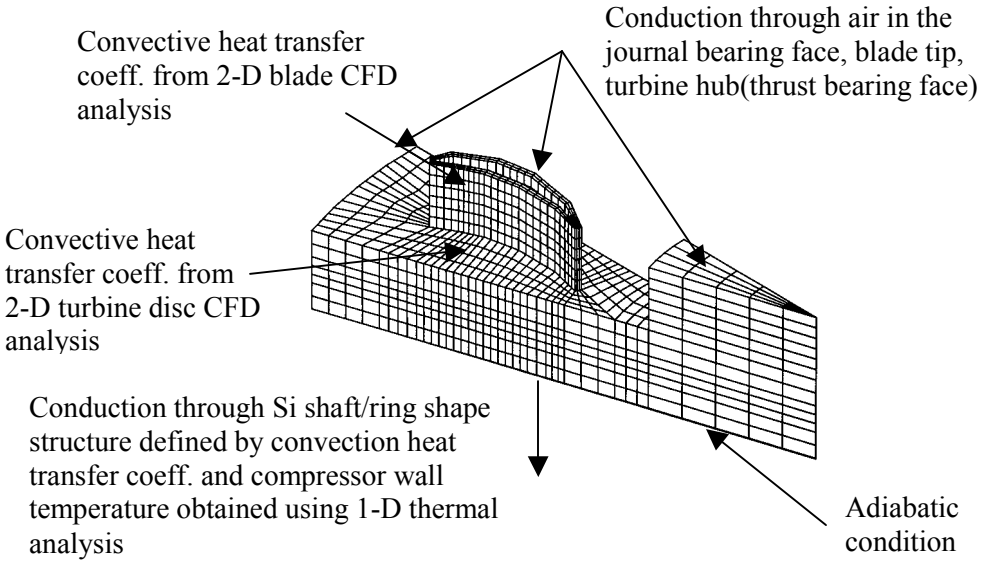

Figure 2.7 Thermal boundary condition for the turbine rotor

As is clear in Figure 2.8(a), the temperature distribution of the turbine rotor with a shaft/ring of 1.5 mm inner radius, 100 μm wall thickness, and 600 μm shaft length, shows a considerable temperature gradient. The highest temperature occurs at the tip of the blade and the lowest at the area adjacent to the shaft end. The lower temperature is lower than that predicted by the 1-D thermal cycle analysis [12]. Similarly the temperature of the compressor side, the shaft heat flux is expected to be less than the prediction of the 1-D cycle analysis by approximately 20 %, which in turn implies that the thermal barrier structures may be more effective than indicated by the preliminary analysis. Figure 2.8(b) and (c) show the effective stress and effective plastic strain, respectively, corresponding to the temperature field. While the high stress state of the SiC in the center indicates that the centrifugal inertial load is carried mostly by the SiC reinforcement, the high stress in the SiC reinforcement below the blade trailing edge is caused by the bending moment due to the blades. The plastic strain developed on the surface of the turbine rotor disk shown in Figure 2.8(c) implies that the elastic material around the deformed zone is still sufficient to support the centrifugal loading, but it may subject to a catastrophic failure owing to the strain softening behavior of Si.

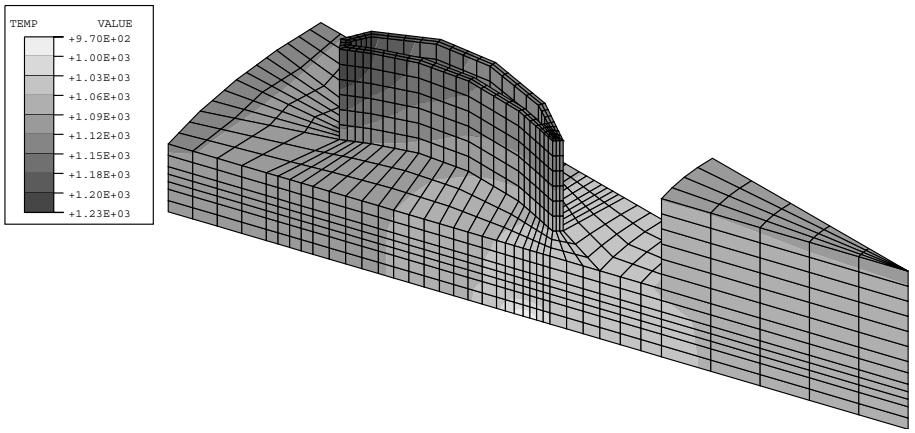

(a)

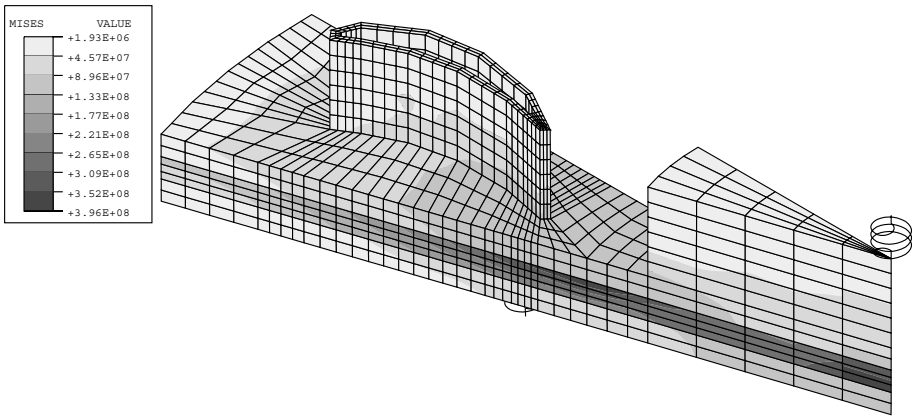

(b)

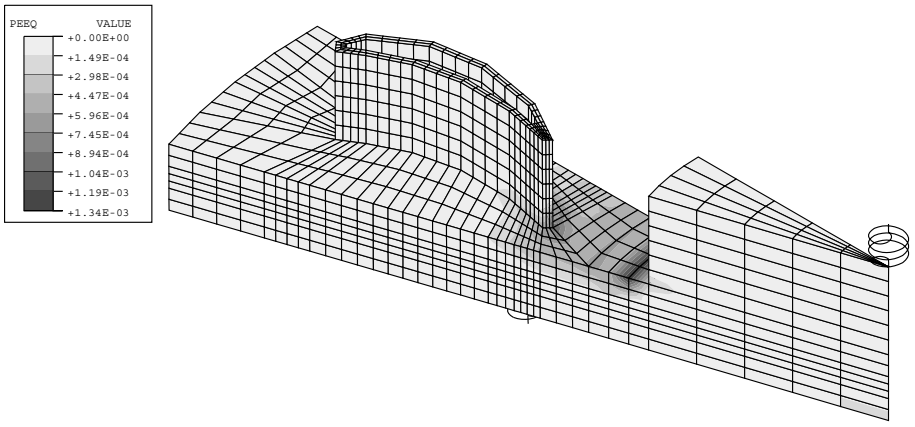

(c)

Figure 2.8 Thermo-mechanical FE analysis results of a turbine rotor when R_i = 1.5 mm, t_{wall} = 100 μm, L_{shaft} = 600 μm, (a) temperature distribution, (b) effective stress distribution, and (c) effective plastic strain

2.3.3 Structural Analysis of Thermal Barrier

The small Biot number of the rotor implies that in order to improve the engine efficiency a significantly low thermal conductance ($1/R_{th} = k_{th} A^*/L$, where Kth is the thermal conductance of Si, A* the area that contacts with the rotor, and L the length of the shaft) is required. This in turn may compromise the overall strength of the structure. In addition the difficulties associated with the deep etching process for the journal bearing face and wafer bonding process impose severe geometrical constraints on the achievable wall thickness and shaft length. For simplicity, the turbine blades and compressor blades were modified so as to apply the equivalent bending moment to the shaft so that an axisymmetric FE model can be used. The thermal boundary conditions were again based on the previous analysis [2]. Figure 2.9 shows the FE results of the thermal insulation structure between the turbine and compressor rotors in the case where $A/A^* = 0.2$ (R_i = 1.5 mm, t_{wall} = 0.4 μm, and L_{shaft} = 0.4 μm). Figure 2.9(b) and (c) represent the shear and normal stress in the axial direction, respectively, corresponding to the temperature field shown in Figure 2.9(a). Both the shear stress and normal stress were significant due to the bending moment from the blades and the discrepancies in the radial expansion of the turbine and compressor rotors.

The temperatures at both ends of the shaft are plotted on Figure 2.10(a) together with predictions using the 1-D thermal cycle analysis. Given the temperatures and the thermal conductance as a function of temperature, the shaft heat flux was calculated and compared with the thermal cycle analysis prediction in Figure 2.10(b). In Figure 2.10(c), the stress states as a function of normalized thermal conductance are shown. From the FE results, it is concluded that given the micro-fabrication limits, a thermal barrier structure is feasible, satisfying both thermal and structural requirements.

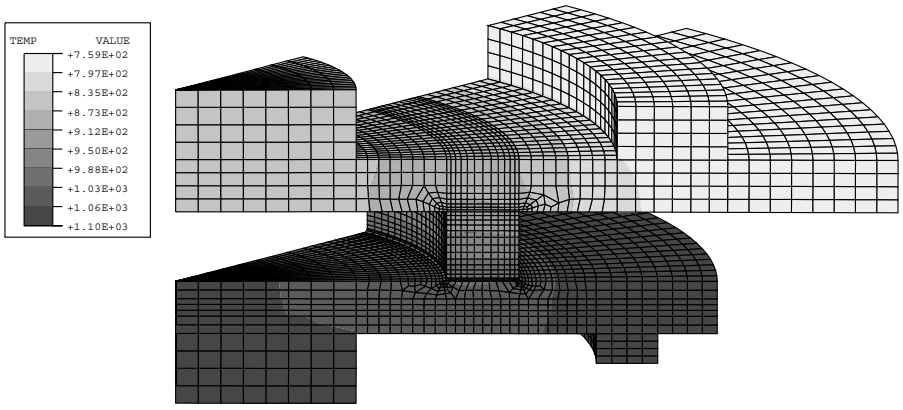

(a)

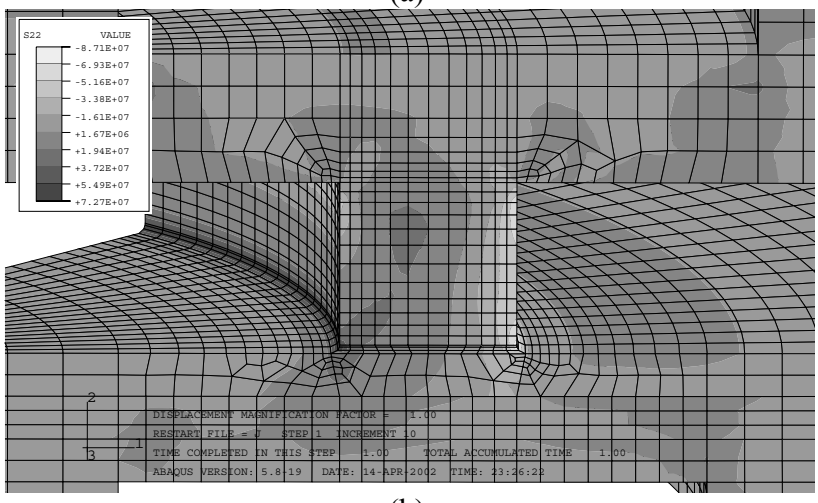

(b)

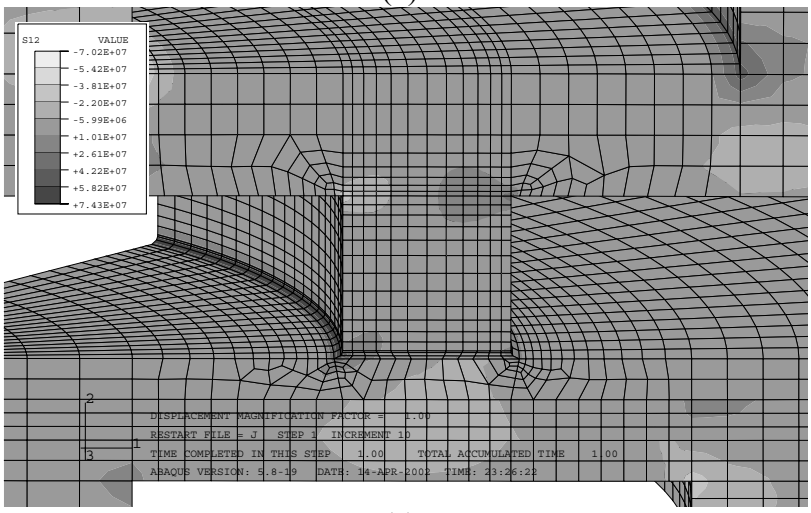

(c)

Figure 2.9 FE results for the thermal insulation structure between the turbine and compressor disks in the case where $A/A^* = 0.2$ ($R_i = 1.5$ mm, $t_{wall} = 0.4$ μm, and $L_{shaft} = 0.4$ μm), (a) temperature distribution, (b) σ_{22}, and (c) σ_{12}

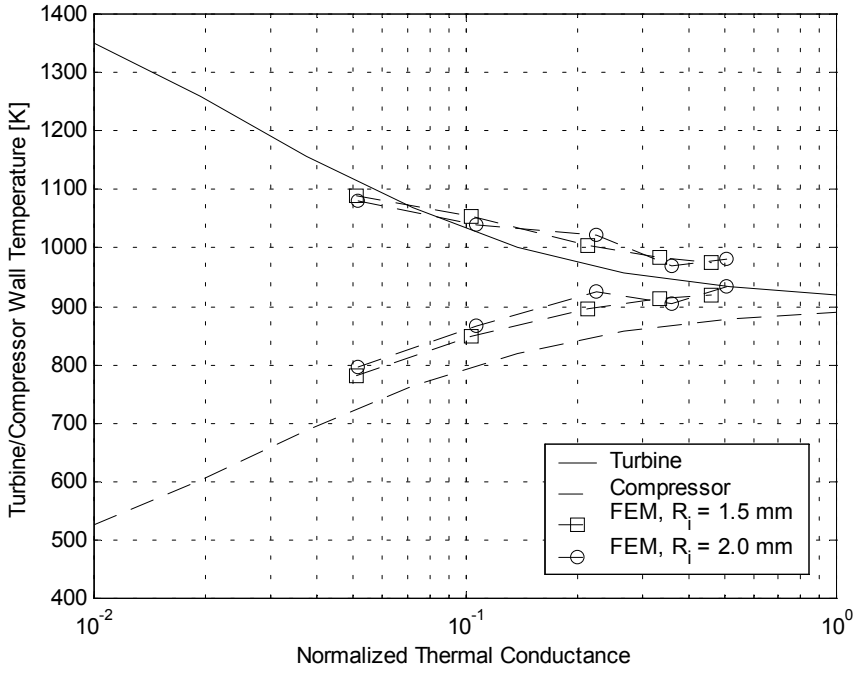

(a)

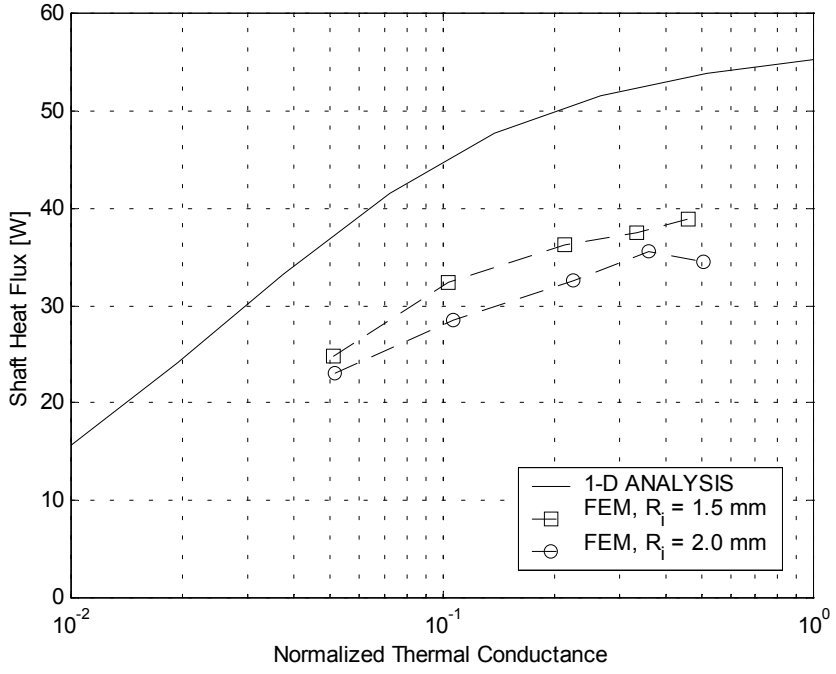

(b)

Figure 2.10 Comparison of FE results for the thermal insulation structure with a 1-D cycle analysis, (a) temperatures of the both ends of the shaft, (b) shaft heat flux, and (c) stresses on the corner of the shaft.

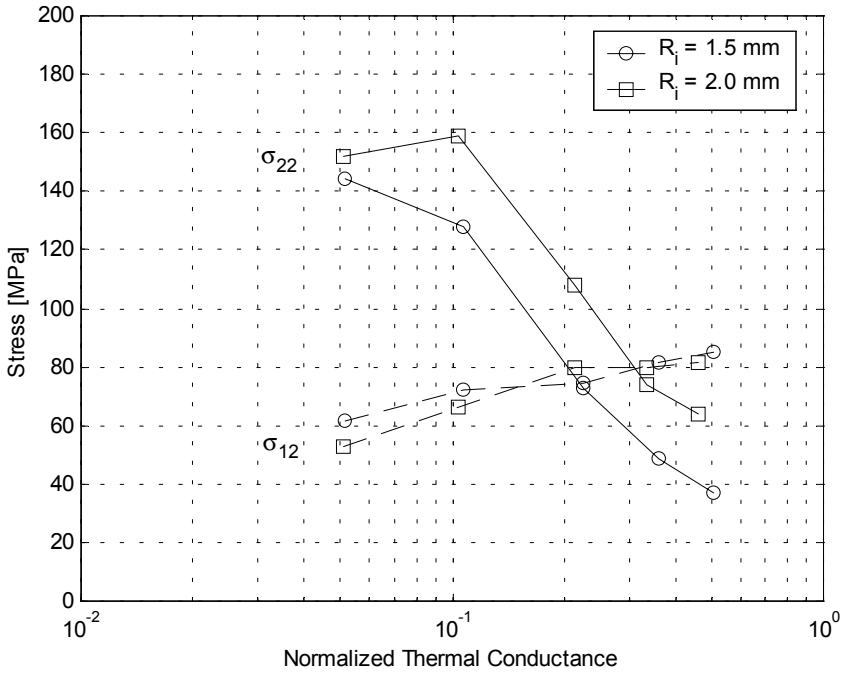

(c)

Figure 2.10 (continued) Comparison for the FE results of thermal insulation structure with a 1-D cycle analysis, (a) temperatures of the both ends of the shaft, (b) shaft heat flux, and (c) stresses on the corner of the shaft.

2.4 Discussion

While the structural analysis presented so far verified the potential of Si/SiC hybrid structures as a medium term approach to improving the overall engine efficiency, the primary concerns associated with the mechanical behavior of Si at elevated temperatures (pronounced strain-softening of Si) remained unresolved. At the temperatures higher than the design temperature for the all-silicon microengine, the design of the turbine structure is likely to be limited by creep. This section assesses the structural and material issues in the design of high temperature Si/SiC hybrid structures that have not been taken into considerations in the structural analysis to date.

First, it is unclear whether the structural design based on the values for the yield strength of Si used in the analysis is a conservative one. Figure 2.11 shows stress-strain curves for Si at various levels of initial dislocation density. It is apparent that the upper yield strength of Si is determined by the initial density of dislocations. Some measurements of

the upper yield strength are also plotted in Figure 2.12. Note that the upper yield strength of Si is a function of temperature, strain rate, and initial density of dislocations. Figure 2.13 compares the lower yield strength of Si and the values of the Si yield strength used in the analysis of the Si/SiC hybrid structures. The upper yield strength of Si has been adopted for the allowable stress in the analysis so far. Therefore, the key question is whether or not the structural design of Si/SiC hybrid structures can rely on the upper yield strength of Si. Some of the micro-fabrication processes such as the CVD process and thermal cycling may induce an increase of dislocation density within the Si crystal, which in turn may reduce the usable upper yield strength. Second, it is desirable that the service life of the Si/SiC hybrid turbine rotor be reliably estimated. At the temperatures of interest, the Si/SiC hybrid turbine rotor is susceptible to the radial growth and blade distortion due to the creep of Si, effects which have not been accounted for in the previous FE analysis. While Walters performed a preliminary study of the Si creep and observed the localized deformation (an unexpected failure mechanism of single crystal Si consisting of slip bands), the creep parameters do not seem to be sufficiently accurate [13]. Finally, sharp corners such as the blade root or hub root, sites for high stress concentration, may cause structural instabilities when combined with the creep and strain softening of Si.

In order to design a structure safe from these concerns, it is imperative to develop a better material model for single crystal Si based on more rigorous mechanical testing at high temperatures. In addition to the advanced Si material model, it is also crucial to assess the integrity of the interface between the Si and CVD SiC films (both the deposition and bonding interfaces) under the stresses and temperatures expected in service.

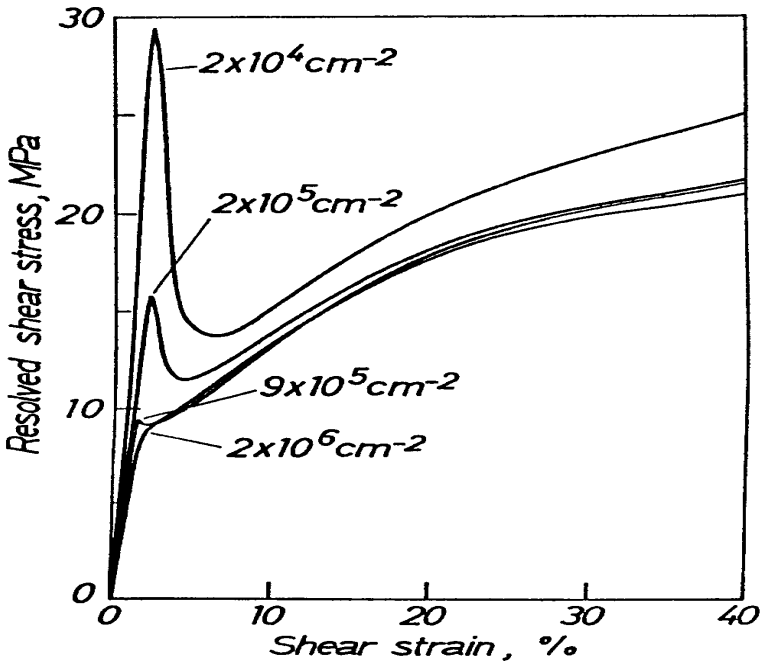

Figure 2.11 Stress-strain curves of high-purity FZ-Si crystals in tensile deformation along the [123] direction as dependent on the initial density of dislocations. [K. Sumino, Deformation behavior of silicon, Metallurgical and Materials Transactions A, Vol. 30A, pp1465-1479, 1999]

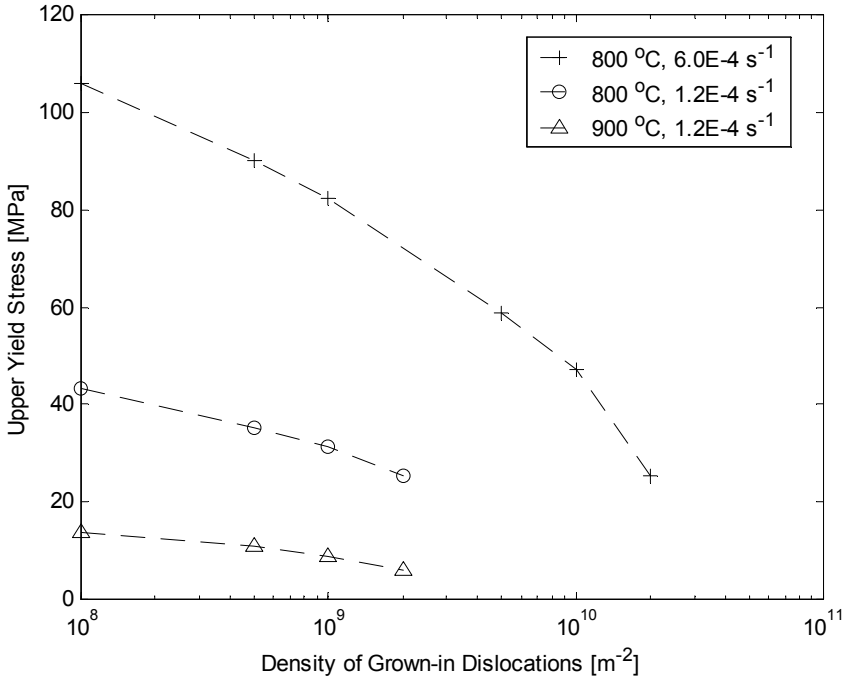

Figure 2.12 Upper yield strength as a function of temperature, strain rate, and grown-in dislocation density [H. Alexander, Ch. 35 Dislocations in Covalent Crystals, ed. F. R. N. Nabarro, Elsevier Science Publishers, 1986].

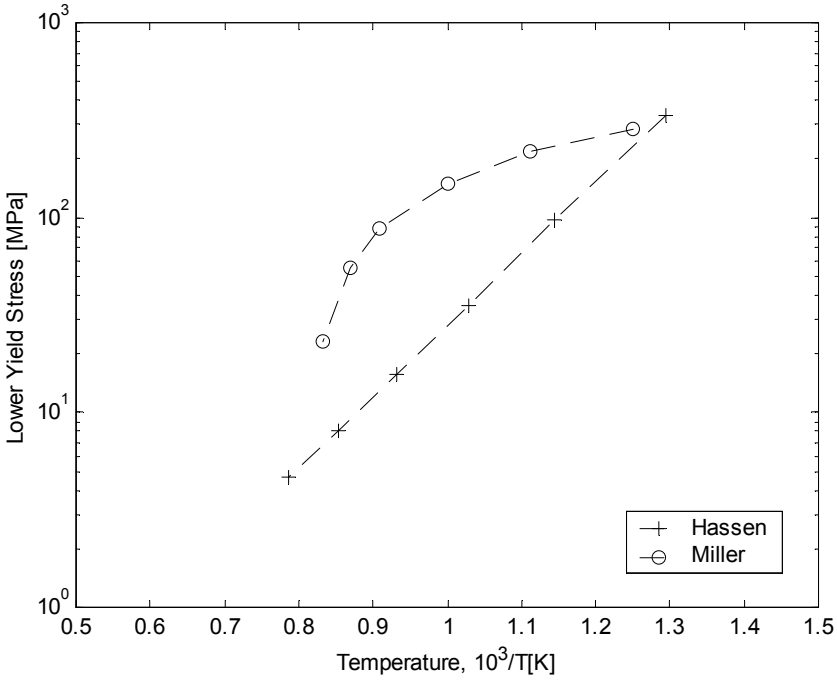

Figure 2.13 Lower yield strength of Si compared with the values in Miller's [1] analysis [H. Alexander, Ch. 35 Dislocations in Covalent Crystals, ed. F. R. N. Nabarro, Elsevier Science Publishers, 1986]

2.5 Summary

The thermo-mechanical FE analysis results presented in this chapter verified the potential of Si/SiC hybrid structures as a medium term approach to improve the overall engine efficiency. However, several key concerns associated with the mechanical behavior of Si at elevated temperatures have not yet been addressed. The detailed discussion of the Si yield strength identified the following three issues: (i) the safety margin of the structural design of Si/SiC hybrid structures based on the upper yield strength of Si, (ii) reliable estimation of the sevice life of the Si/SiC hybrid turbine rotor, and (iii) structural instabilities caused by the combination of high stress concentration, creep, and strain softening. This chapter concluded with an assessment of the need for the development of a better material model for single crystal Si based on more rigorous mechanical testing at high temperatures.

The next chapter reviews the previous work on the characterization of the Si mechnical behavior at elevated temperatures. Chapters 4 and 5 are devoted to the development of a constitutive model for single crystal silicon at elevated temperature and providing the answers to the questions raised in this chapter.

Reference

1. B. Miller, Hybrid Silicon/Silicon Carbide Microstructures and Silicon Bond Strength Tests for the MIT Microengine, S. M. Thesis, Dept. of Aeronautics and Astronautics, MIT, Cambridge, MA, 2000.
2. K.-S. Chen, Materials Characterization and Structural Design of Ceramic Micro Turbomachinery, Ph. D. Thesis, Dept. of Mechanical Engineering, MIT, Cambridge, MA, 1999.
3. Properties of crystalline silicon, INSPEC, the Institution of Electrical Engineers, 1999.
4. K. Jackson, R. Edwards, W. Sharpe, Jr., Mechanical properties of thin film silicon carbide, Mat. Res. Soc. Symp. Proc., Vol. 687, B6.3, Fall 2001.
5. R. J. Shinavski, W. S. Steffier, Enhanced Strength, Nanolayered SiC for Micro-Gas Turbine Portable power Generation, ARO report by Hyper-Therm Inc., 1999.
6. J. J. Hall, Phys. Rev., Vol. 161, p. 756, 1967.
7. Yu. A. Burenkov, S. P. Nikanorov, Sov. Phys.-Solid State, Vol. 16, p. 963, 1974.
8. ABAQUS Reference Manuals, 2001, Providence, RI.
9. Properties of CVD silicon carbide, CVD silicon carbide specification No. SC001, Morton Advanced Materials, Woburn, MA, 1997.
10. MSC/NASTRAN v69, The MacNeal-Schwendler Corporation, 2001.
11. B. Philippon, S. M. Thesis, Dept. of Aeronautics and Astronautics, MIT, Cambridge, MA, 2001.
12. J. Protz, The design and development of a MEMS silicon micro gas turbine engine, Ph. D. Thesis, Dept. of Aero & Astro, MIT, 2000.
13. D. S. Walters, Creep characterization of single crystal silicon in support of the MIT micro-engine project, MS. Mech. Dept., MIT, 1999.

Chapter 3

Literature Review on the Material Characterization of Single Crystal Silicon at High Temperature

3.1 Overview

The design of the MIT microengine is limited in part by the material capability of Si, specifically, the pronounced thermal-softening and strain-softening at temperatures higher than the brittle-to-ductile transition temperature (BDT), approximately 850 K, as discussed in Chapter 1 and Chapter 2. In order to circumvent this limitation, it has been proposed to reinforce the Si with CVD SiC in strategic locations to create a Si/SiC hybrid microengine turbine spool. The feasibility of this hybrid turbine spool design has been investigated by a series of finite element analyses involving primitive material models (ABAQUS^{TM} STANDARD Elasticity and Plasticity [1]) by Chen [2] and Miller [3] and also in Chapter 2. While this previous work has assessed the potential of the Si/SiC hybrid microturbine structure for improving engine efficiency, as well as maintaining structural integrity, a structural design based on the deflection- and strength-limited design is likely to fail to answer the questions involving deformation with time [4]. Furthermore, the stress concentration within a part made of single crystal Si exhibiting the strain-softening behavior may accelerate and propagate the localized deformation, which in turn results in a failure of the part in service. The thermo-mechanical structural analysis and experimental study conducted thus far led to the following specific questions associated with the structures and materials in the design of elevated temperature Si/SiC hybrid structures:

(1) Can we rely on the upper yield strength of Si in designing a part that is to be in service at temperatures higher than the BDT?
(2) Can we estimate the admissible operating conditions and service life of a part?
(3) Will stress concentrations, such as fillet radii, be susceptible to localized creep/plasticity deformation?

These three questions provide the key motivations of the work, and the entire thesis is devoted to seeking the answers. As a first step to obtaining a more reliable design for the Si/SiC hybrid structures, it is imperative that the mechanical behavior of Si at the high temperatures and stresses of interest be better understood and a more accurate constitutive model for Si be developed.

In Section 2, a general description of creep is given, and the creep mechanisms primarily responsible for the steady-state creep regime are described in detail. Section 3 focuses on the experimental studies that have been conducted to characterize the creep of single crystal Si at various temperature and stress ranges. In Section 4, various constitutive equations describing materials at elevated temperatures, although developed mostly for metals, are also discussed. They should be easily modified for single crystal silicon at elevated temperature. This chapter concludes with comparisons of various creep testing methods for ceramics or brittle materials and suggestions for the subsequent work.

3.2 Creep mechanisms

As temperature is raised, loads that give no permanent deformation at room temperature cause materials to creep. Creep, slow and continuous deformation with time, depends on temperature and time as well as the applied stress [5-9]:

$$\varepsilon = f(\sigma, t, T) \tag{3.1}$$

In general, creep effects start when $T > 0.3$ to $0.4T_M$ for metals and $T > 0.4$ to $0.5\ T_M$ for ceramics, where T_M is the melting temperature in Kelvin. The representative creep curves illustrated in Figure 3.1 can often be conveniently divided into three stages. In Stage I, termed the primary or transient creep regime, the creep strain $\dot{\varepsilon}$ decreases continuously with time and strain. This is somewhat analogous to the behavior observed during work-hardening in the sense that the micro-structure changes with increasing strain; for example, the dislocation density increase and subgrain structure formation that is observed in many materials. During Stage II creep, termed the secondary or steady-state creep, a steady-state invariant microstructure is formed, which implies that recovery effects are concurrent with deformation during Stage II. In other words, Stage II creep

can be considered as a deformation regime in which the intrinsic work-hardening of the material is balanced by recovery effects due to the increased thermal activation energy. Subsequent to Stage II creep, tertiary or Stage III creep is observed, in which the accelerating creep deformation leads to eventual material fracture. Often microscopic examination reveals the onset of recrystallization, the coarsening of second-phase particles and/or the formation of internal cracks or voids, which are the precursors to fracture.

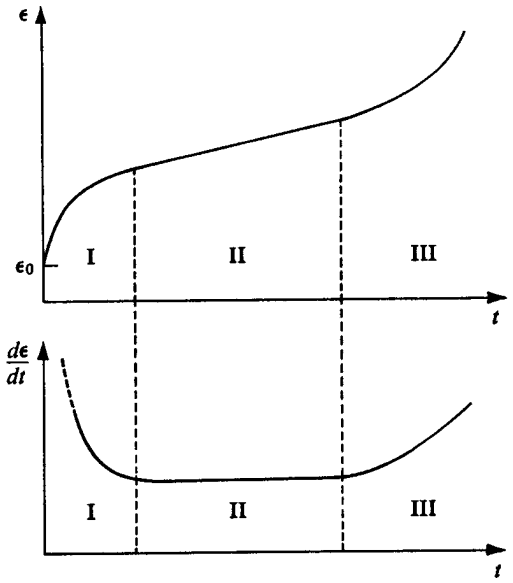

Figure 3.1 Schematic of a general creep curve

For many materials, the steady-state creep rate, which in practice is a design criterion for long-term elevated temperature use, can be correlated with both stress and temperature by an equation of the form

$$\dot{\varepsilon} = A\sigma^n \exp(-Q_c / RT), \tag{3.2}$$

where A and n are material constants, Q_c is the creep activation, R is the gas constant (8.31 Jmol-1K-1), and T is the absolute temperature in Kelvin. At elevated temperatures at which creep processes are the rate-controlling mechanisms, the activation energy Q_c is independent of stress and temperature and nearly equal to the activation energy for self-diffusion. This empirical creep equation can be correlated with the microstructure and the applied external temperature and stress by the descriptions of rate-controlling

mechanisms such as dislocation glide, dislocation recovery, or other diffusional-flow. Several mechanisms, however, are speculative in that they cannot be verified by direct microstructural examination. For the remaining part of this section, the creep mechanisms primarily developed for the secondary creep regime are explained in detail [5, 10, 11].

3.2.1 Dislocation glide creep

Even at relatively low temperatures, given a sufficient level of applied stress, thermal activation affects lattice resistance so that dislocation glide can take place while overcoming obstacles lying on the dislocation glide plane [12]. The work required to overcome the barrier is provided in part by the applied stress and the remainder by thermal energy. In this dislocation glide creep, overcoming such obstacles is not associated with diffusional flow mechanisms. The dislocation glide creep rate can be modeled using kinetic principles as follows:

$$\dot{\varepsilon} = \dot{\varepsilon}_0 \exp(-U_0 / kT)\exp(\tau b a_s / kT), \tag{3.3}$$

where $\dot{\varepsilon}_0$ is a material constant, U_0 is the work required to overcome the obstacle, τ is the applied stress, b is Burgers vector, a_s is the slip plane area, and k is Boltzmann's constant.

3.2.2 Diffusional flow creep

Diffusional flow creep is also termed grain boundary creep because this deformation process involves the grain boundaries. It can be subdivided into two separate mechanisms: Nabarro-Herring creep [13, 14] and Coble creep [15]. A consequence of all grain boundary mechanisms is that adjacent grains become displaced with respect to each other, with the displacement occurring at or close to the grain boundary plane. Both of the creep mechanisms are operative in regimes of low stress and high temperature.

If the vacancies flow through the grains, the process is termed Nabarro-Herring creep, and the steady state creep rate is given by

$$\dot{\varepsilon}_{NH} = A_{NH}\left(D_L / d^2\right)(\sigma\Omega / kT), \tag{3.4}$$

where A_{NH} is a geometrical factor, D_L is the coefficient for lattice self-diffusion, d is grain size, and Ω is the atomic volume.

If the vacancies flow along the grain boundaries, the process is termed Coble creep and the steady state creep rate is given by

$$\dot{\varepsilon}_C = A_C \left(D_{GB}\delta' / d^3\right)(\sigma\Omega / kT), \tag{3.5}$$

where A_C is a geometrical factor, δ' is an effective width of the grain boundary for vacancy diffusion, and D_{GB} is the grain boundary diffusivity. Coble creep is favored over Nabarro-Herring creep when the grain size is very small and at lower temperatures because $Q_{GB} < Q_L$, where Q_{GB} and Q_L are the activation energies for grain boundary and lattice diffusion, respectively. In practice, the Nabarro-Herring and Coble creep processes operate independently, so that the rates are additive and the total creep rate can be expressed as

$$\dot{\varepsilon}_{DIFF} = \dot{\varepsilon}_{NH} + \dot{\varepsilon}_C = A_{NH}(D_L / d^2)(\sigma\Omega / kT)(1 + D_{GB}\delta' / D_L d). \tag{3.6}$$

3.2.3 Nabarro-Herring creep of subgrains

Nabarro-Herring creep of subgrains [16] can take place when a subgrain structure, an ideal source and sink for vacancies, is formed during creep as if the grain size d in Equation 4 is replaced with d'. Experimentally, d' is found to be inversely proportional to applied stress, that is, $d' \sim K/\sigma$, where K is a material constant. Thus, the subgrain creep rate can be given as

$$\dot{\varepsilon}_{SG} = A_{SG} D_L \left(\sigma^2 / K^2\right)(\sigma\Omega / kT). \tag{3.7}$$

3.2.4 Dislocation glide-climb creep

Many materials exhibit stress exponents of ~3 to 7 and creep rates that are independent of the grain size over a broad range of moderate stresses and temperatures. This behavior is usually interpreted in terms of the glide and climb of intragranular dislocations, where the dislocations pile-up and the climb processes are rate-controlling mechanisms [17, 18]. This creep mechanism can conveniently be considered as a competitive process between

work-hardening and recovery by thermal activation. Recovery processes are related to non-conservative dislocation motions such as dislocation climb, in which obstacles to dislocation motion are overcome, or by which dislocations are removed from the structure. Various mechanisms to explain this type of creep have been postulated, but they are mostly speculative with little experimental evidence. The steady state creep rate for this mechanism is often assumed to be the power law creep equation, Equation 2, for which parameters can be determined by fitting experimental data.

3.2.5 Summary of creep mechanisms

Although many theoretical mechanisms have been developed for intragranular and intergranular deformation with various formulations as presented so far, all of them can be expressed in a similar form as

$$\dot{\varepsilon}_i = A_i D_i (\sigma / G)^{n'} (\sigma\Omega / kT)(b / d)^p . \tag{3.8}$$

The values of the parameters n and p as well as the type of activation energy are listed in Table 3.1 for the mechanisms described.

For single crystals, lattice mechanisms should be the rate-controlling processes because there are no grain boundaries, thus grain boundary mechanisms can be neglected. Nevertheless, subgrain creep may be involved in single crystals with a high dislocation density. The most likely mechanisms involved in the creep process of single crystals are lattice diffusion mechanisms such as dislocation glide-climb and subgrain creep.

Table 3.1 Values of the parameters n′, p, and the type of activation energy associated with the mechanisms expressed in Equation 7 for the steady-state creep rate

Mechanisms	Favored by	n′	p	Q
Nabarro-Herring creep	High temperature, low stress and large grain sizes	0	2	Q_L
Coble creep	Low stress, fine grain sizes, and temperatures less than those for which N-H creep dominates	0	3	Q_{GB}
Nabarro-Herring creep of subgrains	High temperature and stresses such that the subgrain size is less than the grain size	2	0	Q_L
Generalized power law creep	High stress, lower temperatures in comparison to Coble creep and large grain size	2~6	0	Q_L or Q_{CI}*

*Q_{CI} is the chemical interdiffusion of solute atoms and pipe diffusion along the dislocation cores. (Data in table adapted from references [5, 10, 11])

3.3 Single crystal silicon creep characterization

The body of literature describing the creep behavior of single crystals is significantly smaller than the available data for polycrystalline materials because single crystal studies have tended to focus primarily either on a determination of the critical resolved shear stress as a function of temperature for a selected slip system or on a detailed investigation of the dislocation configurations and interactions. Creep data for various crystalline ceramics are summarized by Cannon and Langdon in their reviews [10, 11]. A review of steady-state creep in single-phase crystalline materials by Takeuchi and Argon [19] includes primarily metals with only limited data on non-metallic systems. High temperature creep behaviors of single crystal oxides also have been compared by Deng [20] in order to find potential candidates as reinforcements for high temperature structural applications.

Silicon creep data is limited to date as are the creep stress and temperature ranges for which it has been obtained. Most of the creep experiments for silicon were performed in the late 60's and 70's, notably by Alexander and Haasen [21, 22], Myshlyaev and co-workers [23, 24], and Taylor and Barrett [25]. Recently, Walters [4] performed a series of flexural creep tests in support of the MIT microengine project. Creep stress and

temperature ranges at which those experiments were performed are shown in Figure 3.2 while the microengine operating zone is designated with an ellipse. Silicon deforming as a plastic material under monotonic loading has been identified and modeled in a series of experiments performed by Patel and Chaudhuri [26], Yonenaga and Sumino [27, 28], and Fruhauf et al [29]. In this section, the previous work by Alexander and Haasen [21, 22], Myshlyaev and co-workers [23, 24], and Taylor and Barrett [25] as well as Walters [4] is discussed in more detail.

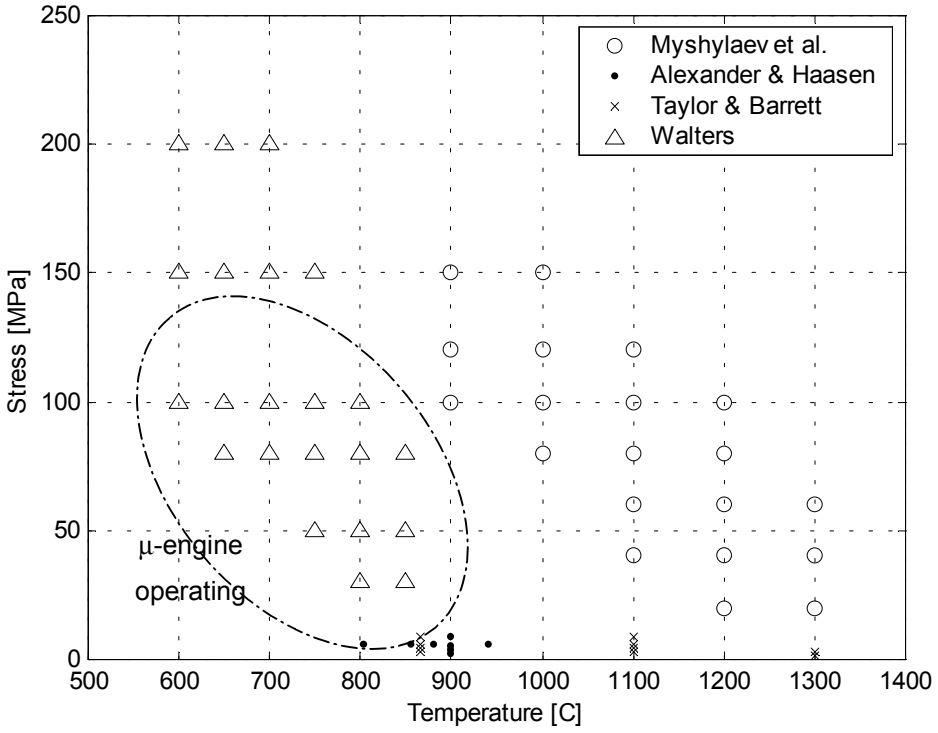

Figure 3.2 Temperature and stress ranges at which a series of silicon creep tests were performed (Data in the plot adapted from references [4, 21-25])

Alexander and Haasen [21, 22] investigated the role of dislocations in plastic flow of diamond structure materials (Si, Ge, …) for the purpose of the derivation of macroscopic plastic properties from measured dislocation mobilities and densities. They performed creep testing with silicon in compression over a temperature range of 800 to 940 °C and a resolved shear stress range of 2 to 7 MPa. As shown in Figure 3.3, an S-shaped strain-time relation for constant stress was observed in diamond structure crystals consisting of an incubation stage, stationary creep, and a work-hardening stage. Initially, there is

exponential dislocation multiplication and an associated accelerating creep response. Then the internal shear stress produced by the dislocations becomes noticeable and slows down dislocation motion and multiplication, where the curvature of the strain versus time plot changes from positive to negative. Finally, the slope tends to zero as internal stress compensates for the applied stress. Moreover, the functional dependence of the strain rate at the stationary stage (inflection point) on stress and temperature can be expressed in a power law form. The activation energy extracted from their experiments has been estimated as 232 kJ/mol, in accordance with the activation energy of the dislocation velocity, and the stress exponent was found to be 3. A creep model was suggested based on the dislocation density evolution.

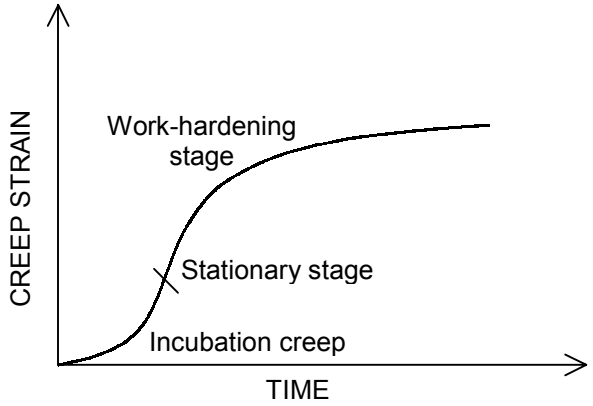

Figure 3.3 A typical creep curve of diamond structure crystals

Myshlyaev et al. [23, 24] performed creep tests with silicon single crystals under uniaxial compression over a stress range of 20 to 150 MPa and a temperature range of 900 to 1300 °C. In contrast to Alexander and Haasen's results, they observed that, at relatively high stresses and temperatures, the initial stages disappeared and the creep curves of silicon became similar to those of metals. That is, the instantaneous initial deformation was followed by transient, steady, and accelerating creep stages resulting in a rupture failure. A further increase in temperature led to the accelerating creep stage immediately followed by the transient creep stage. Thus, they concluded that in this high stress and temperature range silicon deforms much like metals with an activation energy about equal to that for self-diffusion and a high stress dependence. Based on the experimental

data, they suggested a kinetic equation that governs the steady creep rate of silicon crystals within the tested temperature and stress ranges as follows:

$$\dot{\varepsilon} = \dot{\varepsilon}_0 \exp(-(U_0 - V\sigma)/RT), \tag{3.9}$$

where the energy barrier, U_0, is 5.6eV (540kJ/mol) and the activation volume, V, is 2.7×10^{-21} cm^3.

In order to characterize the kinetics of high temperature creep for a covalent crystal oriented for single slip, Taylor and Barrett [25] conducted creep testing with silicon crystals oriented such that the $(\bar{1}\,11)[01\,\bar{1}]$ slip system experienced the maximum shear stress for uniaxial compressive loading. This contrasts with the work of Myshlyaev et al., who oriented their crystals along the <111> direction, which activates multiple slip systems, as is the case for most of the work done on polycrystalline metallic materials. Creep experiments were carried out at temperatures above 0.6Tm. They concluded that below about 1000 °C, the creep strain can be represented by the equation

$$\gamma = \alpha \ln(\nu t+1), \tag{3.10}$$

where typical values for α and ν are 10^{-3} and 2.5 min^{-1} respectively, whereas above approximately 1000 °C steady state creep is observed. The activation energies for creep in the temperature range of 900 to 1300 °C are consistent with a glide controlled mechanism. These activation energies are summarized in Table 3.2, together with experimental activation energies for glide and self-diffusion and the calculated activation energies. They also observed the evolution of subgrain structures, the partitioning of the crystal into cells of relatively low dislocation density and dislocation walls of high density.

Table 3.2 Summary of creep activation energies along with measured and predicted activation energies for dislocation motion (Adapted from Reference [25])

Type of activation energy	Q [kJ/mol)
Logarithmic creep (~900°C)	184.0
High temperature steady state creep	163.8
Dislocation velocity activation energy	166.3 ~ 218.4
Self-diffusion activation energy	497.7
Predicted activation energy for glide	205.8

Recently, Walters [4] performed four-point bend creep testing to investigate the mechanical behavior of silicon in the stress and temperature ranges at which the MIT microengine operates. While the localized deformation at the inner loading points due to the high stress concentration hampered extraction of accurate creep data, a high density of slip bands, revealed after slight etching as shown in Figure 3.4, confirmed the role of dislocation glide in determining the macroscopic deformation at elevated temperature.

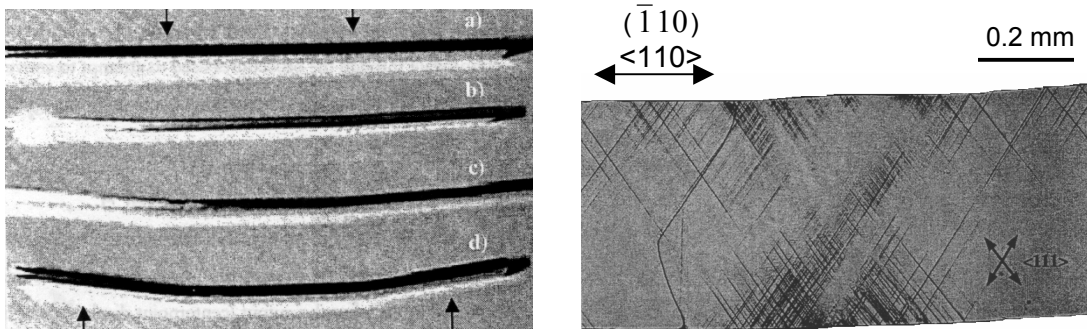

(a) (b)

Figure 3.4 (a) Si sample after a 4-point bend test at high temperature, (b) active slip bands revealed by dilute etching [D. Walters, MS Thesis, MIT, 1999]

Discussions of the creep experiments for Si in this section have provided clues as to the controlling mechanisms of the mechanical behavior of single crystal Si at elevated temperatures, and the key ingredients required for constitutive modeling. In particular, it is believed that the experimental results and proposed equations by Alexander and Haasen [21, 22] and Myshlyaev and co-workers [23, 24] can be combined to yield a description of the deformation of Si over the ranges of interest. The next section provides a short review on the constitutive equations for creep.

3.4 Constitutive equations for creep

Most of the discussion in this section is based on a review of constitutive equations for creep by White and Goodman [30]. Although the constitutive laws described here have been developed mostly for metals, they should be easily modified for the high temperature behavior of ceramics materials, particularly single crystal silicon.

3.4.1 General classification of constitutive equations

Inelastic strains are usually considered as volume-conserving and are traditionally modeled as plasticity (strains subject to a yield condition and time-independent) and/or creep (strains with no particular stress threshold and exhibiting a time-dependence). In classical 'superposition models', it is assumed that the total stain tensor $\boldsymbol{\varepsilon}$ may be composed of a thermoelastic strain ε^e and an inelastic strain ε^{in} which, in turn, may be divided into a plastic strain $\boldsymbol{\varepsilon}^p$ and a creep strain ε^c

$$\varepsilon = \varepsilon^e + \varepsilon^{in} = \varepsilon^e + \varepsilon^p + \varepsilon^c. \tag{3.11}$$

Further assumptions are normally made for a conventional plasticity theory lead to the formal constitutive equation structure. Interactions between creep and plasticity are modeled using internal variables that do not solely apply to either the plasticity or creep terms.

However, the classical constitutive formulation has been criticized because all the inelastic strain is fundamentally time-dependent. This in turn calls for a 'unified formulation' that assumes a single measure of inelastic strain ε^{in} given by a time-dependent law of the form:

$$\varepsilon^{in} = \hat{\varepsilon}^{in}(\sigma, T, a_1, a_2, ...) \tag{3.12a}$$

$$a_i = \hat{a}_i(\sigma, T, a_1, a_2, ...) \tag{3.12b}$$

where T is temperature, a_i's are internal variables. Thus, the difficulties of interaction are avoided in principle, but this approach has some disadvantages. First, data-fitting may be difficult since many material properties having different time scales tend to be introduced, and second, it is often numerically expensive due to the high stress sensitivity of the strain rate function. Nevertheless, the dislocation mechanics in combination with a "unified formulation" will form a potential candidate for a constitutive model of Si at elevated temperatures and high stresses.

3.4.2 Creep laws for isotropic materials

Often a set of data for creep strain ε^c at different tensile stresses σ, temperature T, and time t may be expressed as

$$\varepsilon^c = g(\sigma, T, t), \tag{3.13a}$$

$$\dot{\varepsilon}^c = \frac{\partial}{\partial t} g(\sigma, T, t). \tag{3.13b}$$

Specific forms of this representation include:

(a) 'theta representation' [31]

$$\varepsilon^c = \theta_1\{1 - \exp(-\theta_2 t)\} + \theta_3\{1 - \exp(-\theta_4 t)\} \tag{3.14}$$

(b) a form termed de Lamcombe [32]

$$\varepsilon^c = C_1 t^{p_1} + C_2 t^{p_2} \quad (0<p_1<1, p_2>1) \tag{3.15}$$

(c) and that of Graham and Walles [33]

$$\varepsilon^c = C_1 t^{1/3} + C_2 t + C_3 t^3, \tag{3.16}$$

where $\theta_1, \ldots, \theta_4, C_1, \ldots, C_4$ are fitted positive functions of σ and T.

Equation 3.13 is the basis of 'time-hardening' and 'strain-hardening' constitutive laws that are used to extend test data to general variations of σ and T. In time-hardening, Equation 3.13b is assumed to apply with instantaneous values of σ, T, and t so that t is employed as an internal variable. In principle, this rule is incorrect, but reasonable results may often be obtained if σ varies slowly. In strain-hardening, t is eliminated from Equation 3.13 to yield

$$\dot{\varepsilon}^c = h(\sigma, T, \varepsilon^c) \tag{3.17}$$

and this relation is assumed to apply with instantaneous values of σ, T, and t so that ε^c is employed as an internal variable measuring hardening and/or softening.

These uniaxial constitutive laws can be generalized to multiaxial states by assuming that the relation between the Mises equivalent values $\dot{\bar{\varepsilon}}^c$, $\bar{\sigma}$, $\bar{\varepsilon}^c$ is as in the uniaxial case and that $\dot{\varepsilon}^c$ has the direction of the deviatoric stress σ'. That is

$$\dot{\varepsilon}^c = \frac{3}{2}\frac{\partial}{\partial t} g(\bar{\sigma}, T, t)\sigma'/\bar{\sigma} \tag{3.18a}$$

or

$$\dot{\varepsilon}^c = \frac{3}{2} h(\bar{\sigma}, T, \bar{\varepsilon}^c)\sigma'/\bar{\sigma}. \tag{3.18b}$$

It should, however, be noted that this single internal variable formulation would not be valid where tertiary creep is concerned since the hardening in primary creep and softening in tertiary creep are evidently different physical mechanisms.

This generalized formulation can be further extended to single crystal constitutive models by considering the dislocation mechanics or hardening evolutions on each slip system of a crystal. Anand and Balsubramanian [34] developed an elasto-viscoplastic constitutive model for polycrystalline face-centered-cubic (FCC) crystals at low homologous temperatures where the major mechanism of plastic deformation in ductile single crystals is dislocation glide on well-defined crystallographic slip systems in the crystal. Single crystal Si, having a diamond structure, in which two superimposed FCC lattices are displaced by one quarter of the atomic spacing, can be modeled using the same process developed for the FCC materials because it shares the same slip systems in the crystal.

3.5 Ceramics or Brittle materials creep testing

Four-point bending testing has been extensively conducted for ceramic materials because of its relatively easy experimental setup and simple specimen preparation [35-37]. The four-point bending fixture is shown in Figure 3.5(a). However, this method is not adequate to extract post-yielding mechanical properties, particularly for materials with asymmetric (between tension and compression) mechanical properties due to a time-dependent redistribution of the stresses within the flexure specimen as it deforms further. When uniaxial tensile and compressive creep measurements are made, the forms of the constitutive equations are determined directly and the stress distribution in a specimen can be analyzed with ease. The reverse process, however, is not straightforward, as the forms of the constitutive equations in tension and compression have to be assumed for the analysis [38].

Uniaxial compression testing, often performed when the tension test specimen may not be available due to the potential for brittle fracture, is straightforward in terms of test interpretation. The compression creep testing setup is shown in Figure 3.5(b). The most

critical aspect of the compression test is the need to make accurate measurements of the specimen deformation. The simplest method is to measure the displacement of the loading rams after a long thermal settling, while feeler gauges or a long range optical telescope (utilizing SiC fiber attached on the platen of the compression creep testing fixture) can be successfully employed with ±1 μm and ±4 μm resolution, respectively. Friction between the load pad and specimen is also a critical concern, together with alignment issues associated with elastic/plastic buckling and the introduction of an undesirable bending moment. Debschutz [39] determined the difference in behavior between frictionless creep and fully constrained creep, and claimed that the additional stress required to maintain a given creep rate, ranged from 6 to 10 % of the average creep stress for an aspect ratio of specimen base, 2a, to height, h, ranging from 1/3 to 1/1.5. High temperature solid lubricants, such as BN powder, can be applied on the interfaces to minimize the friction at elevated temperatures.

In tensile testing, a uniform tensile stress is applied along the longitudinal axis of the specimen. A key factor in this test is the specimen grip design. In order to apply the load uniformly, the grips must not only hold the specimen without slippage, but also must prevent detrimental concentrated stress distributions from developing around the grip area. Some examples of tensile specimens with various grip designs used for advanced ceramics are illustrated in Figure 3.6.

These three different types of creep testing methods for advanced ceramics or particularly brittle materials are summarized in Table 3.3.

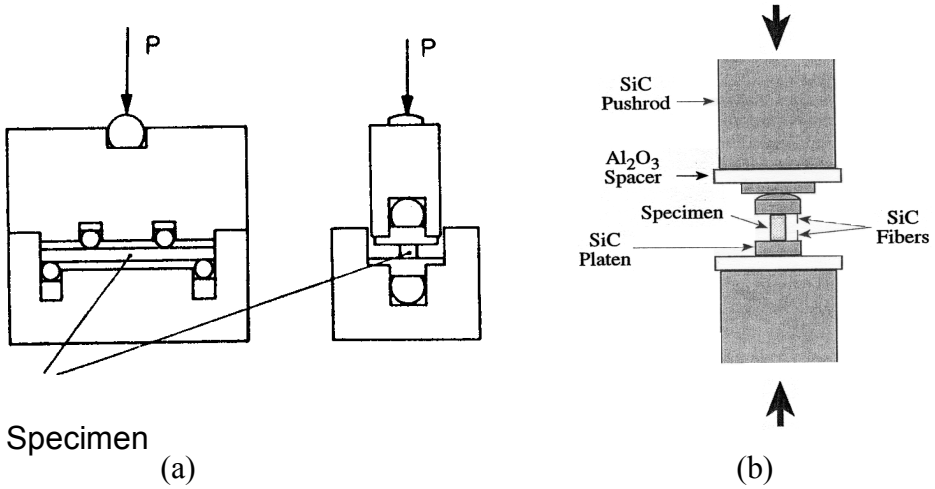

Figure 3.5 (a) Four-point bending fixture for high temperature ceramics testing [G. Grathwohl, Current testing methods—A critical assessment, Int. J. High. Techn. Ceram., Vol. 4, No. 4, p211-225, 1988], (b) Compression creep testing fixture with SiC fibers attached on the platens to be used with an optical telescope measurement [S. M. Wiederhorn, et al., Damage-enhanced creep in siliconized silicon carbide: Phenomenology, J. Amer. Ceram. Soc., Vol. 71, No. 7, p602-608, 1988]

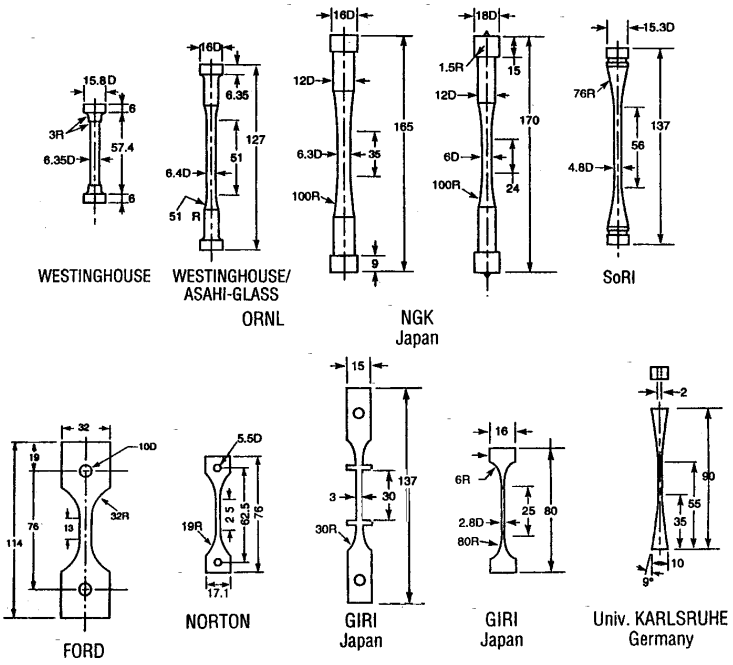

Figure 3.6 Examples of tensile specimens used for advanced ceramics [G. D. Quinn, Strength and proof testing, in Engineered materials Handbook, Vol. 4, Ceramics and Glasses, S. J. Schneider, Jr., Volume Chairman, ASM International, Metals Park, OH, p585-598, 1991]

Table 3.3 Comparison of flexure, tension, and compression creep testing

Flexural testing	Advantages: Low specimen cost Ease of experimental design Minimum of specimen material and preparation Disadvantages: Non-uniform stress distribution over the specimen cross-section Small volume under maximum stress Surface phenomena dominate Indirect determination of stress and strain Typical sources of error: Friction between specimen and loading points Twisting due to improper loading Assumption of linear elastic behavior Enhanced deformation under loading points
Tensile testing	Advantages: Uniform stress distribution Straight-forward calculation of stress and strain Simple load application and measurement Disadvantages: Difficult and complex experimental design such as gripping Expensive test equipment Specimen design and manufacture costly and time consuming Typical sources of error: Failure in gripped region Inaccurate accounting of temperature and stress gradient in specimen Unquantified bending stress
Compressive Testing	Advantages: Cost saving in material preparation Use of small specimens Disadvantages: Limited data on effects of porosity and cavitation Specimen alignment more difficult than with flexure and tension Typical sources of error: Failure to account for barreling Inaccurate accounting of temperature and stress gradient in specimen Stress distribution related to buckling

3.6 Summary

This chapter has discussed creep, the slow continuous deformation of a material with time. Discussions of creep mechanisms primarily developed for the steady-state creep regime lead to a conclusion that the creep process of single crystals most likely involves lattice diffusion mechanisms such as dislocation glide-climb and subgrain creep. Si behaves similarly. The creep experiments for silicon, notably by Alexander and Haasen, Myshlyaev et al., and Taylor and Barrett, and recently, Walters in support of the MIT microengine project, also provide clues on the controlling mechanisms of mechanical behavior of Si at high temperature and the key ingredients required for constitutive modeling of Si. The dislocation mechanics in combination with a "unified formulation", which assumes a single measure of inelastic strain instead of an inelastic strain as the sum of a plastic and a creep strain, will form a potential candidate for a constitutive model of Si at the temperatures and stresses of interest. Finally, the brief comparisons of the ceramic testing methods pointed out that, in case of uniaxial tensile or compression creep testing, the forms of the constitutive equations are determined directly and the stress distribution in a specimen can be analyzed with ease. This is far less straightforward for flexural testing. In the experimental work, compression creep testing will be used to identify the uniaxial characteristics of silicon's mechanical response to various temperature and stress levels, while flexural testing with or without notches will provide the response to multiaxial stress states. The uniaxial test data will be used to calibrate the constitutive model and the flexural data will be used to validate/interrogate the model.

References

1. ABAQUS Reference Manuals, 2001, Providence, RI.
2. K.-S. Chen, Materials Characterization and Structural Design of Ceramic Micro Turbomachinery, Ph. D. Thesis, Dept. of Mechanical Engineering, MIT, Cambridge, MA, 1999.
3. B. Miller, Hybrid Silicon/Silicon Carbide Microstructures and Silicon Bond Strength Tests for the MIT Microengine, S. M. Thesis, Dept. of Aeronautics and Astronautics, MIT, Cambridge, MA, 2000.
4. Douglas S. Walters, Creep characterization of single crystal silicon in support of the MIT micro-engine project, MS. Mech. Dept., MIT, 1999
5. Thomas H. Courtney, "Mechanical Behavior of Materials", 1990, McGraw Hill
6. M. F. Ashby, D. R. H Jones, "Engineering materials I, 2nd Ed", 1996, Butterworth-Heinemann
7. Dietrich Munz, Theo Fett, "Ceramics, Mechanical properties, failure behavior, materials selection", 1999, Springer
8. David J. Green, An Introduction to the mechanical properties of ceramics, 1998, Cambridge University Press
9. Jan. A. H. Hult, Creep in Engineering Structures, 1966, Blaisdell
10. W. Roger Cannon, Terence G. Langdon, Review, creep of ceramics, Part 1 Mechanical Characteristics, J. Mater. Sci., Vol. 18, pp1-50, 1983
11. W. Roger Cannon, Terence G. Langdon, Review, creep of ceramics, Part 2 An examination of flow mechanism, J. Mater. Sci., Vol. 18, pp1-50, 1983
12. J. Weertman, J. Appl. Phys., Vol. 28, p 362, 1957.
13. F. R. N. Nabarro, Report of a conference on strength of solid, Physical Society, London, p 75, 1948.
14. C. Herring, J. Appl. Phys., Vol. 21, p 437, 1950.
15. R. L. Coble, J. Appl. Phys., Vol. 34, p 1679, 1963.
16. J. Friedel, Dislocations, Pergamon, London, Oxford, p 312, 1964.
17. J. Weertman, J. Appl. Phys., Vol. 28, p 362, 1957.
18. J. Weertman, Rate processes in plastic deformation of materials, ed. A. K. Mukherjee, p 315, ASM, Metals Park, OH, 1975.
19. S. Takeuchi, A. S. Argon, "Steady-state creep of single-phase crystalline matter at high-temperature, J. Mater. Sci., Vol. 11, No. 8, pp1542-1566 1976
20. Shiqiang Deng, High temperature creep behavior of single crystal oxides, J. Mater. Sci., Vol. 31, pp 6077-6083, 1996
21. H. Alexander, P. Hassen, Dislocation and plastic flow in the diamond structure, Solid State Physics, pp 27-158, 1968
22. H. Alexander, Dislocations in covalent crystals, in Dislocations in solids, Vol. 7. ed. F. R. N. Navarro, pp 113-234, North-Holland, 1986.
23. M. M. Myshlyaev, V. I. Nikitenko, V. I. Nesterenko, Dislocation structure and macroscopic characteristics of plastic deformation at creep of silicon crystals, Phys. Stat. Sol., Vol. 36, pp 89-95, 1969
24. M. M. Myshlyaev, Dislocation creep, Ann. Rev. Mater. Sci., Vol 11, pp 31-50, 1981

25. T. A. Taylor, C. R. Barrett, “Creep and recovery of silicon single crystals”, Mater. Sci. Eng., Vol. 10, pp 93-101, 1972
26. J. R. Patel, A. R. Chaudhuri, Macroscopic plastic properties of dislocation-free germanium and other semiconductor crystals. I. Yield behavior, J. Appl. Phys., Vol. 34, No. 9., pp 2788-2799, 1963
27. Ichiro Yonenaga, Koji Sumino, Mechanical strength of silicon crystals as a function of the oxygen concentration, J. Appl. Phys., Vol. 56, No. 8, pp 2346-2350, 1984
28. K. Sumino, Deformation behavior of silicon, Metallur. Mater. Trans. A, Vol. 30A, pp 1465-1479, 1999.
29. Jaochim Fruhauf, Eva Gartner, Erhard jansch, Silicon as a plastic material, J. Micromech. Microeng, Vol. 9, pp 305-312, 1999
30. P. S. White, A. M. Goodman, Constitutive equations for creep, J. Strain Analysis for Engineering Design, Vol. 29, No. 3, 1994, Creep of materials and Structures, (Ed) T. H. Hyde
31. B. Wilshire, Creep deformation of engineering ceramics, Mechanics of creep brittle materials-1, pp 75-98, A. Cocks and A. Ponter, Eds., Elsvier Applied Science, 1988
32. W. M. Commings, R. H. King, Extrapolation of creep strain and rupture properties of 0.5 % Cr, 0.5 % Mo, 0.25 % V steel pipe, Report 448, 1970, NEL, Glasgow.
33. A. Graham, K. F. Walles, A relationships between long and short-time creep and tensile properties of a commercial alloy, J. Iron Steel Inst., Vol. 179, No. 105, 1955.
34. S. Balasubramanian, L. Anand, Elasto-viscoplastic constitutive equations for polycrystalline fcc materials at low homologous temperatures, J. Mech. Phys. Solid, Vol. 50, Issue 1, pp101-126, 2001
35. Tze-jer Chuang, Estimation of power-law creep parameters from bend test data, J. Mater. Sci., Vol. 21, pp 165-175, 1986
36. G. W. Hollenberg, G. R. Terwilliger, R. S. Gordon, Calculation of stresses and strains in four-point bending creep tests, J. Am. Ceram. Soc., Vol. 54, No. 4, pp 196-199, 1971
37. Karl Jakus, Sheldon M. Wiederhorn, Creep deformation of ceramics in four-point bending, J. Am. Ceram. Soc., Vol. 71, No. 10, pp 832-36, 1988
38. Patrick K. Talty, Richard A. Dirks, Determination of tensile and compressive creep behavior of ceramic materials from bend tests, J. Mater. Sci., Vol. 13, pp 580-86, 1978
39. Klaus D. Debschutz, Bernhard Caspers, Gerold A. Schneider, Gunter Petzow, Critical evaluation of the compression creep test, J. Am. Ceram. Soc., Vol. 76, No. 10, pp 2468-74, 1993

Chapter 4

Experimental methodology

4.1 Overview

This chapter discusses the experimental methods proposed to investigate the mechanical behavior of Si at the temperatures and stresses of interest and to assess the feasibility of Si/SiC hybrid structures. Separate subsets of the experimental results in turn will allow for both the calibration and validation of the Si constitutive model.

As discussed in the previous chapter, a more reliable design for the Si/SiC hybrid structures requires better understanding of the mechanical behavior of Si and a more accurate constitutive model for Si. In order to achieve these objectives, two types of testing methods were proposed: a uniaxial compression test and a four-point bend test. Si uniaxial compression creep testing was designed to characterize the basic mechanical behavior of Si at high temperatures and stresses and to be used for the calibration of the Si constitutive model. The four-point bend tests were conducted using three kinds of specimens to validate the responses of the Si material model to multi-axial stress states: a uniform Si specimen, a notched Si specimen, and a Si/SiC specimen. Also, testing with each of these flexural specimens focused on tackling the three questions posed in the previous chapter associated with the pronounced thermal softening and strain-softening of Si in designing hybrid Si/SiC microturbine structures. The Si/SiC hybrid flexural specimen was designed as a simple means to verify the utility of the hybrid structure concept for the MIT microengine.

In Section 4.2, the high temperature material testing system is described in brief. The next section discusses the equipment utilized for the Si uniaxial compression test and the testing procedure. Si 4-point bend testing is discussed focusing on the strain-softening of Si and the effect of dislocation density on the peak load. The experimental design of the

notched Si 4-point bend test is presented in Section 4.4 with the details of the stress concentration calculation and specimen preparation. Also, a short description of Chemical Vapor Deposition (CVD) of SiC is given, as it is the key process for the preparation of Si/SiC hybrid flexural specimens. The SiC film thickness variation within a wafer is discussed based on direct measurements.

4.2 Test equipment

The material testing system installed at the MIT Technology Laboratory for Advanced Composites (TELAC) is composed of four sub-systems: an MTS™ 810 Load Frame, an Instron™ 8500 controller, an Instron™ 3118 ceramics testing system, and a data acquisition system with Labview™ 5.0. The ceramics testing system comprises a split furnace with electrical heating elements and an associated control console, alumina push rods with water-cooled adapters, and SiC testing fixtures. Figure 4.1 shows the overall system configuration. This system uses a 50 kN Instron™ load cell for both the measurement and control of the load. The Linear Variable Differential Transducer (LVDT) embedded in the testing machine measures the absolute position of the actuator ram.

Figure 4.2 and 4.3 show the compression anvils and the 4-point bend fixture made of SiC, respectively. By adopting hemispherical and semi-circular supports, the fully-articulated compression anvils and 4-point bend fixture minimize any unwanted bending or torsional moments due to any misalignment in the load train or distortion of the specimen. The spans between the inner rollers and the outer rollers of the 4-point bend fixture are 20 and 40 mm, respectively. The LVDT installed in the lower water-cooled adapter measures the deflection of the flexural specimen transmitted through an alumina internal rod housed inside the lower push rod.

Analog signals from the load cell and LVDT are transmitted to an A/D converter (National Instruments™ GPIB interface) via the Instron™ 8500 controller, and then to a personal computer. A Labview™ 5.0 interface was used to display the output data in real-time on the computer screen and to store the data in the data storage device.

Details of the test equipment specifications can be found in Appendix A.

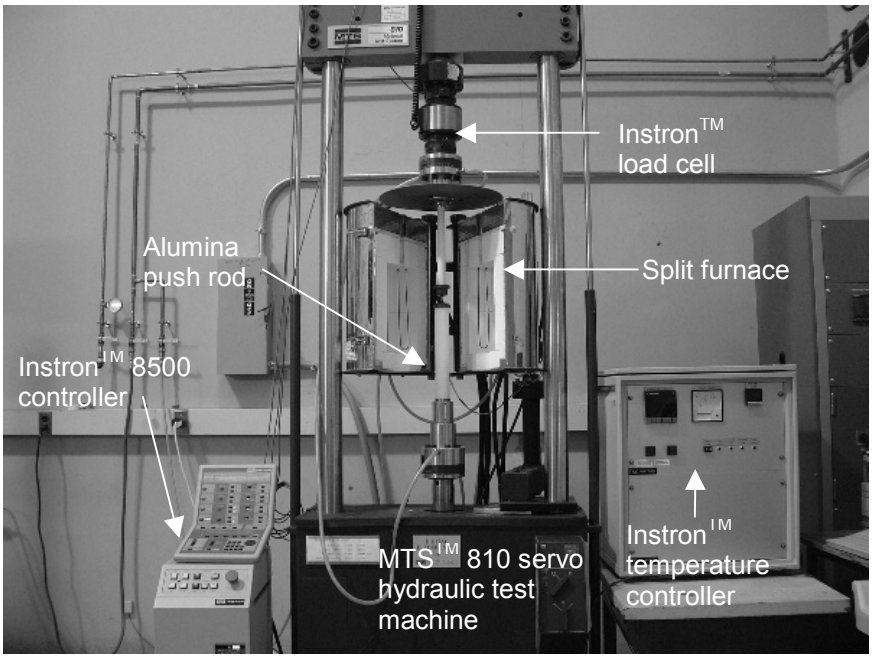

Figure 4.1 Material testing system overall configuration

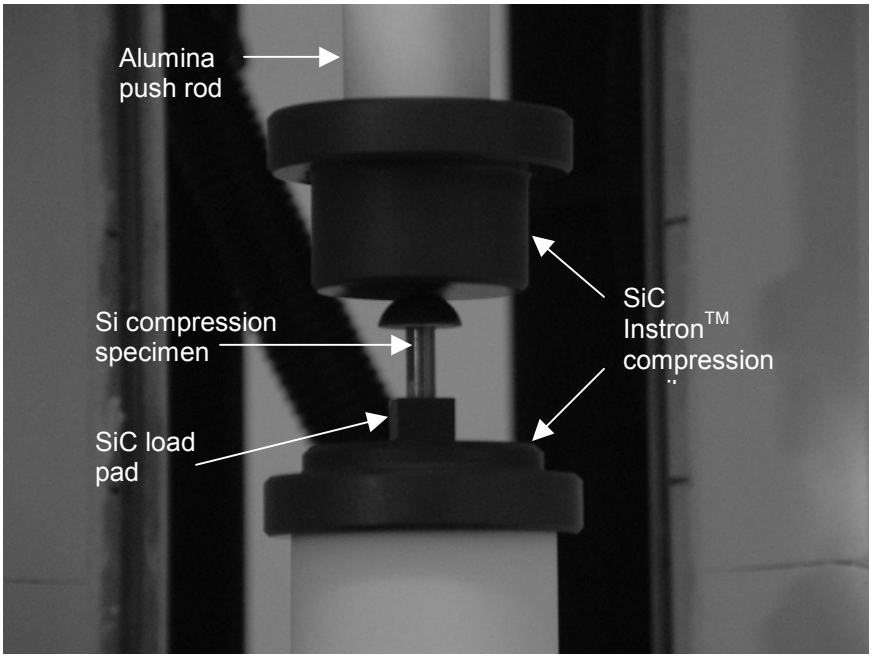

Figure 4.2 Uniaxial compression test setup

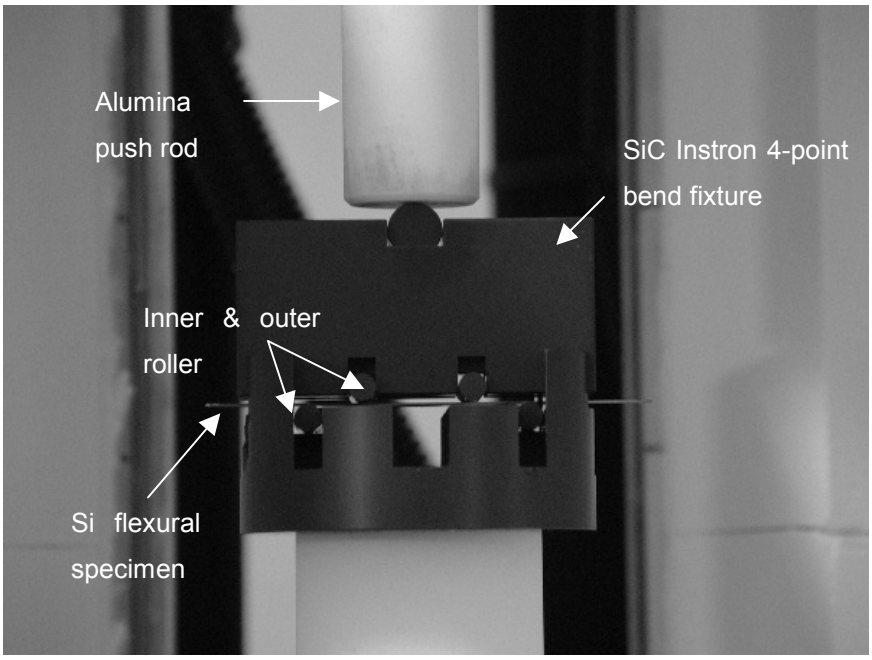

Figure 4.3 Four-point bend test setup

4.3 Si uniaxial compression creep test

4.3.1 Experimental design

In order to understand the mechanical behavior of Si over the temperature and stress ranges of interest for the MIT microengine and to calibrate the Si constitutive model, a series of Si uniaxial compression creep tests were performed for the temperatures and stresses shown in Table 4.1. As was discussed in the previous chapter, friction between the load pad and the specimen is a critical concern in compression testing, together with any misalignment that might cause elastic/plastic buckling and undesirable stress gradients. Load levels allowed by the machine and the resolution in the displacement measurement are also key factors in determining the specimen dimensions.

Table 4.1 Si <100> and <111> compression creep test map

		Normal Stress (MPa)						
		10	20	40	60	80	100	120
Temp. (°C)	600				O	O	O	O
	700			O	O	O	O	
	800		O	O	O	O		
	900	O	O	O				

Considering these issues, the aspect ratio of specimen height to base diameter was chosen to be 2.5. The specimen dimensions are 5 mm in base diameter and 12.5 mm in height. The computed load levels for these specimen dimensions are 2356.2 N for 120 MPa normal stress, which is somewhat higher than the recommended load capacity of the load train, specifically that of the alumina push rods (1 kN at 1500 °C, data not available at lower temperatures from the manufacturer). The compression specimens were machined and provided by Lattice Materials, Inc. such that the multi-slip <100> or <111> orientations of single crystal Si grown by the Czochralski (CZ) method were coincident with the compression axis. With no further processing, as-cut specimens were used for compression testing. A representative creep curve is shown in Figure 4.4. The loading rate of the current material testing system is limited due to problems such as chattering. In the current work, the testing machine was operated at a loading rate of 60 N/s. The inelastic deformation present during the initial ramp loading is negligibly small and ignored from the creep data (See Appendix H). Note that the amount of creep displacement is large enough to measure at the temperatures, load levels, and time frame of interest.

While a creep test can be performed with reasonable accuracy, the high stiffness of the compression specimen prevents the determination of an accurate stress-strain curve using a constant-strain compression test. Appendix C illustrates how the machine compliance affects the load-displacement measurement (in cases where an extensometer cannot be attached). This problem is particularly severe for a material having a nonlinear response.

A 4-point bend test, in which the specimen is usually more compliant, can more easily identify the strain-softening behavior of Si at high temperatures, as evident in Chen's experiments [1].

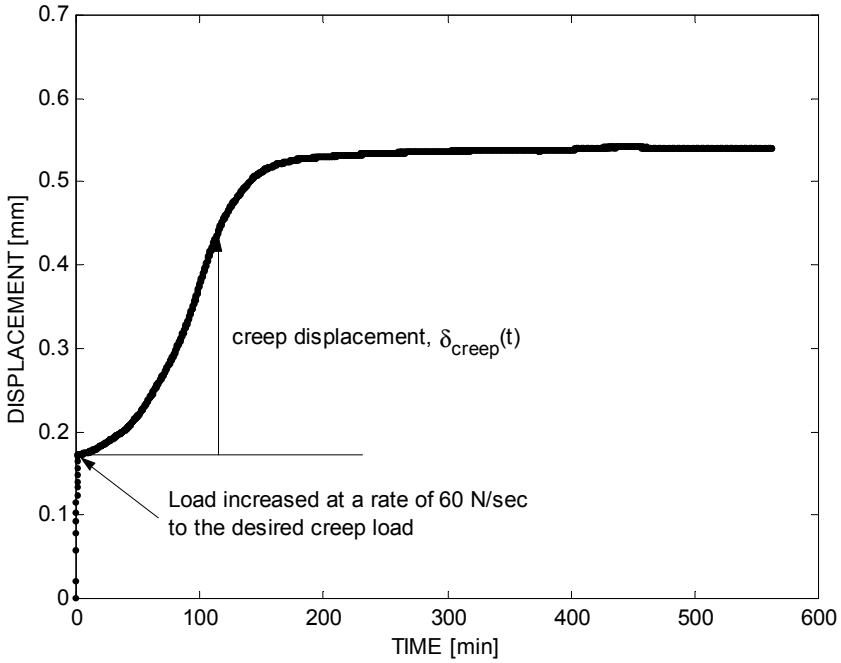

Figure 4.4 Raw creep experimental data at 600 °C and 2356.2 N (120 MPa).

4.3.2 Procedure of uniaxial compression creep test

After assuring that the testing machine is in full working order, BN (Boron Nitride) powder is applied uniformly on the interface of the SiC load pad and the specimen to reduce the effect of friction during testing. With the help of the Load Protect feature of the Instron^{TM} controller, a slight compressive load is applied to hold the assembly of the specimen, load pads, and compression anvils in place as shown in Figure 4.2. Sacrificial blocks can be placed around the specimen to prevent unexpected damage to the testing machine from the misuse of Load Control mode. While the compressive load (usually 1 % of the desired creep load) remains constant under the Load Control mode, the furnace is closed and heated to the desired temperature. To avoid any interference due to thermally-induced strain, the entire apparatus is left to reach equilibrium for 1.5 hours after the target temperature is obtained. A waveform of loading and unloading of an

additional compressive load (5 % of the desired creep load or 50 N, whichever is smaller) is repeated several times to improve the seating of the load train including the specimen and fixture. At this point, a waveform is commanded to increase load to the desired value at a rate of 60 N/s. After the test is completed, the specimen is unloaded. Data is stored, and the apparatus is allowed to cool in an unloaded state until the specimen can be removed and analyzed. Details of the test procedure can be found in Appendix B.

4.4 Four-point bend tests

4.4.1 Experimental design

Four-point bend testing provides not only a simple means to validate the responses of the Si material model to multi-axial stress states as will be described in the following chapter, but also permits the investigation of the feasibility of Si/SiC hybrid structures. Also a notched Si 4-point bend test was designed to assess the effect of stress concentration on the localized deformation.

4.4.1.1 Si 4-point bend test

The earlier work by Chen [1] identified the strain softening behavior of Si at high temperatures through a series of 4-point bend tests. Figure 4.5 shows a Si 4-point bend load-displacement curve at 800 °C and 0.001 mm/s ram speed. According to Sumino and his co-workers [2], it appears that the peak load in the Si 4-point bend test is a function of temperature, strain rate, and grown-in dislocation density. While the effects of the temperature and strain rate on the peak load were considered, the effect of grown-in dislocation density was not explicitly studied in Chen's experiments. The experimental method chosen to further investigate the effect of the dislocation density in the crystal consisted of three steps:

Step 1. Load or position of the actuator ram will be held at a load between the peak and plateau until static relaxation of the specimen occurs.

Step 2. The peak load measured during the reload at a monotonic rate will be compared to the case without the static-relaxation step.

Step 3. The above steps will be repeated for various load levels.

The dislocation density increased at the first loading step may be regarded as the starting dislocation density in the crystal for the second step, which in turn determines the peak load at the reloading step. This experiment will also address how the static load combined with creep affects the overall load-displacement response. Moreover, the discussion will extend to whether or not the structural design can rely on the upper yield strength of the material.

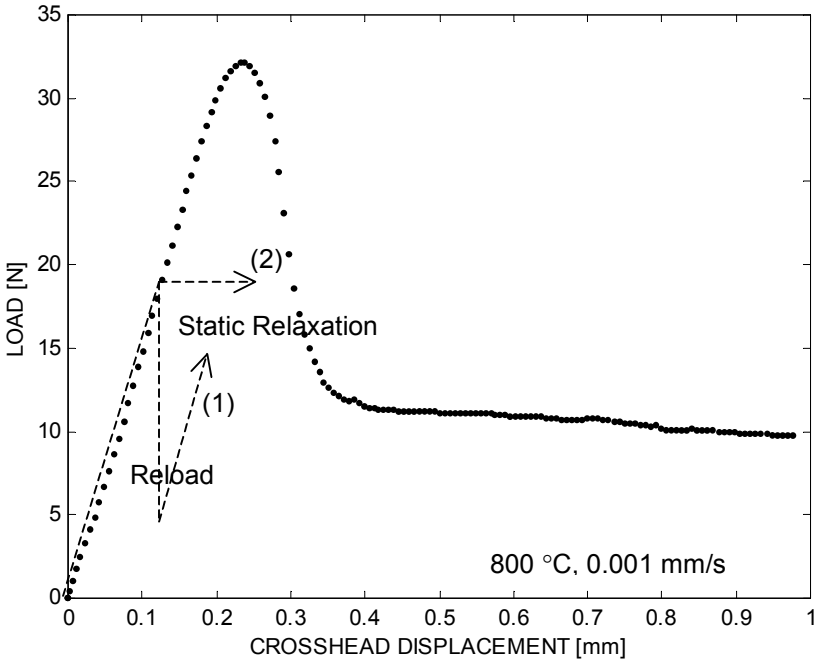

Figure 4.5 Si 4-point bend load-deflection curve at 800 °C and 0.001 mm/s ram speed.

The Si flexural specimens were cut from n-type single crystal Si wafers using a diesaw machine such that the prime cut <110> direction was coincident with the long axis of the specimen, as shown in Figure 4.6. The actual specimen dimensions may vary from the nominal ones due to the starting wafer thickness and the material removal by the amount of the diesaw blade thickness.

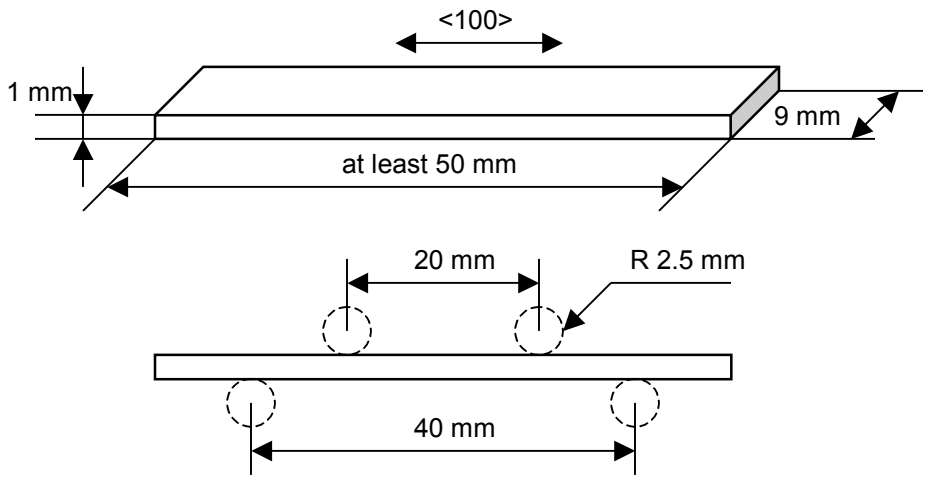

Figure 4.6 Si flexural specimen with the nominal dimensions and material orientation

4.4.1.2 Notched Si 4-point bend test

In order to investigate the effect of stress concentration on the localized deformation when combined with the strain-softening characteristics of Si, a series of 4-point bend tests were performed with the notched specimens. With the aid of linear elastic FE analysis, notch dimensions were determined to provide a range of stress concentration factors. The fillet radii measured from the actual specimens were used. Figure 4.7 shows the FE predictions of the effective stress distribution around the notches. The stress concentration factors, defined by the ratio of the highest stress around the notch and the stress on the outer-most chord of the beam, are tabulated for the proposed notch dimensions in Table 4.2. Note that the stress concentration factor is most sensitive to the fillet radii and notch depth, but relatively insensitive to the notch width. In order to keep the nominal stress the same, the notch depth is controlled to be constant while the stress concentration factor is determined by the fillet radii. Also, a deeper notch is preferred in order to isolate the effect of the notch from that of the load point.

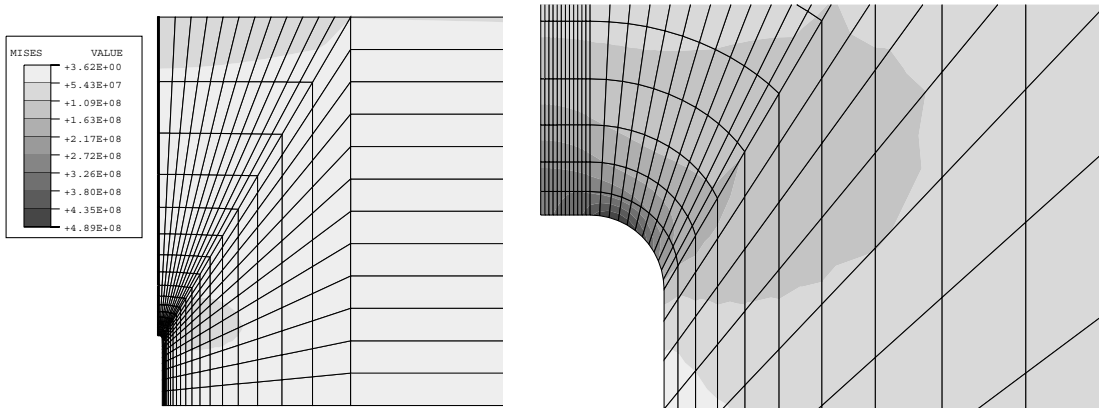

(a)

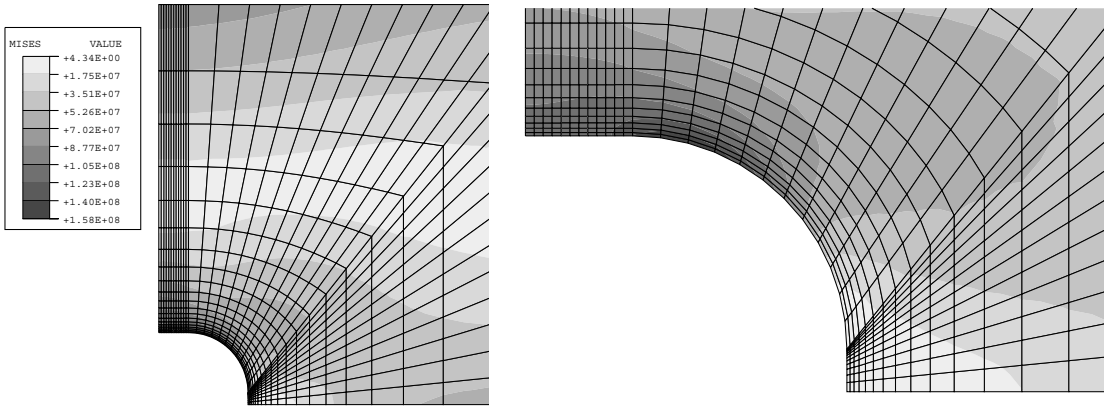

(b)

Figure 4.7 FE predictions on the effective stress distribution around the notches. (a) 25 Width x 180 Depth, 7.5 Fillet Radius (b) 450 W x 180 D, 150 R (dimensions in μm)

Table 4.2 Stress concentration factors corresponding to the proposed notch dimensions.

Dimensions of notches (μm)	Stress concentration factor, K_t
250 (Width) x 200 (Depth), 7.5 (Fillet Radius)	6.4
25 (W) x 180 (D), 7.5 (R)	7.3
25 (W) x 280 (D), 7.5 (R)	9.7
450 (W) x 180 (D), 150 (R)	2.3

The notches were created by a Deep Reactive Ion Etching (DRIE) process, Recipe MIT69 and SF6, developed at the MIT Microsystems Technology Laboratory (MTL). Recipe MIT69 was designed for a high aspect ratio etch while Recipe SF6 was for an isotropic etch. Details of the recipe can be found in Ref. [3]. The etched Si wafers were cut into the flexural specimens using a diesaw such that the prime cut <110> direction is coincident with the long axis of the specimen. Figure 4.8 shows the microphotos of the notches of the flexural specimens. Note the presence of fillet radii around the corners of the notches due to the characteristics of the DRIE process [4]. It is also worth noting that the etch depth varies depending on the size of the Photo Resist (PR) mask openings in this DRIE process as well as the duration of the etch.

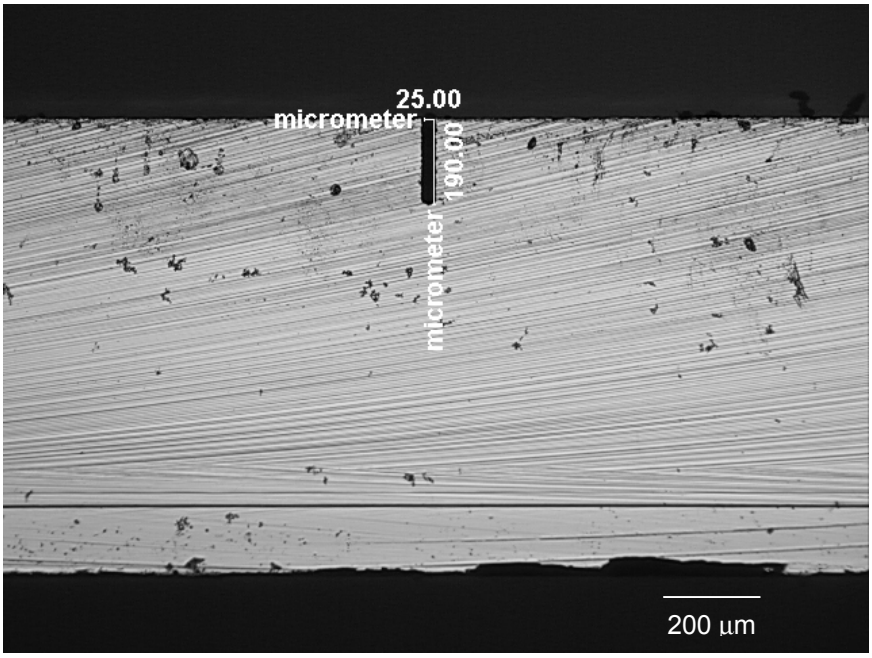

(a)

Figure 4.8 Micrographs of the notches of the Si flexural specimens.

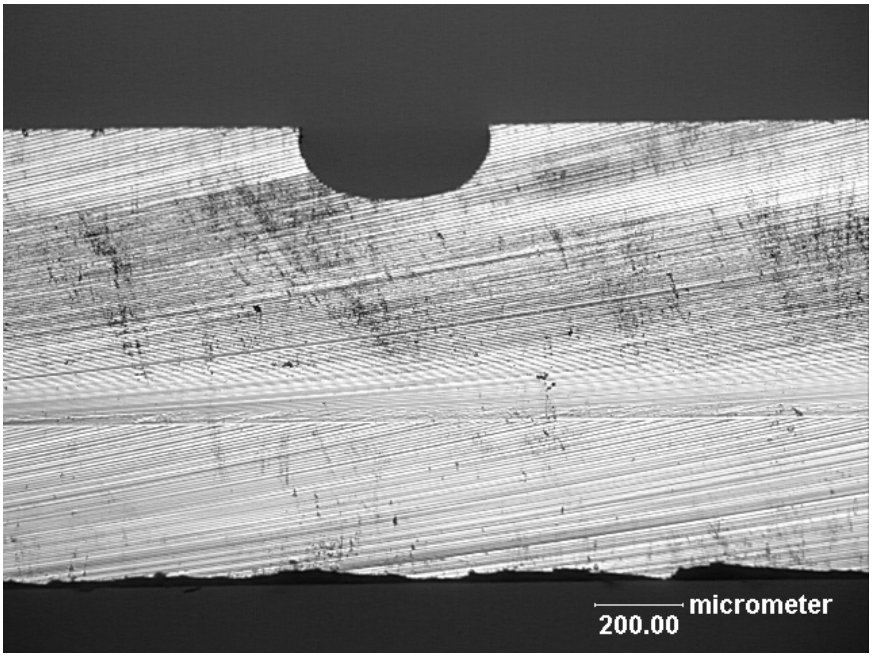

(b)

Figure 4.8 (continued) Micrographs of the notches of the Si flexural specimens.

4.4.1.3 Si/SiC 4-point bend test

Chemical Vapor Deposition (CVD) of SiC is the preferred approach to create SiC reinforcements for the Si/SiC hybrid structures [5]. Hyper-Therm, Inc., a partner of the MIT microengine project and a provider of CVD SiC/Si wafers, focused on the CVD SiC process development ensuring high-strength SiC with a low level of residual stress. The CVD process for SiC is illustrated in Figure 4.9. The recent CVD SiC films processed by Hyper-Therm, Inc. are shown to satisfy most of our specifications such as conformality, low surface roughness, high strength, and low levels of residual stress [6].

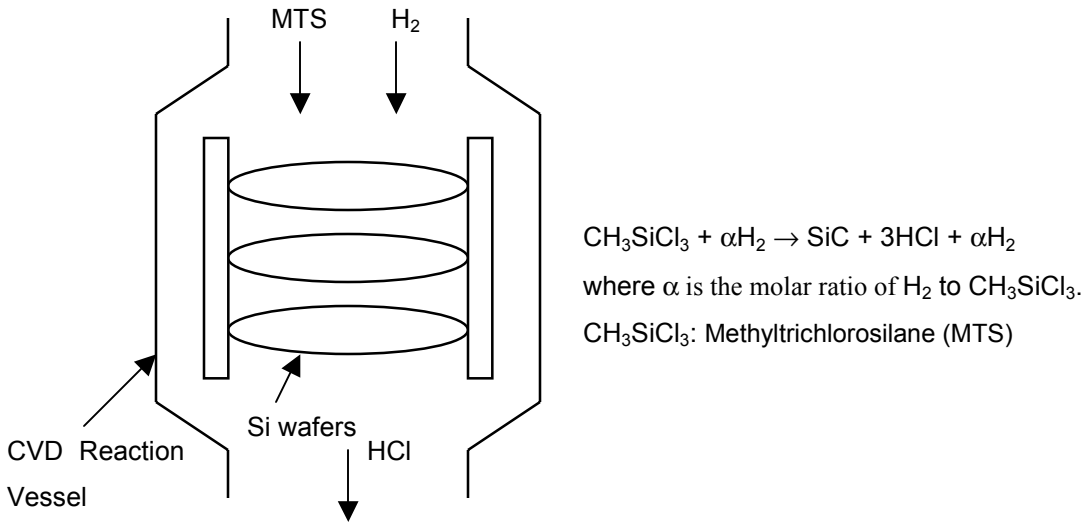

Figure 4.9 CVD SiC processing (Courtesy of Hyper-Therm, Inc. and D. Choi, MIT, 2002)

Four-point bend testing with Si/SiC hybrid specimens as shown in Figure 4.10 was chosen to be a simple means to characterize the mechanical behavior of Hyper-Therm CVD SiC films at elevated temperatures and to prove the concept of Si/SiC hybrid microturbine structures. In terms of loading similarity, the CVD SiC films on the outer-most Si/SiC flexural specimen play a role of the reinforcement that is expected in the Si/SiC hybrid microturine rotor under centrifugal loading. The overall dimensions and material orientations of the Si/SiC specimens are approximately the same as those of the Si flexural specimens.

The thickness measurements of the Si/SiC wafers provided by Hyper-Therm, Inc. are listed in Table 4.3 with the SiC film thickness being a nominal one. The nominal film thickness was obtained by measuring the weight increase during the CVD process divided by the wafer surface area and the SiC density.

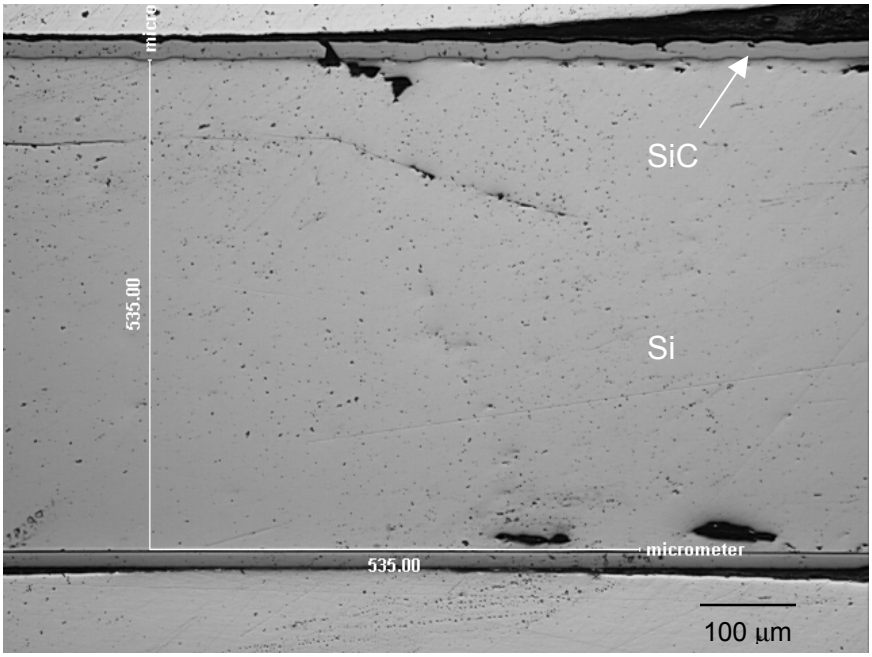

Figure 4.10 Cross-section of a Si/SiC 4-point bend specimen, in which the nominal film thickness is 15 µm. The Si substrate was single-polished.

Table 4.3 Thickness measurements of Si substrates and SiC films. The SiC thickness measurements are the nominal thickness.

Batch number	Si thickness (µm)	SiC thickness (µm)
2-336-2	1061.2	21.8
2-337-2	1059.4	42.4
2-338-2	1067.8	31.5
2-339-2	1069.9	10.9
2-340-2	1067.0	49.5

Figure 4.11 shows the thickness variation of a SiC film between three wafers from different batches. These were deposited during the early CVD SiC process development. It is evident that the thickness of SiC film varies within a wafer from center to edge, which is due to the gas diffusion characteristics of the SiC CVD process. Thus, it is important to account for the film thickness variations in planning experiments as well as performing numerical predictions.

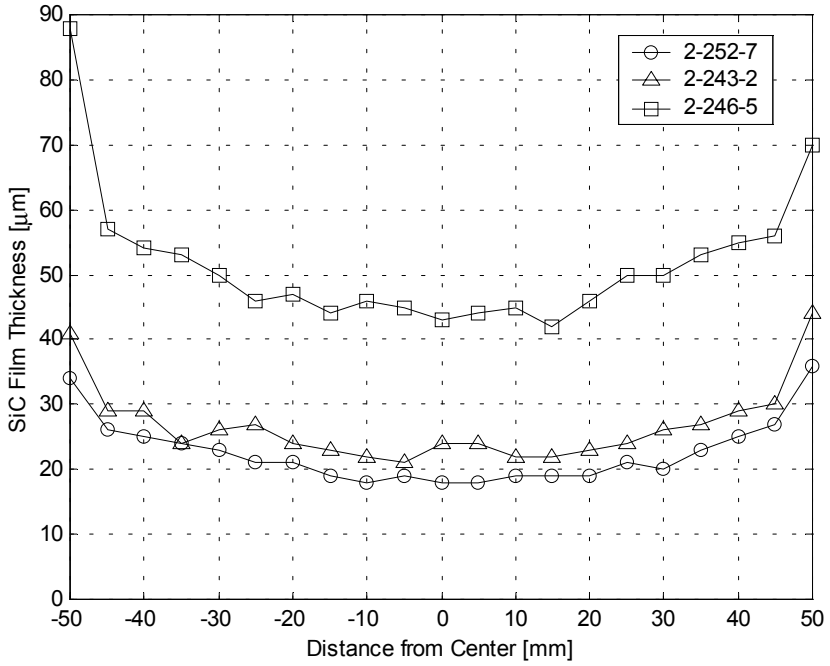

Figure 4.11 Thickness variation of a SiC film within a wafer (Courtesy of Hyper-Therm, Inc. and D. Choi, MIT, 2002). The numbers refer to wafers from the same process batch.

4.4.2 Procedure of 4-point bend test

After assuring that the testing machine is in full working order, the SiC 4-point bend fixture is assembled such that the specimen is centered and sandwiched between the two sets of rollers. The entire fixture is transferred to the lower push rod, where the LVDT is raised to contact the center of the specimen through the opening in the bottom of the fixture. With approximately 1 cm of clearance between the fixture and the top-most push rod, the furnace is closed and heated to the desired temperature. To avoid any interference due to thermally induced strain, the entire apparatus is left to reach equilibrium for 1.5 hours after the target temperature is obtained. At this point, the fixture is carefully brought up to make a contact with the top-most push rod. For a monotonic loading experiment, a waveform is commanded to move the actuator ram to the desired value at the rate of interest. After the test is completed (fracture or maximum displacement achieved), the specimen is unloaded. For a creep test, the control mode is switched from position to load control, and a waveform is commanded to increase the load to the desired value at a rate of 1 N/s. After the test is completed (fracture or desired

creep time achieved), the specimen is unloaded. Data is stored and the apparatus is allowed to cool in an unloaded state until the specimen can be removed and analyzed. (See Appendix B for details of the test procedure.)

4.5 summary

This chapter has described the experimental methods used to investigate the mechanical behavior of Si as a function of temperature and stress and to assess the feasibility of Si/SiC hybrid structures. Si uniaxial compression creep testing was chosen to characterize the mechanical behavior of Si at high temperatures and stresses and to calibrate the Si constitutive model. A 4-point bend test provides not only a simple means to validate the responses of the Si material model to multi-axial stress states, but a simple way to investigate the feasibility of Si/SiC hybrid structures. Once completed, these experiments will answer the three questions posed in the previous chapter associated with the pronounced thermal softening and strain-softening of Si in designing hybrid Si/SiC microturbine structures.

The next chapter presents the development of a constitutive model for Si at high temperatures and stresses based on the mechanisms discussed in the previous chapter. The Si compression creep testing will be fed into the calibration process of the Si model. Experimental results as well as model validation will also be discussed.

Reference

1. K-S. Chen, Materials Characterization and Structural Design of Ceramic Micro Turbomachinery, Ph. D. Thesis, Dept. of Mechanical Engineering, MIT, Cambridge, MA, 1999.
2. K. Sumino, Deformation behavior of silicon, Metallur. Mater. Trans. A, Vol. 30A, pp 1465-1479, 1999.
3. A. A. Ayon, K.-S. Chen, K. A. Lohner, S. M. Spearing, H. H. Sawin, M. A. Schmidt, Deep Reactive Ion Etching of Silicon, Mat. Res. Soc. Symp. Proc., Vol. 546, AA7.1, Fall 1998.
4. K.-S. Chen, A. A. Ayon, S. M. Spearing, Silicon strength testing for mesoscale structural applications, Mat. Res. Soc. Symp. Proc., Vol. 518, N3.8, Spring 1998
5. K. A. Lohner, Microfabricated Refractory Ceramic Structures for Micro Turbomachinery, S. M. Thesis, Dept. of Aeronautics and Astronautics, MIT, Cambridge, MA, 1999.
6. D. Choi, R. J. Shinavski, S. M. Spearing, Process Development of Silicon-Silicon Carbide Hybrid Micro-Engine Structures, Mat. Res. Soc. Symp. Proc., Vol. 687, B5.44, Fall 2001.

Chapter 5

A constitutive Model for Single Crystal Si at Elevated Temperature

5.1 Overview

For homologous temperatures in the range of 0.5 to 0.8, single crystal Si, with an initially small grown-in dislocation density on the order of 10^6 to 10^7 #/m^2, deforms with a behavior characterized by a peak in the stress-strain response. This softening is caused by the rapid increase in the number of dislocations by multiplication mechanisms such as Frank-Read sources [1]. In other words, the plastic shearing rate at the macroscale increases with the increase in the dislocation density. In creep experiments, the rapidly multiplying dislocations are responsible for the initial accelerating primary or incubation creep stage observed in single crystal Si. The infrared photomicrographs shown in Figure 5.1 illustrate the formation of dislocations within a Si crystal in its early creep stages due to a Frank-Read source. The plastic flow favored by the fast dislocation multiplication in diamond-structured materials was investigated by many researchers, including Haasen and co-workers [2, 3]. The initial stages of deformation where the dislocation density is rapidly multiplying will be termed 'Regime 1' from this point on in the present work. As the Si crystal deforms further, the influence of interactions of dislocations becomes important. The increase in the dislocation density, to the extent of forming subgrain structures, leads to a deformation regime where the material history cannot be described by a single measure of the dislocation density but also requires description of the high degrees of interactions among dislocations. Myshlyaev and co-workers estimated the activation energy as being about equal to that for self-diffusion and observed a high stress dependence for Si in this deformation regime [4, 5]. The TEM micrographs in Figure 5.2 show subgrain structures formed within Si, which in turn implies a high degree of interactions between dislocations during the deformation. For simplicity, the deformation

regime characterized by the complicated interactions of dislocations will be termed 'Regime 2' from this point onward.

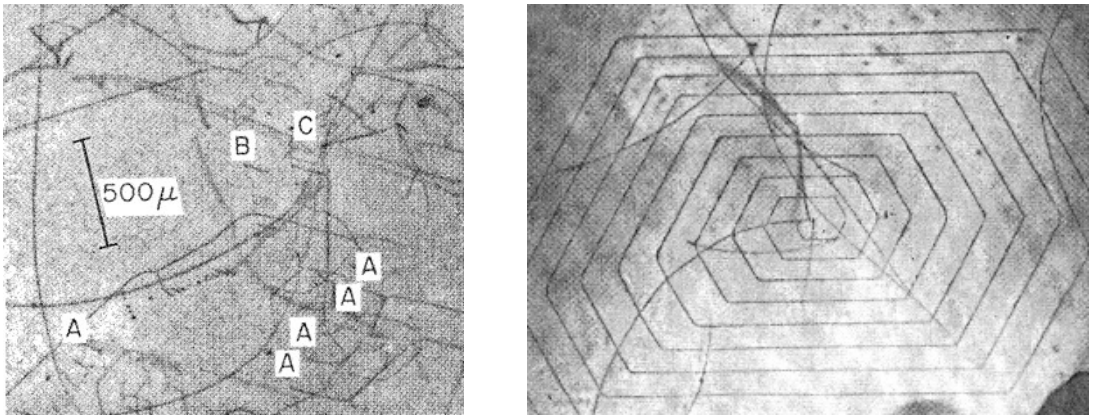

(a) (b)

Figure 5.1 (a) Infrared photomicrograph of deformed Si. Dislocations and trails decorated with Cu. [W. C. Dash, J. Appl. Phys. 29, 705 (1985)]. (b) Si. Infrared photomicrograph of a spiral Frank-Read source decorated with Cu in the interior of a twisted specimen. Viewed in [111] direction. [W. C. Dash, in "Dislocations and Mechanical Properties of Crystals", J. C. Fisher et al., eds., p 57 (1957)].

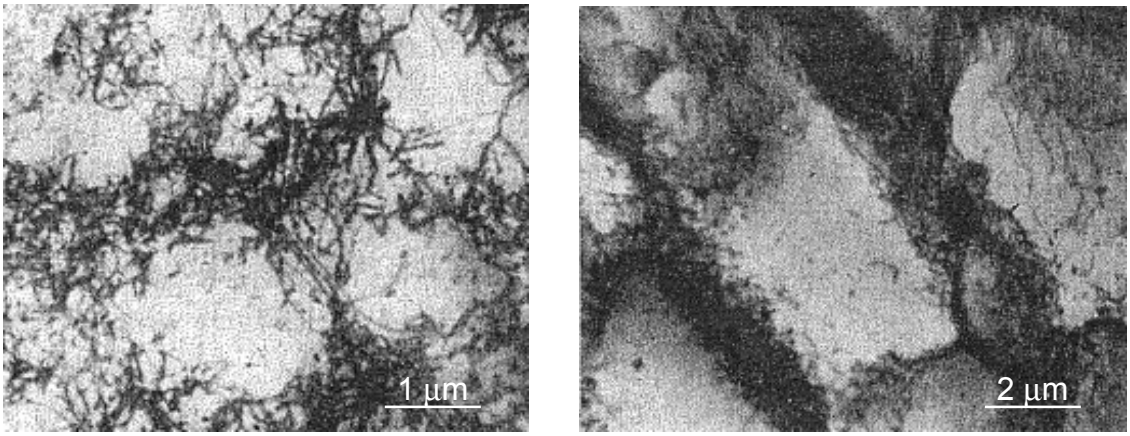

(a) (b)

Figure 5.2 (a) TEM micrograph of cell structures during the decelerating creep stage, revealed by chemical etching. (b) Subgrain structure during steady creep stage. [M. M. Myshlyaev, et al., Dislocation Structure and Macroscopic Characteristics of Plastic Deformation at Creep of Silicon Crystals, Phys. Stat. Sol., Vol. 36, 1969]

This chapter presents the development of a constitutive model to account for these behaviors. An elasto-viscoplastic constitutive model for the deformation of single crystal Si is presented in Section 5.2. A detailed description of the models for Regimes 1 and 2 and the transition between these two regimes is given, together with a complete framework for the displacement-controlled isotropic rate-dependent plasticity. Section 5.3 presents calibration of the model against the compression creep experiments on Si performed at MIT in order to determine the values of the material parameters required for the model. In section 5.4, the calibrated model is then used to predict the response of Si for a series of four-point bend tests at elevated temperatures. This chapter concludes with remarks on the possible additional improvements to the model, as well as its usefulness as a design tool.

5.2 Constitutive equations

In the present work, an elasto-visoplastic constitutive model for the deformation of single crystal Si, initially containing a low dislocation density in the multi-slip <100> and <111> orientations at homologous temperatures of 0.5 to 0.8, is formulated based on the two deformation mechanisms described above. The constitutive model employs two scalar internal variables: a mobile dislocation density ρ_m, which is assumed to be equal to the total dislocation density, $\rho_m = \rho$, which governs the magnitude of the plastic shearing rate in the initial stages of deformation where the dislocation density is rapidly multiplying, and an isotropic resistance to plastic flow, s, which has dimensions of stress, and represents (in a collective sense) the resistance to plastic flow offered by the dislocation substructures in the later stages of deformation after a sufficiently large mobile dislocation density has been generated. The transition between the two deformation regimes takes place at a certain critical dislocation density, above which the material history cannot be described by a single measure of the dislocation density but by the high degrees of interactions among dislocations. This critical dislocation density appears to be a function of only the effective shear stress.

The constitutive model presented here may not be able to represent certain aspects of the behavior of single crystal Si. Currently, this model does not incorporate details of the specific active slip systems or their interactions within crystals, which may play an important role in the predictions of anisotropy or slip bands formed in the material. Instead of a crystal plasticity framework, an isotropic elasto-viscoplastic constitutive model will be formulated. An extension to a crystal plasticity framework will be discussed in Section 5.5. In the following derivations of the model, Gurtin's notation, which is now common in modern continuum mechanics, will be used [6]. The framework of this constitutive model is based on the previous work by Anand and co-workers [e.g., 7, 8].

5.2.1 Governing Variables

The governing variables in this constitutive model are:

$$(\mathbf{T},\ \mathbf{F},\ \mathbf{F}^p,\ \theta,\ \rho,\ s), \tag{5.1}$$

where $\mathbf{T}$ is the Cauchy stress, $\mathbf{F}$ is the deformation gradient tensor, $\mathbf{F}^p$ is the plastic deformation gradient tensor, θ is the absolute temperature in Kelvin, ρ is the dislocation density, and s is the isotropic slip resistance. The deformation gradient tensor $\mathbf{F}$ is defined by a linear operator that relates every material element in the undeformed configuration to the corresponding material element in the deformed configuration. The deformation gradient $\mathbf{F}$ can be multiplicatively decomposed as

$$\mathbf{F} = \mathbf{F}^e\mathbf{F}^p, \tag{5.2}$$

where $\mathbf{F}^e$ ($\det \mathbf{F}^e > 0$) is the elastic part and $\mathbf{F}^p$ ($\det \mathbf{F}^p = 1$) the plastic part. In the elasto-plasticity theory, an elastically deformed configuration is assumed to exist conceptually somewhere between the deformed and undeformed configurations. While the elastic part of the deformation gradient represents the elastic distortion of the material, the plastic part corresponds to the cumulative effect of dislocation motion on the active slip systems.

The dislocation density, ρ, and the average slip resistance, s, are the two key scalar internal variables in this constitutive model that represent the material history during the deformation. The dislocation density, ρ, and its travel speed, $\bar{v}$, determine the internal

shear resistance of the material and in turn the plastic shear strain rate in the early stages of deformation, Regime 1. The isotropic resistance to plastic flow, s, having the physical dimensions of stress, represents the resistance to plastic flow offered by the dislocation substructures in the later stages of deformation, Regime 2. The evolution of the variable, s, accounts for the shape of the isotropic hardening or primary creep (decelerating creep rate followed by a steady-state secondary creep) of the material.

5.2.2 Equations for Stress

The basic constitutive equation for Si is given by the following linear relation:

$$\overline{\mathbf{T}} = \mathscr{E}[\mathbf{E}^e - \alpha_T(\theta - \theta_0)\mathbf{1}], \tag{5.3}$$

where $\overline{\mathbf{T}}$ is the symmetric second Piola-Kirchoff stress tensor,

$$\overline{\mathbf{T}} \equiv (\det \mathbf{F}^e)\mathbf{F}^{e^{-1}}\mathbf{T}\mathbf{F}^{e^{-T}}, \tag{5.4}$$

$\mathbf{E}^e$ is the strain tensor defined by the Green elastic strain measure,

$$\mathbf{E}^e = \tfrac{1}{2}(\mathbf{F}^{e^T}\mathbf{F}^e - \mathbf{1}). \tag{5.5}$$

$\mathscr{E}$ is a fourth-order isotropic elasticity tensor given by:

$$\mathscr{E} \equiv 2\mu I + (\kappa - \tfrac{2}{3}\mu)\mathbf{1} \otimes \mathbf{1}, \tag{5.6}$$

where μ and κ are the shear and bulk modulus, respectively. $\alpha_T \mathbf{1}$ is the second-order isotropic thermal expansion tensor, and θ and θ_0 are the absolute temperature and a reference temperature, respectively. For simplicity, small changes in temperature are assumed in the model so that the material parameters can be considered constant. The constitutive equation given above is nothing more than an extension of the generalized Hooke's law.

5.2.3 Flow Rule

The evolution equation of the plastic deformation is given by

$$\dot{\mathbf{F}}^p = \mathbf{L}^p\mathbf{F}^p, \tag{5.7}$$

where $\mathbf{L}^p$ is the plastic velocity gradient, which is additively decomposable into a symmetric part, $\mathbf{D}^p$, the plastic stretching, and a skew part, $\mathbf{W}^p$, the plastic spin, i.e.:

$$\mathbf{L}^p = \mathbf{D}^p + \mathbf{W}^p = \mathbf{D}^p, \ \mathbf{W}^p = \mathbf{0}. \tag{5.8}$$

It is worth noting that the isotropic constitutive law has no plastic spin. Thus, the evolution equation of the plastic deformation is given by

$$\dot{\mathbf{F}}^p = \mathbf{D}^p \mathbf{F}^p , \tag{5.9}$$

with

$$\mathbf{D}^p = \dot{\bar{\gamma}}^p \frac{\overline{\mathbf{T}}'}{2\bar{\tau}} , \tag{5.10}$$

where $\overline{\mathbf{T}}'$ is the deviatoric part of $\overline{\mathbf{T}}$,

$$\overline{\mathbf{T}}' = \overline{\mathbf{T}} - \tfrac{1}{3}(tr\overline{\mathbf{T}})\mathbf{1} , \tag{5.11}$$

$\bar{\tau}$ is the equivalent shear stress defined by

$$\bar{\tau} = \sqrt{\tfrac{1}{2}\overline{\mathbf{T}}' \cdot \overline{\mathbf{T}}'} , \tag{5.12}$$

and $\dot{\bar{\gamma}}^p$ is the equivalent plastic shear strain rate given by

$$\dot{\bar{\gamma}}^p = \sqrt{2\mathbf{D}^p \cdot \mathbf{D}^p} . \tag{5.13}$$

5.2.4 Evolution Equations

Now what remains to be determined in the model is the plastic shearing rate, $\dot{\bar{\gamma}}^p$. As discussed in Section 5.1, the deformation of single crystal Si at elevated temperatures is governed by rapidly multiplying dislocations and their complicated interactions. The mobile dislocation density, assumed to be equal to the total dislocation density, $\rho = \rho_m$, plays an important role in determining the plastic shearing rate in the early stages of deformation, Regime 1, and the isotropic shear resistance, s, takes over the role of the dislocation density in the later stages of deformation, Regime 2. Both scalar internal variables represent the material history in each deformation regime. The generic functional forms for the two regimes and the transition between the two regimes are:

Regime 1: $(\rho \le \rho_{crit})\ \ \dot{\bar{\gamma}}^p = \hat{\dot{\bar{\gamma}}}^p(\bar{\tau},\theta,\rho),\ \dot{\rho} = \hat{\dot{\rho}}(\bar{\tau},\theta,\rho)$ (5.14a)

Regime 2: $(\rho > \rho_{crit})\ \ \dot{\bar{\gamma}}^p = \hat{\dot{\bar{\gamma}}}^p(\bar{\tau},\theta,s),\ \dot{s} = \hat{\dot{s}}(\bar{\tau},\theta,s)$ (5.14b)

Transition between two regimes: $\rho_{crit} = \hat{\rho}_{crit}(\bar{\tau})$. (5.14c)

The current section describes the details of the evolution equations for each deformation regime, and the transition between the two models will be discussed in the next section.

5.2.4.1 Regime 1 ($\rho \le \rho_{crit}$)

From the experimental and theoretical knowledge of the dislocation velocity and dislocation density, many researchers, including Haasen and co-workers [2, 3], have tried to construct the macroscopic plastic strain rate $\dot{\gamma}^p$ using the general kinematic relation for any stress and temperature. An isotropic constitutive model has also been previously summarized by Dillon and co-workers in this deformation regime [9]. The plastic shear strain rate produced by a crystal is, in general, determined by the Orowan equation [10],

$$\dot{\bar{\gamma}}^p = \rho_m b \bar{v} , \tag{5.15}$$

where ρ_m is the mobile length of dislocations per cubic centimeter, b is the Burgers vector magnitude, and $\bar{v}$ is the average velocity of these dislocations. For small deformations, the mobile dislocation ρ_m can be replaced with the total dislocation density ρ. They found that a statistical arrangement of the dislocations produces a mean internal stress ,

$$\tau_i = \alpha \mu b \sqrt{\rho} , \tag{5.16}$$

where μ is a shear modulus and α is a constant. At certain points in the crystal, τ_i will counteract the applied stress, $\bar{\tau}$. They found that it is an effective stress, the difference between the internal stress and the applied stress, i.e.:

$$\bar{\tau}_{eff} = \bar{\tau} - \tau_i , \tag{5.17}$$

that determines the dislocation velocity and the multiplication rate. Combining the Orowan equation and the dislocation multiplication law (which states that the multiplication of moving dislocations occurs in proportion to their moving length and the distance traveled or $d\rho = \rho \cdot v \cdot dt \cdot \delta$, where δ is the multiplication parameter) yields the multiplication rate as

$$\delta = K \tau_{eff} , \tag{5.18}$$

where K is a multiplication rate constant.

Then, in Regime 1, the dislocation velocity and then the plastic shear strain rate are taken as

$$\dot{\gamma}^p = \hat{\dot{\gamma}}^p(\bar{\tau},\theta,\rho) = \rho b \bar{v} \quad , \quad \bar{v} = \hat{\bar{v}}(\bar{\tau},\theta,\rho) \tag{5.19a}$$

$$\bar{v} = \begin{cases} 0 & if\ \bar{\tau}_{eff} \le 0 \\ \bar{v}_0 \exp(-Q/k\theta)\left(\bar{\tau}_{eff}/\tau_0\right)^{1/m} sign(\bar{\tau}) & if\ \bar{\tau}_{eff} > 0 \end{cases} \tag{5.19b}$$

$$\dot{\bar{\gamma}}^p = \begin{cases} 0 & if\ \bar{\tau}_{eff} \le 0 \\ \rho b \bar{v}_0 \exp(-Q/k\theta)\left(\bar{\tau}_{eff}/\tau_0\right)^{1/m} sign(\bar{\tau}) & if\ \bar{\tau}_{eff} > 0 \end{cases} . \tag{5.19c}$$

Finally, the evolution equation for the dislocation density in Regime 1 is taken as

$$\dot{\rho} = h\dot{\bar{\gamma}}^p \quad , \quad h = \left(\frac{K}{b}\right)\bar{\tau}_{eff} . \tag{5.20}$$

5.2.4.2 Regime 2 ($\rho > \rho_{crit}$)

In this deformation regime, the previous work of Myshlyaev and his co-workers [4, 5] is important. They showed that over a wide range of temperatures and stresses (900 °C to 1300 °C and 20 to 150 MPa) the activation energy of Si crystals is temperature-independent and decreases linearly with increasing stress. The steady creep rate may be represented by the kinetic equation

$$\dot{\bar{\gamma}}^p = \dot{\bar{\gamma}}_0 \exp\left(-\frac{\Delta G^*}{k\theta}\right) = \dot{\bar{\gamma}}_0 \exp\left(-\frac{\Delta F - V\sigma}{k\theta}\right), \tag{5.21}$$

where $\dot{\bar{\gamma}}_0$ is a reference shearing rate, ΔG* is the activation free enthalphy or the Gibb's free energy for activation, ΔF is the activation free energy required to overcome the obstacles to slip without the aid of an applied shear stress, and V is the activation volume. This kinetic equation can be rearranged as

$$\dot{\bar{\gamma}}^p = \dot{\bar{\gamma}}_0 \exp\left(-\frac{\Delta F}{k\theta}\left(1-\frac{\bar{\tau}}{s}\right)\right) \tag{5.22}$$

with the isotropic shear resistance s = ΔF/V, which is now a specific form of the suggestion by Kocks et al. [11],

$$\dot{\bar{\gamma}}^p = \dot{\bar{\gamma}}_0 \exp\left(-\frac{\Delta F}{k\theta}\left(1 - \left(\frac{\bar{\tau}}{s} \right)^p \right)^q \right) \tag{5.23}$$

with p = 1 and q = 1.

To allow for both primary and steady-state creep, the isotropic slip resistance, s, is allowed to vary, and the following simple evolution equation for s is adopted:

$$\dot{s} = h\dot{\bar{\gamma}}^p, \quad h = h_0\left(1 - \frac{s}{s^*} \right), \tag{5.24}$$

where h_0 and s* are additional non-zero positive-valued material parameters that govern the primary creep response. The material parameter s*, which is considered temperature-dependent, is however shown to be reasonably insensitive to temperature changes over the temperature ranges of interest.

5.2.5 Transition between two models

A simple criterion for the transition between Regimes 1 and 2 is the level of the dislocation density within the crystal: as long as the dislocation density is less than a critical value, then the flow and evolution equations for Regime 1 are operative, and Regime 2 becomes operative as soon as the dislocation density reaches the critical value.

According to the creep experiments performed at MIT, the critical dislocation density appears to be nearly insensitive to temperature changes. Thus, the functional form of the critical dislocation density can be given by

$$\rho_{crit} = \hat{\rho}_{crit}(\bar{\tau}) . \tag{5.14c}$$

A simple power law, however, is not appropriate because it breaks down when the applied stress is so small such that the computed critical dislocation density is smaller than the initial value. In order to avoid this problem, the critical value ρ_{crit} is taken to be a modified power-law function of the equivalent shear stress:

$$\frac{\rho_{crit}}{\rho_0} = \begin{cases} A\left(\dfrac{\bar{\tau}}{\tau_0}\right)^n & if\ \rho \geq \rho_{crit0} \\ \dfrac{\rho_{crit0}}{\rho_0} & if\ \rho < \rho_{crit0}\ . \end{cases} \tag{5.25}$$

Here, the parameter ρ_{crit0} is set to be somewhat greater than the initial dislocation density ρ_0 so that the inequality condition does not fail at the first root. Furthermore, in order to guarantee the smooth transition between the two regimes, the plastic shear strain rates for each regime should be the same when the transition takes place. By equating these two plastic shear strain rates for each regime at the transition, i.e.,

$$\dot{\bar{\gamma}}^{p}{}_{regime\ 1} = \dot{\bar{\gamma}}^{p}{}_{regime\ 2} \text{ at } (\rho = \rho_{crit}), \tag{5.26}$$

the shear resistance, s, can be initialized for Regime 2 as follows:

$$s_0 = \hat{s}_0(\rho_{crit}) \tag{5.27a}$$

$$s_0 = \bar{\tau} \cdot \left(1 + \log\left(\frac{\dot{\bar{\gamma}}^{p}{}_{regime\ 1}\Big|_{\rho=\rho_{crit}}}{\dot{\bar{\gamma}}_0}\right)\frac{k\theta}{\Delta F}\right)^{-1}. \tag{5.27b}$$

5.3 Model Calibration

The constitutive model has been implemented by writing a subroutine VUMAT for a commercial finite element program, ABAQUS EXPLICIT™ [12] to facilitate simulations of Si structures. The material parameters in the model have been calibrated using the compression creep experiments on Si performed at MIT and also those reported in the literature [4, 9].

The material parameters in the model can be classified into three groups based on what they do: (i) material parameters for Regime 1, which govern the initial accelerating creep and strain softening, (ii) material parameters for Regime 2, which determine the primary and secondary creep and strain-hardening, and (iii) the transition parameters. These three material parameter groups are somewhat independent of each other.

5.3.1 Material parameters for Regime 1

First, the material parameters for Regime 1 consist of the following:

$$(b, v_0, \tau_0, Q, k_B, m, \rho_0, \rho_{init}, \alpha, K),$$

where b is the Burgers vector magnitude, v_0 is the reference dislocation velocity, τ_0 is the reference shear stress, Q is the activation energy, k_B is Boltzmann's constant, m is the strain rate sensitivity, ρ_0 is the reference dislocation density, ρ_{init} is the initial dislocation density in the crystal, α is the coefficient of the internal shear resistance, and K is the dislocation multiplication rate constant. Dillon and co-workers [9] found the values for these material parameters to calibrate their model to fit the previous experiments performed by Sumino et al [13]. While most of the values suggested by them were reused here, α and K were adjusted to fit the incubation creep stage of the compression creep experiments performed at MIT by the trial and error method. α was adjusted from 0.3 to 2.0, and K from 3.1E-4 m/N to 2.0E-4 m/N. While K determines the initial slope of the creep-time response, a has an effect on the acceleration/deceleration of the dislocation multiplication rate and then the creep rate. Thus, the shape of the incubation creep stage is determined by the combination of these two parameters. These two parameters are also critical in determining the upper yield point in the stress-strain response. The material parameters are found to be:

$b = 3.83E\text{-}10$ m	$m = 0.9091$
$v_0 = 4.3E\text{-}4$ m/sec	$\rho_0 = 2E7$ #/m^2
$\tau_0 = 5.5$ MPa	$\alpha = 2.0$
$Q = 3.47E\text{-}19$ J	$K = 2.0E\text{-}4$ m/N
$k_B = 1.38E\text{-}23$ J/K	

Note that the strain sensitivity of 0.9091 (i. e., close to unity) may support the idea of a deformation mechanism in which the dislocations glide through the lattice opposed by a resistance caused by the Peierl's stress with less active dislocation interactions.

5.3.2 Material parameters for Regime 2

Second, material parameters for Regime 2 are

$$(\dot{\bar{\gamma}}_0, \Delta F, h_0, s^*),$$

where $\dot{\bar{\gamma}}_0$ is the reference plastic shear strain rate for Regime 1, ΔF is the activation free energy, h_0 is the initial hardening coefficient, and s^* is the saturation value of the shear resistance. For the first two parameters, the values reported by Myshlyaev and co-workers [4] were further calibrated using the compression creep experiments on Si performed at MIT. Since they, however, focused only on the secondary creep stage, the next two parameters (hardening parameters) that determine the primary creep were not available in their work. These parameters were found by fitting the creep experiments at MIT by the trial and error method. The calibration results are as follows:

$$\dot{\bar{\gamma}}_0 = 0.5E9 \text{ sec}^{-1}$$

$$\Delta F = 6.6E\text{-}19 \text{ J}$$

$$h_0 = 12.5 \text{ GPa}$$

$$s^* = 330 \text{ MPa}$$

5.3.3 Material parameters for transition between two regimes

Finally, in order to obtain the transition parameters,

$$(A, n, \rho_{crit0}),$$

where A and n are the constants for the power law equation and ρ_{crit0} is the initial critical dislocation density, the critical dislocation density needs to be found for each temperature and stress. Once a series of the critical dislocation densities for the sets of each temperature and stress are obtained by fitting the experimental results, specifically those from the compression creep experiments at MIT, the transition parameters can be found by constructing the power law equation with a least-square method. It is worth noting that the critical dislocation density, or the internal shear stress at this point, is proven to be insensitive to temperature changes as shown in Figure 5.3. The initial critical dislocation density ρ_{crit0} is chosen to be large enough to prevent the inequality condition

from Regime 1 from failing due to the first real root. The transition parameters found are as follows:

$$A = 208.2$$

$$n = 2.11$$

$$\rho_{crit0} = 2E8\ \#/m^3$$

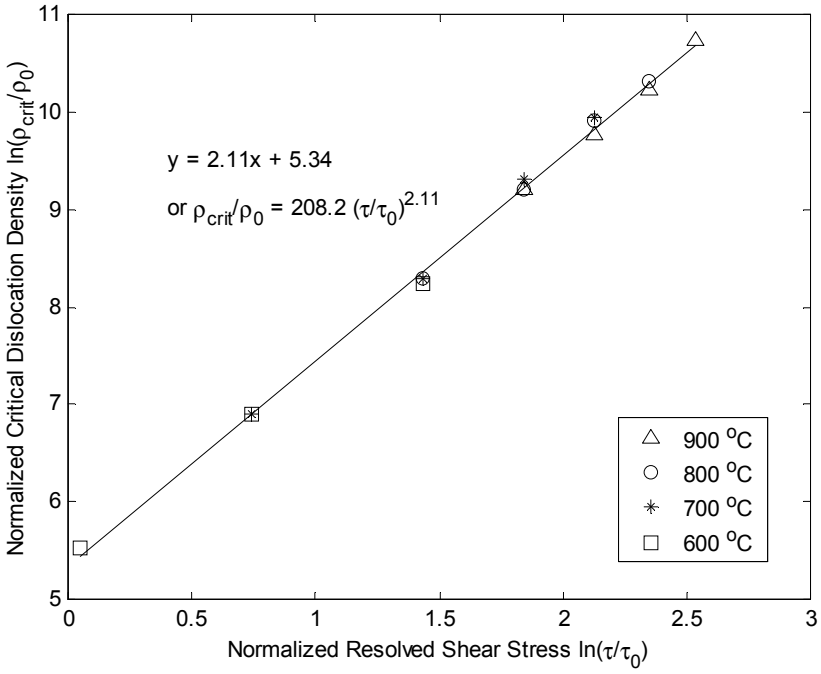

Figure 5.3 Construction of a power law equation for the critical dislocation density using a least-square method. Note that the critical dislocation density is shown to be insensitive to temperature changes, only dependent on stress.

The stress exponent n in the power law equation is found to be close to 2.0. Note that the internal shear stress in Equation 5.16 in Regime 1 is also proportional to the square root of the dislocation density. This in turn provides a good physical correlation with the stress exponent of the power law for the critical dislocation density to be close to 2.0. In this power law equation obtained from the creep experimental data and model calibration, the shear resistance is determined by the critical dislocation density at the transition between the two defomation regimes and initialized for Regime 2.

In the model calibration, finite element calculations using ABAQUS/EXPLICIT™ were performed for simple compression with a single ABAQUS-C3D8R element, a reduced

order three-dimensional continuum element, subjected to the appropriate load and temperature. The material model implemented in the subroutine VUMAT of ABAQUS/EXPLICIT^{TM} is compiled at the beginning of each finite element calculation. The material parameters were fitted to the experimental results through this finite element calculation by the calibration method described in this section. Although this calculation performed on a single element under constant stress or pressure is inappropriate to simulate the actual boundary conditions for the uniaxial compression creep testing, where in effect the cross sectional area constantly changes with deformation, the error in the stress associated with the area change is at most a few percent. Considering the experimental errors inherent in the compression testing, this error can be regarded negligible. Figures 5.4 (a) ~ (d) show the calibration results of the Si model fitted against the creep experiments; the fit is reasonably satisfactory. At relatively low temperatures, the model can describe the observed incubation creep stage with good strain sensitivity and temperature dependence. At high temperatures, the incubation creep stage is almost negligibly small, and the model can be satisfactorily fit to the primary and secondary creep regimes.

In order to validate the calibration of the model using a single element, a fine mesh defined by axisymmetric elements, ABAQUS-CAX4R, was considered as shown in Figure 5.5 Here the SiC load pad is modeled as a rigid surface on which the constant creep loads can be applied. The friction coefficient of 0.1 was used for the contact interface that consists of a pair of SiC load pads, a Si specimen, and BN (Boron Nitride) solid lubricant. The finite element result using this fine mesh was compared with those of the model and the experimental results in Figure 5.6. Although the deformation of the specimen is nearly uniform, the overall recorded displacement of the rigid surface in this calculation was somewhat smaller than those of the model prediction using the single element mesh. The smaller creep strain results from the frictional dissipation in the interface as well as the cross sectional area change of the specimen with the creep strain increase. This leads to an increase in the critical dislocation density ρ_{crit} of a few percent.

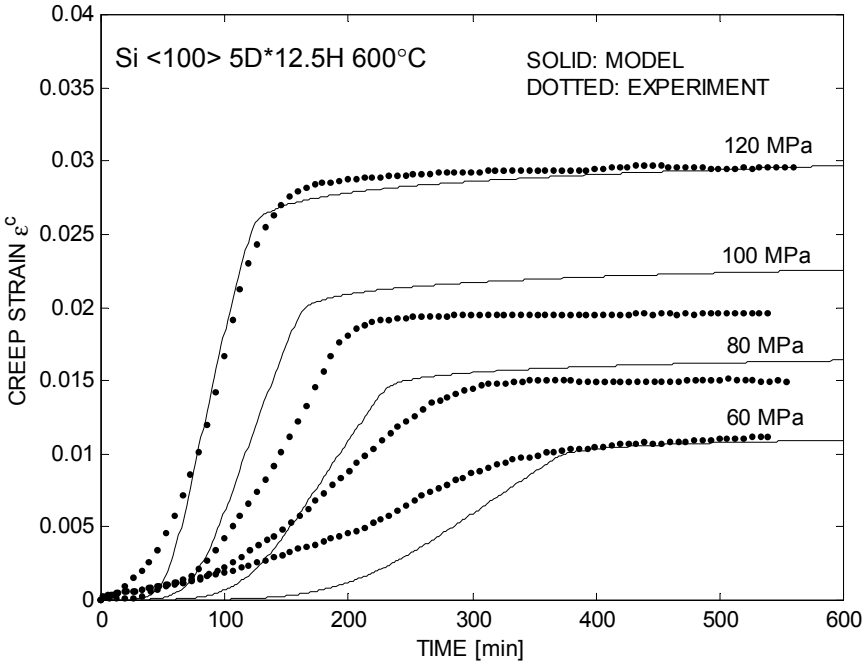

(a) 600 °C

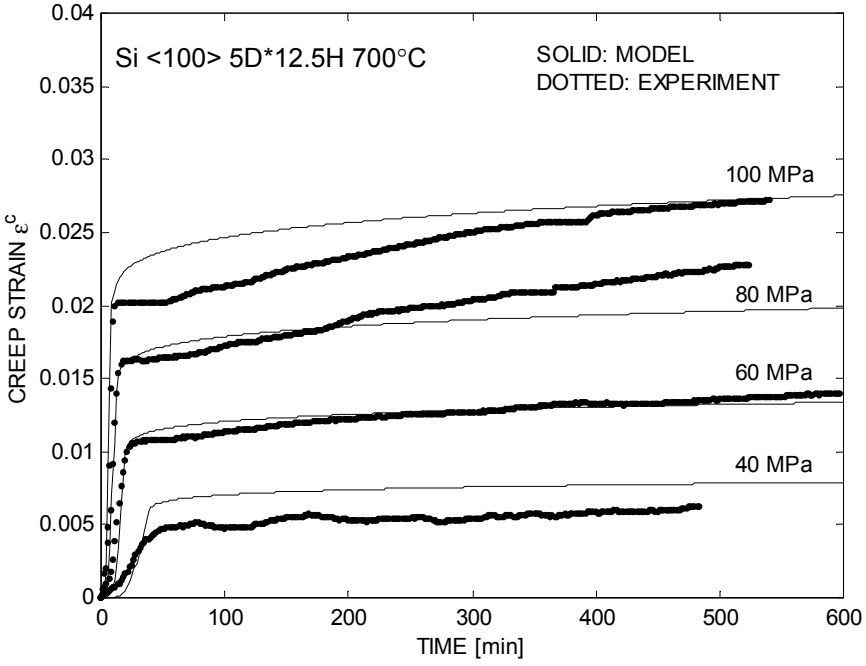

(b) 700 °C

Figure 5.4 Calibration results of the Si model fitted against the creep experimental data. (a) 600 °C, (b) 700 °C, (c) 800 °C, and (d) 900 °C.

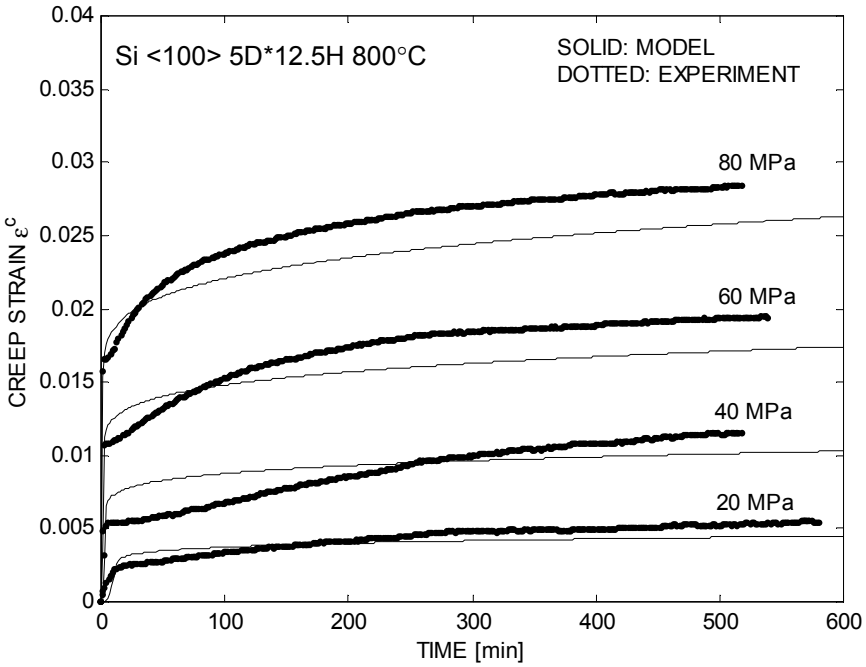

(c) 800 °C

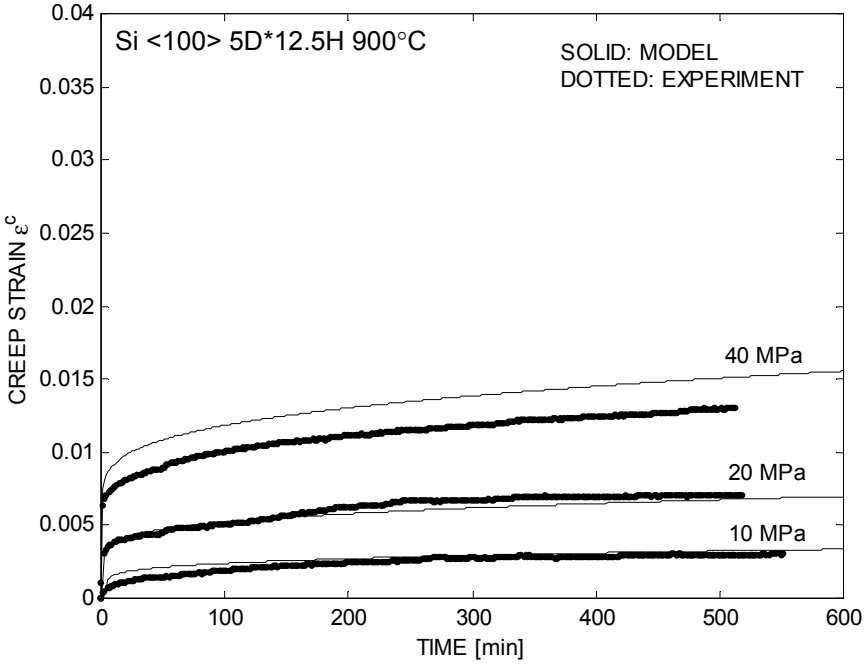

(d) 900 °C

Figure 5.4 (continued) Calibration results of the Si model fitted against the creep experimental data. (a) 600 °C, (b) 700 °C, (c) 800 °C, and (d) 900 °C.

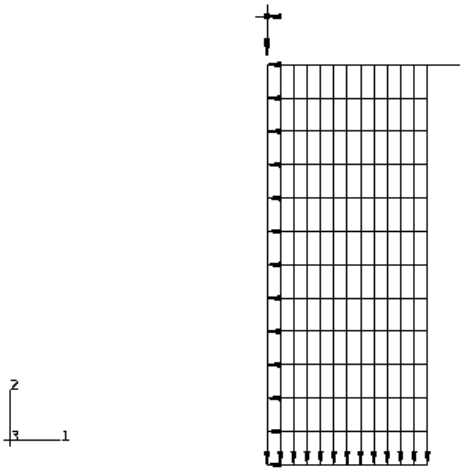

Figure 5.5 Axisymmetric FE mesh for uniaxial compression (creep) testing.

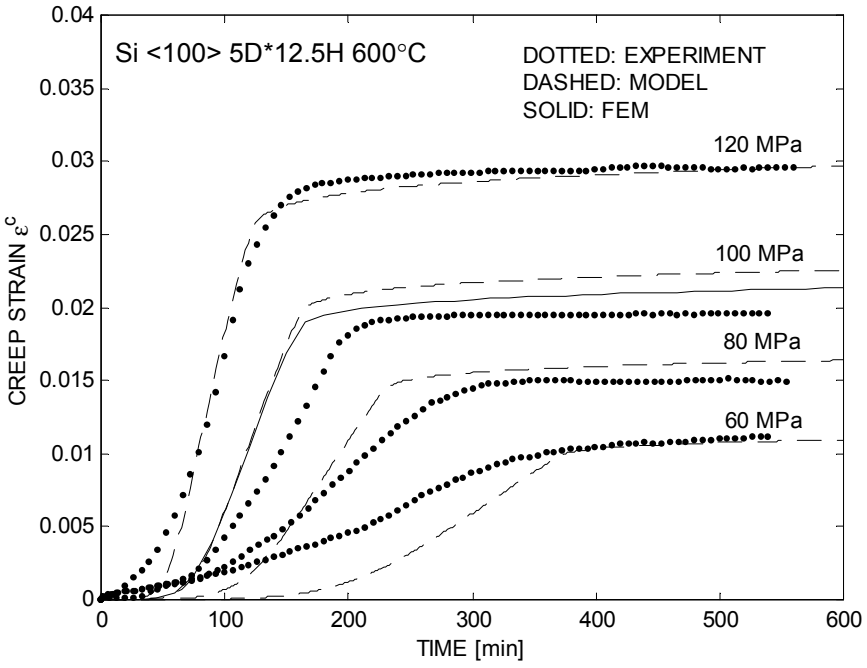

Figure 5.6 Comparison of the finite element calculation for the creep at 600 °C using a fine mesh against the experimental data and the model prediction.

5.4 Model Validation

This section presents more details of the experimental results for the compression creep tests and describes the qualitative behavior of the calibrated model for monotonic loading. The predictive capabilities of the model were also verified by comparing the load-deflection response of Si in a series of four-point bend tests: notched beams in monotonic loading by Chen [14], tests for various loading histories, and tests with notched Si specimens and Si/SiC hybrid specimens.

5.4.1 Si uniaxial compression creep test

Creep tests in unaixial compression, with n-type single crystal Si in multi-slip <100> and <111> orientations, were conducted over a temperature range of 600 to 900 °C and a normal stress range of 10 to 120 MPa. The test results were used to understand better the mechanical behavior of single crystal Si at elevated temperatures and to calibrate the Si constitutive model.

5.4.1.1 Experimental results

Formation of slip bands in a compression specimen

A creep specimen loaded in a <100> orientation tested at 700 °C and 80 MPa was prepared to investigate the deformation pattern at the microscale. A nominal strain of 0.03 was recorded for this specimen after approximately 8 hours of creep. The specimen was mounted in an epoxy molding compound such that the (100) plane of the crystal was exposed, and then polished progressively, finishing with 0.3 μm alumina grit. The uniform slip bands shown in Figure 5.7 were revealed after etching in a solution (97 % HNO_3 + 3% HF (45 % concentration)) for 2 minutes. The slip bands revealed on the (100) plane are aligned in <110> directions. This is consistent with the active family of slip planes being the <111> as expected for diamond (and FCC) structures. Although the micrographs do not allow for the estimation of the dislocation density nor the subgrain structures of dislocations in the crystal, the formation of the uniform slip bands shown in

the micrographs of the compression specimen indicates the high degree of plasticity as well as the homogeneous nature of the deformation.

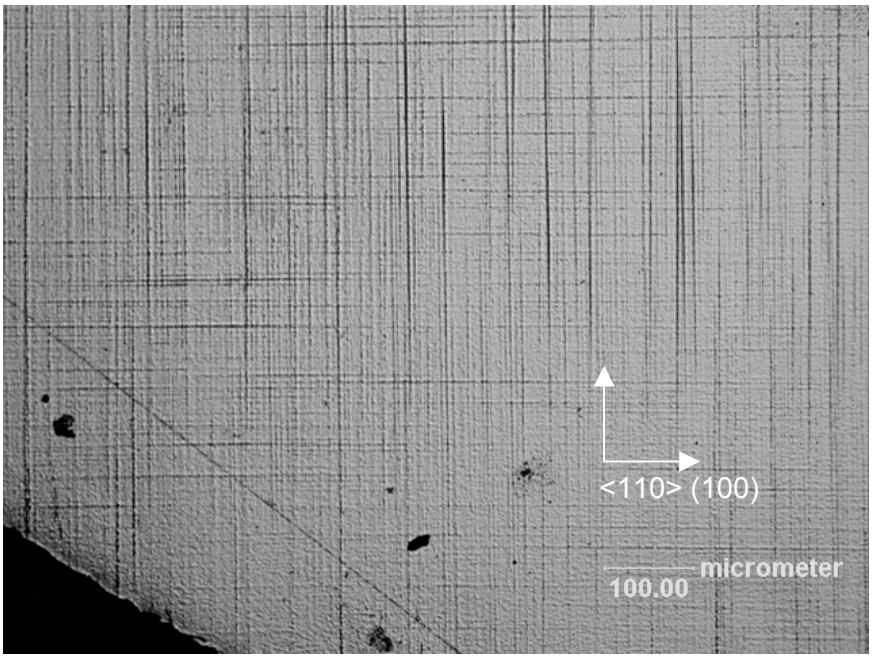

(a)

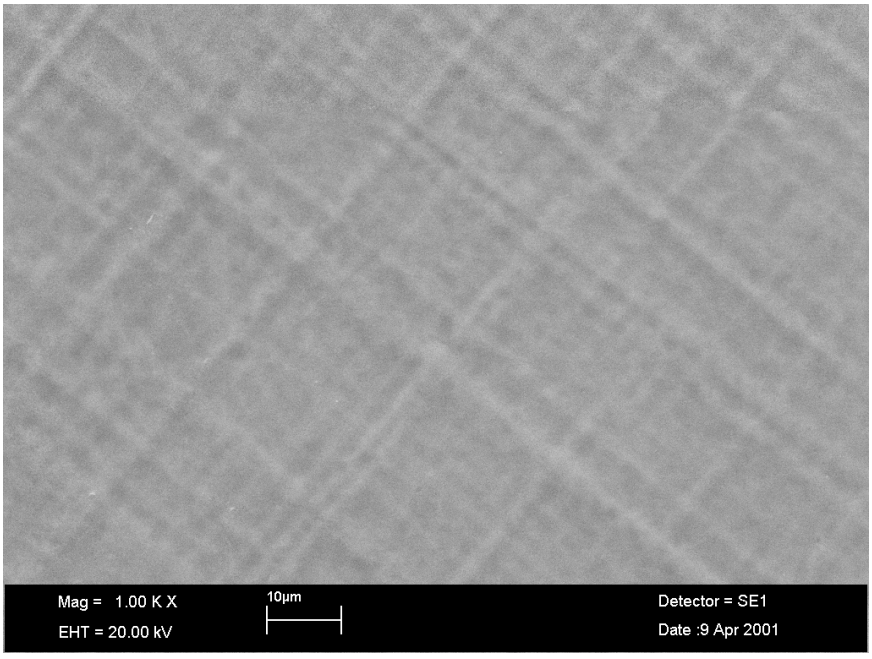

(b)

Figure 5.7 Formation of slip bands in a tested compression specimen with the multi-slip system <100> orientation coincident with the compression axis at 700 °C and 80 MPa.

Effect of crystal orientations on Si creep

Two multi-slip <100> and <111> orientations in the compression axis were considered in order to investigate the effect of crystal orientations on Si creep. Two sets of the creep test results for each orientation were compared in Figure 5.8. Considering the experimental errors associated with the compression creep tests, the creep curves for single crystal Si in the two multi-slip orientations are indistinguishable in terms of the macroscale creep response. To evaluate the validity of the experimental results, a brief analysis is given in this section.

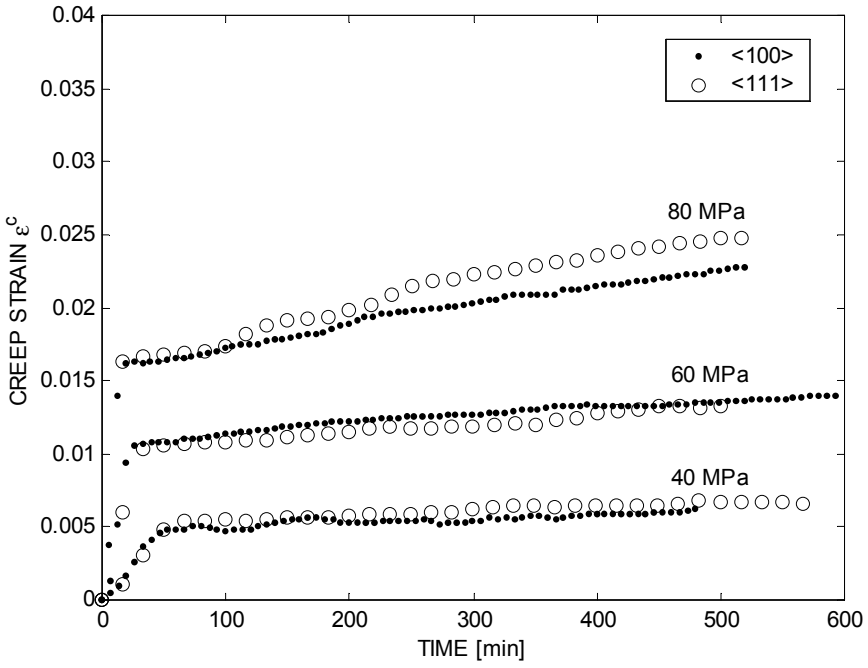

Figure 5.8 Comparison of the experimental creep data for multi-slip systems <100> and <111> orientations

Diamond structures and FCC crystals have twelve slip systems. There are eight slip systems activated when loaded in the <100> orientation as described in Table 5.1, and the slip activity on all the systems is equal. Using the crystal plasticity relations, an equivalent plastic strain rate can be expressed by a slip rate, $\dot{\gamma}^{\alpha}$, on the active slip systems as follows. The plastic velocity gradient $\mathbf{L}^{p}$ is defined by a flow rule as:

$$\mathbf{L}^p = \dot{\mathbf{F}}^p \mathbf{F}^{p^{-1}} = \sum_\alpha \dot{\gamma}^\alpha \mathbf{m}^\alpha \otimes \mathbf{n}^\alpha \,, \tag{5.28}$$

where $\mathbf{m}^\alpha \otimes \mathbf{n}^\alpha$ represents the slip systems in the crystals. By definition, the equivalent plastic strain rate is:

$$\dot{\bar{\varepsilon}}^p = \sqrt{2/3 \mathbf{D}^{p'} \cdot \mathbf{D}^{p'}} \,, \tag{5.29}$$

where $\mathbf{D}^{p'}$ is the deviatoric part of the plastic stretching, $\mathbf{D}^p$,

$$\mathbf{D}^{p'} = \mathbf{D}^p - \tfrac{1}{3} tr(\mathbf{D}^{p'}) \mathbf{1} \,, \tag{5.30}$$

with the plastic stretching, $\mathbf{D}^p$, defined by the symmetric part of the plastic velocity gradient, $\mathbf{L}^p$,

$$\mathbf{D}^p = \tfrac{1}{2} (\mathbf{L}^p + \mathbf{L}^{p^T}) \,. \tag{5.31}$$

By substituting all eight slip systems active in the <100> orientation in Equation 31, the expression for the equivalent plastic strain rate for the multi-slip <100> orientation is obtained as:

$$\dot{\bar{\varepsilon}}^p = 2.0 \dot{\gamma}^\alpha \,. \tag{5.32}$$

Similarly, for the multi-slip <111> orientation, where six slip systems are active, the equivalent plastic strain rate is:

$$\dot{\bar{\varepsilon}}^p = 1.633 \dot{\gamma}^\alpha \,. \tag{5.33}$$

According to the analysis above, ideally the strain rate for compression in the <100> orientation is expected to be approximately 18 % more than that for the <111> orientation. However this is less than the experimental scatter present in the test results. As was discussed in Chapter 3, the sources for the experimental errors in compression creep testing include the friction between the load pad and specimen, seating of the load train, and any misalignment that might cause elastic/plastic buckling and undesirable stress gradients. Moreover, misalignment in the machining of specimens may result in changes in the active slip systems, and consequently the macroscale deformation.

Table 5.1 Active slip systems in the multi-slip <100> and <111> orientations for FCC crystals. Components of $\mathbf{m}^{\alpha}$and $\mathbf{n}^{\alpha}$ are expressed with respect to an orthonormal basis associated with the crystal lattice.

Active slip systems in the <100> orientation		Active slip systems in the <111> orientation	
m^{α}	n^{α}	m^{α}	n^{α}
$\frac{1}{\sqrt{2}}$ $-\frac{1}{\sqrt{2}}$ 0	$\frac{1}{\sqrt{3}}$ $\frac{1}{\sqrt{3}}$ $\frac{1}{\sqrt{3}}$	$\frac{1}{\sqrt{2}}$ 0 $\frac{1}{\sqrt{2}}$	$-\frac{1}{\sqrt{3}}$ $\frac{1}{\sqrt{3}}$ $\frac{1}{\sqrt{3}}$
$\frac{1}{\sqrt{2}}$ 0 $-\frac{1}{\sqrt{2}}$	$\frac{1}{\sqrt{3}}$ $\frac{1}{\sqrt{3}}$ $\frac{1}{\sqrt{3}}$	$\frac{1}{\sqrt{2}}$ $\frac{1}{\sqrt{2}}$ 0	$-\frac{1}{\sqrt{3}}$ $\frac{1}{\sqrt{3}}$ $\frac{1}{\sqrt{3}}$
$\frac{1}{\sqrt{2}}$ 0 $\frac{1}{\sqrt{2}}$	$-\frac{1}{\sqrt{3}}$ $\frac{1}{\sqrt{3}}$ $\frac{1}{\sqrt{3}}$	0 $\frac{1}{\sqrt{2}}$ $\frac{1}{\sqrt{2}}$	$\frac{1}{\sqrt{3}}$ $-\frac{1}{\sqrt{3}}$ $\frac{1}{\sqrt{3}}$
$\frac{1}{\sqrt{2}}$ $\frac{1}{\sqrt{2}}$ 0	$-\frac{1}{\sqrt{3}}$ $\frac{1}{\sqrt{3}}$ $\frac{1}{\sqrt{3}}$	$\frac{1}{\sqrt{2}}$ $\frac{1}{\sqrt{2}}$ 0	$\frac{1}{\sqrt{3}}$ $-\frac{1}{\sqrt{3}}$ $\frac{1}{\sqrt{3}}$
$\frac{1}{\sqrt{2}}$ 0 $-\frac{1}{\sqrt{2}}$	$\frac{1}{\sqrt{3}}$ $-\frac{1}{\sqrt{3}}$ $\frac{1}{\sqrt{3}}$	$\frac{1}{\sqrt{2}}$ 0 $\frac{1}{\sqrt{2}}$	$\frac{1}{\sqrt{3}}$ $\frac{1}{\sqrt{3}}$ $-\frac{1}{\sqrt{3}}$
$\frac{1}{\sqrt{2}}$ $\frac{1}{\sqrt{2}}$ 0	$\frac{1}{\sqrt{3}}$ $-\frac{1}{\sqrt{3}}$ $\frac{1}{\sqrt{3}}$	0 $\frac{1}{\sqrt{2}}$ $\frac{1}{\sqrt{2}}$	$\frac{1}{\sqrt{3}}$ $\frac{1}{\sqrt{3}}$ $-\frac{1}{\sqrt{3}}$
$\frac{1}{\sqrt{2}}$ $-\frac{1}{\sqrt{2}}$ 0	$\frac{1}{\sqrt{3}}$ $\frac{1}{\sqrt{3}}$ $-\frac{1}{\sqrt{3}}$		
$\frac{1}{\sqrt{2}}$ 0 $\frac{1}{\sqrt{2}}$	$\frac{1}{\sqrt{3}}$ $\frac{1}{\sqrt{3}}$ $-\frac{1}{\sqrt{3}}$		

Activation energy and stress exponent

The validity of the creep experiments is again discussed in terms of the activation energy and the stress exponent. Often the steady-state creep rate can be correlated with both stress and temperature by a power law of the form:

$$\dot{\varepsilon} = A\sigma^{n} \exp(-Q_c / RT), \tag{5.34}$$

where A is a material constant, n is a stress exponent, Q_c is the creep activation energy, R is the gas constant (8.31 Jmol-1K-1), and T is the absolute temperature in Kelvin. As pointed out by Haasen and co-workers [2, 3], this empirical equation also can be used to express the functional dependence of the strain rate at the stationary stage (inflection point or point of a maximum strain rate) on stress and temperature. This stationary point in a creep curve and the lower yield point in a monotonic loading share the same strain rate, $\dot{\varepsilon}_{IP}$, and stress, σ_{LY}. In other words, the monotonic loading at a strain rate, $\dot{\varepsilon}_{IP}$, which in a creep test under stress, σ_{LY}, occurs at the stationary stage, yields the same lower yield stress, σ_{LY}. A power law equation was obtained using the maximum strain rates (at the stationary points) of the creep curves at the creep temperatures and stresses.

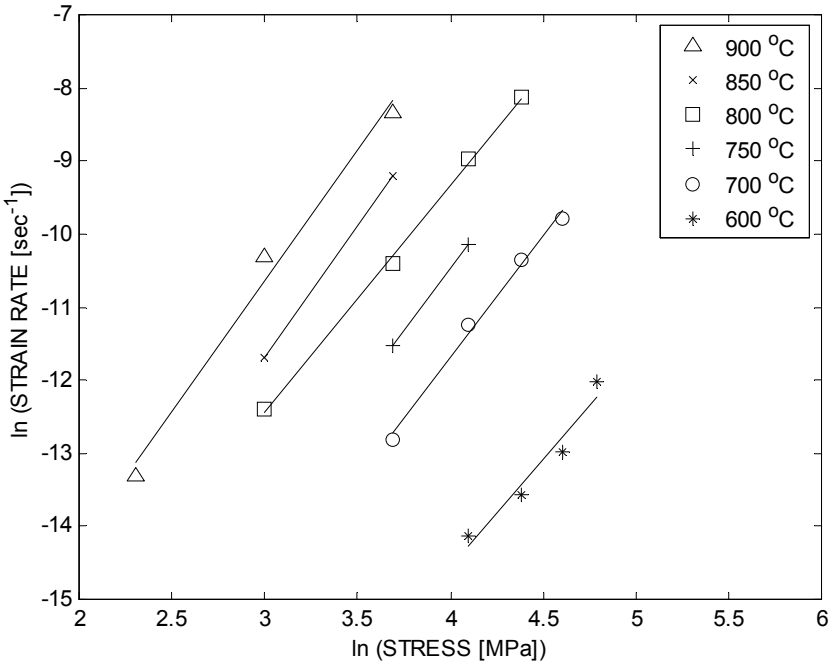

(a)

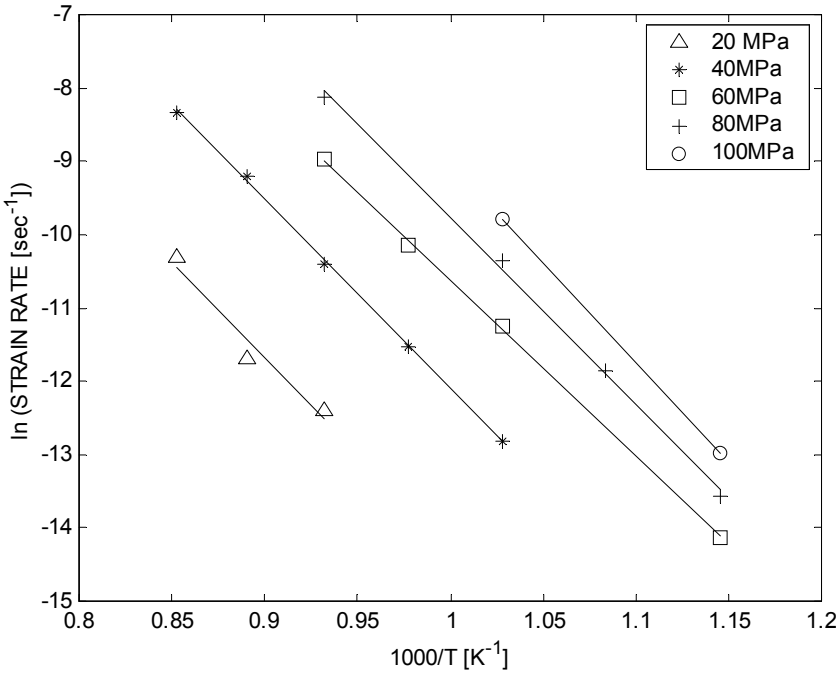

(b)

Figure 5.9 Activation energy and stress exponent for a power law equation to determine the functional dependence of the strain rate at the stationary point on temperature and stress

The activation energy, Q_c, of 213.3 kJ/mol and stress exponent, n, of 3.3 were obtained using a least-square method, as illustrated in Figure 5.9. This is in good agreement with Haasen and co-worker's result [2, 3] who obtained an activation energy Q of 231.6 ± 4.8 kJ/mol and stress exponent of 3.

5.4.1.2 Model response to monotonic loading

The responses of the model to a dynamic loading (constant strain rate or constant ram speed) have been investigated further. Using the same finite element mesh as the one in the model calibration, the uniaxial compression testing was simulated for a series of loading conditions with various temperatures, strain rates, and grown-in dislocation densities. Figure 5.10 illustrates the qualitative behavior of this model for the response to a dynamic loading. The compression testing of Si, when performed with a constant strain rate, is characterized by a pronounced upper yield strength followed by strain-softening, an easy glide region, and strain-hardening similar to that for metals [15]. As supported by the experimental results in the literature [13, 16], the upper yield strength increases with the decrease in temperature, the increase in strain rate, and the decrease in the grown-in dislocation density. Moreover, the strain-hardening curves after an easy glide region appear to converge. With the dislocation density in the crystal increased to a level which yields high levels of interaction between dislocations, the deformation mechanism becomes less sensitive to the changes in temperatures, strain rate, and rather obviously, the dislocation density.

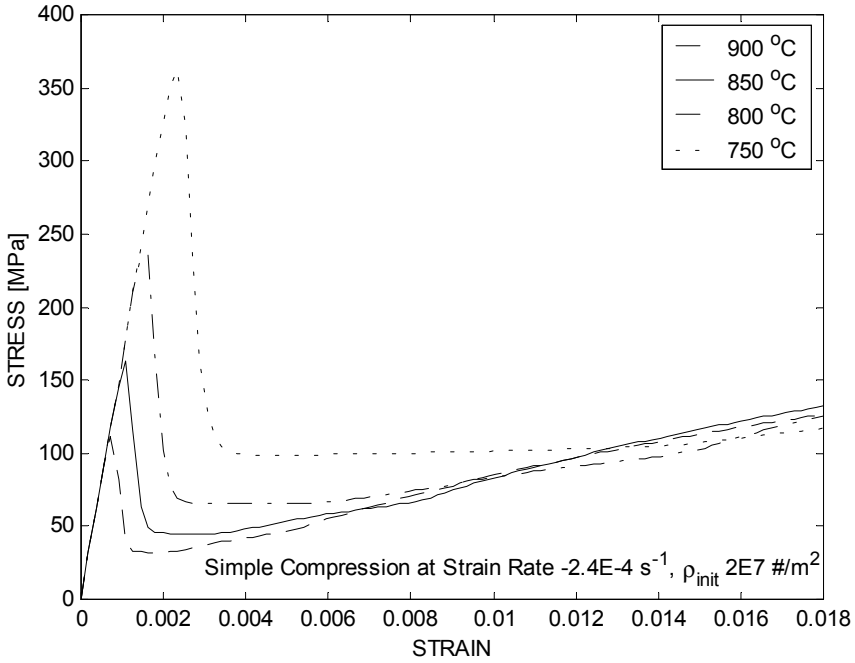

(a)

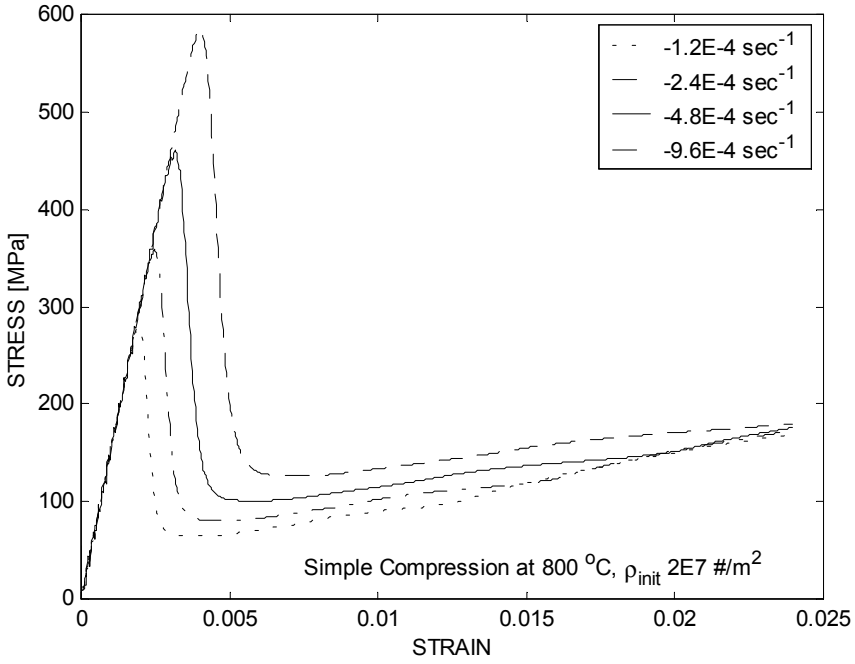

(b)

Figure 5.10 Characteristics of the model in response to a dynamic loading for uniaxial compression testing: (a) Temperature dependence, (b) strain rate dependence, and (c) the dependence of the grown-in dislocation density in the crystal.

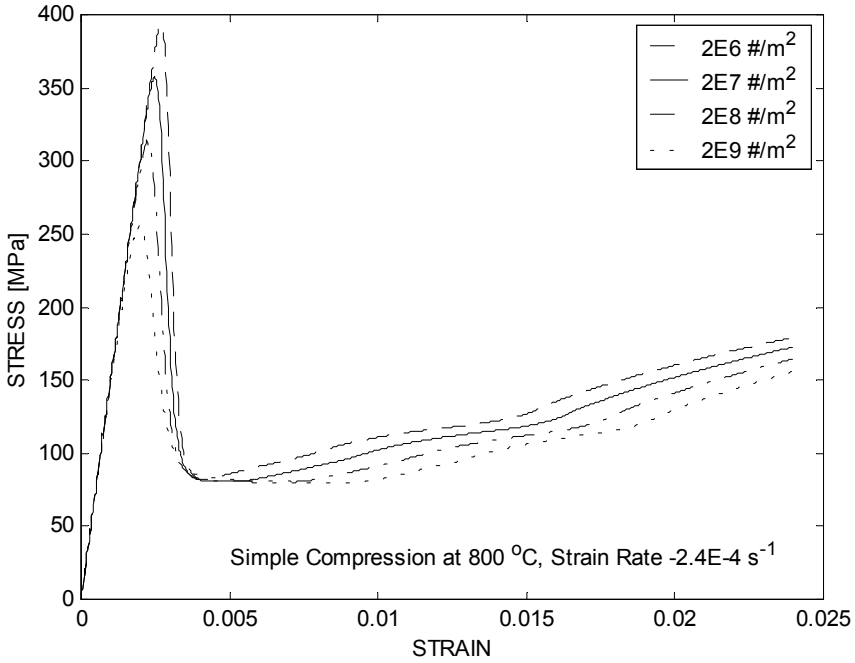

(c)

Figure 5.10 (continued) Characteristics of the model in response to a dynamic loading for uniaxial compression testing: (a) Temperature dependence, (b) strain rate dependence, and (c) the dependence of the grown-in dislocation density in the crystal.

The quantitative response to dynamic loading will be investigated in the next section. The high stiffness of the uniaxial compression specimen usually does not allow us to measure strain-softening behavior accurately. Therefore, instead of compression testing, four-point bend testing with a low specimen stiffness will be used to characterize the strain-softening behavior.

5.4.2 Si 4-point bend test

5.4.2.1 Model response to monotonic loading

The predictive capabilities of the model were verified by comparing the load deflection response of Si in four-point bending at various temperatures and strain rates. A Si flexural specimen with dimensions of 1 mm thick, 8.8mm wide, and 50 mm long was modeled with ABAQUS-CPE4R elements (reduced order plain strain continuum

element) as shown in Figure 5.11 (a). Symmetry is assumed, so only a single inner and outer rollers are modeled. Both the inner and the outer roller, modeled with rigid surfaces, form a frictional interface with the Si specimen. The friction coefficient was assumed to be 0.1. While the inner roller is held fixed, the outer roller moves upward at a speed of 1 μm/s. Figure 5.11 (a) shows both the undeformed and the deformed meshes. Figure 5.11 (b) and (c) show the dislocation density distribution in the specimen and the shear resistance distribution, respectively. Figure 5.11 (d) illustrates that materials within the span of the inner rollers is almost in Deformation Regime 2. However, although a slight concentration both in the dislocation density and the shear resistance can be observed under the inner roller, it is not as noticeable as that observed in the actual experiment. This discrepancy becomes obvious when the displacement in the center is considered. In Figure 5.12, the bow in the center predicted by the finite element calculation is compared with experimental measurements. The experimental results by Walters show a pronounced localized deformation [17, 18]. Experimentally, as the localized deformation proceeds, the span between the inner rollers is flattened out because the lowered stress around the inner rollers reduces the bending moment. In this four-point bend test, the discrepancy in the center displacements can be amplified significantly through the long span of the flexural specimen between the inner rollers. Unlike the experimental result, this isotropic version of the Si constitutive model predicts a monotonic increase for the center displacement. Figure 5.13, a comparison of the load predicted by the finite element analysis against the experimental result, explores further the issue associated with the localized deformation. While it satisfactorily predicts the peak load followed by softening, the finite element calculation deviates from the experiment at larger deflections. The transition between the two regimes appears to take place earlier than is observed experimentally. However, a careful examination shows that this problem may also be related to the progress of the localized deformation that relieves the stress in the Si flexural specimen. This problem may call for a complete crystal plasticity formulation for the Si constitutive model that enables the improved prediction of localized deformations under the rollers.

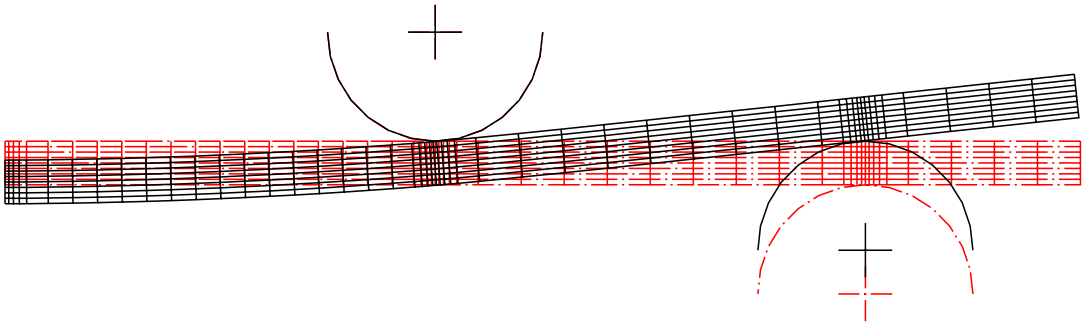

(a)

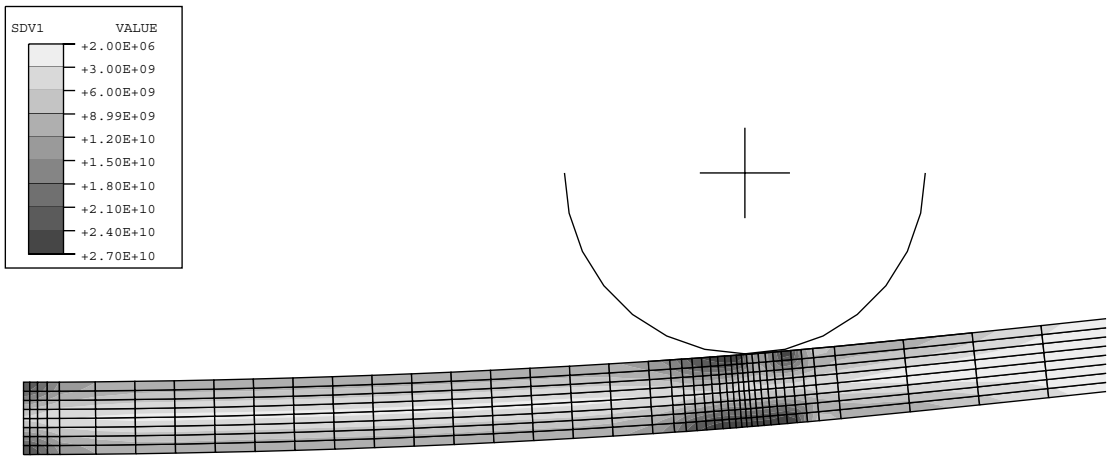

(b)

Figure 5.11 (a) Finite element mesh for a 4-point bending test with the undeformed mesh shown in dashed lines and the deformed one in solid lines, (b) dislocation density distribution, (c) isotropic shear resistance distribution, (d) deformation regime. Analysis performed assuming 800 °C with a ram speed of 1μm/s.

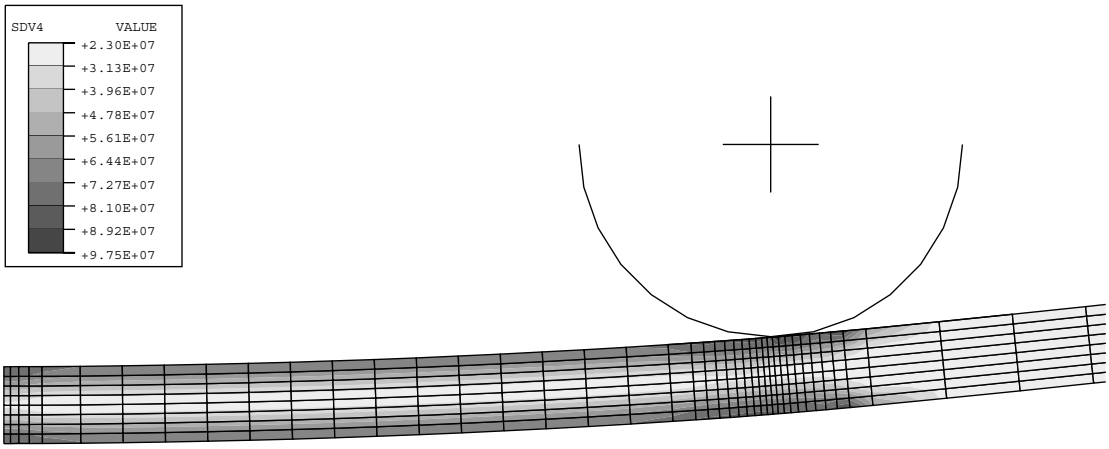

(c)

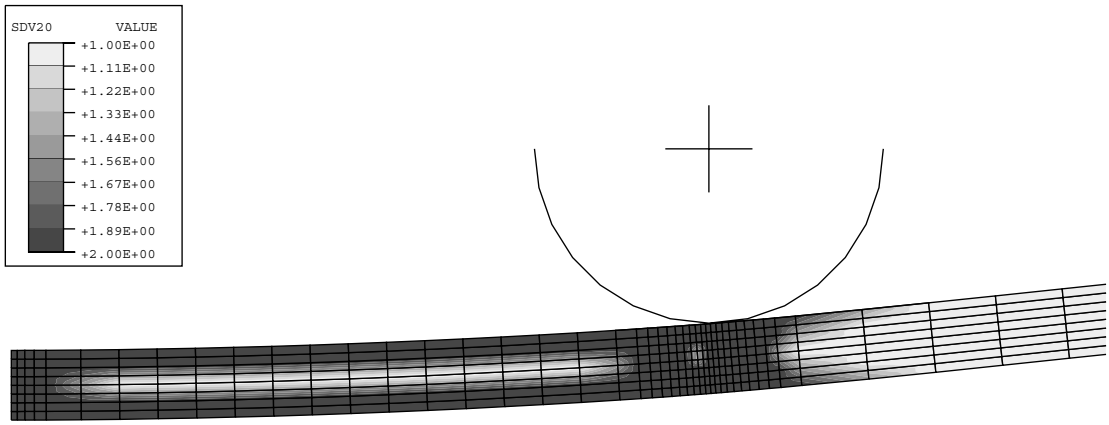

(d)

Figure 5.11 (continued) (a) Finite element mesh for a 4-point bending test with the undeformed mesh shown in dashed lines and the deformed one in solid lines, (b) dislocation density distribution, (c) isotropic shear resistance distribution, (d) deformation regime. Analysis performed assuming 800 °C with a ram speed of 1μm/s.

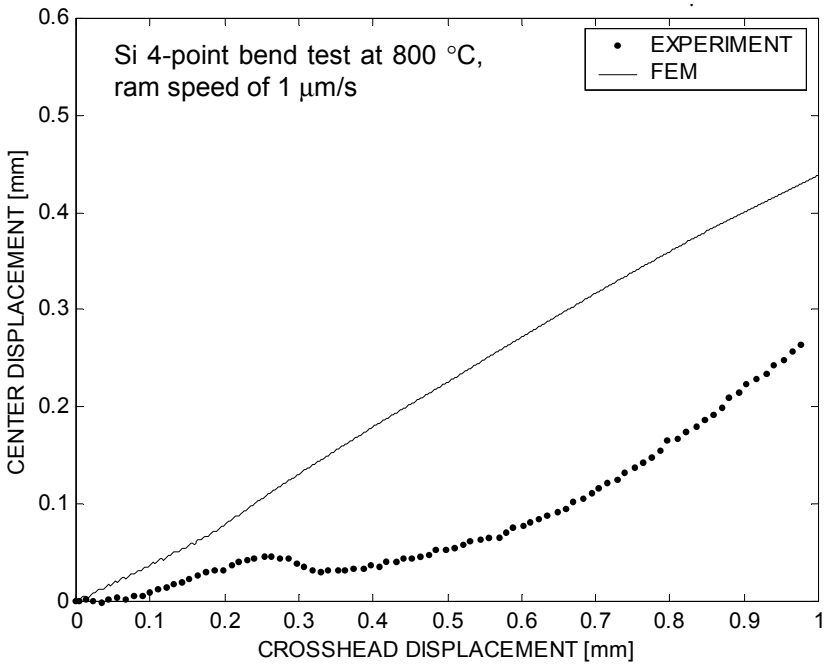

Figure 5.12 Comparison of the finite element prediction of the center displacement as a function of the crosshead displacement predicted for a 4-point bending test against the experimental result.

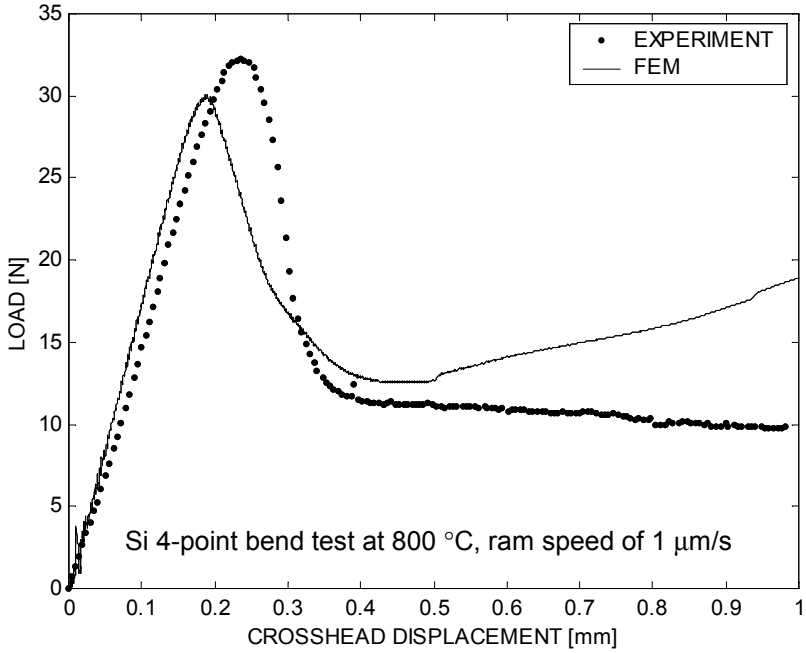

Figure 5.13 Comparison of the finite element prediction of the load as a function of the crosshead displacement predicted for a 4-point bending test against the experimental result.

Note that the peak load and the softening of the 4-point bend test predicted by the finite element calculation are in good agreement with the experimental data as shown in Figure 5.13. This result supports the numerical results for the uniaxial compression test under a monotonic loading illustrated in Figure 5.10 in terms of the qualitative behavior of the model as well as the quantitative model prediction. The predictive capabilities of the model in response to four-point bending were also evaluated with regard to the temperature and strain-rate dependences in Figure 5.14 (a) and (b) against the experimental results by Chen [14]. The model predictions are in reasonably good accordance with the experimental data, capturing the peak loads, plateaus, and the overall trend of the temperature and strain rate dependences. The peak load increases with the decrease in temperature and the increase in strain-rate as observed in the model response to monotonic loading in the compression testing.

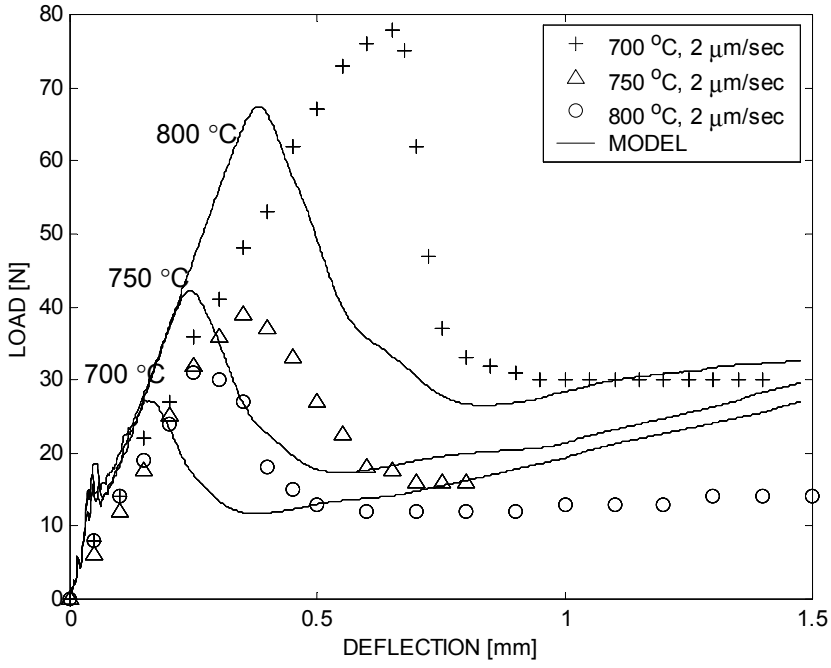

(a)

Figure 5.14 Comparison of the finite element prediction of the four-point bend tests for (a) various temperatures and (b) strain rates.

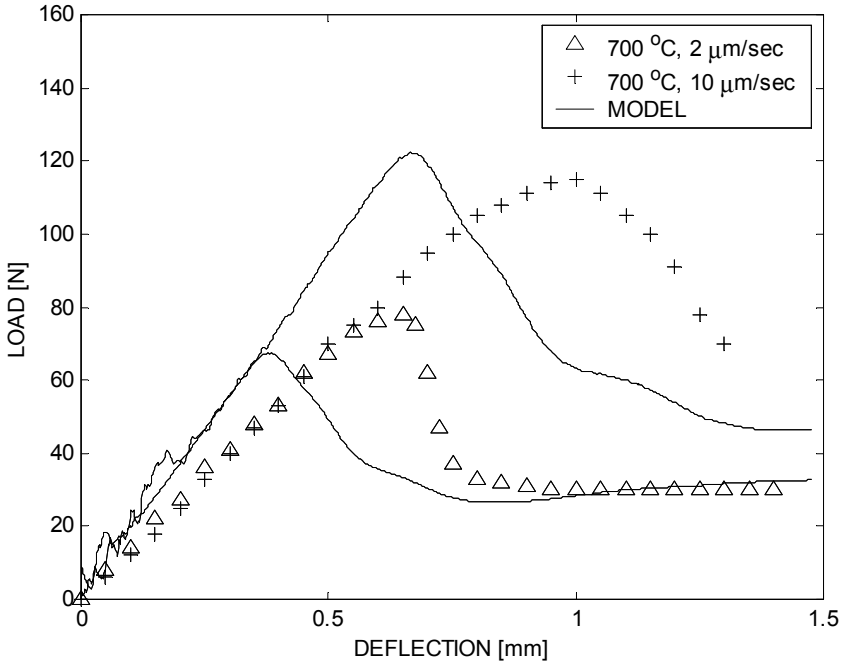

(b)

Figure 5.14 (continued) Comparison of the finite element prediction of the four-point bend tests for (a) various temperatures and (b) strain rates.

5.4.2.2 Effect of load history

In order to investigate the effect of load history, two cases were considered in this study: a combination of monotonic load and the static-relaxation and a combination of monotonic load and creep. The experimental data for the 4-point bend tests are compared in Figure 5.15 with the monotonic load case being the reference. Case 1 started with a monotonic load, stopped at a load in the middle of the peak and the plateau of the reference load-deflection curve to allow static relaxation for approximately 20 minutes, and then reloaded. As shown in Figure 5.15, the peak load at the reloading step was recorded as being significantly lower than that for the monotonic load case. The level of the plateau is more or less the same as that for the reference curve. For case 2, the load again began increasing monotonically. Approximately at the same load as Case 1, the load was held for 6 minutes to allow creep using the Load Control feature of the testing

machine. From the increased intervals of the data points with time, the increasing creep rate can be seen. When the deflection due to creep reached approximately 0.3 mm (where the load-deflection curve meets the strain-softening curve of the reference curve), the Position Control feature was turned on, and the reloading step started. At this point, it was observed that the load decreased with the increase in deflection and followed the same plateau as the reference curve.

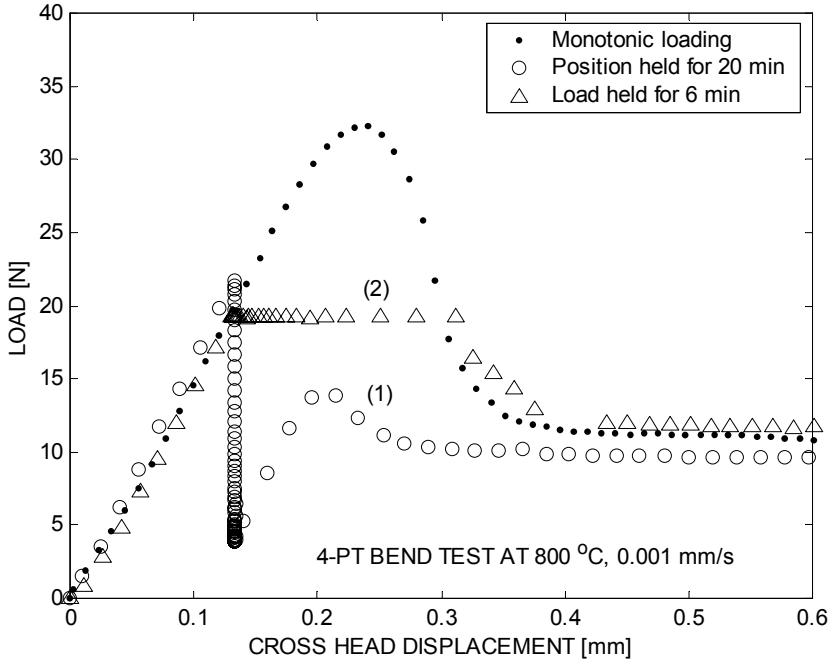

Figure 5.15 Load-deflection responses of single crystal Si in four-point bending for various load histories.

In Figure 5.16, the experimental data for Case 1 was compared with the model prediction. The same FE mesh used in Section 5.4.2.1 was employed in this analysis. The load-deflection curves are plotted in Figure 5.16(a) and are redrawn on the load-time plot in Figure 5.16(b). Overall, the basic phenomena were captured by the model. The model captures the static-relaxation part with a good accuracy, but it deviates from the experiment from the reloading step. It is believed that the inaccurate prediction of the second peak and plateau may result from the faster dislocation nucleation rate, and then the earlier transition between the deformation regimes than is observed experimentally. As mentioned earlier, the progress of the localized deformation that relieves the stress in the specimen may also contribute to the discrepancy at larger deflections.

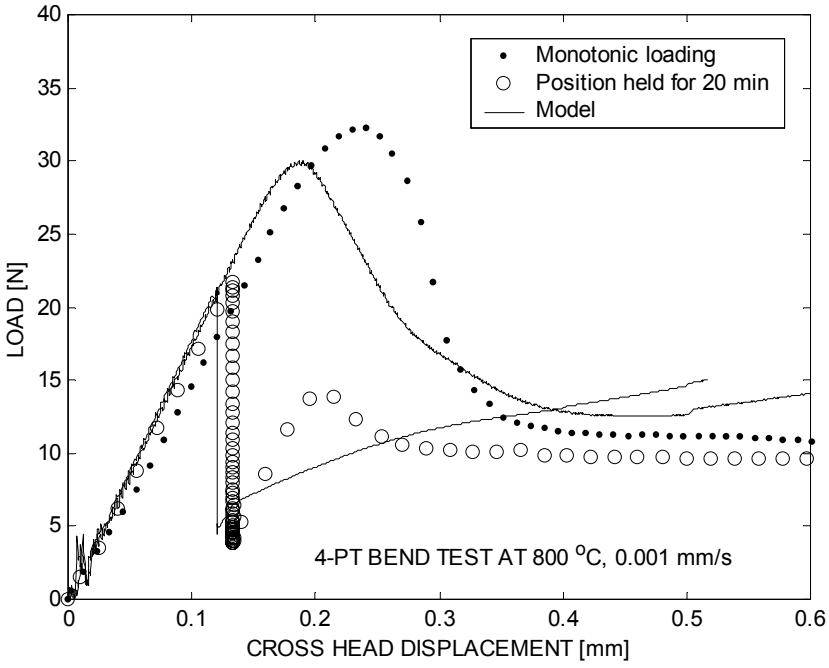

(a)

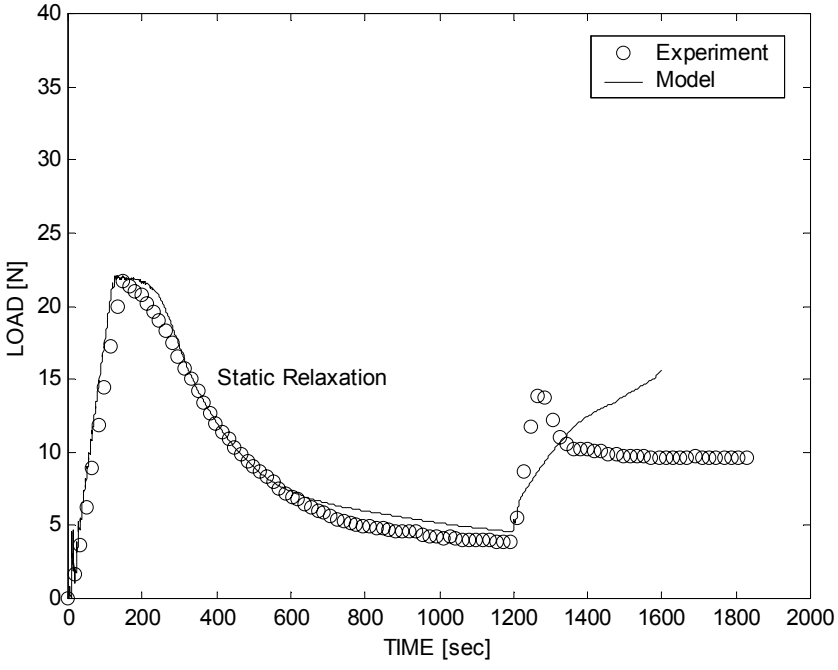

(b)

Figure 5.16 Comparison of the finite element prediction of the load-deflection response of single crystal Si in 4-point bending for the load history consisting of the monotonic loading and static relaxation against the experimental result. (a) load vs. deflection (b) load vs. time.

As discussed in Section 5.3, the peak load (upper yield stress in monotonic compression testing) is a function of temperature, strain-rate, and initial dislocation density. Figure 5.10 showed the dependence of the grown-in dislocation density on the upper yield stress; the upper yield stress decreases with the increase in the grown-in dislocation density in the crystal. Physically, this material behavior of single crystal Si explains why the second peak load recorded at the reloading step of Case 1 is significantly lower than that for the monotonic load case. The dislocation density increased at the initial monotonic loading and static-relaxation steps sets the initial state of the crystal at the reloading step. This in turn lowers the peak load by approximately a factor of two. The level of the peak load at the reloading step will change depending on the stationary load level and the time for static-relaxation. Moreover, the increased dislocation density in the crystal during the monotonic load and creep for Case 2 also explains the load decreasing with the increase in the deflection at the reloading step.

As demonstrated by Case 2 in Figure 5.15, any static load causing stresses between the peak and the plateau stresses is shown to yield a high creep rate. In order to illustrate the creep rate varying with the load levels with regard to the peak and plateau, Walters' creep experimental data [17] were reconstructed to obtain the times taken for the deflection to reach 3 μm at the various static load levels due to creep. Figure 5.17 shows that the time increases exponentially as the static load approaches the plateau.

From the observations in this section, apparently the load-carrying capability of single crystal Si at elevated temperatures is limited by creep. From a microscopic view, the evolution of the dislocation density in the crystal governs the deformation mechanisms (which were discussed early in this chapter), and then the macroscopic load-deflection response. Thus, the peak load can be considered as nothing more than an artifact of the evolution of the dislocation density. Although there are some complications in correlating the 4-point bend test results with the stress-strain curve of single crystal silicon, the consequences of the experimental results presented in this section explicitly

verify that the upper yield stress of single crystal Si is non-conservative in the design of hot Si structures.

As implied in Figure 5.17, the lower yield strength of Si, which should yield a minimal creep strain-rate, can be used as an allowable stress at elevated temperatures. However, from the perspective of the design of Si hot structures, the lower yield strength of single crystal Si is insufficient, particularly for the need of micro-turbomachinery operating at high temperatures and high stresses. Instead of the over-conservative design using the lower yield stress, the recommended approach to the design of Si hot structures will be to utilize the Si model, which is reasonably accurate up to moderate strains, for extracting appropriate operating conditions given the overall design specifications. This design approach also requires the incorporation of SiC into the strategic locations in order to reinforce the Si hot structures.

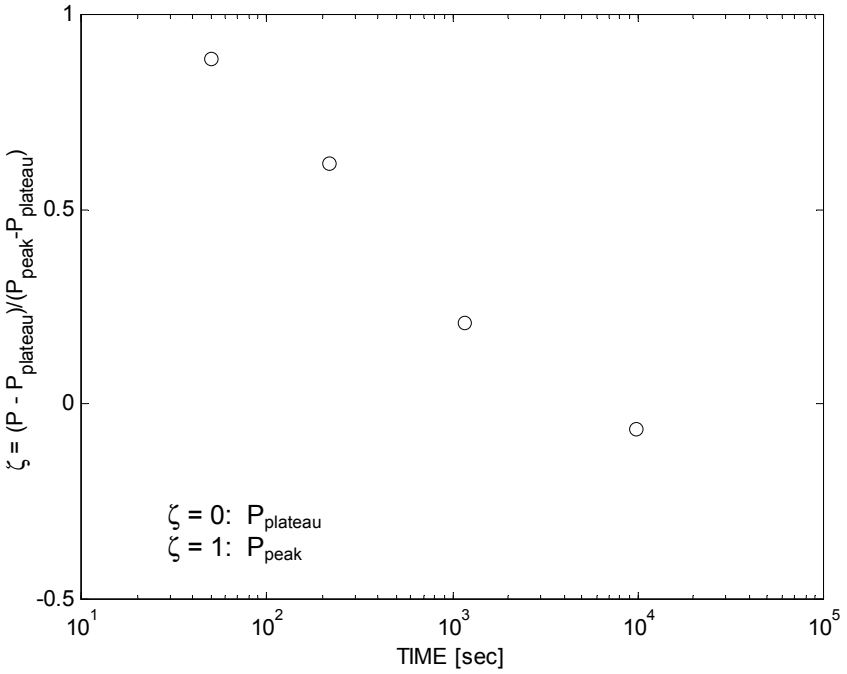

Figure 5.17 Times taken for the Si bend specimen to deflect by 3 μm for various static loads reconstructed from Walters' experimental data [17].

5.4.2.3 Notched Si 4-point bend test

The effect of stress concentrations was considered by comparing the 4-point bend test results for various notches, ranging from sharp to round notches. The notches were created by deep reactive ion etching (DRIE), specifically the round notch by the Recipe SF6 and the sharp one by Recipe MIT69 [19]. This section is devoted to seeking an answer to the question of whether structural instabilities may occur in Si hot structures, particularly at stress concentrations.

Four-point bend tests were performed at 900 °C and a ram speed of 0.001 mm/s for the Si specimens with various notches. Figure 5.18 and 5.19 show the surface of the Si notched specimens after testing. For the two notches having different stress concentration factors, the slip band patterns were observed to be similar. Instead of being concentrated around the sharp corners and propagating from there, the slip bands are relatively uniform and do not correlate with the notch location nor notch shape.

From the macroscopic point of view, the load-deflection curves of the notched Si 4-point bend tests were compared in Figure 5.20. They are virtually indistinguishable, which implies that the stress concentration effect on the overall deformation are not significant, particularly in four-point bending. The peak load in these tests appeared to be reduced from the unnotched only by the amount of reduced thickness due to the notches. The shape of the notches, sharp or round, did not make any significant difference in determining the overall load-deflection responses. This result is consistent with the observations in the slip band patterns in Figure 5.18 and 5.19. Although the formation of the active slip bands around the notches is an indication of the plasticity causing localized deformations, at the same time the plasticity reduces the effect of stress concentrations at the sharp corners of the notch. It is worth noting that materials adjacent to the neutral plane tend to be stiffer at larger deformations in four-point bending. This specific loading condition is also believed to prevent the notched specimens from collapsing plastically.

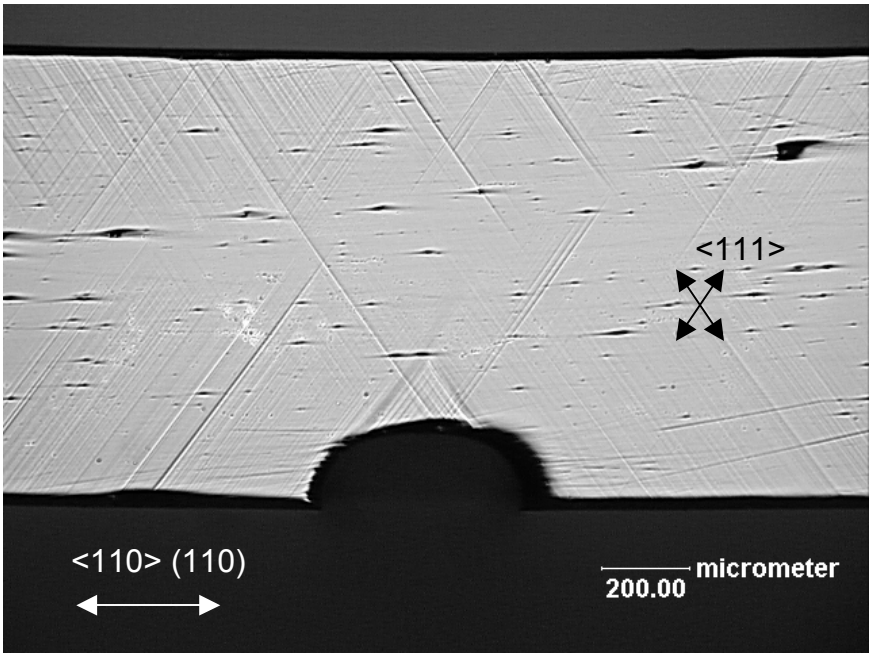

(a)

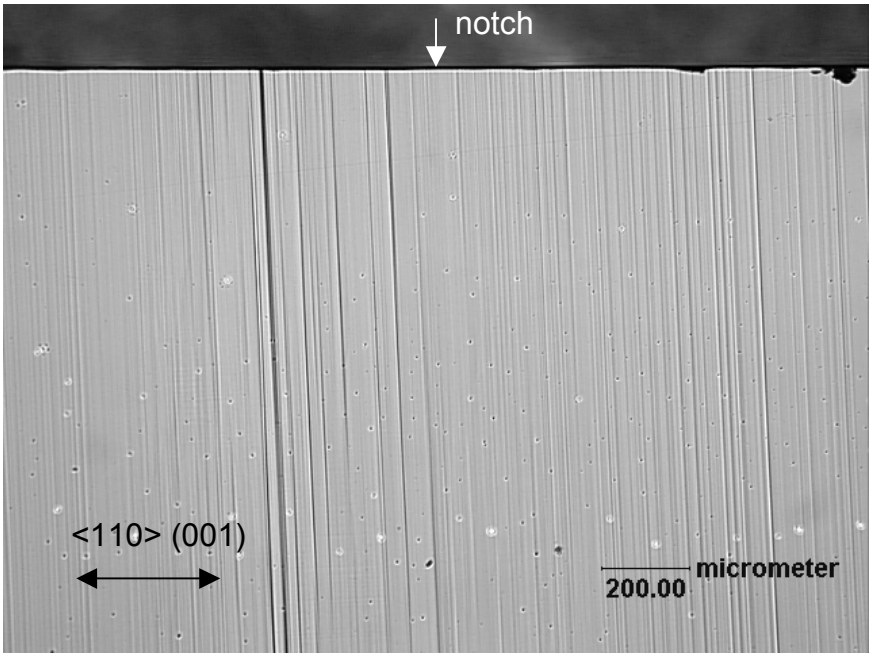

(b)

Figure 5.18 Surface of the Si 4-point bend specimen with a round notch tested at 900 °C and 0.001 mm/s ram speed. (a) side view (b) top view.

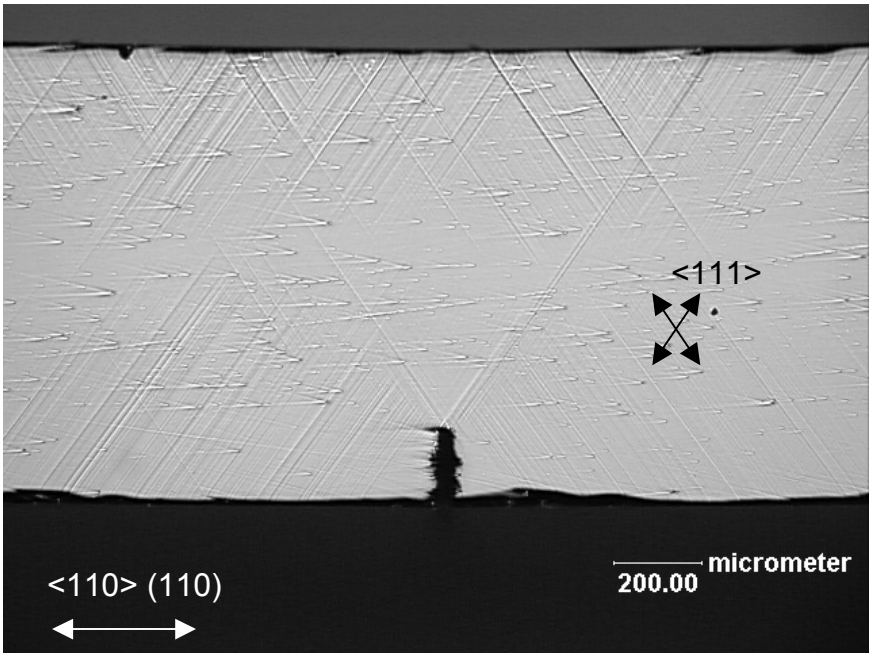

(a)

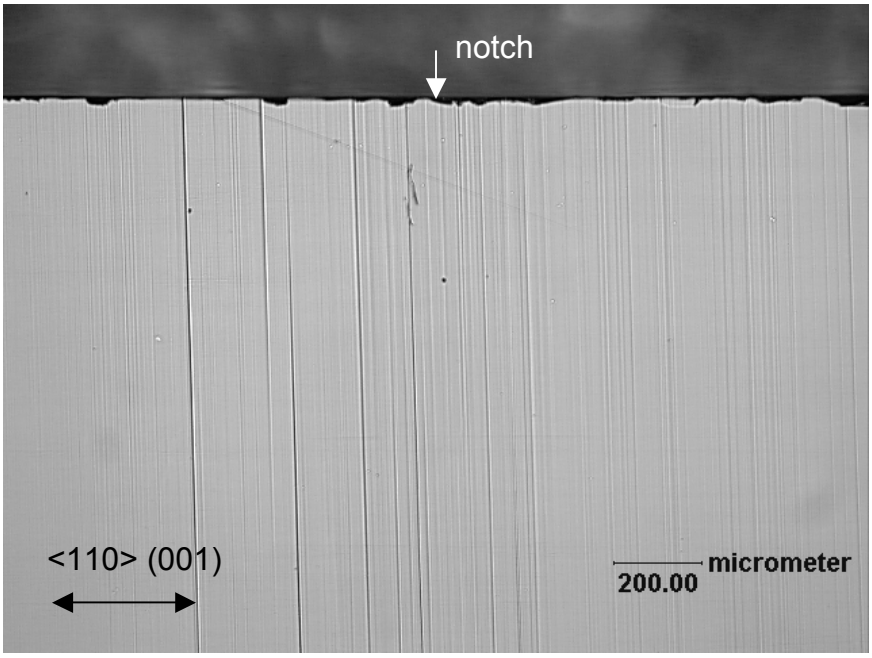

(b)

Figure 5.19 Surface of the Si 4-point bend specimen with a sharp notch tested at 900 °C and 0.001 mm/s ram speed. (a) side view (b) top view.

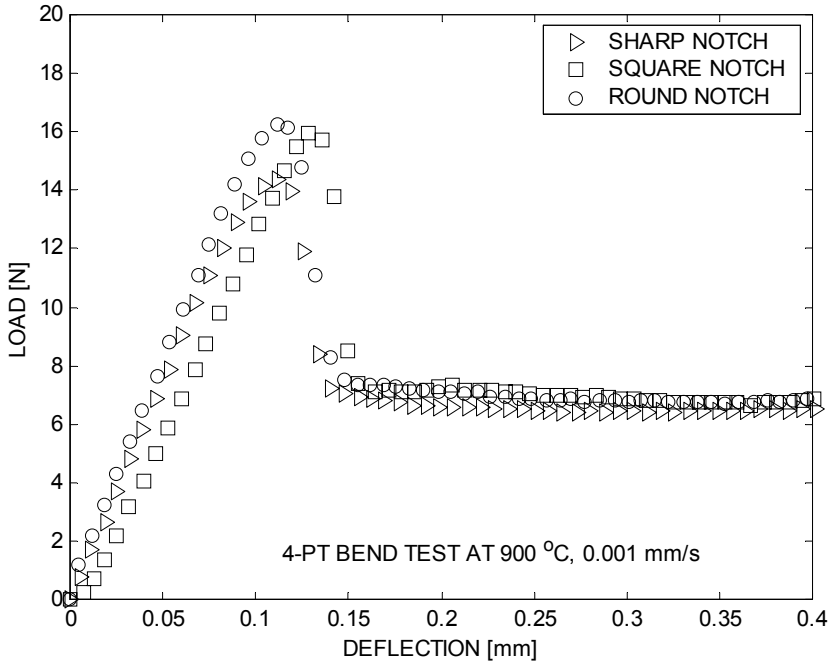

Figure 5.20 Comparison of the experimental data of Si 4-point bend tests with various notches.

From these experimental results, it is concluded that the turbine blades on the microengine rotor are unlikely to collapse due to the strain softening of Si and stress concentrations at the blade roots at the temperatures of interest. Nevertheless, the plasticity of Si hot structures over the service lifetime should be assessed using the Si model in order to ensure the structural integrity.

5.4.2.4 Si/SiC 4-point bend test

This section discusses the mechanical testing results of Si/SiC hybrid structures and assesses the feasibility of the hybrid structures concept for elevated temperature micro-turbomachinery.

Sandwich-type specimens with various SiC film thicknesses were used in the 4-point bend tests. Figure 5.21 shows the overall Si/SiC flexural specimen after testing. The specimen dimensions are 0.5 mm thick, 8.8 mm wide, and 60 mm long. The specimen, coated with 15 μm thick CVD SiC films on both sides, was loaded until fracture at 850

°C and a ram speed of 0.001 mm/s. As shown in Figure 5.21, the SiC film delaminated from the Si substrate on the tension side during the test. The SEM pictures in Figure 5.22 clearly show the delaminated surface of the Si substrate with a high density of striations. The counterpart of the ridges on the Si substrate can be found on the delaminated SiC film. This implies the integrity of the Si/SiC interface was maintained during the plastic deformation at elevated temperatures.

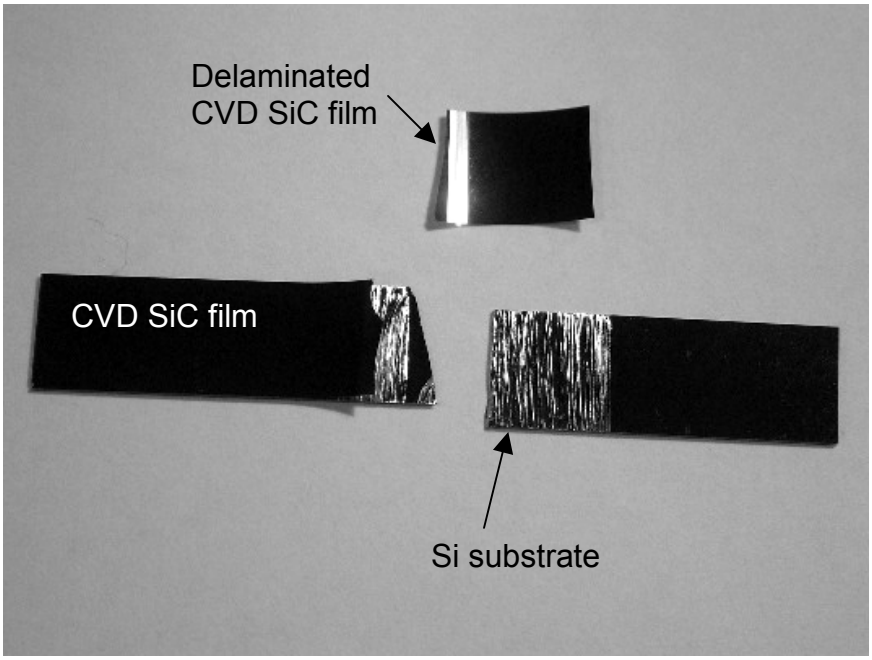

Figure 5.21 Si/SiC bend specimen after testing at 850 °C and a ram speed of 0.001 mm/s.

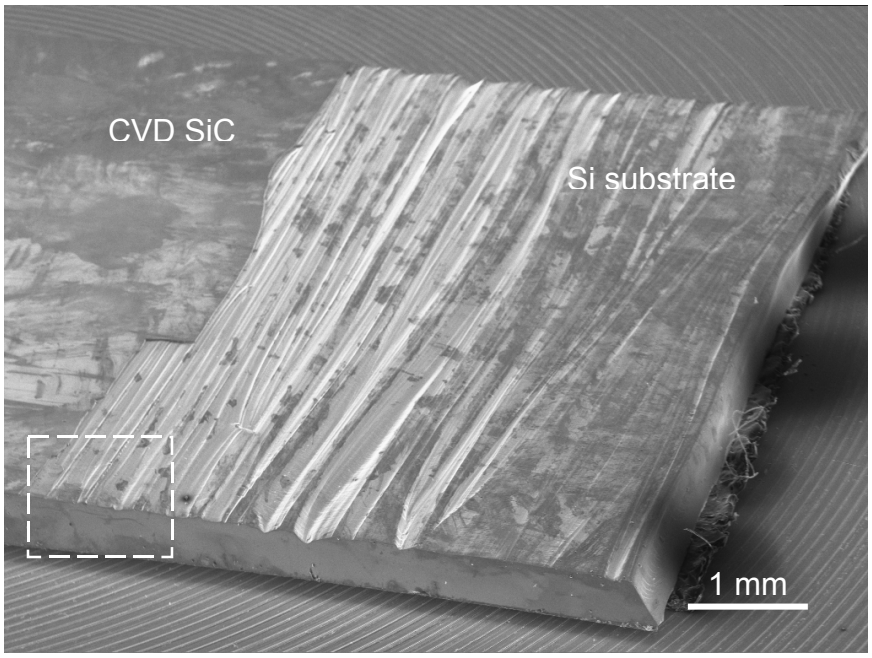

(a)

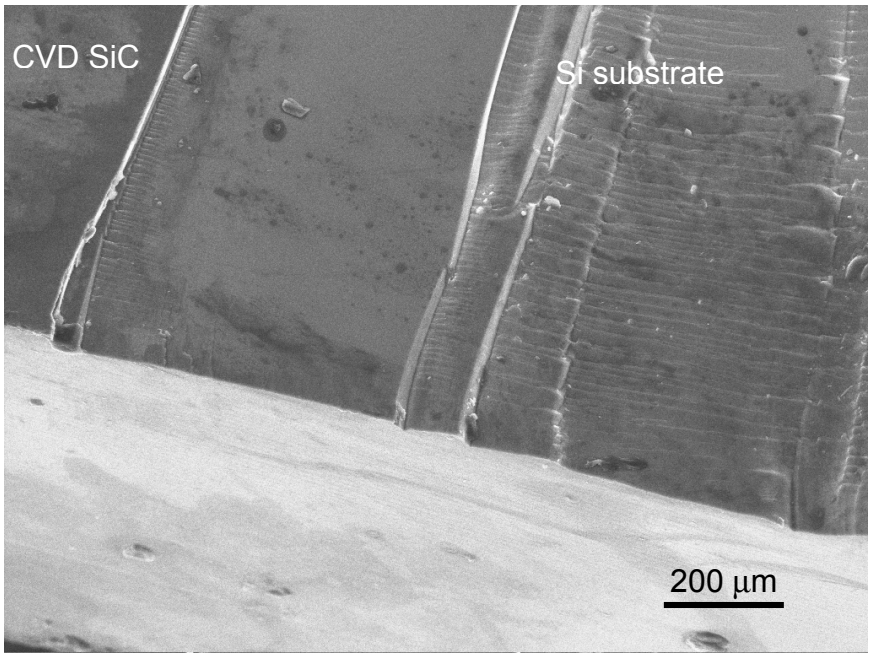

(b)

Figure 5.22 SEM pictures of the Si/SiC flexural specimen after testing at 850 °C and a ram speed of 0.001 mm/s. (a) high density of striations left on the delaminated Si substrate, (b) higher magnification of the boxed area.

Four-point bend tests of the Si/SiC hybrid specimens were conducted for various SiC film thicknesses ranging from approximately 20 to 50 μm at 850 °C and 0.001 mm/s ram speed. The test results are plotted in Figure 5.23. The all Si case is also plotted together for a comparison. Each load-deflection curve changes its slope approximately at 10 N except for the case where the SiC film thickness is 31.5 μm. The initial slope can be obtained by the addition of the flexural rigidities of the Si substrate and SiC films. When the slope changes (or the Si substrate begins to yield), the maximum stress in the Si substrate is calculated to be approximately 20 MPa using composite beam theory, which is close to the flow stress of Si at 900 °C (the stress at the peak is approximately 45 MPa for the case of the 31.5 μm thick SiC films). From this point on, the thin CVD SiC films carry most of the load until fracture. Note that the slope after the Si yields increases with increasing the SiC film thickness.

From the experimental results, it is clear that the thin CVD SiC films significantly increase the load-carrying capability of Si. While the usable load allowed by the all-Si specimen is approximately 10 N (the plateau, as discussed in Section 5.4.2.2), the load that can be carried by the Si/SiC hybrid specimens is higher by approximately a factor of three. This considerable increase in the load-carrying capacity of Si/SiC hybrid specimens supports the overall concept of Si/SiC hybrid structures for elevated temperature micro-turbomachinery.

The fracture strength of CVD SiC films is also a key issue. The average stress in SiC films can be estimated by assuming the Si flow stress of 20 MPa. From bending moment equilibrium, the average stress in SiC at fracture was found to range from 850 to 210 MPa, with the highest for the case of the 21.8 μm thick SiC film and the lowest for the case of the 49.5 μm thick SiC film. Although the brittle nature of SiC films requires Weibull probabilistic analysis to characterize the fracture strength fully, it is believed that the thicker SiC films having more surface defects tend to break at a lower stress. It is worth noting that the fracture strength of CVD SiC is size-dependent, which is favorable for the small scale devices such as the microengine. Also, process conditions and stress-

states within the structures are the key factors determining the fracture strength of brittle materials.

The shape of the load-deflection curve for the case of the SiC film thickness of 31.5 μm is somewhat different from the others. If a line is drawn extending from the linear portion of the curve for larger deflections with the same slope, this line will meet the initial linear-elastic curve as the other curves at a load of approximately 10 N. The difference between this line and the original load-deflection curve is the contribution of the peak load of the Si substrate. As was discussed in Section 5.4.2.1, the peak load is dependent on the grown-in dislocation density within the Si crystal. Therefore, dislocations nucleated in the Si substrate due to the CVD SiC film deposition and thermal cycling may result in a change in the load-deflection response of the hybrid specimen. The CVD SiC process conditions, however, are not always identical from batch to batch , and this may explain the discrepancies.

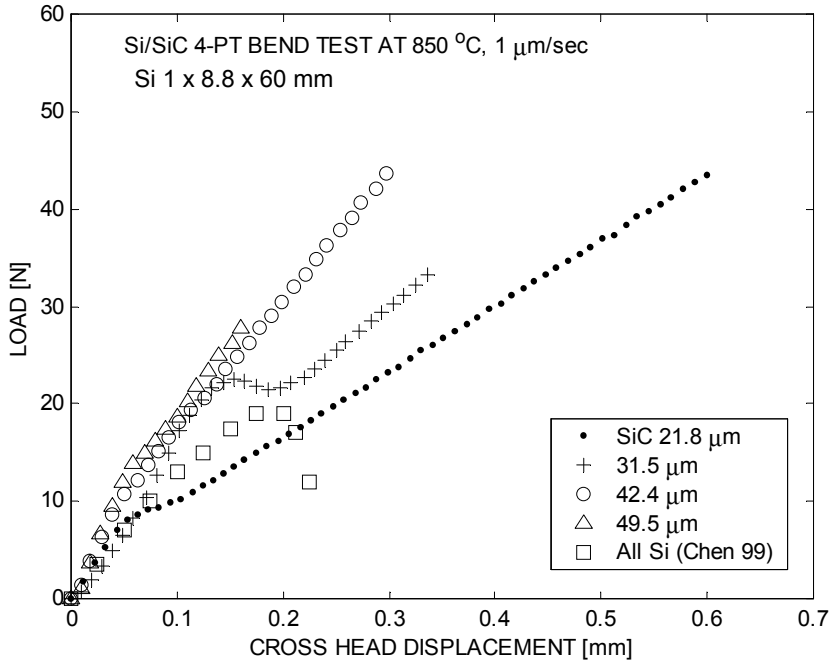

Figure 5.23 4-point bend test results of Si/SiC hybrid specimens with various SiC film thicknesses.

Sudden load drops at the failure of the load-deflection curves in Figure 5.23 may imply a brittle fracture of the Si/SiC specimens. Qualitatively, it appears that the Si substrate was forced to be under the high strain-rate loading due to the abrupt failure of the SiC film. The ductility of the Si substrate, however, does not seem to be sufficient to arrest cracks propagating from the SiC film or to sustain the fracture in a stable way. Initially, no visible precracks were found in the SiC films. The Si/SiC specimens were also investigated at the several intermediate deflections to locate any cracks that might have developed on the SiC films during the experiment, but no cracks were visible. Figure 5.24 shows the load-deflection response of the Si/SiC specimen for multiple reloading steps to investigate indirectly the presence of cracks in the SiC film. The slopes of the load-deflection curves remained unchanged between all the reloading steps. This also implies that the SiC film was free from cracks. This particular specimen was subsequently loaded to a considerably higher load than those subjected to monotonic loading until fracture.

Figure 5.25 shows the crack propagation in the Si substrate underneath the SiC film on the tensile side of a specimen. The shiny ridges on the Si substrate in Figure 5.21 appear to be an artifact of the crack propagation. Considering that there are no indications of any kind of precursor event before fracture, such as sudden changes of the load in the load-deflection curves, the cracks seemed to propagate rapidly at the incident of fracture. Figure 5.26 (a) also shows the broken edge of the specimen, whose clean surface implies a fracture by cleavage. The morphology of this fractured edge of the Si substrate is shown at a higher resolution in Figure 5.26 (b). It is interesting to note that the fine ridges, clearly visible in the micrograph, were observed to form on the broken face of the Si substrate adjacent to the Si/SiC interface on the tensile side, and disappeared at a few tens of micrometers from the delaminated edge. This transition in the fracture morphology may suggest the occurrence of a ductile failure over a short period before the fracture by cleavage. Figure 5.26 (c) shows the fracture morphology of the specimen on the compression side. While the Si predominantly shows clean cleavage fracture, the SiC, the layer in the middle of the picture, did not break in a straight line, and fractured along a tortuous path in the plane perpendicular to the picture.

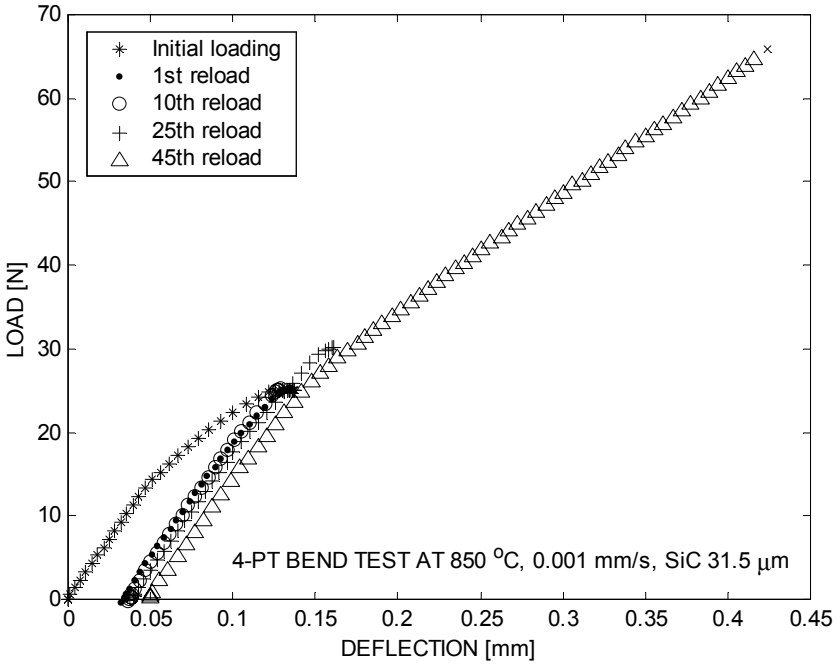

Figure 5.24 Experimental results for the load-deflection response of a Si/SiC specimen in four-point bending with the multiple reloading steps.

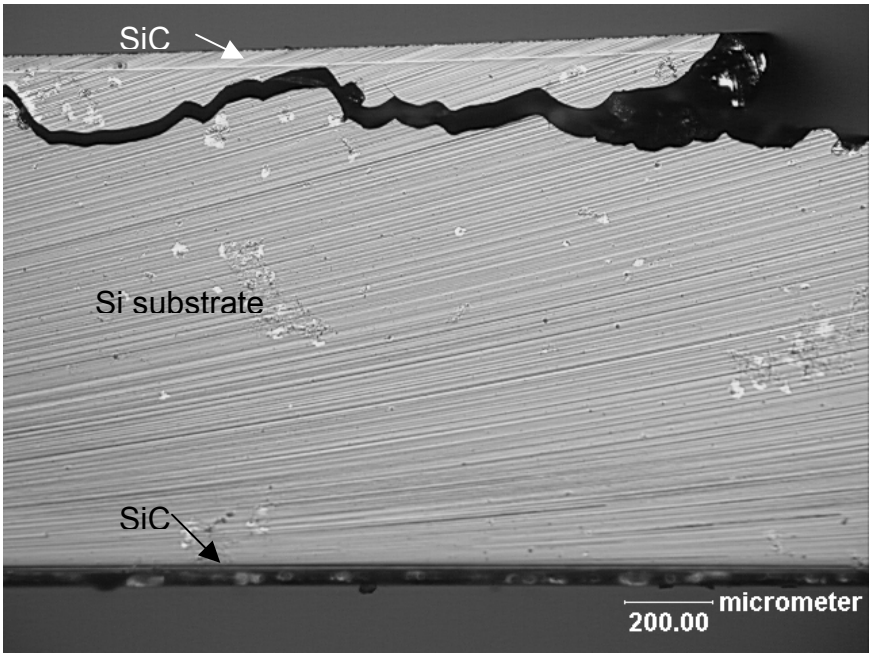

Figure 5.25 Crack propagation in the Si substrate

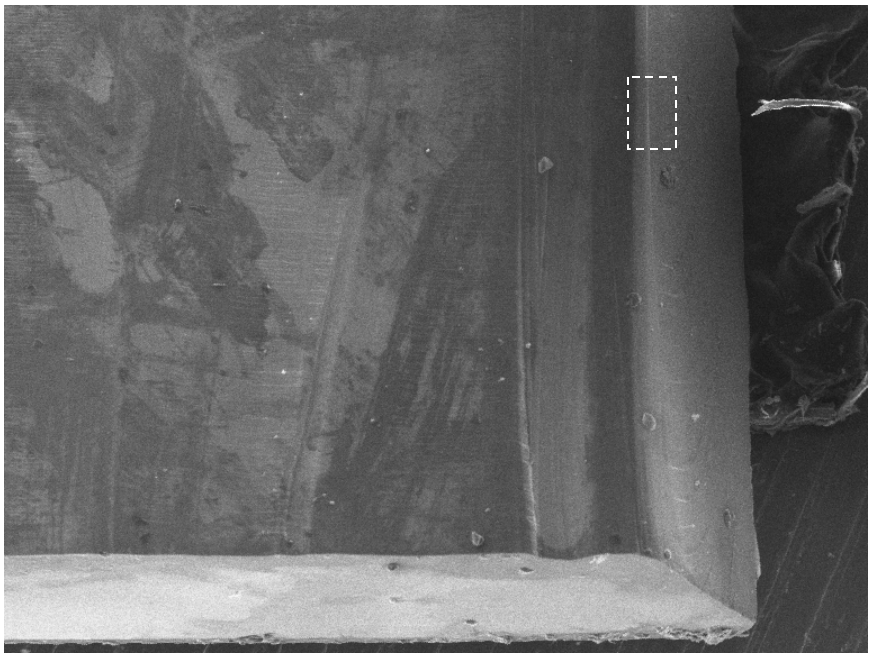

(a)

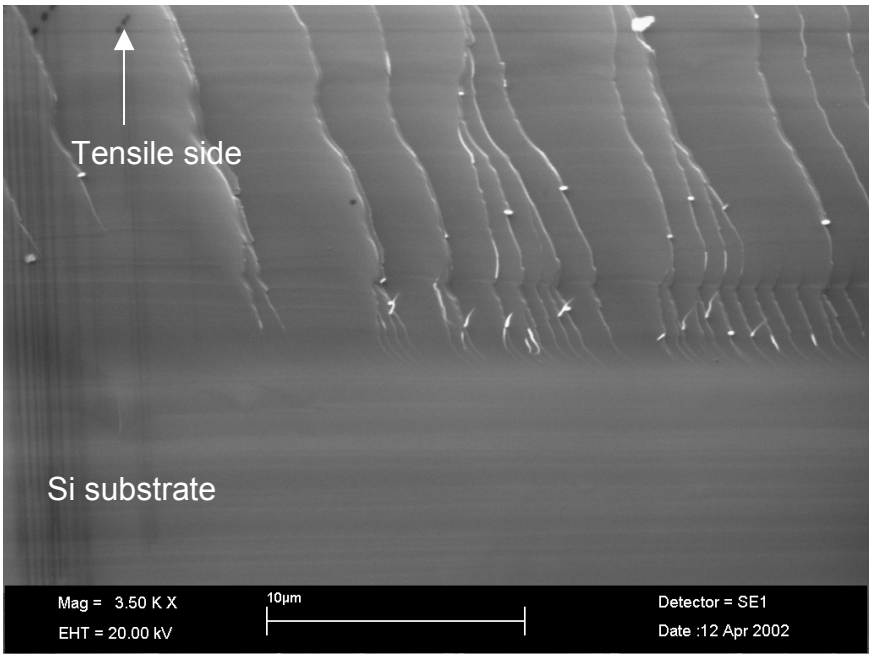

(b)

Figure 5.26 (a) SEM picture of a broken edge of the Si/SiC specimen loaded until fracture at 850 °C and a ram speed of 0.001 mm/s, (b) Morphology of the fractured edge of the Si substrate (magnification of the boxed area), (c) fractured edge of the specimen in compression.

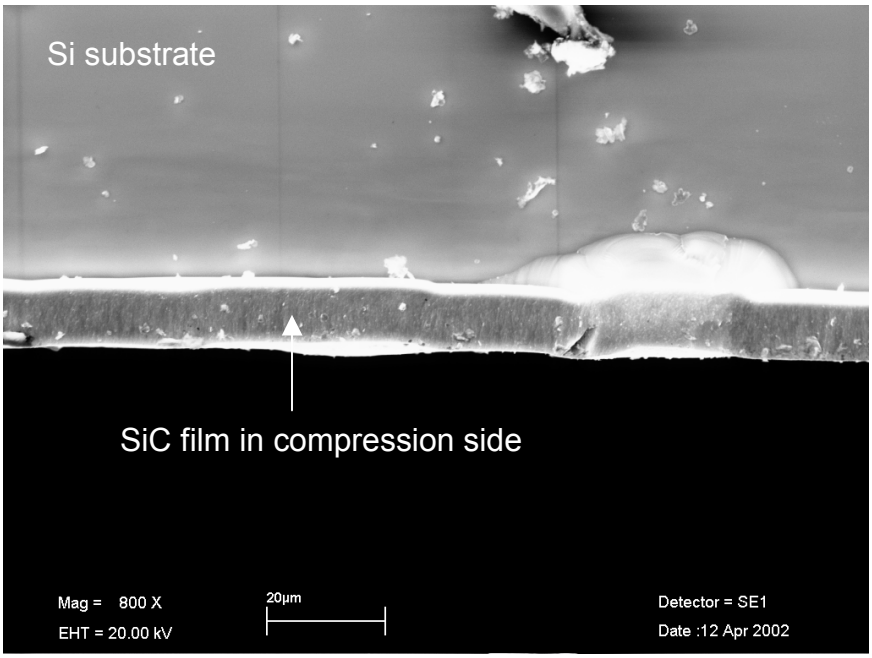

(c)

Figure 5.26 (continued) (a) SEM picture of a broken edge of the Si/SiC specimen loaded until fracture at 850 °C and a ram speed of 0.001 mm/s, (b) Morphology of the fractured edge of the Si substrate (magnification of the boxed area), (c) fractured edge of the specimen in compression.

Figure 5.27 shows the model prediction of a Si/SiC 4-point bend test, which is in good agreement with the experimental results. The model accurately captures the temperature dependence originating from the plasticity of single crystal Si in combination with the elastic-brittle response of the SiC. The experimental data shows the relatively slow change in the initial nonlinear behavior compared to the model prediction. It is speculated that the dislocations nucleated in the Si crystal during the CVD process or thermal cycling during the specimen preparation may reduce the peak load level, and then the shape of the non-linear portion of the curves. In the analysis, no further assumptions were made to adjust the increased dislocation density in the Si crystal. The model prediction of a Si/SiC 4-point bend test could be made more accurate by adopting a better assumption for the value of the dislocation density (supposedly inhomogeneous) in the Si crystal. The residual stress present around the Si/SiC interface should also be taken into consideration in the FE model in order to achieve a better model prediction. Study of the

residual stress induced during the CVD SiC process and thermal cycling is being conducted by Choi [20], also as part of the microengine project.

Finally, the elastic properties data for SiC (E_{siC} = 430 GPa, ν = 0.21) measured by Jackson and co-workers [21] were used in the FE simulations. This agreement with experiment substantiates the accuracy of their measurements.

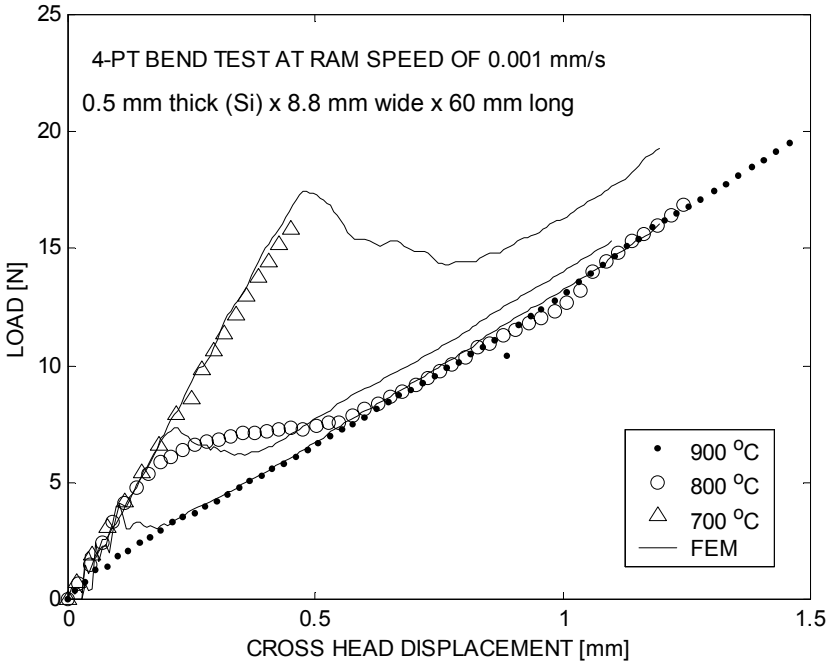

Figure 5.27 Comparison of the model prediction against the 4-point bend test results for Si/SiC hybrid specimens.

5.5 Summary

An isotropic elasto-viscoplastic constitutive model was developed incorporating the key deformation mechanisms that determine the mechanical behavior of single crystal Si with a low grown-in dislocation density at elevated temperature. This model enables a smooth transition between the two regimes, Regime 1 and Regime 2, with the change of the internal variables representing the material history for each deformation regime. After being implemented in the user subroutine VUMAT of ABAQUS/ EXPLICIT^{TM}, this

model was calibrated to fit the creep experimental data. While it is versatile in predicting various aspects of the mechanical behavior of Si at high temperatures, including responses to a dynamic loading, this model may not be effective when the localized deformation dictates the overall structural response. A crystal plasticity formulation may provide a reliable solution for this problem, but only with the addition of expensive computational time. It is noted that the Si model provided in this chapter can be employed with slight modifications in the crystal plasticity formulations. The skeleton of the crystal plasticity version of this Si model can be found in Appendix F.

This Si constitutive model still is a valuable tool for the design of high temperature Si structures. Since the structural design is unlikely to require consideration of deformation beyond the post-hardening regime, most design procedures for Si structures at high temperature should be able to rely on this model with reasonable confidence. In the following chapter, the design of micro-turbomachinery at elevated temperature will be revisited with this advanced design tool. The appropriate design practice will be shaped based on the better knowledge and the experimental observations of the deformation mechanisms of Si and Si/SiC, together with the advanced numerical model for Si.

Reference

1. W. C. Dash, in "Dislocations and Mechanical Properties of Crystals", J. C. Fisher et al., eds., p 57 (1957)
2. H. Alexander, P. Haasen, Dislocation and plastic flow in the diamond structure, Solid State Physics, pp 27-158, 1968.
3. H. Alexander, Dislocations in covalent crystals, in Dislocations in solids, Vol. 7. ed. F. R. N. Navarro, pp 113-234, North-Holland, 1986.
4. M. M. Myshlyaev, V. I. Nikitenko, V. I. Nesterenko, Dislocation structure and macroscopic characteristics of plastic deformation at creep of silicon crystals, Phys. Stat. Sol., Vol. 36, pp 89-95, 1969.
5. M. M. Myshlyaev, Dislocation creep, Ann. Rev. Mater. Sci., Vol 11, pp 31-50, 1981.
6. M. E. Gurtin, An introduction to continuum mechanics, Academic Press, 1981.
7. L. Anand, Constitutive equations for the rate-dependent deformation of metals at elevated temperatures, J. Engine. Mater. Tech., Vol. 104, pp 12-17, 1982
8. S. Balasubramanian, L. Anand, Elasto-viscoplastic constitutive equations for polycrystalline fcc materials at low homologous temperatures, Submitted to J. Mech. Phys. Solid, Vol. 50, Issue 1, pp101-126, 2001
9. W. Dillon, Jr., C. T. Tsai, R. J. DeAngelis, J. Appl. Phys. Vol. 60, p 1784, 1986
10. E. Orowan, Problems of plastic gliding, Philos. Trans. R. Soc. London A 52, 8-22.
11. U. Kocks, A. Argon, M. Ashby, Thermodynamics and kinetics of slip, in Progress in Material Science, Pergamon Press, London, 1975.
12. ABAQUS Reference Manuals, 2001, Providence, RI.
13. K. Sumino, Deformation behavior of silicon, Metallur. Mater. Trans. A, Vol. 30A, pp 1465-1479, 1999.
14. K.-S. Chen, Materials Characterization and Structural Design of Ceramic Micro Turbomachinery, Ph. D. Thesis, Dept. of Mechanical Engineering, MIT, Cambridge, MA, 1999.
15. S. Takeuchi, A. S. Argon, "Steady-state creep of single-phase crystalline matter at high-temperature, J. Mater. Sci., Vol. 11, No. 8, pp1542-1566 1976

16. J. R. Patel, A. R. Chaudhuri, Macroscopic plastic properties of dislocation-free germanium and other semiconductor crystals. I. Yield behavior, J. Appl. Phys., Vol. 34, No. 9., pp 2788-2799, 1963.
17. D. S. Walters, Creep characterization of single crystal silicon in support of the MIT micro-engine project, MS. Mech. Dept., MIT, 1999.
18. D. S. Walters, S. M. Spearing, On the flexural creep of single-crystal silicon, Scripta mater. 42 (8): 769-774 APR 14 2000.
19. A. A. Ayon, K.-S. Chen, K. A. Lohner, S. M. Spearing, H. H. Sawin, M. A. Schmidt, Deep Reactive Ion Etching of Silicon, Mat. Res. Soc. Symp. Proc., Vol. 546, AA7.1, Fall 1998.
20. D. Choi, R. J. Shinavski, S. M. Spearing, Process Development of Silicon-Silicon Carbide Hybrid Micro-Engine Structures, Mat. Res. Soc. Symp. Proc., Vol. 687, B5.44, Fall 2001.
21. K. Jackson, R. Edwards, W. Sharpe, Jr., Mechanical properties of thin film silicon carbide, Mat. Res. Soc. Symp. Proc., Vol. 687, B6.3, Fall 2001.

Chapter 6

Redesign of Si/SiC hybrid micro-turbomachinery

6.1 Overview

In the previous chapter, a constitutive model for single crystal Si at high temperatures and high stresses has been developed that is consistent with the microscale deformation mechanisms, and calibrated and validated against the experimental results at the macroscale. Also, from the experimental results for the sandwich-type Si/SiC hybrid specimens, the feasibility of the Si/SiC hybrid structures concept was successfully verified. This chapter presents further guidelines for the design of Si/SiC hybrid structures for high temperature micro-turbomachinery, based on the knowledge derived from the experimental observations of the mechanical behavior of Si and Si/SiC hybrid structures together with the advanced Si constitutive model.

Miller [1] proposed a design based on a primitive material model for Si plasticity, consisting of a time independent elasto-perfectly plastic behavior. This model and resulting design concept were extended to the full rotor geometry in Chapter 2 of this thesis, which substantiated the proposed design for the Si/SiC hybrid rotor. However, at the time a more detailed structural design was limited by the unavailability of accurate material property data and a constitutive model for the elevated temperature behavior for Si. In the previous analysis for Si/SiC hybrid structures, creep of Si has not been accounted for. In this Chapter, the design of a Si/SiC hybrid rotor is revisited with the Si model in order to provide a basis for re-evaluating Miller's analysis.

Section 6.2 presents FE results for the creep life estimation of the Si/SiC hybrid turbine rotor. Comparison of the model prediction and the previous elasto-plastic analysis by Miller [1] demonstrates the refined modeling capability for the design of Si/SiC hybrid structures provided by the Si model. The FE results are also summarized in a single plot,

which allows for the estimation of the creep life of the hybrid turbine rotor. Section 6.3 summarizes the basic guidelines for the design of Si/SiC hybrid structures for high temperature micro-turbomachinery gathered from the experimental observations and model predictions to date.

6.2 Creep life estimation of a Si/SiC hybrid turbine rotor

This section provides the FE results for creep life estimation of the Si/SiC hybrid turbine rotor at the temperatures of interest using the Si constitutive model developed in Chapter 5.

6.2.1 FE analysis results for creep life estimation of a Si/SiC hybrid turbine rotor.

An axisymmetric FE analysis was performed to estimate the creep life of the Si/SiC hybrid turbine rotor for various SiC relative thicknesses ranging from 0 to 30 % at elevated temperatures. ABAQUS^{TM} EXPLICIT [2], a commercial FE program, was used together with the Si constitutive model implemented in a VUMAT user subroutine. A simple sandwich-type hybrid disc model with SiC reinforcement in between flat Si discs shown in Figure 6.1 was used in the analysis, as was modeled by Miller [1]. The design specifications of the current microengine rotor were considered in this analysis. The SiC reinforcement was described by an elastic material with a Young's modulus of 430 GPa and Poisson's ratio of 0.21, as reported by Jackson [3]. The Si constitutive model developed in this thesis was used for the Si. The FE model assumes a uniform temperature distribution on the hybrid disc and a rotational speed of 1.2 million rpm. This assumption of uniform temperature is justified by a small Biot number of approximately 0.02. It was assumed to take 10 seconds for the rotor to reach the design rotational speed to ensure a quasi-static analysis. The turbine rotor radial growth at the rim was calculated as a function of time using this axisymmetric FE model. The maximum tensile stress in the SiC reinforcement was also computed. This occurs at the rotational axis.

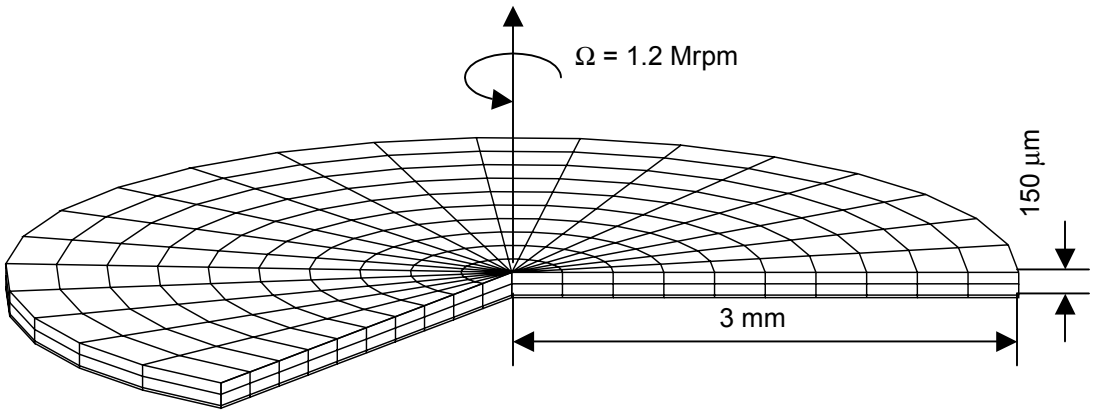

Figure 6.1 Axisymmetric FE mesh to estimate the creep life of a Si/SiC hybrid turbine rotor.

The FE simulation results for creep life estimation of a Si/SiC hybrid turbine rotor are shown in Figure 6.2. The turbine rotor radial growth as a function of time is plotted for the four relative SiC thicknesses ranging from 0 to 30 % in the temperature range of 600 to 900 °C. In Figure 6.3, the FE results are rearranged to illustrate the effect of temperature on the creep growth of the hybrid turbine rotor at each relative SiC thickness. Two points on the time axis indicating half day and three days were marked together as references for the design creep life of the turbine rotor. The radial growth for 10 seconds corresponds to the almost entirely elastic deformation of the turbine rotor while the rotor reaches the design rotational speed of 1.2 million rpm. (For the all-Si case at 900 °C, it is, however, evident that creep begins even before the rotor reaches the design speed).

As shown in Figure 6.2 and 6.3, the all-Si turbine rotor grows significantly more rapidly than the other cases with SiC reinforcements. Apparently, while the amount of SiC in the turbine rotor limits the overall turbine rotor radial growth by creep, the turbine wall temperature determines the time taken to reach a certain level of radial growth for a given thickness of CVD SiC in the turbine rotor. To illustrate the usage of the plots in Figure 6.2 and 6.3, the all-Si current microengine rotor is considered as follows. Figure 6.3 (a), plotted on a different scale from the others, shows the overall radial growth of the all-Si

turbine rotor. At 600 °C, which is the design turbine wall temperature of the all-Si demo engine, it takes approximately 3 hours for the radial growth to reach the current bearing gap of 15 μm. Thus, given the allowable turbine radial growth from the system considerations, the operating conditions and minimum design requirements for Si/SiC hybrid structures can be extracted using these diagrams. In addition to failure due to creep of the Si, fracture of the SiC must be considered.

At the microscale the dislocations nucleated within the Si crystal under the static load (centrifugal load) soften the Si structure, and consequently cause macroscale creep radial growth. As the Si creep proceeds, the load carried by the SiC reinforcement gradually increases. At a certain level of the turbine rotor radial growth, the stress in the SiC may reach its fracture strength. This is dependent on the relative thickness of SiC. This will be discussed in more detail in Section 6.2.2.

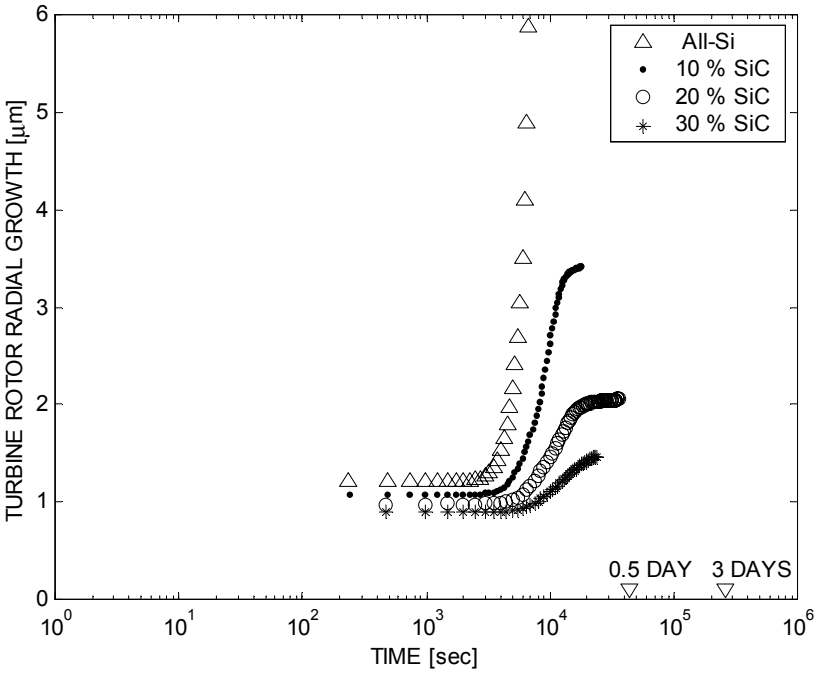

(a) 600 °C

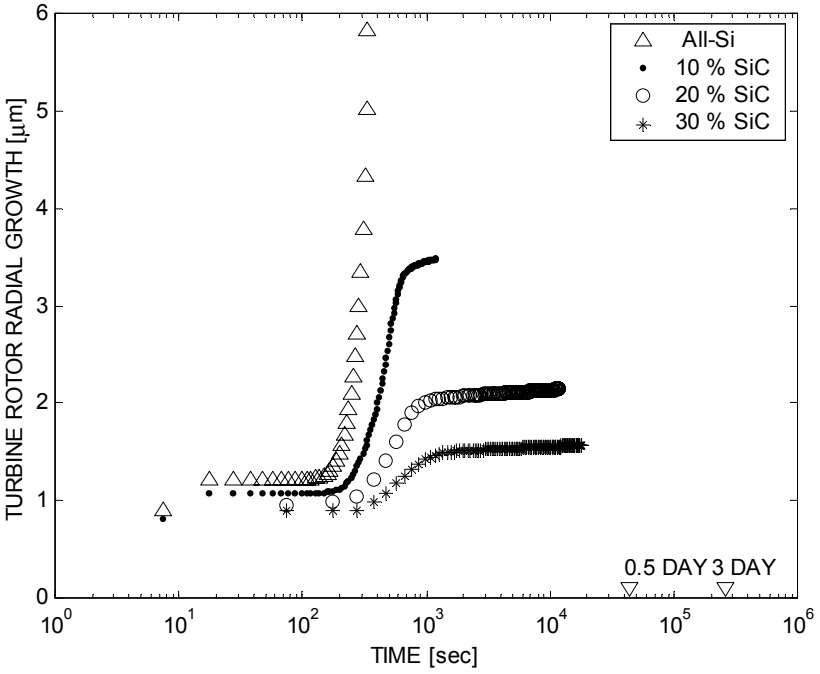

(b) 700 °C

Figure 6.2 Turbine rotor radial growth with time for various SiC relative thicknesses at temperatures ranging from 600 to 900 °C.

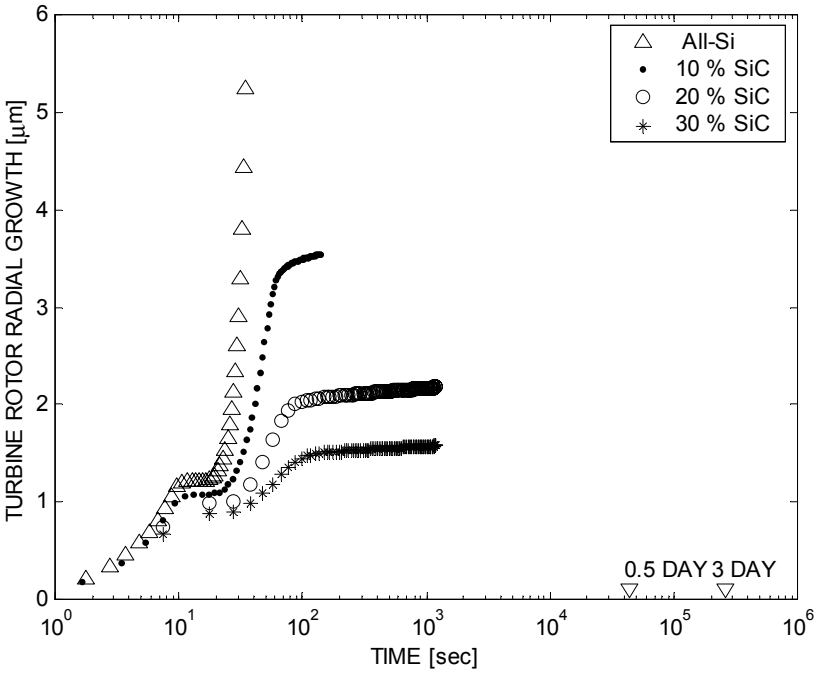

(c) 800 °C

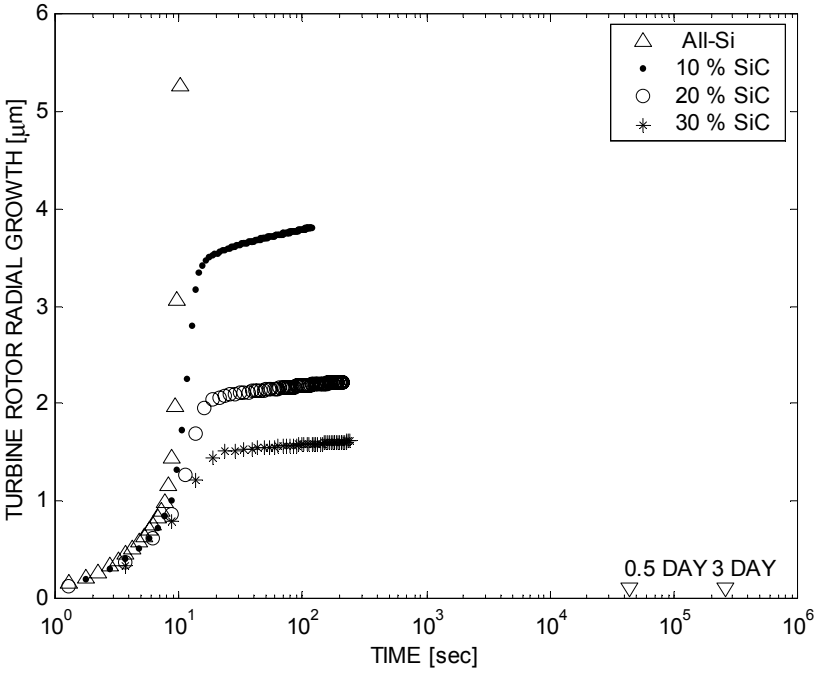

(d) 900 °C

Figure 6.2 (continued) Turbine rotor radial growth with time for various SiC relative thicknesses at temperatures ranging from 600 to 900 °C.

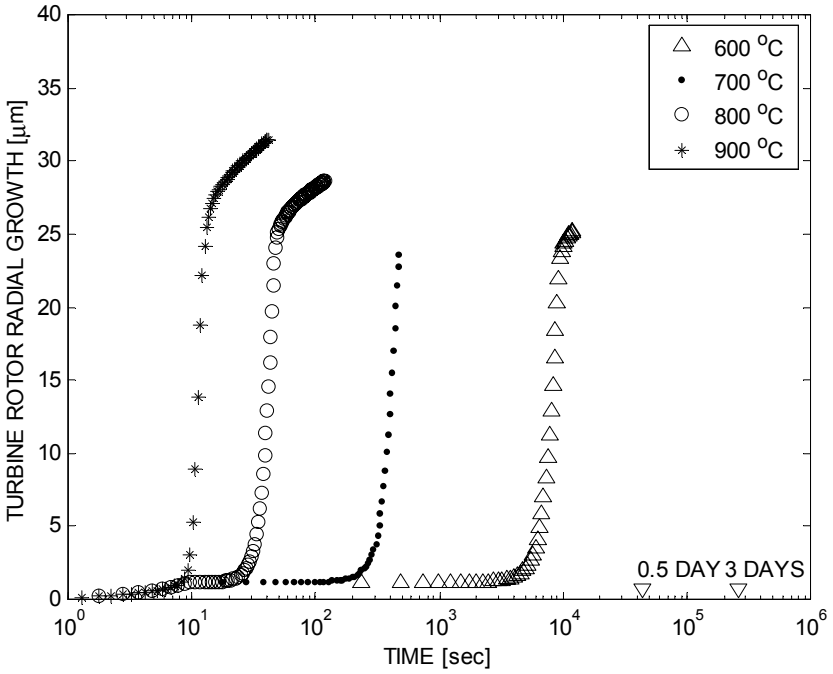

(a) All-Si

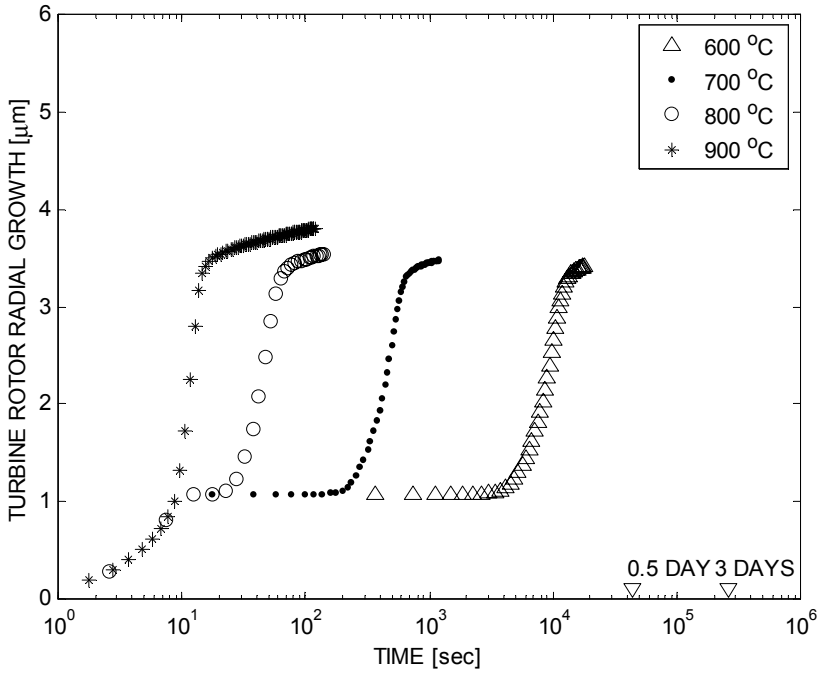

(b) 10 % SiC

Figure 6.3 Rearranged plots for the turbine rotor radial growth with time for various SiC relative thicknesses at temperatures ranging from 600 to 900 °C.

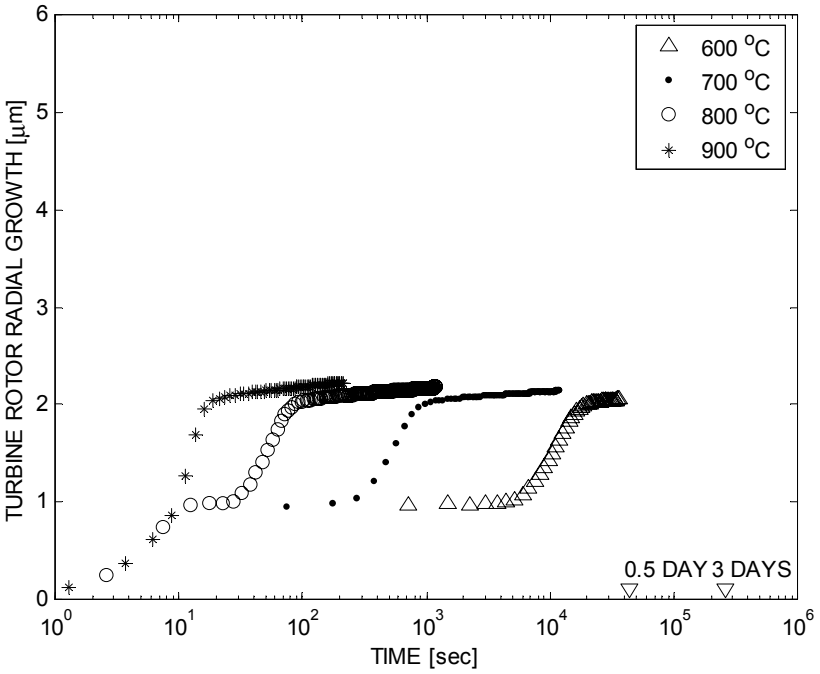

(c) 20 % SiC

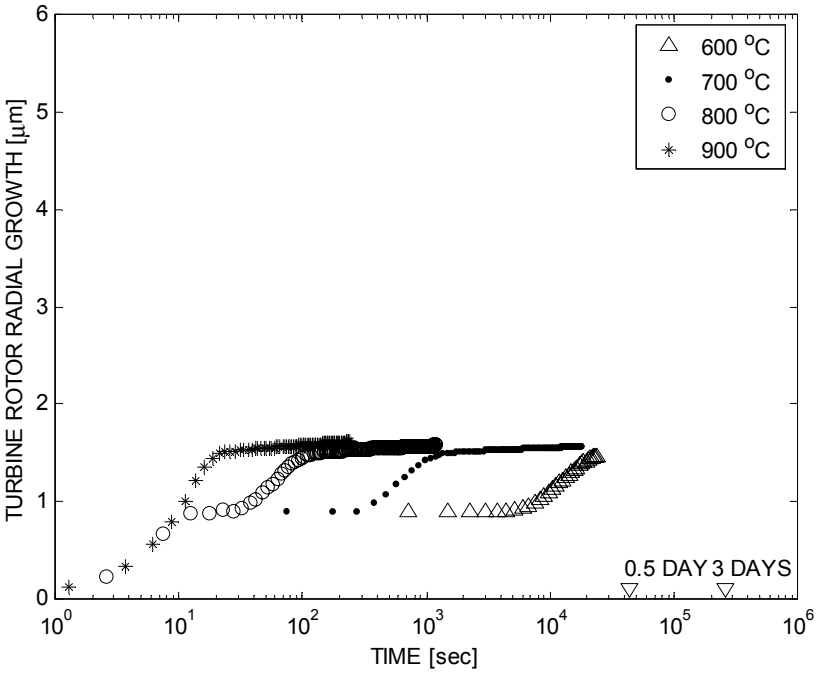

(d) 30 % SiC

Figure 6.3 (continued) Rearranged plots for the turbine rotor radial growth with time for various SiC relative thicknesses at temperatures ranging from 600 to 900 °C.

6.2.2 Comparison of the model prediction for creep life and elasto-plastic analysis

In Figure 6.4, the maximum stress in the SiC is plotted against the turbine wall temperature. These results can be compared directly to those of Miller [1]. The elasto-plastic analysis shows the exponential growth of the stress in the SiC reinforcement with increasing temperature, but the data points are static at a given temperature. On the other hand, the stress in the SiC varies with time according to the model prediction at a given temperature, as the turbine radially grows with time. For the relative SiC thickness of 10 %, the stress in the SiC reaches its assumed fracture strength of 700 MPa at the turbine radial growth of around 1.7 μm. According to the experimental results in Chapter 5, the SiC fracture strength of 700 MPa is easily achievable. However, this nominal strength represents a reasonably conservative value for design purpose. At 600 °C it takes approximately 2 hours for the stress in the SiC reinforcement to reach the nominal fracture strength, and only 10 seconds at 900 °C. However, for the relative SiC thickness of 30 %, the stress in the SiC reinforcement never reaches its fracture stress.

The elasto-plastic analysis by Miller [1] has also predicted a burst-line (temperature) for the hybrid turbine disc, beyond which the Si deforms severely and eventually bursts (numerically the FEM, ABAQUS^{TM} STANDARD, does not converge to a solution because of severe deformation of the Si). According to the results in Figure 6.4(b), the structural integrity of the Si/SiC hybrid turbine, however, is not limited by the SiC fracture strength nor by the severe deformation of the Si. Instead, the structural integrity of the hybrid turbine rotor is likely to be limited by a time scale associated with overall system considerations. For example, the turbine rotor with a SiC layer of 10 % relative thickness lasts for only 10 seconds at 900 °C. This rotor is obviously useless. However, depending on the allowable operating time for a device, the turbine rotor with a SiC layer of 10 % relative thickness operating at 600 °C, which will eventually fail by fracture after 3 to 4 hours, may be quite acceptable from a design point of view.

As illustrated in this section, the creep life estimation of the Si/SiC hybrid turbine rotor using the Si model provides more comprehensive data for the design of Si/SiC hybrid

structures. Section 6.2.3 further develops a design criterion for a Si/SiC hybrid turbine rotor in terms of creep life by integrating the numerical results presented in Section 6.2.1 and 6.2.2.

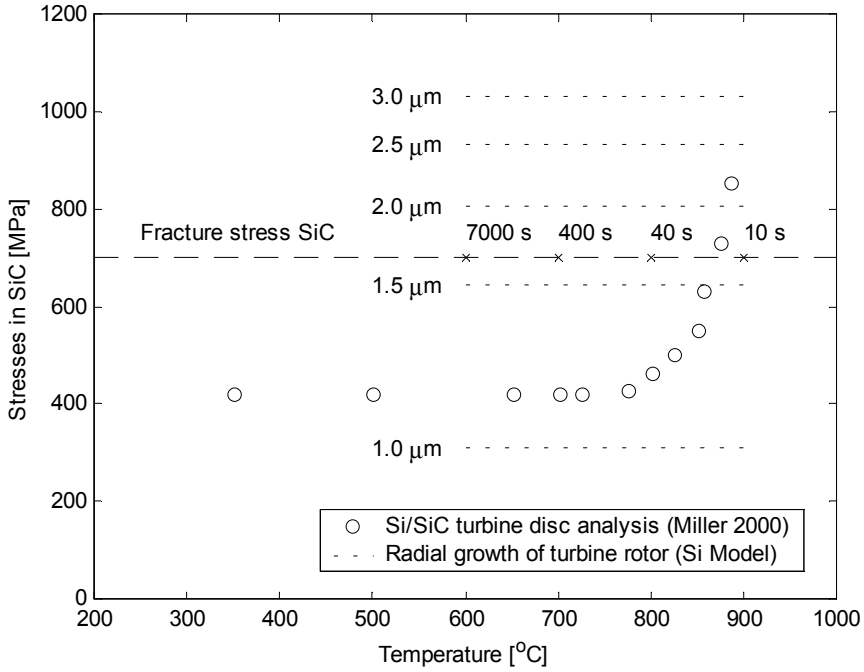

(a) 10 % SiC

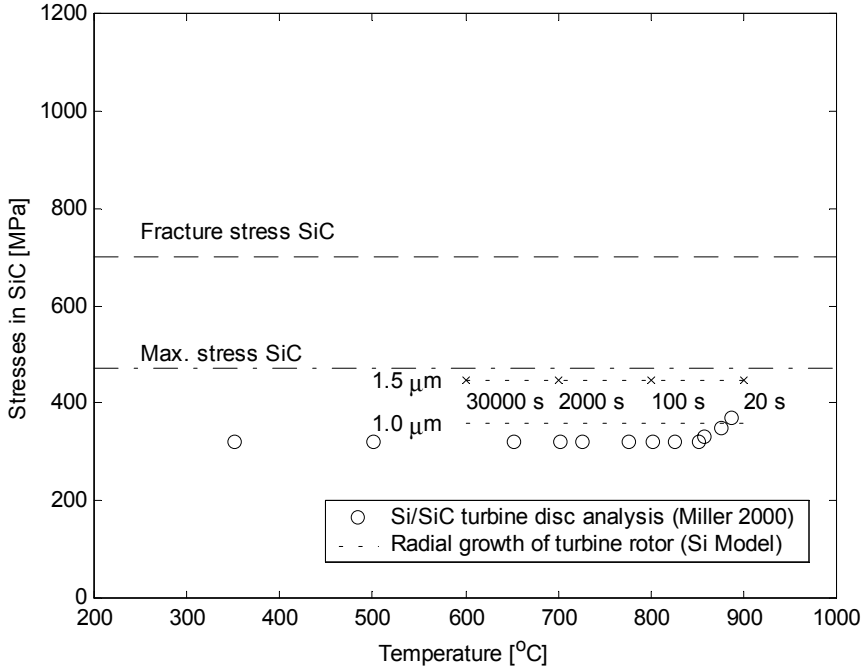

(b) 30 % SiC

Figure 6.4 Model prediction for creep life vs. elasto-plastic analysis (a) relative SiC thickness of 10 %, (b) relative SiC thickness of 30 %.

6.2.3 Design criterion for the SiC reinforcement of a Si/SiC hybrid turbine rotor

Integrating all the information from the FE results presented in Section 6.2.1 and 6.2.2, a criterion for the SiC reinforcement of a Si/SiC hybrid turbine rotor with regard to creep life is suggested in Figure 6.5. The maximum turbine radial growth for the relative thickness of SiC was obtained from Figure 6.3. Note that the relative SiC thickness determines the radial growth by creep almost irrespective of the turbine wall temperature. Here, 10^6 seconds was used as a reference time for the turbine service life, and the data are based on the analysis over the temperature range of 600 to 900 °C. Of course, depending on the reference time for the desired turbine operation, the whole curve can be adjusted, but not significantly. The dotted horizontal lines correspond to the various levels of the SiC fracture strength which given the relative thickness of SiC, correspond to the maximum stress in the SiC reinforcement at the reference time. As discussed in Chapter 5, Weibull statistics would be required to characterize fully the appropriate fracture strength distribution for SiC. From system considerations, such as the requirement for stable bearing operation, another horizontal line, corresponding to an allowable radial growth, can also be drawn as an additional constraint. This stability margin for the bearing operation can be further adjusted as the study progresses.

In order to illustrate the usage of the plot (i.e., Figure 6.5), the following case was considered. Assuming the SiC fracture strength of 700 MPa and the stability margin for the bearing operation of 5 μm, the turbine rotor needs a SiC reinforcement with at least a relative SiC thickness of 20 %. This configuration corresponds to a SiC layer of 60 μm for the design specifications of the current microengine rotor. This has been demonstrated in deposition experiments [4, 5]. Note that this design requirement is relatively conservative because Figure 6.5 provides the relative SiC thickness based on the desired turbine service life of the turbine of 10^6 seconds irrespective of the turbine wall temperature. The deformation-time results in Figure 6.2 and 6.3 would be useful when the turbine operating conditions are specified more in detail. The effect of the turbine rotor rotational speed was also considered. The reduction of the rotational speed by 20 % allows for a thinner SiC layer down to the relative SiC thickness of 10 %. This

result implies that the level of the SiC reinforcement needs to be determined from the trade-off between the overall system requirements and the constraints imposed by the micro-fabrication of Si/SiC hybrid structures. Moreover, it is clear that this design requirement on the SiC thickness is driven by the fracture strength of SiC for this case. Finally, it is worth noting that the turbine rotor radial growth due to the elastic deflection is approximately 1 μm, which is not a negotiable value (See Section 6.2.1).

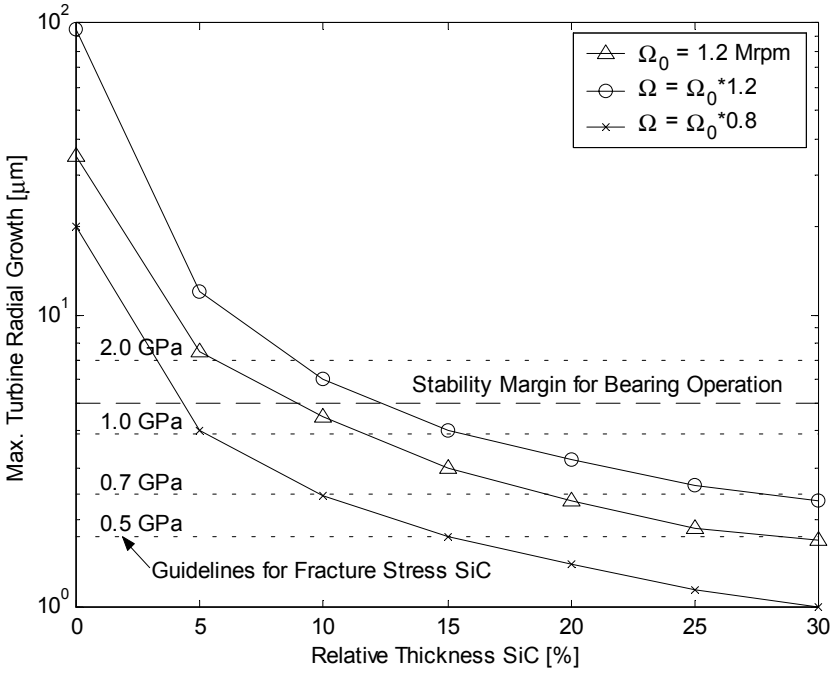

1. Rotational speed of the turbine rotor of 1.2 million rpm was used for a baseline in the analysis.
2. 10^6 seconds was used as a reference time for the maximum turbine radial growth.
3. Based on the analysis over the temperature range of 600 to 900 °C.
4. Stability margin for the bearing operation from Teo [6].

Figure 6.5 Effect of SiC reinforcements on the radial growth of a Si/SiC hybrid turbine rotor

6.3 Basic guidelines for the design of Si/SiC hybrid rotor

This section provides the basic guidelines for the design of Si/SiC hybrid structures at elevated temperatures from the experimental observations and model predictions. The scope of this section is limited to the materials and structures issues pertaining to the proposed configuration of the Si/SiC hybrid turbine rotor. However, the concepts

underlying the issues considered in this section can be utilized in the design of the general Si/SiC hybrid structures or other powerMEMS.

1. The upper yield strength of single crystal Si is non-conservative in the design of Si hot structures. As discussed in Chapter 5, any static load, which results in stress levels between the peak and the plateau in a stress-strain curve of single crystal Si, has been shown to yield a high creep rate. Also from the perspective of the design of Si hot structures, the lower yield strength of Si is insufficient, particularly for micro-turbomachinery operating at elevated temperatures and high stresses. The values for the lower yield strength of Si can be found in Chapter 2. The recommended approach to the design of Si hot structures is to use the Si model for extracting appropriate operating conditions, given the overall design requirements, and to reinforce the Si structures with SiC in strategic locations. Even with SiC reinforcement, the design of Si/SiC hybrid turbine rotor should account for creep-limited design as implied from the FE results presented in this chapter.

2. At elevated temperatures, the effect of stress concentrations is not as significant as in low temperature Si structures. According to the experimental results for the notched Si 4-point bend tests in Chapter 5, the effect of stress concentrations on the structural instabilities of Si hot structures does not appear to be sufficient to cause plastic collapse, particularly in structures subject to bending moments. Unlike the low temperature Si structures, where stress concentrations at the sharp corners may lead to a catastrophic brittle fracture, at high temperatures the plasticity present adjacent to the sharp corners reduces the effect of stress concentrations. Although catastrophic failure seems unlikely, the distortion of the turbine blade with time still needs to be carefully estimated using the Si model.

3. The creep life of the all-Si turbine rotor was predicted to be approximately 3 hours at 600 °C. This is a functional failure since it takes approximately 3 hours for the turbine radial growth to close the current bearing gap of 15 μm. The rotational speed of the turbine rotor of 1.2 million rpm was used in the analysis. The stability margin

for the bearing operation may further reduce the allowable creep life of the all-Si turbine rotor. From a design point of view, the creep life of the all-Si turbine of 3 hours may be sufficient for the purpose of the demo microengine. However, from a practical standpoint the all-Si turbine is not feasible at higher temperatures.

4. The design space for the structural design of the microengine turbine rotor can be extended by incorporating SiC in the Si structures. In Chapter 5, the Si/SiC hybrid structural concept was verified. The experimental results assessed the integrity of the Si/SiC interface during deformations at high temperatures as well as the material properties of CVD SiC. The significant increase in the load carrying capability of the Si/SiC hybrid specimens compared to the all-Si specimens provides more design space for the design of the Si/SiC hybrid turbine rotor for the next generation microengine.

5. The turbine rotor of the next generation microengine requires SiC reinforcement by at least a relative thickness of 20 % provided that the SiC fracture strength is 700 MPa and the stability margin for the bearing operation is 5 μm. The relative SiC thickness of 20 % corresponds to a layer of 60 μm for the design specifications of the current microengine rotor. This value is relatively conservative. More precise predictions can be made using the FE results in Figure 6.2 and 6.3 once the more specific turbine operating conditions are available. More accurate values for the SiC fracture strength and the stability margin are needed for a better prediction.

6. Si hollow blades reduce the distortion of the blades themselves as well as the umbrella-shape deflection of the microengine turbine. The aerodynamics of the rotor operation depends on the well-defined 3-D geometry of the blades. In order to minimize the distortion of the blade, the Si half-hollow blade was suggested in the previous work by Miller [1] and the initial structural analysis presented in Chapter 2. Furthermore, the SiC reinforcement in the mid plane is not effective in reducing the umbrella-shape deflection. This deflection mode can also be reduced by adopting the

Si hollow blades as suggested earlier. SiC reinforcement in the blade is not desirable because of the complications associated with micro-fabrication.

6.4 Summary

An axisymmetric FE analysis was performed to estimate the creep life of the Si/SiC hybrid turbine rotor for various SiC thicknesses at the temperatures of interest. The FE results identified the limit of the all-Si turbine rotor of the current microengine as well as the superior performance of the Si/SiC hybrid rotor in terms of creep life. Comparison of the model prediction for creep life estimation and the previous elasto-plastic analysis by Miller [1] demonstrated the additional refined modeling capability for the design of Si/SiC hybrid structures provided by the Si model. Furthermore, the FE results for the creep life estimation were applied to yield a design criterion for the SiC reinforcement. Finally, based on the experimental observations and model predictions, improved guidelines to the design of Si/SiC hybrid structures for high temperature micro-turbomachinery were summarized.

Chapter 7 provides the overall conclusions and suggestions for future work.

Reference

1. B. Miller, Hybrid Silicon/Silicon Carbide Microstructures and Silicon Bond Strength Tests for the MIT Microengine, S. M. Thesis, Dept. of Aeronautics and Astronautics, MIT, Cambridge, MA, 2000.
2. ABAQUS Reference Manuals, 2001, Providence, RI.
3. K. Jackson, R. Edwards, W. Sharpe, Jr., Mechanical properties of thin film silicon carbide, Mat. Res. Soc. Symp. Proc., Vol. 687, B6.3, Fall 2001.
4. D. Choi, R. J. Shinavski, S. M. Spearing, Process Development of Silicon-Silicon Carbide Hybrid Micro-Engine Structures, Mat. Res. Soc. Symp. Proc., Vol. 687, B5.44, Fall 2001.
5. R. J. Shinavski, W. S. Steffier, Enhanced Strength, Nanolayered SiC for Micro-Gas Turbine Portable power Generation, ARO report by Hyper-Therm Inc., 1999.
6. C. J. Teo, Personal communications, Gas Turbine Lab, MIT, 2002

Chapter 7

Conclusions and future work

7.1 Overall summary

Detailed design of Si/SiC hybrid structures for high temperature micro-turbomachinery has been hampered by the relatively poor performance of single crystal Si at elevated temperatures and high stresses and by the unavailability of accurate material properties data for both Si and SiC at the temperatures of interest. From previous work [1, 2, 3], the critical structures and materials issues to be resolved, in order to proceed with the design of high temperature Si/SiC hybrid structures, were identified as follows:

1. the safety margin of the structural design of Si/SiC hybrid structures based on the upper yield strength of Si
2. reliable estimation of the service life of the Si/SiC hybrid structures
3. structural instabilities caused by the combination of high stress concentration, creep, and strain softening.

In the course of this thesis, these issues provided the key motivations of the work, and have been substantially resolved.

A constitutive model for single crystal Si with low grown-in dislocation density at high temperatures and high stresses, necessary to predict accurately the deformation of Si/SiC hybrid structures, has been developed that takes into consideration both the microscale deformation mechanisms and the experimental results at the macroscale. This Si constitutive model accounts for the two deformation regimes: Regime 1, the initial deformation stages characterized by the rapidly multiplying dislocations, and Regime 2, the later stages of deformation after a sufficiently large mobile dislocation density has been generated. At the macroscale, this model is versatile in predicting various aspects of the pronounced material characteristic of Si at elevated temperatures, namely, strain-softening, thermal softening, and the various creep stages. The Si model, implemented in

an ABAQUS™ user subroutine, VUMAT [4], has been calibrated using the uniaxial compression creep tests and then validated against the experimental results for a series of 4-point bend tests.

From the experimental observations and model validation, basic guidelines for the design of Si/SiC hot structures have been provided. First, the use of the upper yield strength of single crystal Si for design purpose is non-conservative. Also from the perspective of the design of Si hot structures, the lower yield strength is insufficient, particularly for micro-turbomachinery operating at elevated temperatures and high stresses. The recommended approach to the design of Si hot structures is to use the Si model for extracting appropriate operating conditions, given the overall design specifications, and to reinforce the Si structures with SiC in strategic locations. Second, at high temperatures, the effect of stress concentrations is not crucial. Unlike the low temperature Si structures, the plasticity present adjacent to the sharp corners reduces the effect of stress concentrations. Third, the Si/SiC hybrid structures concept was verified. The considerable increase in the load carrying capability of the Si/SiC hybrid specimens encourages the development of Si/SiC hybrid structures for elevated temperature micro-turbomachinery in order to increase the available design space. Finally, the FE results for the creep life estimation of the Si/SiC hybrid turbine rotor identified the limit of the all-Si turbine rotor of the current microengine as well as the superior performance of the Si/SiC hybrid rotor in terms of creep life. According to the model prediction, SiC reinforcement is required for the turbine rotor of the next generation microengine with at least a relative layer thickness of 20 %.

7.2 Conclusions

The primary goal of this research, as a part of the microengine project, is to design a high temperature Si/SiC hybrid rotor that improves the overall engine efficiency while maintaining structural integrity. In the course of this thesis, two main objectives derived from the overall goal of this work have been achieved.

First, a constitutive model for single crystal Si at elevated temperature and high stresses to support the design process has been developed. The model has been calibrated and validated against elevated temperature mechanical test data for Si and Si/SiC structures. The test data for Si represents the most comprehensive data set yet produced. The test data for Si/SiC is the first of its kind and this is the first experimental validation of the Si/SiC hybrid structure concept.

Second, this thesis provides the basic guidelines for a self-consistent design of Si/SiC hybrid structures for elevated temperature micro-turbomachinery, given the constraints imposed by the micro-fabrication processes and system considerations. The guidelines, although specific to the Si/SiC hybrid turbine rotor, can be applied to the more general application of Si/SiC hybrid structures in PowerMEMS or other microsystems.

7.3 Contributions

The contribution of this work includes the following accomplishments:

1. A constitutive model for single crystal Si at elevated temperatures and high stresses to support design process has been developed.
2. The Si model has been calibrated and validated against mechanical test data for Si and Si/SiC structures.
3. The test data for Si represents the most comprehensive data set yet produced.
4. The test data for Si/SiC is the first of its kind, and the first experimental validation of the Si/SiC hybrid structure concept.
5. Given the constraints imposed by the micro-fabrication processes and system considerations, the basic guidelines for a self-consistent design of Si/SiC hybrid structures for elevated temperature micro-turbomachinery have been provided.

7.4 Future work

There are two major aspects of this work that should be extended in the future: improvements for Si constitutive model, which is of general applicability, and development of a Si/SiC hybrid rotor for the next generation microengine, more specific to the overall microengine project.

7.4.1 Improvements for Si constitutive model

1. The overall modeling process from model calibration to validation needs to be refined. The Si constitutive model has been calibrated using the experimental data for the Si uniaxial compression creep tests. However, despite the simplicity of the testing procedure, the compression creep testing is not an ideal method for model calibration simply because of the inherent experimental errors (approximately 15 %) due to effects such as friction, seating of the load train, accurate strain measurement, and plastic buckling. According to the model, the calibrated dislocation nucleation rate appears to be faster, and the transition between the deformation regimes earlier than is observed experimentally. If properly designed, specifically with attention to the grips and strain measurement technique, uniaxial tension testing in monotonic loading has the potential to provide more accurate results.

2. More concrete explanation of the effect of stress concentrations on the localized deformation needs to be further explored. The experimental results with the notched specimens were somewhat difficult to interpret because of the materials adjacent to the neutral plane stiffening with deflection. The effect of stress concentrations on the localized deformation and overall load could not be quantified from the experimental results. Thus, it is desirable to isolate the pure effect of stress concentrations on the localized deformation from the effect of the loading conditions. Tensile testing would also facilitate this.
3. The Si model implemented in the crystal plasticity frame-work is critical for the description of the effect of crystal orientations and shear localizations. The

isotropic version of the Si model was not effective in capturing the localized deformations at stress concentrations. Moreover, the efforts to investigate the effect of crystallographic orientations on the structural response was not fruitful because of the experimental errors associated with the compression creep testing. The improved predictive capabilities of the Si model could be obtained through the Si model implemented in the crystal plasticity frame-work together with more accurate mechanical testing results.

7.4.2 Development of Si/SiC hybrid rotor

1. Given the constraints imposed by the micro-fabrication processes and system considerations, design iterations of the Si/SiC hybrid rotor using a better material model and thermal BC's need to be conducted. Thermo-mechanical FE analysis is required to obtain temperature and stress fields of Si/SiC hybrid structures using the Si material model, to assess the advantage of the hybrid structure, and to provide structural design criteria and fabrication requirements. Moreover, since accurate heat transfer coefficients around the rotor are essential, numerical iterations with fluidic domain calculations will be performed to provide them, which will lead to obtaining more accurate temperature fields.

2. It is critical for the development of Si/SiC hybrid structures to characterize material property data of CVD SiC, particularly the fracture strength. According to the analysis of the creep life of the Si/SiC hybrid turbine rotor, the fracture strength of SiC is the limiting factor for the structural integrity of the turbine rotor. The factors determining the fracture strength of SiC are the dimensions of the device, process conditions, and stress-states within the structures. As was conducted on the Si fracture strength at room temperature, Weibull statistics needs to be performed on the CVD SiC films. Moreover, a more complete understanding on the failure mechanisms of the hybrid structures composed of a brittle material and a ductile material should be obtained.

3. Si/SiC hybrid structures may include thin interlayer materials because of the Si/SiC micro-fabrication processes. Currently, the candidate materials are SiO_2 or poly-Si. In either case, the integrity of the bond or deposition interface and the effect of thin layers on the overall structural response should be assessed at elevated temperatures.

Reference

1. K.-S. Chen, Materials Characterization and Structural Design of Ceramic Micro Turbomachinery, Ph. D. Thesis, Dept. of Mechanical Engineering, MIT, Cambridge, MA, 1999.
2. B. Miller, Hybrid Silicon/Silicon Carbide Microstructures and Silicon Bond Strength Tests for the MIT Microengine, S. M. Thesis, Dept. of Aeronautics and Astronautics, MIT, Cambridge, MA, 2000.
3. D. S. Walters, Creep Characterization of Single Crystal Silicon in Support of the MIT Microengine, S. M. Thesis, Dept. of Mechanical Engineering, MIT, Cambridge, MA, 1999.
4. ABAQUS Reference Manuals, 2001, Providence, RI.

APPENDIX A

Specifications for High Temperature Material Testing System

Instron™ 3118 Ceramics Testing System

Furnace type	Single zone split cylindrical
Furnace dimensions	Height: 520 mm Diameter: 360 mm Internal bore: 100 mm Hot zone height: 280 mm
Heating elements	6 kanthal supper 33 (molybdenum disilicide)
Temperature range	800 to 1500 °C
Maximum heating rate	12 °C/min
Power requirements	3.6 kW
Thermocouples	2 Type B with facility for a third unit
Furnace Controller	Eurotherm 818P microprocessor controller with computer interface
Furnace controller dimension	Height: 615 mm Width: 550 mm Depth: 500 mm
Over-temperature protection	Eurotherm 106 temperature alarm
Power supply	240 V, 50 Hz single-phase fused at 25 A
Cooling water minimum flow rates	1 l/min for furnace 1 l/min for load-train
Cooling water maximum pressure	6 bar
Cooling water maximum inlet temperature	30 °C
Pushrod material	Alumina
Pushrod dimensions	Upper – solid 25 mm diameter Lower – hollow 45 mm outside dia., 30 mm inside dia.
Pushrod load capacity	1 kN at 1500 °C
Deflection measuring system	LVDT operated by probe in lower compression rod. LVDT position manually adjustable along the longitudinal axis
LVDT range	± 1 μm
Testing fixture material	SiC
Testing fixture type and dimensions	Bend fixture: 3118-300, 4-point, fully articulating, 40/20 mm span Compression anvils: 3118-303, partially articulating, 50 mm diameter

APPENDIX B

Detailed Compression/Flexural Testing Procedure

B.1 Si Compression Creep Testing Procedure

Preparing the workplace for testing

1. If needed, remove previous specimen from SiC fixture and clean apparatus to remove debris and oils.
2. Set load and position limits.
3. Turn on the hydraulics and actuator.
4. Set a sinusoidal position waveform of 15 mm at 0.5 Hz. Ensure range of motion is within the limits set above (adjust pushrod height manually with ▲▼ keys if necessary) and run the waveform for about 24 cycles. Press FINISH when done, then turn off actuator and hydraulics.
5. Check channels and cables into LabView™ interface: make sure program diagram matches setup.
6. Ensure that the units and gain values are correct both for Instron™ and LabView™ interface. (Ensure whole range of possible values is covered in 10V range.)
7. Make sure the Load Cell is reading properly and is calibrated. If necessary, calibrate Load cell using "Auto Calibration" procedure.

Specimen loading

8. Apply the specimen and the SiC load pads uniformly with the mixture of BN power and acetone.
9. Set Load Protect at 10N. Ensure load and position limits are on.
10. Set up specimen, along with the SiC compression anvils, in the testing machine. Check alignment, making sure that the sample and load pads are centered. ***Be very careful and gentle when handling and assembling the SiC fixture.***

11. Manually raise lower pushrod, using slow speed ▲ with Load Protect on. (If the pushrod stutters as it is raised, try increasing the value for Load Protect slightly. Sometimes the noise in the load cell causes the Load Protect to be tripped during normal pushrod activity.)
12. Set Load Gain Control:
    a. Press Load "SETUP"
    b. Press "loop", "prop" and enter the appropriate gain level. For 1000μm Si, use a value between 26-30.
13. Turn off Load Protect.
14. Switch from position control to load control by pressing "LOAD", then "IMMED". (The load should remain near the pre-existing value. If the load fluctuates sharply, return to position control by pressing "POSSITION", then "IMMED". Once in position control, turn LOAD PROTECT back on. Fluctuations are usually caused by improperly set gain values. Recheck the gain as in step 25. If correct (around 26), reduce by one or two and try switching to load control again as described above.)
15. Set load at -10 N using "Go To" command.
16. Command a load ramp waveform of –50 N at 30 N/s. Do another of 50 N at the same speed. Do not forget to press Finish. Repeat several times. This step is required to improve the seating of the load-train.

Setting the temperature controller

17. Close the oven being careful of thermocouples. Turn on water and circuit breaker for furnace. (Watch cables behind testing machines.)
18. Turn on temperature controller by pressing the left-most square green button.
19. Set temperature profile as needed. A typical temperature cycle is:

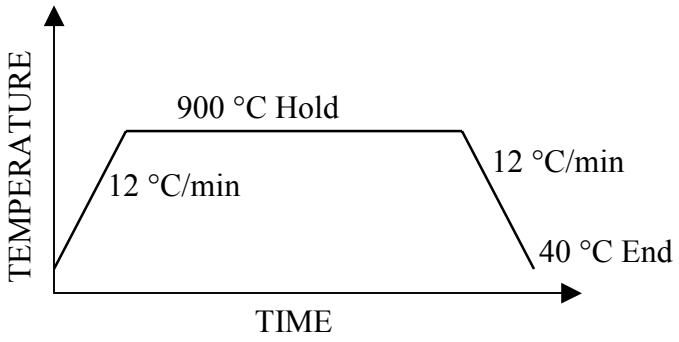

a. Hold ↻ until display changes; press ↻ again to display PROG.
b. Press ↕ to select.
c. Press ↻ to cycle through program options use △▽ to change.
d. Return to main display by ↕ and ↻.

Do not heat/cool the furnace at a rate faster than 12 °C/min.

20. Press ||> twice to start and then hold the program. Press right-most square green button to commence heating and ||> again to resume the program.
21. Start LabView™ program on the computer.
22. After the desired temperature has been reached, wait an additional 1.5 hours so that the load-train can settle thermally (until the saturation of the thermal elongation)

Beginning the test sequence

23. Command a load ramp waveform of –50 N at 30 N/s. Do another of 50 N at the same speed. Do not forget to press Finish. Repeat this step several times.
24. Restart LabView™'s data collection and check that all readings on the computer match the real time displays.
25. Set the sampling rate to 5 Hz.
26. Load the machine using a ramp waveform up to the desired static load. Once the desired load is achieved, load control will maintain it until additional input is received.
27. Change the sampling rate back to 0.5 Hz. (Smaller sampling rate for longer tests.)
28. Allow the specimen to creep until either the specimen fails or the desired creep strain/time.

Completing the test

29. When stop point is reached, return to position control by pressing "POSITION", then "IMMED".
30. Carefully lower the pushrod manually with the ▼▼ key.
31. Turn off actuator and hydraulics.
32. Press "STOP and RECORD" in LabView™ and save file to detailed filename:

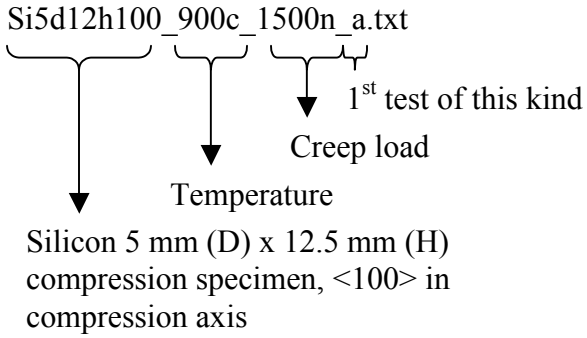

33. On temperature controller, press ||> to hold program. While held reduce duration time to 0 with ▼ key. Resume the temperature waveform. Once cooling ramp has started, wait until the temperature is under 400 °C before opening the furnace. Turn off furnace circuit breaker and then turn off water. (Caution should be used when allowing furnace to cool in isolation. The resistor coils can suffer thermal shock if cooled too quickly.)

    Under no circumstances should the furnace be opened with the temperature above 400 °C.

34. Take necessary safety precautions to prevent injury on hot furnace and let cool.
35. Remove and analyze sample when cooled.
36. Clear up the workplace

B.2 Si 4-Point Bend Testing (Monotonic loading) Procedure

Preparing the workplace for testing

1. Follow Steps 1-7 in 2.1 Si compression creep testing procedure.
2. If LVDT "SETUP" light is flashing, calibrate manually as shown below. If not, proceed to the next step.
    a. Turn on the Hydraulics and Actuator. Remove position limits and raise lower pushrod using slow speed, ▲, so that the LVDT is compressed to it's zero point as indicated by the display. (note – this is NOT complete compression of the black nub but rather the mid-point of its range of motion)
    b. Press the LVDT's "SETUP" button.
    c. Select "Calibrate", "Cal", "Manual", "Coarse Balanace", and "Go"
    d. Relay on. Press "SPAN", "Go". It will span the range. When it is settled and is reading 1mm, press "Go" again.
    e. Relay off. Press "Fine balance", "Zero Point", "Go". The light will stop blinking when calibration is completed.

Specimen loading

3. Place specimen in SiC 4-pt bend fixture being careful about alignment.
4. Transfer assembled SiC fixture with loaded specimen to push rod. Make sure LVDT is through opening in bottom of fixture and compressed to about 1mm.
5. Check alignment and clearance, making sure that the sample is centered in the 1cm groove so that its edges will not touch the fixture as it deforms.
6. Place cut cylinder flat side down on top of SiC fixture.
7. Set Load Protect at 10N. Ensure load and position limits are on.
8. Turn on hydraulics and actuator.
9. Manually raise lower pushrod until top of fixture is about 1cm from top pushrod. Turn off actuator and hydraulics.

Setting the temperature controller

10. Follow Steps 17-22 in Si compression creep testing procedure.

Beginning the test sequence (Monotonic loading)

11. Turn on hydraulics and actuator
12. After thermal settling, raise fixture until it makes gentle contact with the top pushrod using the ▲ key. To determine contact, watch both the real time load display and the real time LVDT display. The load should switch from near-zero to negative and the LVDT should compress very slightly upon making contact.
13. Change position gain to 1mm/V in LabView™ and on Instron™ output.
14. Calibrate Load Cell using "Automatic Calibration".
15. Set a single ramp waveform down to –0.2 mm with a ram speed of 0.001 mm/s, (which may be altered as desired.)
16. Start collecting data in LabView™ and cross check with Instron™ display.
17. Run the waveform.
18. Watch Instron™ output and LabView™ data plots for the desired deflection or fracture. Press HOLD at stop point.

Completing the test

19. Save data.
20. FINISH waveform and lower pushrod manually with ▼ key. Lower LVDT manually with thumb wheel in base of bottom pushrod if still under strain.
21. Turn off actuator and hydraulics.
22. On temperature controller, press ||> to hold program. While held, reduce duration time to 0. Resume the temperature waveform. Once cooling ramp has started turn off furnace, turn off water, turn off furnace circuit breaker.
23. Take necessary safety precautions to prevent injury on hot furnace and let cool.
24. Remove and analyze sample when cooled.

B.3 Si 4-Point Bend Creep Testing Procedure

Follow the same procedure with 2.3 Si 4-point bend testing (monotonic loading) procedure except for Steps at "*beginning of the test sequence*"

Beginning the test sequence (Monotonic loading)

1. Turn on hydraulics and actuator.
2. Calibrate Load Cell using "Automatic Calibration".
3. Raise fixture until it makes gentle contact with the top pushrod using the ▲ key.
4. Change position gain to 0.5mm/V in LabView™ and on Instron™ outputs.
5. Watching the real-time load display, switch from position control to load control by pressing "LOAD", then "IMMED". Set an integer-valued load using "Go To" command.
6. Set single ramp load waveform:
   SRAMP to desired load at a loading rate of 1 N/s.
7. Restart LabView™'s data collection and check that all readings on the computer match the real time displays.
8. Run the waveform by pressing "START". Once the desired load is achieved, load control will maintain it until additional input is received.
9. Allow the specimen to creep until either the specimen fails or the fixture reaches maximum compression (the LVDT reading should not drop below –1 mm).
10. When stop point is reached, return to position control by pressing "POSITION", then "IMMED".

APPENDIX C

Effect of Machine Compliance on Strain Measurements

As pointed out in Chapter 4, the high stiffness of the compression specimen prevents the determination of an accurate stress-strain curve using a constant-strain compression test. Here, how the machine compliance affects the displacement measurement (in case where an extensometer cannot be attached) is illustrated using load-displacement curves of a fictitious material. Figure C.1 shows the schematic of a testing machine and specimen represented by linear/nonlinear springs.

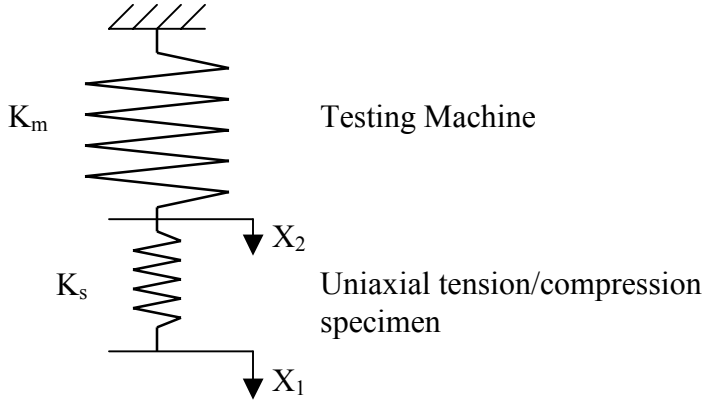

Figure C.1 Schematic of a testing machine and specimen

Given the crosshead displacement, X_1, and spring constants for the machine and specimen, the problem is to find the force measured by the load cell installed on the testing machine. For simplicity, the spring constant of the testing machine was assumed to be linear, and the specimen nonlinear (a 3rd order polynomial to describe strain-softening).

Testing machine elongation: $\delta_m = X_2$

Specimen displacement: $\delta_s = X_1 - X_2$

Force measured by the load cell: $F_m = K_m * \delta_m$

Force applied to the specimen: $F_s = K_s(\delta_s)$

$= \delta_s^3 - 6* \delta_s^2 + 11*\delta_s$

From force equilibrium,

$$F_m = F_s \text{ or}$$

$$K_m * \delta_m = \delta_s^3 - 6 * \delta_s^2 + 11 * \delta_s$$

Substituting $\delta_m = X_2$ and $\delta_s = X_1 - X_2$, and solving the nonlinear equation for X_2, the force F_m (or F_s) can be obtained. Two spring constants for the testing machine were considered. Figure C.2 and C.3 show the results. As shown in the plots, the high stiffness of the uniaxial specimen does not allow for an accurate load-displacement measurement.

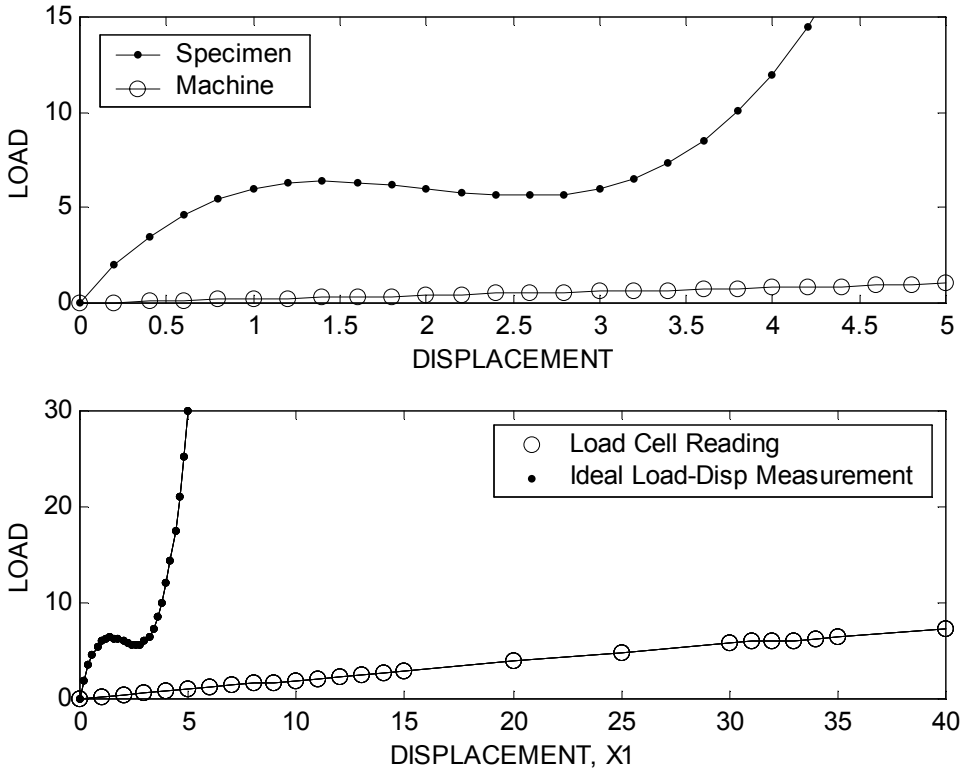

Figure C.2 Load-displacement curve obtained using a testing machine more compliant than the specimen.

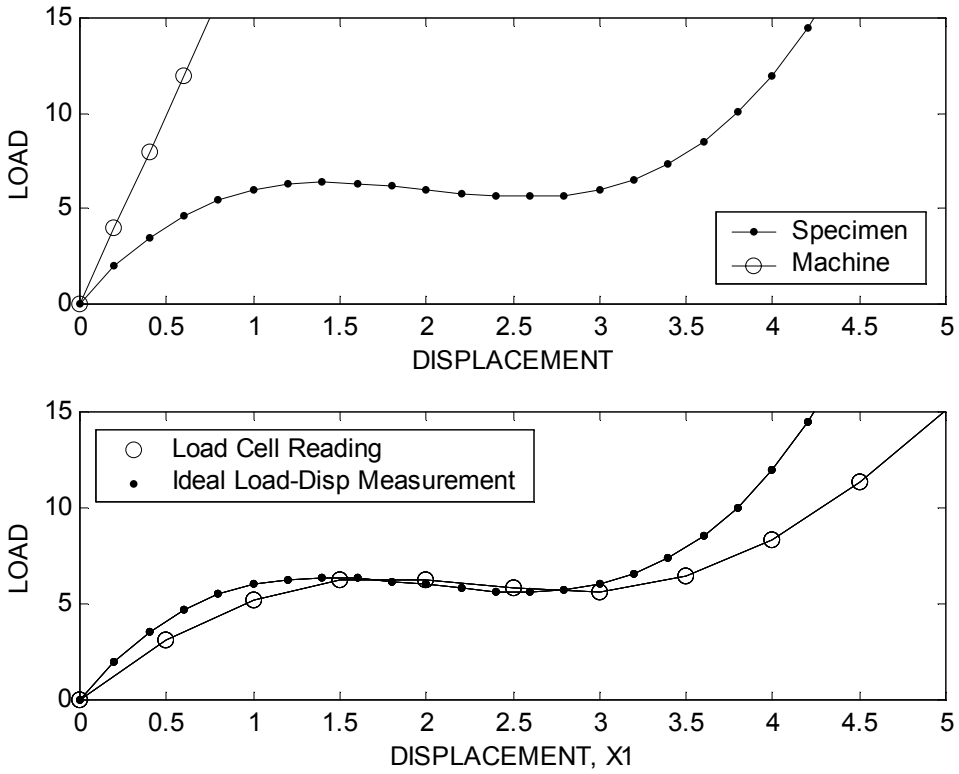

Figure C.3 Load-displacement curve obtained using a testing machine stiffer than the specimen.

APPENDIX D

ABAQUS™ EXPLICIT VUMAT User Subroutine

```
C**********************************************************************
C                   USER MATERIAL SUBROUTINE VUMAT FOR
C                   Silicon at high T, isotropic model
C                   (TO BE USED WITH ABAQUS VERSION 5.8)
C
C             THIS VUMAT IS NOT FOR USE IN PLANE STRESS OR IN ANY OTHER
C             SITUATION WHEN THERE ARE MORE STRAIN TERMS THAN STRESS TERMS.
C
C             COPYRIGHT H.-S. Moon, L. Anand; April 2002
C
C**********************************************************************
C      CONTENTS OF PROPS VECTOR (*USER MATERIAL, CONSTANTS = 19) :
C      PROPS(I)
C 1    EYOUNG
C 2    ANU
C 3    BV
C 4    ALPHA
C 5    V0
C 6    TAU0
C 7    Q
C 8    AKB
C 9    AM
C 10   RHO0
C 11   AK
C 12   GDOT0
C 13   DELF
C 14   H0
C 15   S0
C 16   SSAT
C 17   RHOCRIT0
C 18   THETA0
C 19   ALPHAT
C
C      STATE VARIABLES
C      *DEPVAR
C      21            :
C
C      STATEV(1) = RHO     -- DISLOCATION DENSITY
C      STATEV(2) = GBARDOTP --SCALAR PLASTIC SHEARING STRAIN RATE.
C      STATEV(3) = GBARP   -- SCALAR PLASTIC SHEARING STRAIN.
C      STATEV(4) = S       -- SHEAR RESISTANCE
C      STATEV(5) = FP(1,1) -- PLASTIC DEFORMATION GRADIENT, (1,1) COMP.
C      STATEV(6) = FP(1,2) -- PLASTIC DEFORMATION GRADIENT, (1,2) COMP.
C      STATEV(7) = FP(1,3) -- PLASTIC DEFORMATION GRADIENT, (1,3) COMP.
C      STATEV(8) = FP(2,1) -- PLASTIC DEFORMATION GRADIENT, (2,1) COMP.
C      STATEV(9) = FP(2,2) -- PLASTIC DEFORMATION GRADIENT, (2,2) COMP.
C      STATEV(10) = FP(2,3) -- PLASTIC DEFORMATION GRADIENT, (2,3) COMP.
C      STATEV(11) = FP(3,1) -- PLASTIC DEFORMATION GRADIENT, (3,1) COMP.
C      STATEV(12) = FP(3,2) -- PLASTIC DEFORMATION GRADIENT, (3,2) COMP.
C      STATEV(13) = FP(3,3) -- PLASTIC DEFORMATION GRADIENT, (3,3) COMP.
C
C      STATEV(14) = S_STRESS(1,1)
C      STATEV(15) = S_STRESS(2,2)
C      STATEV(16) = S_STRESS(3,3)
C      STATEV(17) = S_STRESS(2,3)
C      STATEV(18) = S_STRESS(1,3)
```

```
C      STATEV(19) = S_STRESS(1,2)
C
C      STATEV(20) = IPHASE
C      STATEV(21) = PWRINC
C
C*****************************************************************

        SUBROUTINE VUMAT (
C       Read only (unmodifiable) variables :-
     +                    NBLOCK, NDIR, NSHR, NSTATEV, NFIELDV,
     +                    NPROPS, LANNEAL, STEP_TIME, TOTAL_TIME,
     +                    DT, CMNAME, COORD_MP, CHAR_LENGTH, PROPS,
     +                    DENSITY, STRAIN_INC, REL_SPIN_INC,
     +                    TEMP_OLD, STRETCH_OLD, DEFGRAD_OLD,
     +                    FIELD_OLD, STRESS_OLD, STATE_OLD,
     +                    ENER_INTERN_OLD, ENER_INELAS_OLD, TEMP_NEW,
     +                    STRETCH_NEW, DEFGRAD_NEW, FIELD_NEW,
C       Read and write (modifiable) variables :-
     +                    STRESS_NEW, STATE_NEW, ENER_INTERN_NEW,
     +                    ENER_INELAS_NEW)

        INCLUDE 'VABA_PARAM.INC'
C
C             ALL ARRAYS DIMENSIONED BY (*) ARE NOT USED IN
C             THIS ALGORITHM
C
        DIMENSION COORD_MP(NBLOCK,*), CHAR_LENGTH(NBLOCK),
     +            PROPS(NPROPS), DENSITY(NBLOCK),
     +            STRAIN_INC(NBLOCK,NDIR+NSHR),
     +            REL_SPIN_INC(NBLOCK,NSHR), TEMP_OLD(NBLOCK),
     +            STRETCH_OLD(NBLOCK,NDIR+NSHR),
     +            DEFGRAD_OLD(NBLOCK,NDIR+NSHR+NSHR),
     +            FIELD_OLD(NBLOCK,NFIELDV),
     +            STRESS_OLD(NBLOCK,NDIR+NSHR),
     +            STATE_OLD(NBLOCK,NSTATEV),
     +            ENER_INTERN_OLD(NBLOCK),
     +            ENER_INELAS_OLD(NBLOCK), TEMP_NEW(NBLOCK),
     +            STRETCH_NEW(NBLOCK,NDIR+NSHR),
     +            DEFGRAD_NEW(NBLOCK,NDIR+NSHR+NSHR),
     +            FIELD_NEW(NBLOCK,NFIELDV),
     +            STRESS_NEW(NBLOCK,NDIR+NSHR),
     +            STATE_NEW(NBLOCK,NSTATEV),
     +            ENER_INTERN_NEW(NBLOCK),
     +            ENER_INELAS_NEW(NBLOCK)

       CHARACTER*8 CMNAME

       CHARACTER*80  FILE1

       INTEGER  I, KM, IPHASE

       REAL*8 FT(3,3),FPT(3,3),RHOT,RHOTAU,DTIME,TOT_TIME,
     +         FTAU(3,3),FPTAU(3,3),
     +         ST,STAU, UTAU(3,3),UTAUINV(3,3), RTAU(3,3),
     +         RTAU_TRANS(3,3),TEMP1(3,3),
     +         STRESS_POWER, GBARPT, GBARPTAU,GBARDOTPT,
     +         GBARDOTPTAU,PWRINC,PWRINCT,
     +         STRESSTAU(3,3),ABASTRESS(3,3),
     +         CHIT,CHITAU,S_STRESST(3,3),S_STRESSTAU(3,3),
     +         THETAT,THETATAU

       REAL*8 EYOUNG,ANU,AMU,AKAPPA,ALAMBDA
       REAL*8 BV,ALPHA,V0,TAU0,Q,AKB,AM,RHO0,AK,THETA0
```

```
      COMMON/MATPEL/EYOUNG,ANU,AMU,AKAPPA,ALAMBDA
      COMMON/MATPRD1/BV,ALPHA,V0,TAU0,Q,AKB,AM,RHO0,AK
      COMMON/MATPRD2/GDOT0,DELF,H0,SO,SSAT,RHOCRIT0,THETA0,ALPHAT
      COMMON/TIMEINFO/TOT_TIME

      PARAMETER(ZERO=0.D0, ONE=1.D0, ONE_HALF=0.5D0, TWO=2.D0,
     +          ONE_THIRD=1.D0/3.D0, TWO_THIRD=2.D0/3.D0,
     +          THREE=3.D0,THREE_HALF=1.5D0,E_EULER=DEXP(1.D0),
     +           ROOT_THREE =DSQRT(3.D0), PI=4.0*DATAN(1.0D0)       )
C-----------------------------------------------------------------------
C                       INITIALIZATION
C-----------------------------------------------------------------------
      DTIME = DT
      TOT_TIME = TOTAL_TIME

      FILE1= '/u4/hsmoon/ANAND/short2.073/vumat_T/VUMAT_MSGS'
      OPEN(UNIT=80,FILE=FILE1,STATUS='UNKNOWN')

      EYOUNG  = PROPS(1)
      ANU     = PROPS(2)

      BV     = PROPS(3)
      ALPHA  = PROPS(4)
      V0     = PROPS(5)
      TAU0   = PROPS(6)
      Q       = PROPS(7)
      AKB    = PROPS(8)
      AM     = PROPS(9)
      RHO0    = PROPS(10)
      AK      = PROPS(11)
      GDOT0   = PROPS(12)
      DELF    = PROPS(13)
      H0      = PROPS(14)
      S0      = PROPS(15)
      SSAT    = PROPS(16)
      RHOCRIT0 = PROPS(17)
      THETA0   = PROPS(18)
      ALPHAT   = PROPS(19)

C-----------------------------------------------------------------------
C                       START COMUPTATION
C-----------------------------------------------------------------------
       DO 1000 KM = 1,NBLOCK

C
C      Copy the old and new Deformation gradients into FT and FTAU,
C      respectively, and the old and new stretches into UT and UTAU.
C

         FT(1,1) = DEFGRAD_OLD(KM,1)
         FT(2,2) = DEFGRAD_OLD(KM,2)
         FT(3,3) = DEFGRAD_OLD(KM,3)
         FT(1,2) = DEFGRAD_OLD(KM,4)

         FTAU(1,1) = DEFGRAD_NEW(KM,1)
         FTAU(2,2) = DEFGRAD_NEW(KM,2)
         FTAU(3,3) = DEFGRAD_NEW(KM,3)
         FTAU(1,2) = DEFGRAD_NEW(KM,4)

         UTAU(1,1) = STRETCH_NEW(KM,1)
         UTAU(2,2) = STRETCH_NEW(KM,2)
         UTAU(3,3) = STRETCH_NEW(KM,3)
```

```
            UTAU(1,2) = STRETCH_NEW(KM,4)

            IF (NSHR .EQ. 1) THEN
              FT(2,3) = 0.D0
              FT(3,1) = 0.D0
              FT(2,1) = DEFGRAD_OLD(KM,5)
              FT(3,2) = 0.D0
              FT(1,3) = 0.D0

              FTAU(2,3) = 0.D0
              FTAU(3,1) = 0.D0
              FTAU(2,1) = DEFGRAD_NEW(KM,5)
              FTAU(3,2) = 0.D0
              FTAU(1,3) = 0.D0

              UTAU(2,3) = 0.D0
              UTAU(3,1) = 0.D0
              UTAU(2,1) = UTAU(1,2)
              UTAU(3,2) = 0.D0
              UTAU(1,3) = 0.D0
            ELSE
              FT(2,3) = DEFGRAD_OLD(KM,5)
              FT(3,1) = DEFGRAD_OLD(KM,6)
              FT(2,1) = DEFGRAD_OLD(KM,7)
              FT(3,2) = DEFGRAD_OLD(KM,8)
              FT(1,3) = DEFGRAD_OLD(KM,9)

              FTAU(2,3) = DEFGRAD_NEW(KM,5)
              FTAU(3,1) = DEFGRAD_NEW(KM,6)
              FTAU(2,1) = DEFGRAD_NEW(KM,7)
              FTAU(3,2) = DEFGRAD_NEW(KM,8)
              FTAU(1,3) = DEFGRAD_NEW(KM,9)

              UTAU(2,3) = STRETCH_NEW(KM,5)
              UTAU(3,1) = STRETCH_NEW(KM,6)
              UTAU(2,1) = UTAU(1,2)
              UTAU(3,2) = UTAU(2,3)
              UTAU(1,3) = UTAU(3,1)
            ENDIF

C
C       AT THE START OF AN ABAQUS CALCULATION THE STATE
C       VARIABLES ARE PASSED INTO VUMAT WITH ZERO VALUES.
C       INITIALIZE THE STATE VARIABLES.
C       AT THIS POINT,
C       THE TIME TOTAL_TIME AND STEP_TIME BOTH HAVE A VALUE
C       EQUAL TO 0.0. AND DT IS EQUAL TO 1.D0
C

      IF (TOTAL_TIME .EQ. 0.0D0 .OR. STEP_TIME .EQ. 0.0D0) THEN

            STATE_OLD(KM,1)  = RHO0
            STATE_OLD(KM,2)  = 0.D0
            STATE_OLD(KM,3)  = 0.D0
            STATE_OLD(KM,4)  = S0

            STATE_OLD(KM,5)  = 1.D0
            STATE_OLD(KM,6)  = 0.D0
            STATE_OLD(KM,7)  = 0.D0
            STATE_OLD(KM,8)  = 0.D0
            STATE_OLD(KM,9)  = 1.D0
            STATE_OLD(KM,10)  = 0.D0
            STATE_OLD(KM,11) = 0.D0
```

```
            STATE_OLD(KM,12) = 0.D0
            STATE_OLD(KM,13) = 1.D0

            STATE_OLD(KM,14)  = 0.D0
            STATE_OLD(KM,15)  = 0.D0
            STATE_OLD(KM,16)  = 0.D0
            STATE_OLD(KM,17)  = 0.D0
            STATE_OLD(KM,18)  = 0.D0
            STATE_OLD(KM,19)  = 0.D0

            STATE_OLD(KM,20) = 1
            STATE_OLD(KM,21) = 0.D0

          ENDIF

C
C         STORE THE VALUE OF THE DEFORMATION RESISTANCE AT
C         THE BEGINNING OF THE TIME STEP IN ST
C
          RHOT       = STATE_OLD(KM,1)
          GBARDOTPT  = STATE_OLD(KM,2)
          GBARPT     = STATE_OLD(KM,3)
          ST         = STATE_OLD(KM,4)

C
C         STORE THE COMPONENTS OF THE PLASTIC DEFORMATION
C         GRADIENT AT THE BEGINNING OF THE TIME STEP IN ARRAY FPT
C
          FPT(1,1) = STATE_OLD(KM,5)
          FPT(1,2) = STATE_OLD(KM,6)
          FPT(1,3) = STATE_OLD(KM,7)
          FPT(2,1) = STATE_OLD(KM,8)
          FPT(2,2) = STATE_OLD(KM,9)
          FPT(2,3) = STATE_OLD(KM,10)
          FPT(3,1) = STATE_OLD(KM,11)
          FPT(3,2) = STATE_OLD(KM,12)
          FPT(3,3) = STATE_OLD(KM,13)

          S_STRESST(1,1) = STATE_OLD(KM,14)
          S_STRESST(2,2) = STATE_OLD(KM,15)
          S_STRESST(3,3) = STATE_OLD(KM,16)
          S_STRESST(2,3) = STATE_OLD(KM,17)
          S_STRESST(1,3) = STATE_OLD(KM,18)
          S_STRESST(1,2) = STATE_OLD(KM,19)
          S_STRESST(3,2) = S_STRESST(2,3)
          S_STRESST(3,1) = S_STRESST(1,3)
          S_STRESST(2,1) = S_STRESST(1,2)

          IPHASE  = STATE_OLD(KM,20)
          PWRINCT = STATE_OLD(KM,21)

          THETAT = TEMP_OLD(KM)
          THETATAU = TEMP_NEW(KM)

C
C         CALCULATE THE  LAME MODULI
C

          AMU     = EYOUNG/(2.D0*(1.D0 + ANU))
          AKAPPA  = EYOUNG/(3.D0*(1.D0 - 2.D0*ANU))
          ALAMBDA = AKAPPA - TWO_THIRD*AMU

C-----------------------------------------------------------------------
```

```
C               TIME INTEGRATION PROCEDURE FOLLOWS
C-----------------------------------------------------------------------
        CALL     KINTEG(FT,FPT,S_STRESST,RHOT,GBARPT,GBARDOTPT,
     +             ST,DTIME,FTAU,FPTAU,S_STRESSTAU,STRESSTAU,RHOTAU,
     +             GBARDOTPTAU,GBARPTAU,STAU,IPHASE,PWRINCT,THETAT,
     +             THETATAU)
C
C       Update the state variables
C

      IF (DTIME .NE. ONE) THEN

         STATE_NEW(KM,1)  = RHOTAU
         STATE_NEW(KM,2)  = GBARDOTPTAU
         STATE_NEW(KM,3)  = GBARPTAU
         STATE_NEW(KM,4)  = STAU
         STATE_NEW(KM,5)  = FPTAU(1,1)
         STATE_NEW(KM,6)  = FPTAU(1,2)
         STATE_NEW(KM,7)  = FPTAU(1,3)
         STATE_NEW(KM,8)  = FPTAU(2,1)
         STATE_NEW(KM,9)  = FPTAU(2,2)
         STATE_NEW(KM,10)  = FPTAU(2,3)
         STATE_NEW(KM,11) = FPTAU(3,1)
         STATE_NEW(KM,12) = FPTAU(3,2)
         STATE_NEW(KM,13) = FPTAU(3,3)
         STATE_NEW(KM,14)  = S_STRESSTAU(1,1)
         STATE_NEW(KM,15)  = S_STRESSTAU(2,2)
         STATE_NEW(KM,16)  = S_STRESSTAU(3,3)
         STATE_NEW(KM,17)  = S_STRESSTAU(2,3)
         STATE_NEW(KM,18)  = S_STRESSTAU(1,3)
         STATE_NEW(KM,19)  = S_STRESSTAU(1,2)
         STATE_NEW(KM,20) = IPHASE
         STATE_NEW(KM,21) = PWRINCT

       ENDIF
C
C       UPDATE THE STRESS-MEASURE, ABASTRESS=( (R^T) T R)
C       USED BY ABAQUS/EXPLICIT
C
         CALL KMINV(UTAU,UTAUINV,DET_UTAUINV)
         CALL KMPROD(FTAU,UTAUINV,RTAU)
         CALL KMTRANS(RTAU,RTAU_TRANS)
         CALL KMPROD(RTAU_TRANS,STRESSTAU,TEMP1)
         CALL KMPROD(TEMP1,RTAU,ABASTRESS)

        DO 200 I = 1,NDIR
            STRESS_NEW(KM,I) = ABASTRESS(I,I)
200     CONTINUE

        IF (NSHR .NE. 0) THEN
            STRESS_NEW(KM,NDIR+1) = ABASTRESS(1,2)
            IF (NSHR .NE. 1) THEN
              STRESS_NEW(KM,NDIR+2) = ABASTRESS(2,3)
              IF (NSHR .NE. 2) THEN
                STRESS_NEW(KM,NDIR+3) = ABASTRESS(1,3)
              ENDIF
            ENDIF
        ENDIF

250     CONTINUE

C
C       Update the specific internal energy
```

```
C
           STRESS_POWER = 0.D0
           DO 300 I = 1,NDIR
             STRESS_POWER = STRESS_POWER +
     +       0.5*((STRESS_OLD(KM,I)+STRESS_NEW(KM,I))*
     +            STRAIN_INC(KM,I))
300        CONTINUE
           IF (NSHR .NE. 0) THEN
             STRESS_POWER = STRESS_POWER +
     +       0.5*((STRESS_OLD(KM,NDIR+1)+STRESS_NEW(KM,NDIR+1))*
     +            STRAIN_INC(KM,NDIR+1))
             IF (NSHR .NE. 1) THEN
               STRESS_POWER = STRESS_POWER +
     +        0.5*((STRESS_OLD(KM,NDIR+2)+STRESS_NEW(KM,NDIR+2))*
     +             STRAIN_INC(KM,NDIR+2))
               IF (NSHR .NE. 2) THEN
                 STRESS_POWER = STRESS_POWER +
     +           0.5*((STRESS_OLD(KM,NDIR+3)+STRESS_NEW(KM,NDIR+3))*
     +                STRAIN_INC(KM,NDIR+3))
               ENDIF
             ENDIF
           ENDIF

           ENER_INTERN_NEW(KM) = ENER_INTERN_OLD(KM) +
     +                           STRESS_POWER/DENSITY(KM)


          ENER_INELAS_NEW(KM) = ENER_INELAS_OLD(KM) +
     +                           PWRINCT/DENSITY(KM)

1000   CONTINUE

       RETURN
       END

C**********************************************************************
       SUBROUTINE KINTEG(FT,FPT,S_STRESST,RHOT,GBARPT,GBARDOTPT,
     +              ST,DTIME,FTAU,FPTAU,S_STRESSTAU,STRESSTAU,RHOTAU,
     +              GBARDOTPTAU,GBARPTAU,STAU,IPHASE,PWRINCT,THETAT,
     +              THETATAU)

C      THIS SUBROUTINE UPDATES THE STATE VARIABLES FOR A GIVEN TIME
C      INCREMENT.
C
C**********************************************************************

       IMPLICIT REAL*8 (A-H,O-Z)

       COMMON/MATPEL/EYOUNG,ANU,AMU,AKAPPA,ALAMBDA
       COMMON/MATPRD1/BV,ALPHA,V0,TAU0,Q,AKB,AM,RHO0,AK
       COMMON/MATPRD2/GDOT0,DELF,H0,SO,SSAT,RHOCRIT0,THETA0,ALPHAT
       COMMON/TIMEINFO/TOT_TIME

       PARAMETER(ZERO=0.D0, ONE=1.D0, ONE_HALF=0.5D0, TWO=2.D0,
     +          ONE_THIRD=1.D0/3.D0, TWO_THIRD=2.D0/3.D0,
     +          THREE=3.D0,THREE_HALF=1.5D0,E_EULER=DEXP(1.D0),
     +           ROOT_THREE =DSQRT(3.D0), PI=4.0*DATAN(1.0D0)       )

       REAL*8 FT(3,3),FPT(3,3), S_STRESST(3,3),FTAU(3,3),FPTAU(3,3),
     +       S_STRESSTAU(3,3),STRESSTAU(3,3),
     +       FPTINV(3,3),FETAU(3,3),RETAU(3,3),RETAUT(3,3),EETAU(3,3),
     +       FPTT(3,3),BPT(3,3),DEV_BPT(3,3),SIGMAT(3,3),DPT(3,3),
     +       FPTAUINV(3,3),DEV_EETAU(3,3),DEV_SSTRESST(3,3),
```

```
     +      AIDEN(3,3),FTEMP(3,3),TEMP1(3,3),TEMP2(3,3)

       REAL*8  NPLAS(3,3)

C
C             INITIALIZE
C
       CALL KZEROM(STRESSTAU)
       CALL KZEROM(S_STRESSTAU)
       CALL KONEM(FPTAU)
       CALL KONEM(AIDEN)
       CALL KZEROM(FTEMP)

       RHOTAU       = RHOT
       GBARDOTPTAU  = ZERO
       GBARPTAU     = GBARPT
       STAU         = ST
       PWRINCT      = ZERO

C%%%%%%%%%%%%%%%%%%%%%%%%%%%%%%%%%%%%%%%%%%%%%%%%%%%%%%%%%%%%%%%%%%%%%%%%%%%
C          FOR THE INITIAL DUMMY STEP
C          RETURN WITH APPROPRIATE VALUES
C          CORRESPONDING TO NO PLASTIC DEFORMATION
C

       IF (DTIME .EQ. ONE) THEN
C
C         CALCULATE THE  ELASTIC DEFORMATION GRADIENT
C
         CALL KMINV(FPT,FPTINV,DET_FPTINV)
         CALL KMPROD(FTAU,FPTINV,FETAU)

C
C         PERFORM THE POLAR DECOMPOSITION
C         FOR THE  ELASTIC DEFORMATION GRADIENT,
C         AND CALCULATE THE  LOGARITHMIC ELASTIC STRAIN
C         TOGETHER WITH OTHER KINEMATICAL QUANTITIES
C
         CALL KSKINEM(FETAU,DETFETAU,RETAU,EETAU)

C
C         CALCULATE THE  STRESS  S_STRESS AT TIME TAU
C
           DO 10 I = 1,3
           DO 10 J = 1,3
             S_STRESSTAU(I,J) = 2.0D0*AMU*EETAU(I,J)
     +        +ALAMBDA*(EETAU(1,1)+EETAU(2,2)+EETAU(3,3))*AIDEN(I,J)
     +        -3.D0*AKAPPA*ALPHAT*(THETAT-THETA0)*AIDEN(I,J)
10         CONTINUE

           CALL KMTRANS(RETAU,RETAUT)
           DO 20 I = 1,3
           DO 20 J = 1,3
             TEMP1(I,J) = S_STRESSTAU(I,J)/DETFETAU
20         CONTINUE
           CALL KMPROD(TEMP1,RETAUT,TEMP2)
           CALL KMPROD(RETAU,TEMP2,STRESSTAU)

            CALL KONEM(FPTAU)
            RHOTAU      = RHOT
            GBARDOTPTAU = ZERO
            GBARPTAU  = ZERO
            STAU      = ST
```

```
            IPHASE    = 1
            PWRINCT   = ZERO
           GO TO 999
         ENDIF
C%%%%%%%%%%%%%%%%%%%%%%%%%%%%%%%%%%%%%%%%%%%%%%%%%%%%%%%%%%%%%%%%%%%%%%%%%%%%%%%%
         CALL KDEVM(S_STRESST,DEV_SSTRESST)
         CALL KDOTPM(DEV_SSTRESST,DEV_SSTRESST,TEMP3)
         TAUBART = SQRT(0.5D0*TEMP3)

         IF (TAUBART .LT. TAU0*1.D-15) THEN
           TAUBART = TAU0*1.D-15
         ENDIF

C
C
C

            DO 110 I=1,3
            DO 110 J=1,3
              DPT(I,J) = GBARDOTPT* DEV_SSTRESST(I,J)/2.0D0/TAUBART
110         CONTINUE

C
C        CALCULATE  F^P AT TIME TAU AND ITS INVERSE
C

            DO 120 I=1,3
            DO 120 J=1,3
               FTEMP(I,J) = AIDEN(I,J) + DTIME*DPT(I,J)
120         CONTINUE
            CALL KMPROD(FTEMP,FPT,FPTAU)
C
C             NORMALIZE FPTAU SO THAT ITS DET IS ONE

            CALL KMDET(FPTAU,DET_FPTAU)

            VAL = ONE/(DET_FPTAU**ONE_THIRD)

            DO 130 I=1,3
            DO 130 J=1,3
                FPTAU(I,J) = FPTAU(I,J)*VAL
130         CONTINUE

            CALL KMINV(FPTAU,FPTAUINV,DET_FPTAUINV)

C
C        CALCULATE  F^E AND ASSOCIATED KINEMATICAL
C                QUANTITIES  AT TIME TAU
C
         CALL KMPROD(FTAU,FPTAUINV,FETAU)
        CALL KSKINEM(FETAU,DETFETAU,RETAU,EETAU)

C
C        CALCULATE  S_STRESS AT TIME TAU
C

C
C         CALCULATE TRACE_EETAU AND DEV_EETAU
C
        TRACE_EETAU = (EETAU(1,1)+EETAU(2,2)+EETAU(3,3))
        DO 140 I=1,3
        DO 140 J=1,3
```

```
          DEV_EETAU(I,J)= EETAU(I,J)-ONE_THIRD*TRACE_EETAU*AIDEN(I,J)
140      CONTINUE

C
C       CALCULATE THE MEAN NORMAL PRESSURE
C       CORESSPONDING TO THE S_STRESS AT TIME TAU
C


          PRESSTAU = - AKAPPA*TRACE_EETAU
C
C       CALCULATE THE  S_STRESS AT TIME TAU
C

          DO 150 I=1,3
          DO 150 J=1,3
            S_STRESSTAU(I,J)=2.0D0*AMU*DEV_EETAU(I,J)-PRESSTAU*AIDEN(I,J)
     +        -3.D0*AKAPPA*ALPHAT*(THETAT-THETA0)*AIDEN(I,J)
150       CONTINUE

C
C       CALCULATE THE CAUCHY  STRESS AT TIME TAU
C
           CALL  KMTRANS(RETAU,TEMP1)
           CALL  KMPROD(S_STRESSTAU,TEMP1,TEMP2)
           CALL  KMPROD(RETAU,TEMP2,STRESSTAU)

            DO 160 I=1,3
            DO 160 J=1,3
             STRESSTAU(I,J)= STRESSTAU(I,J)/DETFETAU
160         CONTINUE

C
C      CALCULATE THE CRITICAL DISLOCATION DENSITY
C
        RHOCRIT = 2.0D7*208.2D0*1.0*(TAUBART/TAU0)**2.11D0
        IF (IPHASE .EQ. 2) THEN
           RHOCRIT = RHOCRIT0
        ELSEIF (RHOCRIT .LT. RHOCRIT0) THEN
           RHOCRIT = RHOCRIT0
        ENDIF

        IF (RHOT .LE. RHOCRIT) THEN
C
C     REGIME I
C
          TAUINTT = ALPHA*AMU*BV*RHOT**0.50D0
          TAUEFFT = DABS(TAUBART)-TAUINTT
          IF (TAUEFFT .GT. 0.D0) THEN

            IF (TAUBART .GE. 0.D0) THEN
               VBART = V0*DEXP(-Q/AKB/THETAT)*(TAUEFFT/TAU0)**(1.D0/AM)
            ELSE
               VBART = -V0*DEXP(-Q/AKB/THETAT)*(TAUEFFT/TAU0)**(1.D0/AM)
            ENDIF

            GBARDOTPT = RHOT*BV*VBART
            GBARDOTPTAU = GBARDOTPT
            RHOTAU = RHOT + DTIME*AK/BV*TAUEFFT*GBARDOTPT
            GBARPTAU = GBARPT + DTIME*GBARDOTPT
            STAU = ST

          ELSE
```

```
              VBART = 0.D0
              GBARDOTPT = 0.D0
             GBARDOTPTAU = 0.D0
              RHOTAU = RHOT
              GBARPTAU = GBARPT
              STAU = ST

           ENDIF

         ELSE
C
C     REGIME II
C

           IF (IPHASE .EQ. 1) THEN
            TAUINTT = ALPHA*AMU*BV*RHOT**0.50D0
            TAUEFFT = DABS(TAUBART)- TAUINTT

            IF (TAUBART .GE. 0.D0) THEN
              VBART = V0*DEXP(-Q/AKB/THETAT)*(TAUEFFT/TAU0)**(1.D0/AM)
            ELSE
              VBART = -V0*DEXP(-Q/AKB/THETAT)*(TAUEFFT/TAU0)**(1.D0/AM)
            ENDIF

            GBARDOTPT = RHOT*BV*VBART
            ST = TAUBART/(1.D0+DLOG(GBARDOTPT/GDOT0)*(AKB*THETAT/DELF))
            IPHASE = 2
           ENDIF

           TAU_CRIT = ST*(1.D0+DLOG(1.D3/GDOT0)*(AKB*THETAT/DELF))

           IF (TAUBART .GE. TAU_CRIT) TAUBART = TAU_CRIT

           RHOTAU = RHOT
           GBARDOTPT = GDOT0*DEXP(-DELF/AKB/THETAT*(1.D0-TAUBART/ST))
           GBARDOTPTAU = GBARDOTPT
           GBARPTAU = GBARPT + DTIME*GBARDOTPT
           SDOTT = H0*(1.D0-ST/SSAT)*GBARDOTPT
           STAU = ST + DTIME*SDOTT

         ENDIF

         CALL KDOTPM(S_STRESST,DPT,PWRINCT)


C%%%%%%%%%%%%%%%%%%%%%%%%%%%%%%%%%%%%%%%%%%%%%%%%%%%%%%%%%%%%%%%%%%%%%%%%%%%%%%%

999    CONTINUE

       RETURN
       END
C ***********************************************************************
C***********************************************************************
C      THE NEXT SUBROUTINE CALCULATES VARIOUS KINEMATICAL QUANTITIES
C      ASSOCIATED WITH THE DEFORMATION GRADIENT
C***********************************************************************
       SUBROUTINE KSKINEM(F,DETF,R,E)

C      THIS SUBROUTINE PERFORMS THE RIGHT POLAR DECOMPOSITION
C      [F] = [R][U] OF THE DEFORMATION GRADIENT [F] INTO
C      A ROTATION [R] AND THE RIGHT  STRETCH TENSOR [U].
C      THE EIGENVALUES AND EIGENVECTORS OF [U] AND
```

```
C      THE LOGARITHMIC STRAIN [E] = LN [U]
C      ARE ALSO RETURNED.
C***********************************************************************

       IMPLICIT REAL*8 (A-H,O-Z)
       DIMENSION F(3,3),FTRANS(3,3), C(3,3), OMEGA(3),
     +           UEIGVAL(3),EIGVEC(3,3), EIGVECT(3,3),
     +            U(3,3),E(3,3),UINV(3,3),R(3,3),TEMPM(3,3)

C      F(3,3) -- THE DEFORMATION GRADIENT MATRIX WHOSE
C                POLAR DECOMPOSITION IS DESIRED.
C      DETF   -- THE DETRMINANT OF [F]; DETF > 0.
C      FTRANS(3,3)   -- THE TRANSPOSE OF [F].
C      R(3,3) -- THE ROTATION MATRIX; [R]^T [R] = [I];
C                OUTPUT.
C      U(3,3) -- THE RIGHT STRETCH TENSOR; SYMMETRIC
C                AND POSITIVE DEFINITE; OUTPUT.
C      UINV(3,3)     -- THE INVERSE OF [U].
C      C(3,3) -- THE RIGHT CAUCHY-GREEN TENSOR = [U][U];
C                SYMMETRIC AND POSITIVE DEFINITE.
C      OMEGA(3)-- THE SQUARES OF THE PRINCIPAL STRETCHES.
C      UEIGVAL(3)    -- THE PRINCIPAL STRETCHES; OUTPUT.
C      EIGVEC(3,3)   -- MATRIX OF EIGENVECTORS OF [U];OUTPUT.
C      EIGVECT(3,3)     -- TRANSPOSE OF THE ABOVE.
C      E(3,3) -- THE LOGARITHMIC STRAIN TENSOR, [E]=LN[U];
C                OUTPUT.
C***********************************************************************

C      STORE THE IDENTITY MATRIX IN  [R], [U], AND [UINV]

       CALL KONEM(R)
       CALL KONEM(U)
       CALL KONEM(UINV)

C      STORE THE ZERO MATRIX IN [E]

       CALL KZEROM(E)

C             CHECK IF THE DETERMINANT OF [F] IS GREATER THAN ZERO.
C      IF NOT, THEN PRINT DIAGNOSTIC AND STOP.

        CALL KMDET(F,DETF)
        IF (DETF .LE. 0.D0) THEN
          WRITE(80,100)
          STOP
        ENDIF

C             CALCULATE THE RIGHT CAUCHY GREEN STRAIN TENSOR [C]

        CALL  KMTRANS(F,FTRANS)
        CALL  KMPROD(FTRANS,F,C)

C      CALCULATE THE EIGENVALUES AND EIGENVECTORS OF  [C]

       CALL KSPECTRAL(C,OMEGA,EIGVEC)

C      CALCULATE THE PRINCIPAL VALUES OF [U] AND [E]

       UEIGVAL(1) = DSQRT(OMEGA(1))
       UEIGVAL(2) = DSQRT(OMEGA(2))
       UEIGVAL(3) = DSQRT(OMEGA(3))

       U(1,1) = UEIGVAL(1)
```

```
       U(2,2) = UEIGVAL(2)
       U(3,3) = UEIGVAL(3)

       E(1,1) = DLOG( UEIGVAL(1) )
       E(2,2) = DLOG( UEIGVAL(2) )
       E(3,3) = DLOG( UEIGVAL(3) )

C      CALCULATE THE COMPLETE TENSORS [U] AND [E]

       CALL KMTRANS(EIGVEC,EIGVECT)
       CALL KMPROD(EIGVEC,U,TEMPM)
       CALL KMPROD(TEMPM,EIGVECT,U)
       CALL KMPROD(EIGVEC,E,TEMPM)
       CALL KMPROD(TEMPM,EIGVECT,E)

C      CALCULATE [UINV]

       CALL KM3INV(U,UINV)

C      CALCULATE [R]

       CALL KMPROD(F,UINV,R)
100     FORMAT(5X,'--ERROR IN KINEMATICS-- THE DETERMINANT OF [F]',
     +         ' IS NOT GREATER THAN 0')

       RETURN
       END
C*********************************************************************
C      THE FOLLOWING SUBROUTINES CALCULATE THE SPECTRAL
C      DECOMPOSITION OF A SYMMETRIC THREE BY THREE MATRIX
C*********************************************************************
       SUBROUTINE KSPECTRAL(A,D,V)
C
C      THIS SUBROUTINE CALCULATES THE EIGENVALUES AND EIGENVECTORS OF
C      A SYMMETRIC 3 BY 3 MATRIX [A].
C
C      THE OUTPUT CONSISTS OF A VECTOR D CONTAINING THE THREE
C      EIGENVALUES IN ASCENDING ORDER, AND
C      A MATRIX [V] WHOSE COLUMNS CONTAIN THE CORRESPONDING
C      EIGENVECTORS.
C*********************************************************************

       IMPLICIT REAL*8 (A-H,O-Z)
       PARAMETER(NP=3)
       DIMENSION D(NP),V(NP,NP)
       DIMENSION A(3,3),E(NP,NP)

       DO 2 I = 1,3
          DO 1 J= 1,3
            E(I,J) = A(I,J)
1         CONTINUE
2      CONTINUE

       CALL KJACOBI(E,3,NP,D,V,NROT)
       CALL KEIGSRT(D,V,3,NP)

       RETURN
       END

C*********************************************************************
       SUBROUTINE KJACOBI(A,N,NP,D,V,NROT)

C      COMPUTES ALL EIGENVALUES AND EIGENVECTORS OF A REAL SYMMETRIC
```

```
C      MATRIX [A], WHICH IS OF SIZE N BY N, STORED IN A PHYSICAL
C      NP BY BP ARRAY. ON OUTPUT, ELEMENTS OF [A] ABOVE THE DIAGONAL
C      ARE DESTROYED, BUT THE DIAGONAL AND SUB-DIAGONAL ARE UNCHANGED
C      AND GIVE FULL INFORMATION ABOUT THE ORIGINAL SYMMETRIC MATRIX.
C      VECTOR D RETURNS THE EIGENVALUES OF [A] IN ITS FIRST N ELEMENTS.
C      [V] IS A MATRIX WITH THE SAME LOGICAL AND PHYSICAL DIMENSIONS AS
C      [A] WHOSE COLUMNS CONTAIN, ON OUTPUT, THE NORMALIZED
C      EIGENVECTORSOF [A]. NROT RETURNS THE NUMBER OF JACOBI ROTATIONS
C      WHICH WERE REQUIRED.

C      THIS SUBROUTINE IS TAKEN FROM "NUMERICAL RECIPES", PAGE 346.
C*********************************************************************

       IMPLICIT REAL*8 (A-H,O-Z)
       PARAMETER (NMAX =100)
       DIMENSION A(NP,NP),D(NP),V(NP,NP),B(NMAX),Z(NMAX)

C      INITIALIZE [V] TO THE IDENTITY MATRIX

       DO 12 IP = 1,N
         DO 11 IQ = 1,N
           V(IP,IQ) = 0.D0
11         CONTINUE
           V(IP,IP) = 1.D0
12     CONTINUE

C      INITIALIZE [B] AND [D] TO THE DIAGONAL OF [A], AND Z TO ZERO.
C      THE VECTOR Z WILL ACCUMULATE TERMS OF THE FORM T*A_PQ AS
C      IN EQUATION (11.1.14)

       DO 13 IP = 1,N
         B(IP) = A(IP,IP)
         D(IP) = B(IP)
         Z(IP) = 0.D0
13     CONTINUE
C
       NROT = 0
       DO 24 I = 1,50

C      SUM OFF-DIAGONAL ELEMENTS

           SM = 0.D0
           DO 15 IP = 1, N-1
             DO 14 IQ = IP + 1, N
              SM = SM + DABS ( A(IP,IQ ))
14           CONTINUE
15         CONTINUE

C      IF SUM = 0., THEN RETURN. THIS IS THE NORMAL RETURN
C      WHICH RELIES ON QUADRATIC CONVERGENCE TO MACHINE
C      UNDERFLOW.

           IF ( SM .EQ. 0.D0) RETURN
C
C        IF ( SM .LT. 1.0D-15) RETURN

C      IN THE FIRST THREE SWEEPS CARRY OUT THE PQ ROTATION ONLY IF
C      |A_PQ| > TRESH, WHERE TRESH IS SOME THRESHOLD VALUE,
C      SEE EQUATION (11.1.25). THEREAFTER TRESH = 0.

           IF ( I .LT. 4) THEN
             TRESH = 0.2D0*SM/N**2
           ELSE
```

```
            TRESH = 0.D0
          ENDIF
C
          DO 22 IP = 1, N-1
            DO 21 IQ = IP+1,N
              G = 100.D0*DABS(A(IP,IQ))

C      AFTER FOUR SWEEPS, SKIP THE ROTATION IF THE
C      OFF-DIAGONAL ELEMENT IS SMALL.

             IF ((I .GT. 4) .AND. (DABS(D(IP))+G .EQ. DABS(D(IP)))
     +            .AND. ( DABS(D(IQ))+G .EQ. DABS(D(IQ)))) THEN
               A(IP,IQ) = 0.D0
             ELSE IF ( DABS(A(IP,IQ)) .GT. TRESH) THEN
               H = D(IQ) - D(IP)
               IF (DABS(H)+G .EQ. DABS(H)) THEN

C      T = 1./(2.*THETA), EQUATION(11.1.10)

                 T =A(IP,IQ)/H
               ELSE
                 THETA = 0.5D0*H/A(IP,IQ)
                 T =1.D0/(DABS(THETA)+DSQRT(1.D0+THETA**2))
                 IF (THETA .LT. 0.D0) T = -T
               ENDIF
               C = 1.D0/DSQRT(1.D0 + T**2)
               S = T*C
               TAU = S/(1.D0 + C)
               H = T*A(IP,IQ)
               Z(IP) = Z(IP) - H
               Z(IQ) = Z(IQ) + H
               D(IP) = D(IP) - H
               D(IQ) = D(IQ) + H
               A(IP,IQ) = 0.D0

C      CASE OF ROTATIONS 1 <= J < P

               DO 16 J = 1, IP-1
                 G = A(J,IP)
                 H = A(J,IQ)
                 A(J,IP) = G - S*(H + G*TAU)
                 A(J,IQ) = H + S*(G - H*TAU)
16             CONTINUE

C      CASE OF ROTATIONS P < J < Q

               DO 17 J = IP+1, IQ-1
                 G = A(IP,J)
                 H = A(J,IQ)
                 A(IP,J) = G - S*(H + G*TAU)
                 A(J,IQ) = H + S*(G - H*TAU)
17             CONTINUE

C      CASE OF ROTATIONS Q < J <= N

               DO 18 J = IQ+1, N
                  G = A(IP,J)
                 H = A(IQ,J)
                 A(IP,J) = G - S*(H + G*TAU)
                 A(IQ,J) = H + S*(G - H*TAU)
18             CONTINUE
               DO 19 J = 1,N
                 G = V(J,IP)
```

```
                H = V(J,IQ)
                V(J,IP) = G - S*(H + G*TAU)
                V(J,IQ) = H + S*(G - H*TAU)
19             CONTINUE
               NROT = NROT + 1
              ENDIF
21          CONTINUE
22        CONTINUE

C       UPDATE D WITH THE SUM OF T*A_PQ, AND REINITIALIZE Z

          DO 23 IP = 1, N
            B(IP) = B(IP) + Z(IP)
            D(IP) = B(IP)
            Z(IP) = 0.D0
23        CONTINUE
24      CONTINUE

C       IF THE ALGORITHM HAS REACHED THIS STAGE, THEN
C       THERE ARE TOO MANY SWEEPS, PRINT A DIAGNOSTIC
C       AND STOP.

        WRITE (80,'(/1X,A/)') '50 ITERS IN KJACOBI SHOULD NEVER HAPPEN'

        RETURN
        END

C*************************************************************************
        SUBROUTINE KEIGSRT(D,V,N,NP)

C       GIVEN THE EIGENVALUES [D] AND EIGENVECTORS [V] AS OUTPUT FROM
C       KJACOBI, THIS ROUTINE SORTS THE EIGENVALUES INTO ASCENDING ORDER,
C       AND REARRANGES THE COLUMNS OF [V] ACCORDINGLY.

C       THIS SUBROUTINE IS TAKEN FROM "NUMERICAL RECIPES", P. 348.
C*************************************************************************

        IMPLICIT REAL*8 (A-H,O-Z)
        DIMENSION D(NP),V(NP,NP)

        DO 13 I = 1,N-1
          K = I
          P = D(I)
          DO 11 J = I+1,N
            IF (D(J) .GE. P) THEN
              K = J
              P = D(J)
            END IF
11        CONTINUE
          IF (K .NE. I) THEN
            D(K) = D(I)
            D(I) = P
            DO 12 J = 1,N
              P = V(J,I)
              V(J,I) = V(J,K)
              V(J,K) = P
12          CONTINUE
          ENDIF
13      CONTINUE

        RETURN
        END
```

```
C*********************************************************************
C      THE FOLLOWING SUBROUTINES ARE UTILITY ROUTINES
C*********************************************************************
       SUBROUTINE KZEROV(V,SIZE)

C      THIS SUBROUTINE STORES THE ZERO VECTOR IN A VECTOR V
C      OF SIZE SIZE.
C*********************************************************************

       INTEGER SIZE
       REAL*8 V(0:SIZE-1)

       DO 1 I=0,SIZE
         V(I) = 0.D0
1      CONTINUE

       RETURN
       END

C*********************************************************************
       SUBROUTINE KZEROM(A)
C
C      THIS SUBROUTINE SETS ALL ENTRIES OF A 3 BY 3 MATRIX TO 0.D0.
C*********************************************************************

        REAL*8 A(3,3)

       DO 1 I=1,3
         DO 1 J=1,3
           A(I,J) = 0.D0
1      CONTINUE
C
       RETURN
       END

C*********************************************************************
       SUBROUTINE KONEM(A)

C      THIS SUBROUTINE STORES THE IDENTITY MATRIX IN THE
C      3 BY 3 MATRIX [A]
C*********************************************************************

        REAL*8 A(3,3)
        DATA ZERO/0.D0/
        DATA ONE/1.D0/

       DO 1 I=1,3
         DO 1 J=1,3
           IF (I .EQ. J) THEN
              A(I,J) = 1.0
            ELSE
              A(I,J) = 0.0
            ENDIF
1       CONTINUE

       RETURN
       END

C*********************************************************************
       SUBROUTINE KMTRANS(A,ATRANS)

C      THIS SUBROUTINE CALCULATES THE TRANSPOSE OF AN 3 BY 3
C      MATRIX [A], AND PLACES THE RESULT IN ATRANS.
```

```
C*********************************************************************

       REAL*8 A(3,3),ATRANS(3,3)

       DO 1 I=1,3
         DO 1 J=1,3
           ATRANS(J,I) = A(I,J)
1      CONTINUE

       RETURN
       END

C*********************************************************************
       SUBROUTINE KMPROD(A,B,C)

C      THIS SUBROUTINE MULTIPLIES TWO 3 BY 3 MATRICES [A] AND [B],
C      AND PLACE THEIR PRODUCT IN MATRIX [C].
C*********************************************************************

       REAL*8 A(3,3),B(3,3),C(3,3)

       DO 2 I = 1, 3
         DO 2 J = 1, 3
           C(I,J) = 0.D0
           DO 1 K = 1, 3
             C(I,J) = C(I,J) + A(I,K) * B(K,J)
1          CONTINUE
2      CONTINUE
C
       RETURN
       END

C*********************************************************************
       SUBROUTINE KMPROD4(A,B,C)

C      THIS SUBROUTINE MULTIPLIES TWO 3 BY 3 MATRICES [A] AND [B],
C      AND PLACE THEIR PRODUCT IN MATRIX [C].
C*********************************************************************

       REAL*8 A(4,4),B(4,4),C(4,4)

       DO 2 I = 1, 4
         DO 2 J = 1, 4
           C(I,J) = 0.D0
           DO 1 K = 1, 4
             C(I,J) = C(I,J) + A(I,K) * B(K,J)
1          CONTINUE
2      CONTINUE

       RETURN
       END

C*********************************************************************
       SUBROUTINE KDOTPM(A,B,C)

C      THIS SUBROUTINE CALCULATES THE SCALAR PRODUCT OF TWO
C      3 BY 3 MATRICES [A] AND [B] AND STORES THE RESULT IN THE
C      SCALAR C.
C*********************************************************************

       REAL*8 A(3,3),B(3,3),C

       C = 0.D0
```

```
      DO 1 I = 1,3
        DO 1 J = 1,3
           C = C + A(I,J)*B(I,J)
1     CONTINUE
C
      RETURN
      END

C*********************************************************************
      SUBROUTINE KMDET(A,DET)

C     THIS SUBROUTINE CALCULATES THE DETERMINANT
C     OF A 3 BY 3 MATRIX [A].
C*********************************************************************

      REAL*8  A(3,3), DET

      DET =    A(1,1)*A(2,2)*A(3,3)
     +         + A(1,2)*A(2,3)*A(3,1)
     +         + A(1,3)*A(2,1)*A(3,2)
     +        - A(3,1)*A(2,2)*A(1,3)
     +        - A(3,2)*A(2,3)*A(1,1)
     +        - A(3,3)*A(2,1)*A(1,2)

      RETURN
      END

C*********************************************************************
      SUBROUTINE KM3INV(A,AINV)

C     THIS SUBROUTINE CALCULATES THE THE INVERSE OF A 3 BY 3 MATRIX
C     [A] AND PLACES THE RESULT IN [AINV].
C     IF DET(A) IS ZERO, THE CALCULATION
C     IS TERMINATED AND A DIAGNOSTIC STATEMENT IS PRINTED.
C*********************************************************************

      REAL*8  A(3,3), AINV(3,3), DET, ACOFAC(3,3), AADJ(3,3)

C     A(3,3)         -- THE MATRIX WHOSE INVERSE IS DESIRED.
C     DET           -- THE COMPUTED DETERMINANT OF [A].
C     ACOFAC(3,3)   -- THE MATRIX OF COFACTORS OF A(I,J).
C                      THE SIGNED MINOR (-1)**(I+J)*M_IJ
C                      IS CALLED THE COFACTOR OF A(I,J).
C     AADJ(3,3)     -- THE ADJOINT OF [A]. IT IS THE MATRIX
C                      OBTAINED BY REPLACING EACH ELEMENT OF
C                      [A] BY ITS COFACTOR, AND THEN TAKING
C                      TRANSPOSE OF THE RESULTING MATRIX.
C     AINV(3,3)     -- RETURNED AS INVERSE OF [A].
C                      [AINV] = [AADJ]/DET.
C---------------------------------------------------------------------

      CALL KMDET(A,DET)
      IF ( DET .EQ. 0.D0 ) THEN
        WRITE(80,10)
        STOP
      ENDIF
      CALL KMCOFAC(A,ACOFAC)
      CALL KMTRANS(ACOFAC,AADJ)
      DO 1 I = 1,3
      DO 1 J = 1,3
           AINV(I,J) = AADJ(I,J)/DET
1     CONTINUE
10    FORMAT(5X,'--ERROR IN KM3INV--- THE MATRIX IS SINGULAR',/,
```

```
     +         10X,'PROGRAM TERMINATED')

       RETURN
       END
C*********************************************************************
       SUBROUTINE KMCOFAC(A,ACOFAC)

C      THIS SUBROUTINE CALCULATES THE COFACTOR OF A 3 BY 3 MATRIX [A],
C      AND PLACES THE RESULT IN [ACOFAC].
C*********************************************************************

       REAL*8  A(3,3), ACOFAC(3,3)

       ACOFAC(1,1) = A(2,2)*A(3,3) - A(3,2)*A(2,3)
       ACOFAC(1,2) = -(A(2,1)*A(3,3) - A(3,1)*A(2,3))
       ACOFAC(1,3) = A(2,1)*A(3,2) - A(3,1)*A(2,2)
       ACOFAC(2,1) = -(A(1,2)*A(3,3) - A(3,2)*A(1,3))
       ACOFAC(2,2) = A(1,1)*A(3,3) - A(3,1)*A(1,3)
       ACOFAC(2,3) = -(A(1,1)*A(3,2) - A(3,1)*A(1,2))
       ACOFAC(3,1) = A(1,2)*A(2,3)  - A(2,2)*A(1,3)
       ACOFAC(3,2) = -(A(1,1)*A(2,3) - A(2,1)*A(1,3))
       ACOFAC(3,3) = A(1,1)*A(2,2) - A(2,1)*A(1,2)

       RETURN
       END
C*********************************************************************
       SUBROUTINE KMINV(A,AINV,DET_AINV)

C      This subroutine calculates the inverse of a {3 x 3} matrix and the
C      determinant of the inverse
C*********************************************************************

       IMPLICIT REAL*8(A-H,O-Z)

       DIMENSION A(3,3), AINV(3,3)


       PARAMETER(ZERO=0.D0, ONE=1.D0)

       DET_A = A(1,1)*(A(2,2)*A(3,3) - A(3,2)*A(2,3)) -
     +         A(2,1)*(A(1,2)*A(3,3) - A(3,2)*A(1,3)) +
     +         A(3,1)*(A(1,2)*A(2,3) - A(2,2)*A(1,3))

       IF (DET_A .LE. ZERO) THEN
         WRITE(80,*) 'WARNING: DET OF MAT IS ZERO/NEGATIVE !!'
       ENDIF

       DET_AINV = ONE/DET_A

       AINV(1,1) = DET_AINV*(A(2,2)*A(3,3) - A(3,2)*A(2,3))
       AINV(1,2) = DET_AINV*(A(3,2)*A(1,3) - A(1,2)*A(3,3))
       AINV(1,3) = DET_AINV*(A(1,2)*A(2,3) - A(2,2)*A(1,3))
       AINV(2,1) = DET_AINV*(A(3,1)*A(2,3) - A(2,1)*A(3,3))
       AINV(2,2) = DET_AINV*(A(1,1)*A(3,3) - A(3,1)*A(1,3))
       AINV(2,3) = DET_AINV*(A(2,1)*A(1,3) - A(1,1)*A(2,3))
       AINV(3,1) = DET_AINV*(A(2,1)*A(3,2) - A(3,1)*A(2,2))
       AINV(3,2) = DET_AINV*(A(3,1)*A(1,2) - A(1,1)*A(3,2))
       AINV(3,3) = DET_AINV*(A(1,1)*A(2,2) - A(2,1)*A(1,2))

       RETURN
       END
C*********************************************************************
        SUBROUTINE KINVAR(A,IA,IIA,IIIA)
```

```
C      THIS SUBROUTINE CALCULATES THE PRINCIPAL INVARIANTS
C      IA, IIA, IIIA OF A TENSOR [A].
C*********************************************************************

        REAL*8 A(3,3), AD(3,3),AD2(3,3), DETA, IA,IIA,IIIA

        DO 1 I=1,3
          DO 1 J=1,3
            AD(I,J) = A(I,J)
1       CONTINUE
        IA = AD(1,1) + AD(2,2) + AD(3,3)

C      CALCULATE THE SQUARE OF [AD]

        CALL KMPROD(AD,AD,AD2)
        IIA =0.5D0 * ( IA*IA - ( AD2(1,1) + AD2(2,2) + AD2(3,3) ) )

        CALL  KMDET(AD,DETA)
        IIIA = DETA

        RETURN
        END

C*********************************************************************
       SUBROUTINE KTRACEM(A,TRA)

C      THIS SUBROUTINE CALCULATES THE TRACE OF A 3 BY 3 MATRIX [A]
C      AND STORES THE RESULT IN THE SCALAR TRA
C*********************************************************************

       REAL*8 A(3,3),TRA

       TRA = A(1,1) + A(2,2) + A(3,3)

       RETURN
       END

C*********************************************************************
       SUBROUTINE KDEVM(A,ADEV)

C      THIS SUBROUTINE CALCULATES THE DEVIATORIC PART OF A
C      3 BY 3 MATRIX [A]
C*********************************************************************

       REAL*8 A(3,3),TRA,ADEV(3,3),IDEN(3,3)

       CALL KTRACEM(A,TRA)
       CALL KONEM(IDEN)
       CALL KZEROM(ADEV)

       DO 1 I = 1,3
         DO 1 J = 1,3
           ADEV(I,J) = A(I,J) - (1.D0/3.D0)*TRA*IDEN(I,J)
1      CONTINUE

       RETURN
       END
C *********************************************************************
        SUBROUTINE KPRESS(A,PRA)
C
C       THIS SUBROUTINE CALCULATES THE MEAN NORMAL PRESSURE
C       OF A 3 BY 3 MATRIX [A]
```

```
C       AND STORES THE RESULT IN THE SCALAR PRA
C -------------------------------------------------------------------
C       VARIABLES
C
        REAL*8 A(3,3),PRA

        PRA = -(1.D0 / 3.D0)*( A(1,1) + A(2,2) + A(3,3) )

        RETURN
        END
C*********************************************************************
C*********************************************************************
       SUBROUTINE KEQUIVS(S,SB)

C      THIS SUBROUTINE CALCULATES THE EQUIVALENT SHEAR STRESS SB
C      CORRESPONDING TO A 3 BY 3 STRESS MATRIX [S]
C*********************************************************************

       REAL*8 S(3,3),SDEV(3,3),SDOTS,SB

       SB = 0.D0
       SDOTS = 0.D0

       CALL KDEVM(S,SDEV)
       CALL KDOTPM(SDEV,SDEV,SDOTS)
       SB = DSQRT(0.5D0* SDOTS)

       RETURN
       END
C*********************************************************************
       SUBROUTINE KEQSTNRT(S,SB)

C      THIS SUBROUTINE CALCULATES THE EQUIVALENT TENSILE STRESS SB
C      CORRESPONDING TO A 3 BY 3 STRESS MATRIX [S]
C*********************************************************************

       REAL*8 S(3,3),SDEV(3,3),SDOTS,SB

       SB = 0.D0
       SDOTS = 0.D0

       CALL KDEVM(S,SDEV)
       CALL KDOTPM(SDEV,SDEV,SDOTS)
       SB = DSQRT((2.D0/3.D0)* SDOTS)

       RETURN
       END
C*********************************************************************
       SUBROUTINE KPRTMAT(A,M,N)
C*********************************************************************

       INTEGER M,N
       REAL*8 A(M,N)

       DO 10 K=1,M
         WRITE(80,'(2X,6E12.4,2X)') (A(K,L), L=1,N)
10      CONTINUE

        RETURN
        END

C*********************************************************************
       SUBROUTINE KPRTVEC(A,M)
```

```
C*********************************************************************

       INTEGER M
       REAL*8 A(M)

       WRITE(80,'(2X,6E12.4,2X)') (A(K), K=1,M)

        RETURN
       END

C*********************************************************************
C
C      THE FOLLOWING  SUBROUTINE IS THE GENERIC ROOT FINDING ROUTINE
C
C **********************************************************************
       SUBROUTINE KRTSAFE(FUNCD,X1,X2,ROOT,XACC,iterk,itererr)
C
C      THIS IS A FAIL-SAFE SUBROUTINE TO SOLVE AN IMPLICIT EQUATION
C      F(X) = 0 FOR ITS ROOT. THIS ROUTINE UTILIZES
C      A COMBINATION OF THE BISECTION AND THE NEWTON-RAPHSON SCHEMES.
C      THE HYBRID ALGORITHM TAKES A BISECTION STEP WHENEVER NEWTON-
C      RAPHSON WOULD TAKE THE SOLUTION OUT OF THE BOUNDS (X1
C      IS THE CURRENT LOWER BOUND ON X, AND X2 IS THE CURRENT
C      UPPER BOUND ON X), OR WHENEVER NEWTON-RAPHSON IS NOT REDUCING
C      THE SIZE OF THE BRACKETS RAPIDLY ENOUGH.
C
C      THE ROOT, RETURNED AS ROOT, IS REFINED UNTIL ITS ACCURACY
C      IS KNOWN WITHIN |ROOT|< XACC.
C
C      FUNCD IS A USER SUPPLIED SUBROUTINE WHICH RETURNS BOTH THE
C      FUNCTION VALUE AND THE FIRST DERIVATIVE OF THE FUNCTION.
C
C      THIS SUBROUTINE IS BASED ON THE ONE GIVEN IN ''NUMERICAL
C      RECIPES'', PAGE 258.
C ---------------------------------------------------------------------------
C      VARIABLES
C
       IMPLICIT REAL*8 (A-H,O-Z)
       REAL*8 X1,X2,ROOT,XACC
        EXTERNAL FUNCD
       PARAMETER(MAXIT=100)

       iterk = 0
       itererr = 0

       CALL FUNCD(X1,FL,DF)
       CALL FUNCD(X2,FH,DF)
C
C             VERIFY THAT THERE IS A ROOT WITHIN THE ORIGINAL
C             INTERVAL
C
       IF(FL*FH .GE. 0.D0) THEN
          WRITE(80,'(/1X,A/)') 'ROOT MUST BE BRACKETED'
          STOP
       END IF
C
C             ORIENT THE SEARCH SO THAT F(XL) < 0.
C
       IF( FL .LT. 0.D0 ) THEN
           XL = X1
           XH = X2
       ELSE
           XH = X1
```

```
           XL = X2
           SWAP = FL
           FL = FH
           FH = SWAP
        END IF
C
C             INITIALIZE THE GUESS FOR THE ROOT, THE ''STEP SIZE
C             BEFORE LAST'', AND THE LAST STEP
C
        ROOT = 0.5D0 *( X1 + X2)
        DXOLD = DABS(X2 - X1)
        DX = DXOLD

        CALL FUNCD(ROOT,F,DF)

C
C                    LOOP OVER ALLOWED ITERATIONS
C
        DO 10 J = 1,MAXIT
C
C                    BISECT IF NEWTON OUT OF RANGE, OR NOT DECREASING
C                    FAST ENOUGH.
C
           IF( ((ROOT-XH)*DF - F)*((ROOT - XL)*DF -F) .GE. 0.D0
     +         .OR. DABS(2.D0*F) .GT. DABS(DXOLD*DF) ) THEN

               DXOLD = DX
               DX = 0.5D0*(XH-XL)
               ROOT = XL + DX
               IF( XL .EQ. ROOT ) THEN
C
C                    CHANGE IN ROOT IS NEGLIGIBLE
C
                  RETURN
               END IF

           ELSE
C
C                    NEWTON STEP IS ACCEPTABLE. TAKE IT.
C
               DXOLD = DX
               DX = F/DF
               TEMP = ROOT
               ROOT = ROOT - DX
               IF( TEMP .EQ. ROOT) THEN
C
C                     CHANGE IN ROOT IS NEGLIGIBLE
C
                  RETURN
              END IF

           END IF
C
C              CONVERVEGENCE CRITERION
C
           IF( DABS(DX) .LT. XACC) then
               iterk = j
               RETURN
        endif
C
C                    THE ONE NEW FUNCTION EVALUATION PER ITERATION
C
           CALL FUNCD(ROOT,F,DF)
```

```
C
C             MAINTAIN THE BRACKET ON THE ROOT
C
          IF( F .LT. 0.D0) THEN
              XL = ROOT
              FL = F
          ELSE
              XH = ROOT
              FH = F
          END IF

 10     CONTINUE

        iterk = maxit +1
        itererr = 1

        WRITE(6,'(/1X,A)') 'RTSAFE EXCEEDING MAXIMUM ITERATIONS'
        RETURN
        END
C ***********************************************************************
```

APPENDIX E

ABAQUS™ Input Files

```
*HEADING
ONE ELEMENT SIMPLE COMPRESSION CREEP
**
**    Model Definition
**
*NODE,NSET=NALL
1,0.,0.,0.
2,1.E-03,0.,0.
3,1.E-03,1.E-03,0.
4,0.,1.E-03,0.
5,0.,0.,1.E-03
6,1.E-03,0.,1.E-03
7,1.E-03,1.E-03,1.E-03
8,0.,1.E-03,1.E-03
*ELEMENT,TYPE=C3D8R,ELSET=ELALL
1,1,2,3,4,5,6,7,8
*SOLID SECTION,ELSET=ELALL,MATERIAL=silicon
*MATERIAL, NAME=silicon
**
**    Material Properties Data
**
*USER MATERIAL, CONSTANT=19
150.8E9,0.23,3.83E-10,2.000,6.40E4,0.55E7,3.53E-19,1.38E-23
0.9091,2.0E6,2.0E-4,0.5E9,6.6E-19,12.5E9,25.E6,330.E6
2E8,1073.,4.0E-6
*DEPVAR
21
*DENSITY
1.E15
**
** Normal Density is 0.234E4 kg/m^3
**
** Initial BCS
**
*NSET,NSET=XZERO
1,4,5,8
*NSET,NSET=YZERO
1,2,5,6
*NSET,NSET=ZZERO
1,2,3,4
*BOUNDARY
**XZERO,1
**YZERO,2
ZZERO,3
*NSET,NSET=XTOP
2,3,6,7
*NSET,NSET=YTOP
3,4,7,8
*NSET,NSET=ZTOP
```

```
5,6,7,8
*NSET,NSET=XTOP1
3,6,7
*NSET,NSET=YTOP1
4,7,8
*NSET,NSET=ZTOP1
6,7,8
*EQUATION
**2
**XTOP1,1,1.0,2,1,-1.0
**2
**YTOP1,2,1.0,3,2,-1.0
2
ZTOP1,3,1.0,5,3,-1.0
*BOUNDARY
1,1,3
2,2
*NSET,NSET=REF
5
*RESTART,WRITE,NUM=10
**
*initial condition, type=temperature
nall, 1073
*AMPLITUDE,DEFINITION=SMOOTH STEP,NAME=RAMP
0.0,0.0,60.,1.0,36000,1.0
*AMPLITUDE, NAME=AMP_TEMP
0.,1073.,36000,1073.
**
**Step Definition
**
*STEP
*DYNAMIC,EXPLICIT
,36000
*DLOAD,AMP=RAMP
ELALL,P2,60.E6
*TEMPERATURE, AMPLITUDE=AMP_TEMP
NALL, 1.
**
**    Output request
**
*FILE OUTPUT,NUM=10
*history output, time interval=30
*EL FILE
S,SDV
E
*NODE FILE
U,RF
*el history, elset=elall
s,sdv
le
*node history, nset=nall
u,rf
*MONITOR, NODE=5, DOF=3
*END STEP
**
```

```
*HEADING
ONE ELEMENT 3-D COMPRESSION, CONSTANT STRAIN
**
**    Model Definition
**
*NODE,NSET=NALL
1,0.,0.,0.
2,1.E-3,0.,0.
3,1.E-3,1.E-3,0.
4,0.,1.E-3,0.
5,0.,0.,1.E-3
6,1.E-3,0.,1.E-3
7,1.E-3,1.E-3,1.E-3
8,0.,1.E-3,1.E-3
*ELEMENT,TYPE=C3D8R,ELSET=ELALL
1,1,2,3,4,5,6,7,8
*SOLID SECTION,ELSET=ELALL,MATERIAL=MAT
1.,
*MATERIAL, NAME=MAT
**
**    Material Properties Data
**
*USER MATERIAL,CONSTANTS=19
151.E9,0.23,3.83E-10,2.000,6.4E4,0.55E7,3.53E-19,1.38E-23
0.9091,2E6,2.0E-4,0.5E9,6.6E-19,12.5E9,25.E6,330.E6
2E8,1073.,4.0e-6
*DEPVAR
21
*DENSITY
1.E13
**
** REAL DENSITY 1210 KG/M^3
**
*NSET,NSET=BOT
1,2,3,4
*BOUNDARY
BOT,3
1,1,2
2,2
*NSET,NSET=TOP
5,6,7,8
*NSET,NSET=TOP1
6,7,8
*EQUATION
2
TOP1,3,1.0,5,3,-1.0
*NSET,NSET=REF
5
*INITIAL CONDITION, TYPE=TEMPERATURE
NALL, 1073.
*AMPLITUDE, NAME=AMP_TEMP
0.,1073.,100.,1073.
**
**    Step Definition
**
*STEP
*DYNAMIC,EXPLICIT
```

```
,100.
*RESTART,WRITE,NUM=400
*BOUNDARY,TYPE=VELOCITY
REF,3,,-2.4E-7
*TEMPERATURE,AMPLITUDE=AMP_TEMP
NALL,1.
**
**    Output Request
**
*Output, field
*Node Output
U, RF
*Element Output
S, LE, SDV
*FILE OUTPUT,NUM=400
*NODE FILE
U,RF
*EL FILE
S,LE,SDV
*MONITOR,NODE=5,DOF=3
*End Step
**
```

```
*HEADING
Si 4-PT BEND TEST, MONOTONIC LOADING
*RESTART,WRITE,NUM=10
**
**    Model Definition
**
*NODE
1, 0., 0.
5, 0.0005, 0.
6, 0.001, 0.
20, 0.0087, 0.
21, 0.009, 0.
30, 0.010, 0.
39, 0.011, 0.
40, 0.0113, 0.
48, 0.019, 0.
49, 0.0195, 0.
53, 0.020, 0.
57, 0.0205, 0.
58, 0.021, 0.
62, 0.025, 0.
8001, 0., 0.001
8005, 0.0005, 0.001
8006, 0.001, 0.001
8020, 0.0087, 0.001
8021, 0.009, 0.001
8030, 0.010, 0.001
8039, 0.011, 0.001
8040, 0.0113, 0.001
8048, 0.019, 0.001
8049, 0.0195, 0.001
8053, 0.020, 0.001
8057, 0.0205, 0.001
8058, 0.021, 0.001
8062, 0.025, 0.001
*NSET,NSET=B1
1
*NSET,NSET=B2
5
*NSET,NSET=B3
6
*NSET,NSET=B4
20
*NSET,NSET=B5
21
*NSET,NSET=B5M
30
*NSET,NSET=B6
39
*NSET,NSET=B7
40
*NSET,NSET=B8
48
*NSET,NSET=B9
49
*NSET,NSET=B9M
53
```

```
*NSET,NSET=B10
57
*NSET,NSET=B11
58
*NSET,NSET=B12
62
*NSET,NSET=T1
8001
*NSET,NSET=T2
8005
*NSET,NSET=T3
8006
*NSET,NSET=T4
8020
*NSET,NSET=T5
8021
*NSET,NSET=T5M
8030
*NSET,NSET=T6
8039
*NSET,NSET=T7
8040
*NSET,NSET=T8
8048
*NSET,NSET=T9
8049
*NSET,NSET=T9M
8053
*NSET,NSET=T10
8057
*NSET,NSET=T11
8058
*NSET,NSET=T12
8062
*NFILL,NSET=BOT1,BIAS=0.8
B1,B2,4,1
*NFILL,NSET=BOT2
B3,B4,14,1
*NFILL,NSET=BOT3L,BIAS=1.11
B5,B5M,9,1
*NFILL,NSET=BOT3R,BIAS=0.9
B5M,B6,9,1
*NFILL,NSET=BOT4
B7,B8,8,1
*NFILL,NSET=BOT5L,BIAS=1.25
B9,B9M,4,1
*NFILL,NSET=BOT5R,BIAS=0.8
B9M,B10,4,1
*NFILL,NSET=BOT6
B11,B12,4,1
*NFILL,NSET=TOP1,BIAS=0.8
T1,T2,4,1
*NFILL,NSET=TOP2
T3,T4,14,1
*NFILL,NSET=TOP3L,BIAS=1.11
T5,T5M,9,1
*NFILL,NSET=TOP3R,BIAS=0.9
```

```
T5M,T6,9,1
*NFILL,NSET=TOP4
T7,T8,8,1
*NFILL,NSET=TOP5L,BIAS=1.25
T9,T9M,4,1
*NFILL,NSET=TOP5R,BIAS=0.8
T9M,T10,4,1
*NFILL,NSET=TOP6
T11,T12,4,1
*NFILL,NSET=NALL
BOT1,TOP1,8,1000
BOT2,TOP2,8,1000
BOT3L,TOP3L,8,1000
BOT3R,TOP3R,8,1000
BOT4,TOP4,8,1000
BOT5L,TOP5L,8,1000
BOT5R,TOP5R,8,1000
BOT6,TOP6,8,1000
*NSET,NSET=MIDDLE,GEN
1,8001,1000
*ELEMENT,TYPE=CPE4R,ELSET=ELALL
1,1,2,1002,1001
*ELGEN,ELSET=ELALL
1,61,1,1,8,1000,1000
*NODE,NSET=NRIGID1
90001,0.01,0.0035
*RIGID BODY,REF NODE=90001
*NODE,NSET=NRIGID2
90002,0.02,-0.0025
*RIGID BODY,REF NODE=90002
*SOLID SECTION,ELSET=ELALL,MATERIAL=SILICON,CONTROL=B
0.009,
*SECTION CONTROLS, HOURGLASS=STIFFNESS, STRESS RATE=SPIN, NAME=B
*MATERIAL, NAME=SILICON
**
**    Material Properties Data
**
*USER MATERIAL, CONSTANT=19
155.8E9,0.23,3.83E-10,2.000,6.40E4,0.55E7,3.53E-19,1.38E-23
0.9091,2.0E6,2.0E-4,0.5E9,6.6E-19,12.5E9,25.E6,330.E6
2E8,1073.,4.0e-6
*DEPVAR
21
*DENSITY
5.0E13
*BOUNDARY
MIDDLE,1
90001,1,2
*INITIAL CONDITION, TYPE=TEMPERATURE
NALL, 1073.
*AMPLITUDE,NAME=RAMP
0.,0.,0.5,1.,1000.,1.
*AMPLITUDE,NAME=AMP_TEMP
0.,1073.,750.,1073.
**
**    Step Definition
**
```

```
*STEP
*DYNAMIC,EXPLICIT
,750.
*ELSET,ELSET=TOP,GEN
7020,7041,1
*ELSET,ELSET=BOT,GEN
48,57,1
*RIGID SURFACE,NAME=ROLLER1,TYPE=SEGMENTS,REF NODE=90001
START,0.0125,0.0035
CIRCL,0.0100,0.001,0.010,0.0035
CIRCL,0.0075,0.0035,0.010,0.0035
*SURFACE DEFINITION,NAME=INNER
TOP
*SURFACE INTERACTION,NAME=IN_ROL1
*FRICTION
0.1,
*CONTACT PAIR,INTERACTION=IN_ROL1
ROLLER1,INNER
*RIGID SURFACE,NAME=ROLLER2,TYPE=SEGMENTS,REF NODE=90002
START,0.0175,-0.0025
CIRCL,0.0200,0.,0.020,-0.0025
CIRCL,0.0225,-0.0025,0.020,-0.0025
*SURFACE DEFINITION,NAME=OUTER
BOT,S1
*SURFACE INTERACTION,NAME=OUT_ROL2
*FRICTION
0.1,
*CONTACT PAIR,INTERACTION=OUT_ROL2
ROLLER2,OUTER
*BOUNDARY,TYPE=VELOCITY,AMPLITUDE=RAMP
90002,2,,2.E-6
*TEMPERATURE, AMPLITUDE=AMP_TEMP
NALL,1.
**
**    Output Request
**
*MONITOR,NODE=90002,DOF=2
*FILE OUTPUT,NUM=2,TIMEMARKS=YES
*EL FILE
S,LE
*NSET,NSET=MONITOR
1
90001
90002
*HISTORY OUTPUT, TIME=1.00
*NODE HISTORY, NSET=MONITOR
U2,RF2
*NODE FILE, NSET=NRIGID2
U,RF
*energy file
allke, allie
*energy history
allie, allke
*END STEP
```

```
*HEADING
Si/SiC HYBRID ROTATING DISC
*RESTART, WRITE, NUM=10
**
**    Model Definition
**
*NODE
1, 0., 0.
11, 3.e-3, 0.
1001, 0., 0.045e-3
1011, 3.e-3, 0.045e-3
3001, 0., 0.15e-3
3011, 3.e-3, 0.15e-3
*ngen, nset = bot
1, 11
*ngen, nset = middle
1001, 1011
*nfill,nset = sic
bot,middle,1,1000
*ngen, nset = top
3001, 3011
*nfill,nset=si
middle,top,2,1000
*element, type = cax4r, elset = sic
1, 1, 2, 1002, 1001
*elgen, elset = sic
1, 10, 1, 1, 1, 1000, 10
*element, type = cax4r, elset = si
11, 1001,1002,2002,2001
*elgen, elset = si
11,10,1,1,2,1000,10
*nset, nset = rotaxis,generate
1, 3001,1000
*nset, nset = symm, generate
1, 11, 1
**
*SOLID SECTION,ELSET=SI,MATERIAL=SILICON
*MATERIAL,NAME=SILICON
**
**    Material Properties Data
**
*USER MATERIAL, CONSTANT=19
155.8E9,0.23,3.83E-10,2.000,6.40E4,0.55E7,3.53E-19,1.38E-23
0.9091,2.0E6,2.0E-4,0.5E9,6.6E-19,12.5E9,25.E6,330.E6
2E8,300.,4.0E-6
*DEPVAR
21
*DENSITY
2.33E14
*SOLID SECTION,ELSET=SIC,MATERIAL=SIC
*MATERIAL,NAME=SIC
*ELASTIC, TYPE=ISOTROPIC
430.00E+09,0.21
*expansion
4.5E-6
*density
3.2E14
```

```
**
*BOUNDARY
  rotaxis, 1
  symm, 2
*initial condition, type=temperature
si, 300
sic, 300
*amplitude,name=centrif
0.,0.,10.,1.,36000,1.
*amplitude,name=amp_temp
0.,300.,10.,1073.,36000,1073.
**
**    Step Defintion
**
*STEP
*DYNAMIC,EXPLICIT
,120
**
**    Centrifugal LOAD BC
**
*DLOAD,amplitude=centrif
1,br,0.0999E11
2,br,0.233E11
3,br,0.380E11
4,br,0.528E11
5,br,0.678E11
6,br,0.826E11
7,br,0.976E11
8,br,1.126E11
9,br,1.275E11
10,br,1.426E11
11,br,0.0728E11
12,br,0.170E11
13,br,0.277E11
14,br,0.385E11
15,br,0.494E11
16,br,0.602E11
17,br,0.711E11
18,br,0.820E11
19,br,0.929E11
20,br,1.039E11
21,br,0.0728E11
22,br,0.170E11
23,br,0.277E11
24,br,0.385E11
25,br,0.494E11
26,br,0.602E11
27,br,0.711E11
28,br,0.820E11
29,br,0.929E11
30,br,1.039E11
*temperature,amplitude=amp_temp
si,1
sic,1
*nset,nset=all
si
sic
```

```
*elset,elset=all
si
sic
*nset,nset=monitor
11
3011
*elset,elset=el_mon
1
11
**
**    Output Request
**
*MONITOR,NODE=3011,DOF=1
*FILE OUTPUT,NUM=2,TIMEMARKS=YES
*history output,time=1.0
*node history,nset=monitor
u1
*el history,elset=el_mon
s
*energy history
allke,allie
*el file, elset=all
s,le
*node file, nset = all
u,v
*energy file
allke,allie
*END STEP
**
```

APPENDIX F

Crystal Plasticity Framework for Si Model

Governing Variables

$(\mathbf{T},\ \mathbf{F},\ \mathbf{F}^p,\ \theta,\ \rho,\ s)$,

where $\mathbf{T}$ is the Cauchy stress, $\mathbf{F}$ is the deformation gradient tensor, $\mathbf{F}^p$ is the plastic deformation gradient tensor, θ is the absolute temperature in Kelvin, ρ is the dislocation density, and s is the isotropic slip resistance.

Equations for Stress

Multiplicative decomposition of $\mathbf{F}$: $\mathbf{F} = \mathbf{F}^e\mathbf{F}^p$

Strain Tensor (Green elastic strain): $\mathbf{E}^e = 1/2(\mathbf{F}^{e^T}\mathbf{F}^e - \mathbf{1})$

Piola-Kirchoff stress tensor: $\overline{\mathbf{T}} = (\det \mathbf{F}^e)\mathbf{F}^{e^{-1}}\mathbf{T}\mathbf{F}^{e^{-T}}$

Constitutive law: $\overline{\mathbf{T}} = \mathscr{C}[\mathbf{E}^e - \alpha_T(\theta - \theta_0)\mathbf{1}]$,

where $\alpha_T\mathbf{1}$ is the second-order isotropic thermal expansion tensor, and θ and θ_0 are the absolute temperature and a reference temperature, respectively.

Flow Rule

$$\dot{\mathbf{F}}^p\mathbf{F}^{p^{-1}} = \sum_{\alpha=1}^{12}\dot{\gamma}^\alpha m^{(\alpha)} \otimes n^{(\alpha)}$$

where $\dot{\gamma}^\alpha$ is plastic shearing rate in the α slip system and $m^{(\alpha)} \otimes n^{(\alpha)}$ are slip systems. FCC or diamond-structured crystals have twelve slip systems as listed in Table A6.1.

Table A6.1 Components of $\mathbf{m}^{\alpha}$ and $\mathbf{n}^{\alpha}$ referred to an orthonormal basis $\{\mathbf{e}_i^c\}$ associated with the crystal lattice for FCC and diamond-structured crystals.

m^{α}	n^{α}
$1/\sqrt{2}$ $-1/\sqrt{2}$ 0	$1/\sqrt{3}$ $1/\sqrt{3}$ $1/\sqrt{3}$
$-1/\sqrt{2}$ 0 $1/\sqrt{2}$	$1/\sqrt{3}$ $1/\sqrt{3}$ $1/\sqrt{3}$
0 $1/\sqrt{2}$ $-1/\sqrt{2}$	$1/\sqrt{3}$ $1/\sqrt{3}$ $1/\sqrt{3}$
$1/\sqrt{2}$ 0 $1/\sqrt{2}$	$-1/\sqrt{3}$ $1/\sqrt{3}$ $1/\sqrt{3}$
$1/\sqrt{2}$ $1/\sqrt{2}$ 0	$-1/\sqrt{3}$ $1/\sqrt{3}$ $1/\sqrt{3}$
0 $1/\sqrt{2}$ $-1/\sqrt{2}$	$-1/\sqrt{3}$ $1/\sqrt{3}$ $1/\sqrt{3}$
$1/\sqrt{2}$ 0 $-1/\sqrt{2}$	$1/\sqrt{3}$ $-1/\sqrt{3}$ $1/\sqrt{3}$
$1/\sqrt{2}$ $1/\sqrt{2}$ 0	$1/\sqrt{3}$ $-1/\sqrt{3}$ $1/\sqrt{3}$
0 $-1/\sqrt{2}$ $-1/\sqrt{2}$	$1/\sqrt{3}$ $-1/\sqrt{3}$ $1/\sqrt{3}$
$1/\sqrt{2}$ $-1/\sqrt{2}$ 0	$1/\sqrt{3}$ $1/\sqrt{3}$ $-1/\sqrt{3}$
$1/\sqrt{2}$ 0 $1/\sqrt{2}$	$1/\sqrt{3}$ $1/\sqrt{3}$ $-1/\sqrt{3}$
0 $-1/\sqrt{2}$ $-1/\sqrt{2}$	$-1/\sqrt{3}$ $-1/\sqrt{3}$ $1/\sqrt{3}$

Regime I ($\rho^{\alpha} \le \rho_{crit}$)

Orowan equation: $\dot{\gamma}^{\alpha} = \rho_m^{\alpha} b \bar{v}^{\alpha}$. $\rho^{\alpha} \cong \rho_m^{\alpha}$ in Regime I

Internal shear resistance: $\tau_i^{\alpha} = \alpha \mu b \sqrt{\rho^{\alpha}}$

Resolved shear stress: $\tau^{\alpha} = m^{(\alpha)} \cdot \overline{\mathbf{T}} n^{(\alpha)}$

Effective shear resistance; $\tau_{eff}^{\alpha} = \left|\tau^{\alpha}\right| - \tau_i^{\alpha}$

Dislocation velocity:
$$\bar{v}^{\alpha} = \begin{cases} 0 & if\ \tau_{eff}^{\alpha} \le 0 \\ v_0 \exp(-Q/k\theta)\left(\tau_{eff}^{\alpha}/\tau_0\right)^{1/m} sign(\tau^{\alpha}) & if\ \tau_{eff}^{\alpha} > 0 \end{cases}$$

Plastic shear rate:
$$\dot{\gamma}^{\alpha} = \begin{cases} 0 & if\ \tau_{eff}^{\alpha} \le 0 \\ \rho b v_0 \exp(-Q/k\theta)\left(\tau_{eff}^{\alpha}/\tau_0\right)^{1/m} sign(\tau^{\alpha}) & if\ \tau_{eff}^{\alpha} > 0 \end{cases}$$

Evolution equation for dislocation density:

$$\dot{\rho}^{\alpha} = \sum_{\beta} g^{\alpha\beta} \left|\dot{\gamma}^{\beta}\right|$$

$$g^{\alpha\beta} = q^{\alpha\beta} g^{\beta} = [q_l + (1 - q_l)\delta^{\alpha\beta}] g^{\beta}$$

$$\dot{\rho}^{\beta} = g^{\beta} \left|\dot{\gamma}^{\beta}\right| = (K/b)\tau_{eff}^{\beta} \left|\dot{\gamma}^{\beta}\right|,$$

where K is a multiplication rate constant.

Regime II ($\rho^{\alpha} > \rho_{crit}$)

Plastic shear rate: $$\dot{\gamma}^{\alpha} = \dot{\gamma}_0 \exp\left(-\frac{\Delta F}{k\theta}\left(1-\frac{\tau^{\alpha}}{s^{\alpha}}\right)\right)$$

where $\dot{\bar{\gamma}}_0$ is a reference shearing rate, and ΔF is the activation free energy required to overcome the obstacles to slip without the aid of an applied shear stress.

Evolution equation for shear resistance:

$$\dot{s}^{\alpha} = \sum_{\beta} h^{\alpha\beta}\left|\dot{\gamma}^{\beta}\right|$$

$$h^{\alpha\beta} = p^{\alpha\beta}\ h^{\beta} = [p_l + (1-p_l)\delta^{\alpha\beta}]h^{\beta}$$

$$\dot{s}^{\beta} = h^{\beta}\left|\dot{\gamma}^{\beta}\right|$$

$$\dot{s}^{\alpha} = h_0\left(1-\frac{s^{\alpha}}{s^{*\alpha}}\right)\dot{\gamma}^{\alpha}$$

Transition between two models

Critical dislocation density: $$\frac{\rho^{\alpha}{}_{crit}}{\rho_0} = \begin{cases} A\left(\dfrac{\bar{\tau}}{\tau_0}\right)^n & if\ \rho^{\alpha} \geq \rho_{crit0} \\ \dfrac{\rho_{crit0}}{\rho_0} & if\ \rho^{\alpha} < \rho_{crit0}\ . \end{cases}$$

Shear resistance initialization:

$$\dot{\bar{\gamma}}^{p}{}_{regime\ 1} = \dot{\bar{\gamma}}^{p}{}_{regime\ 2}\ \text{ at } (\rho^{\alpha} = \rho_{crit}),$$

$$s_0 = \hat{s}_0(\rho_{crit})$$

$$s_0 = \bar{\tau}\cdot\left(1+\log\left(\frac{\dot{\bar{\gamma}}^{p}{}_{regime\ 1}\Big|_{\rho=\rho_{crit}}}{\dot{\bar{\gamma}}_0}\right)\frac{k\theta}{\Delta F}\right)^{-1}.$$

APPENDIX G

Experimental Data

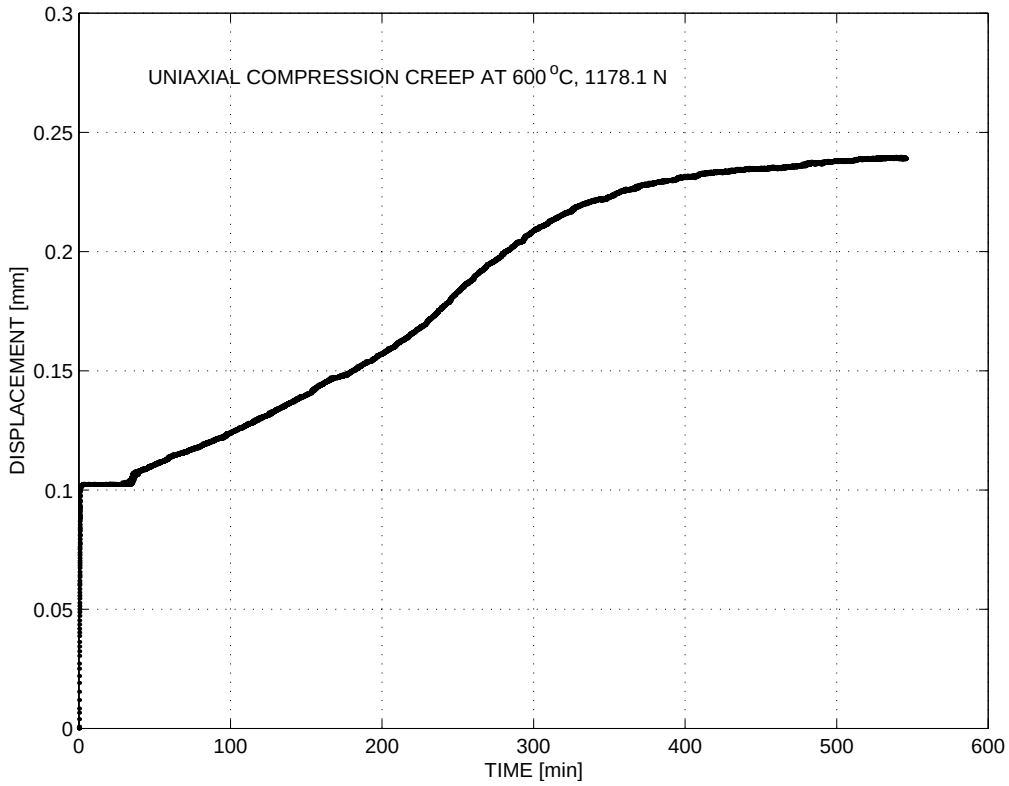

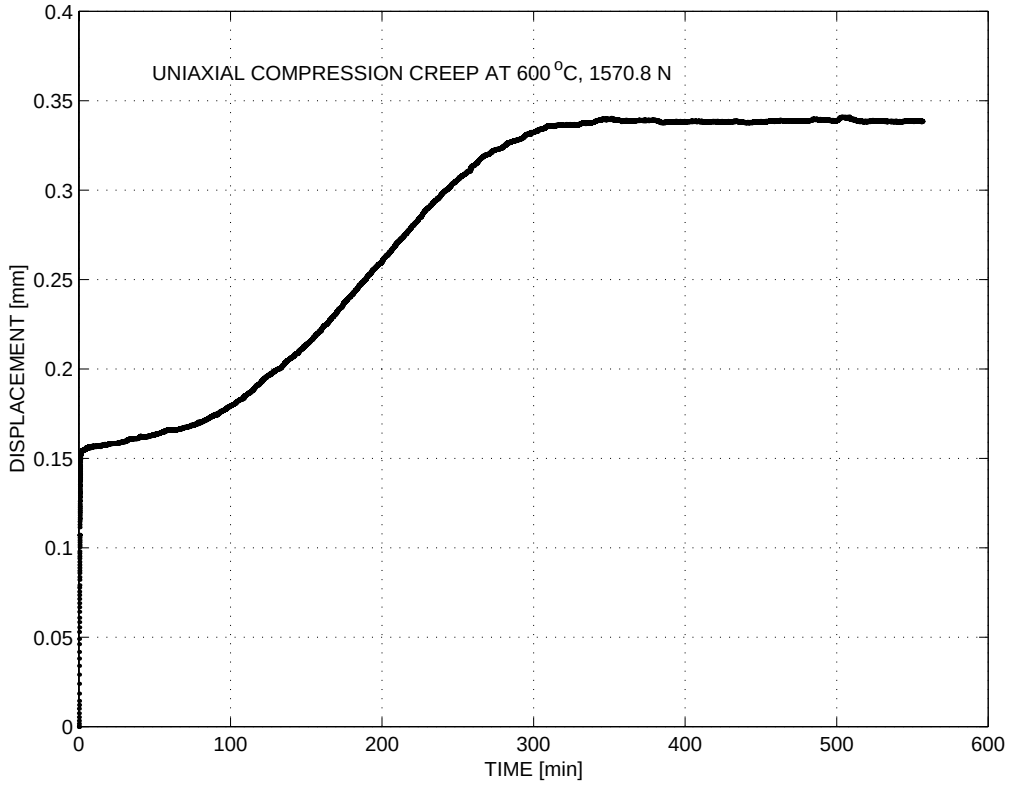

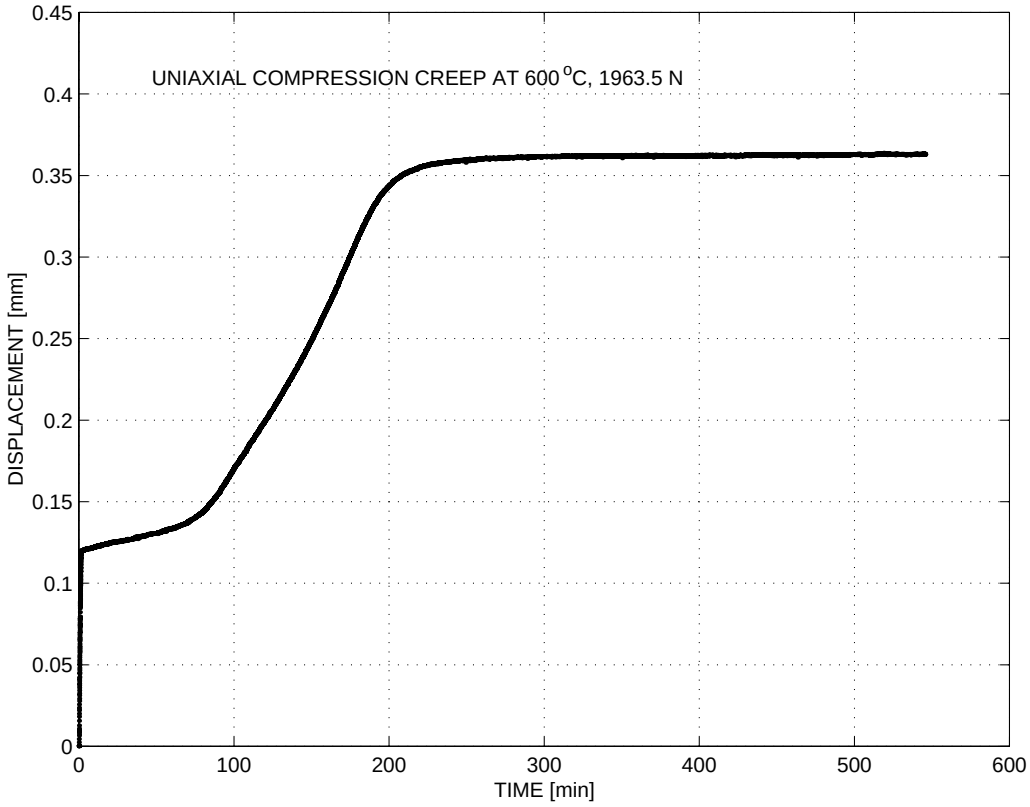
UNIAXIAL COMPRESSION CREEP AT 600 °C, 1963.5 N
DISPLACEMENT [mm]
TIME [min]
0.45
0.4
0.35
0.3
0.25
0.2
0.15
0.1
0.05
0
0
100
200
300
400
500
600

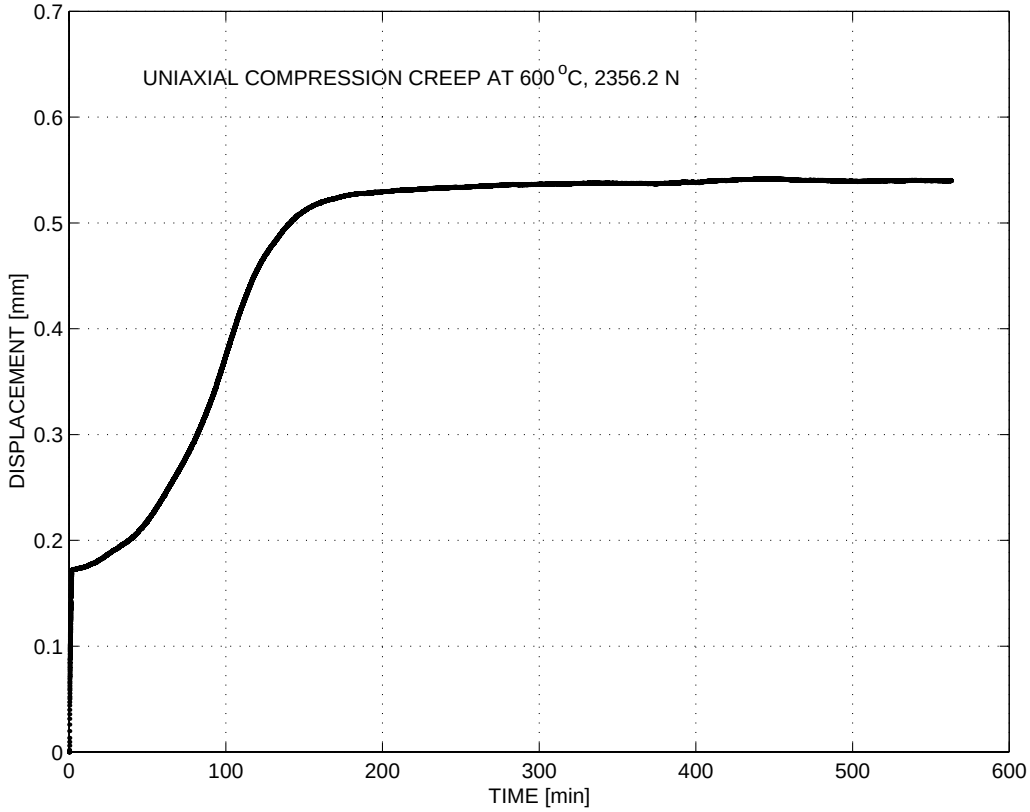
UNIAXIAL COMPRESSION CREEP AT 600 °C, 2356.2 N
DISPLACEMENT [mm]
TIME [min]
0.7
0.6
0.5
0.4
0.3
0.2
0.1
0
0
100
200
300
400
500
600

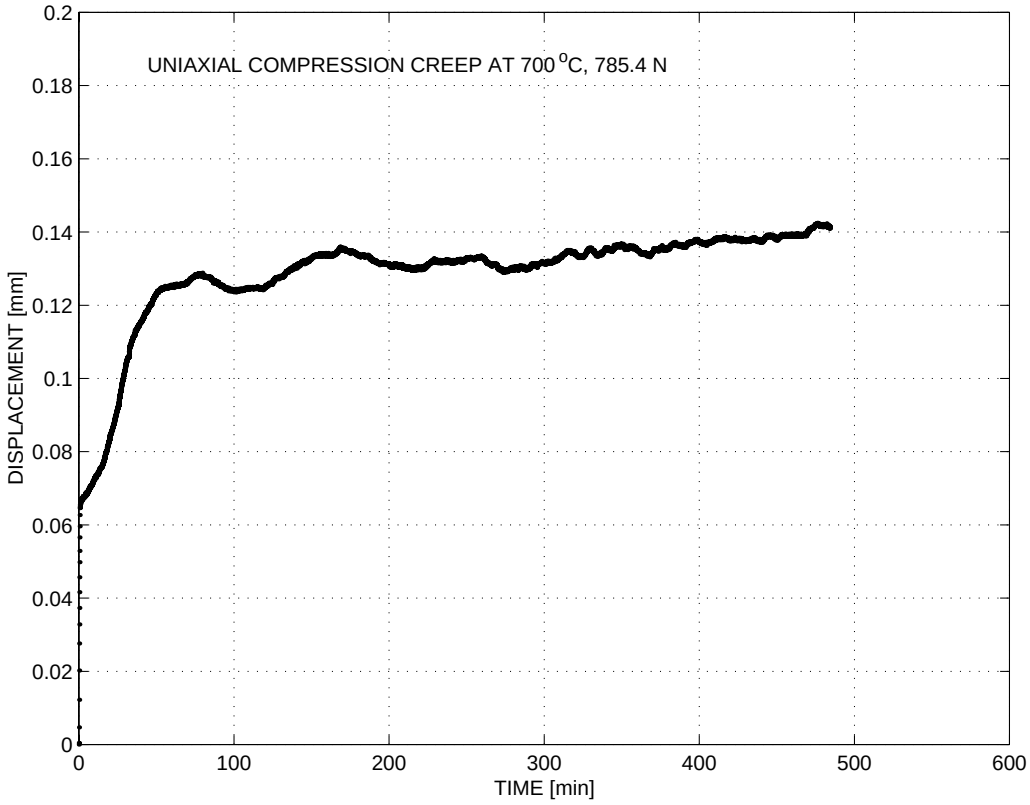
UNIAXIAL COMPRESSION CREEP AT 700 °C, 785.4 N
DISPLACEMENT [mm]
TIME [min]
0
0.02
0.04
0.06
0.08
0.1
0.12
0.14
0.16
0.18
0.2
0
100
200
300
400
500
600

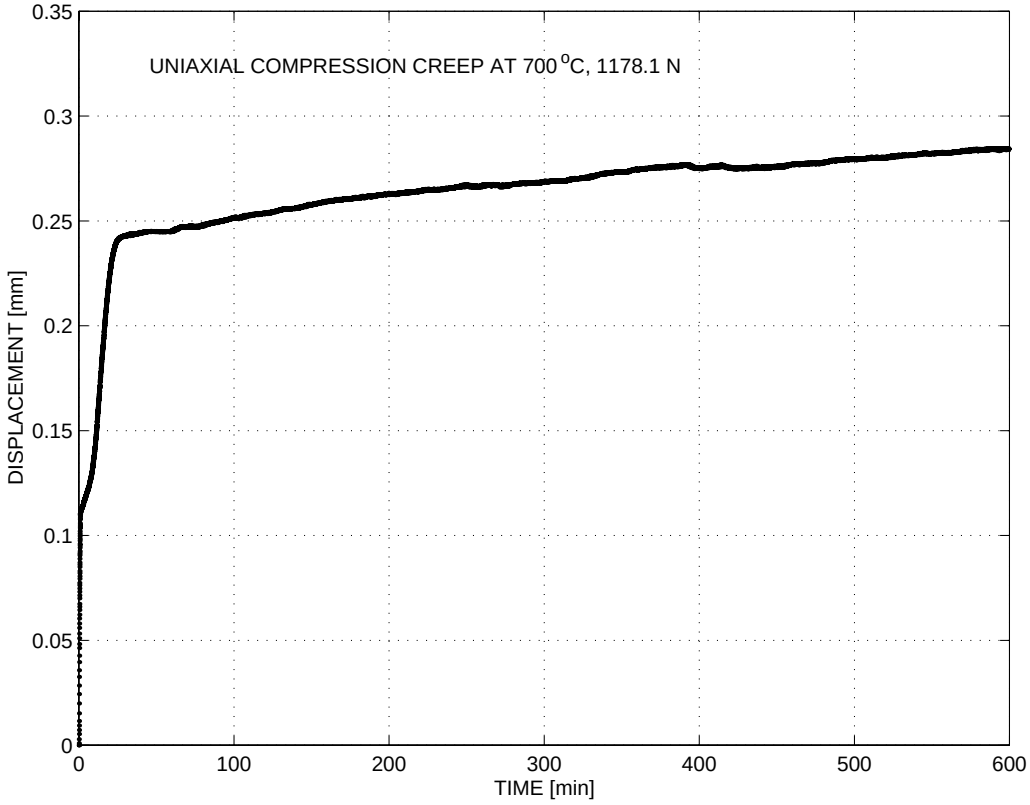
UNIAXIAL COMPRESSION CREEP AT 700 °C, 1178.1 N
DISPLACEMENT [mm]
TIME [min]
0
0.05
0.1
0.15
0.2
0.25
0.3
0.35
0
100
200
300
400
500
600

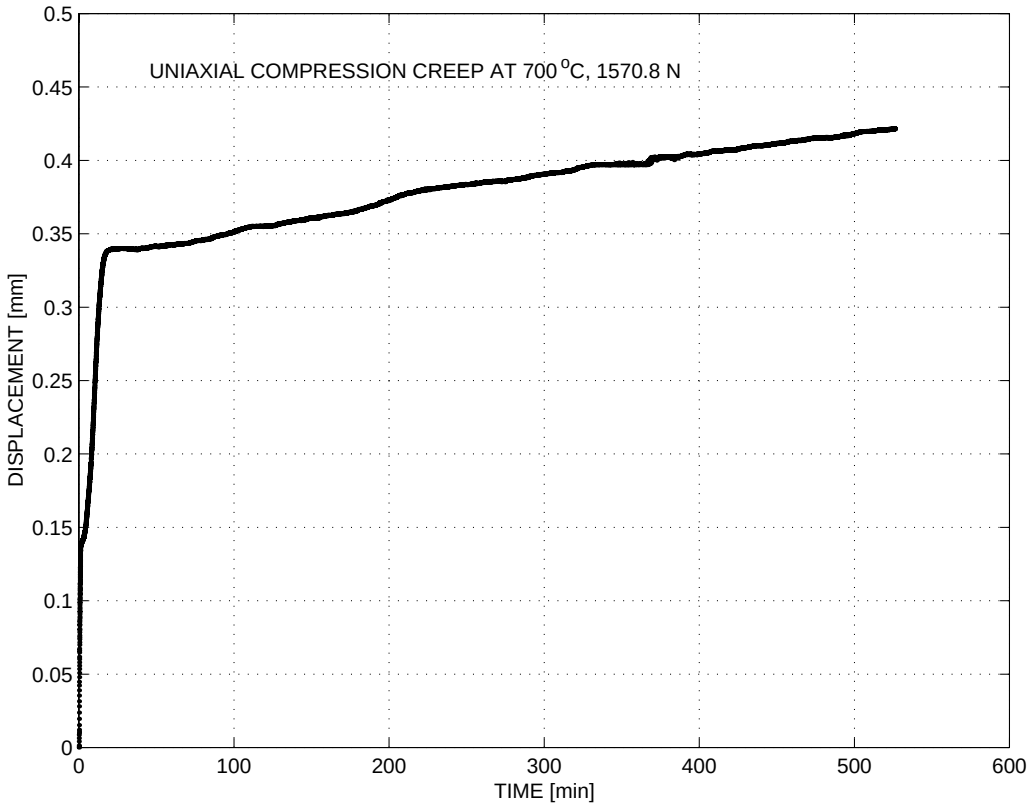
UNIAXIAL COMPRESSION CREEP AT 700 °C, 1570.8 N
DISPLACEMENT [mm]
TIME [min]
0
0.05
0.1
0.15
0.2
0.25
0.3
0.35
0.4
0.45
0.5
0
100
200
300
400
500
600

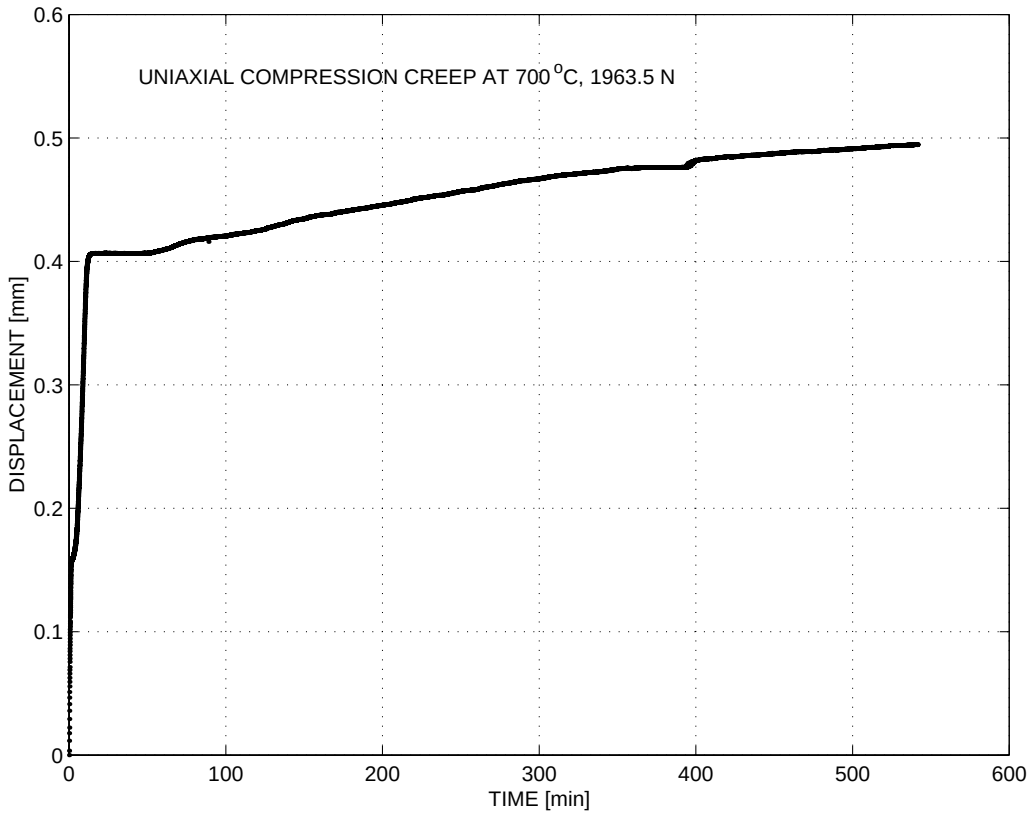
UNIAXIAL COMPRESSION CREEP AT 700 °C, 1963.5 N
DISPLACEMENT [mm]
TIME [min]
0
0.1
0.2
0.3
0.4
0.5
0.6
0
100
200
300
400
500
600

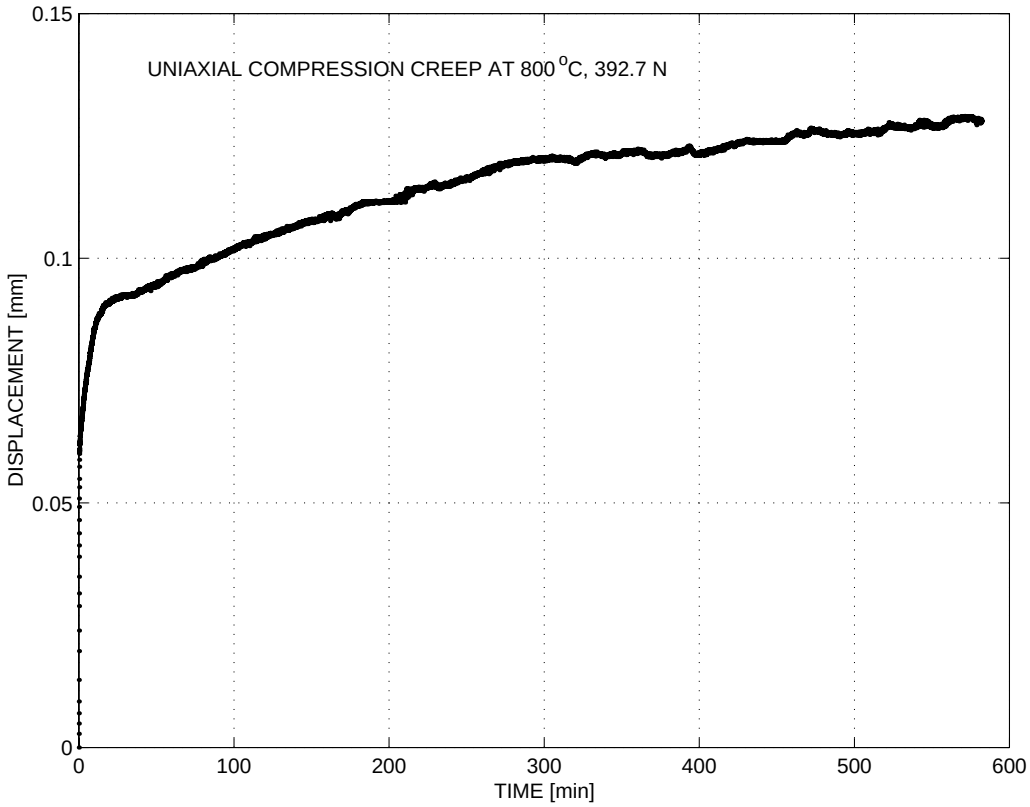
UNIAXIAL COMPRESSION CREEP AT 800 °C, 392.7 N
DISPLACEMENT [mm]
TIME [min]
0.15
0.1
0.05
0
0
100
200
300
400
500
600

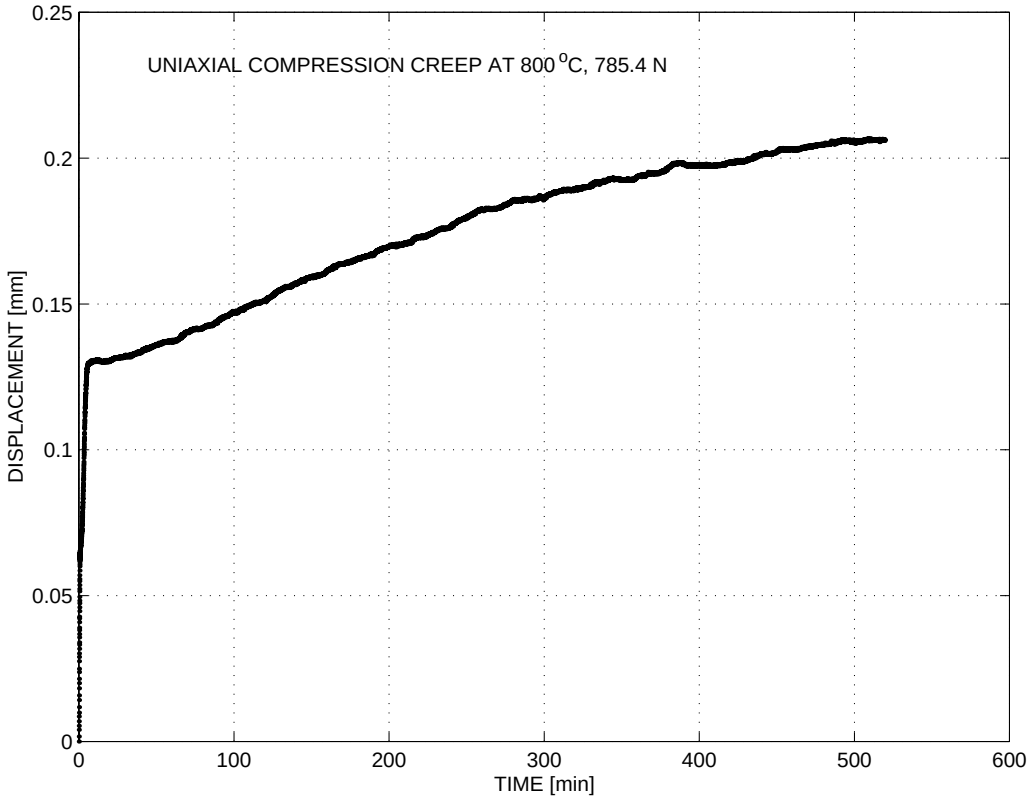
UNIAXIAL COMPRESSION CREEP AT 800 °C, 785.4 N
DISPLACEMENT [mm]
TIME [min]
0.25
0.2
0.15
0.1
0.05
0
0
100
200
300
400
500
600

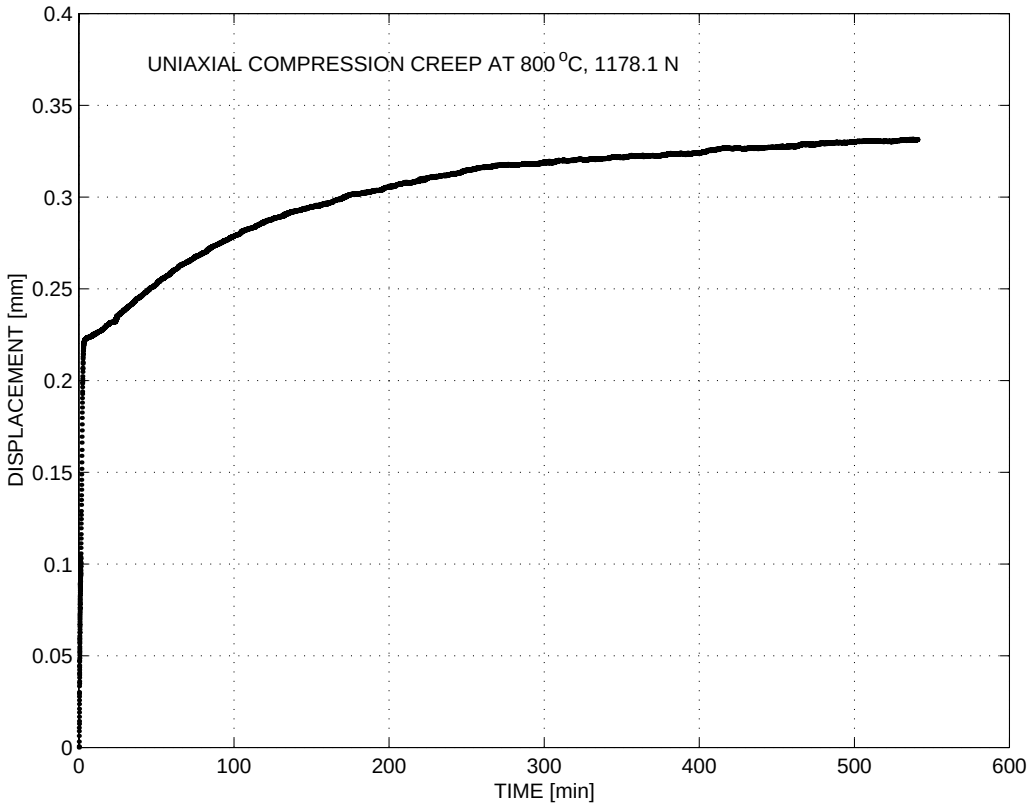
UNIAXIAL COMPRESSION CREEP AT 800 °C, 1178.1 N
DISPLACEMENT [mm]
TIME [min]
0
0.05
0.1
0.15
0.2
0.25
0.3
0.35
0.4
0
100
200
300
400
500
600

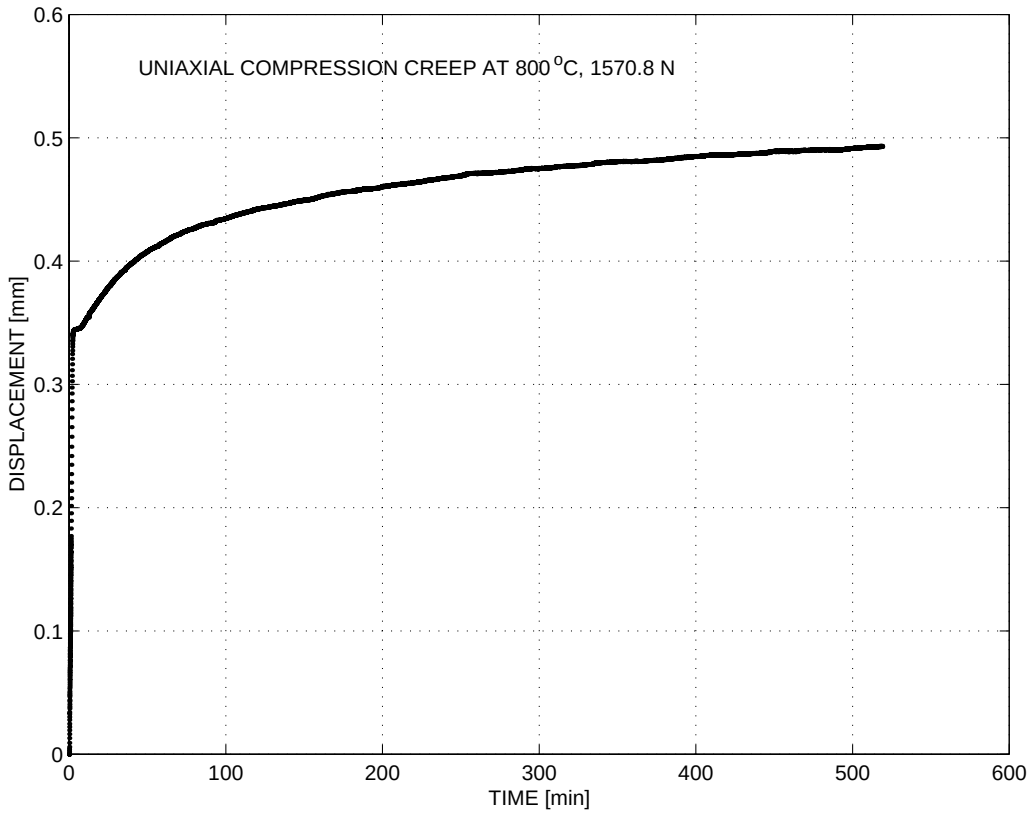
UNIAXIAL COMPRESSION CREEP AT 800 °C, 1570.8 N
DISPLACEMENT [mm]
TIME [min]
0
0.1
0.2
0.3
0.4
0.5
0.6
0
100
200
300
400
500
600

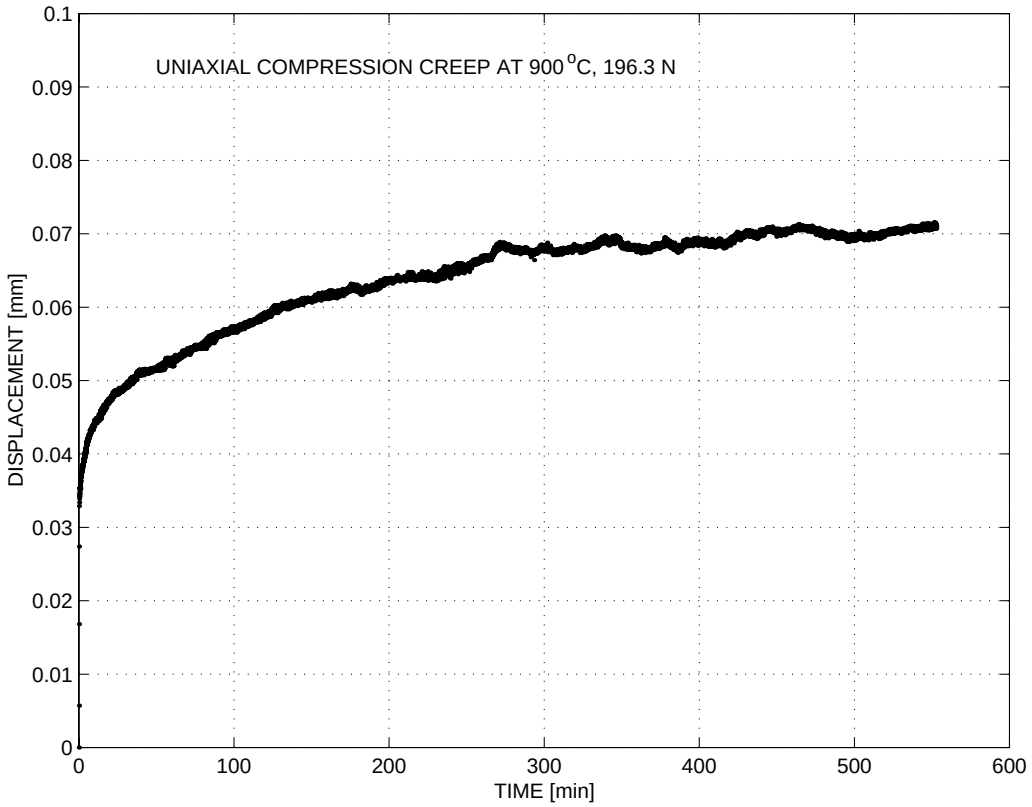
UNIAXIAL COMPRESSION CREEP AT 900 °C, 196.3 N
DISPLACEMENT [mm]
TIME [min]
0
0.01
0.02
0.03
0.04
0.05
0.06
0.07
0.08
0.09
0.1
0
100
200
300
400
500
600

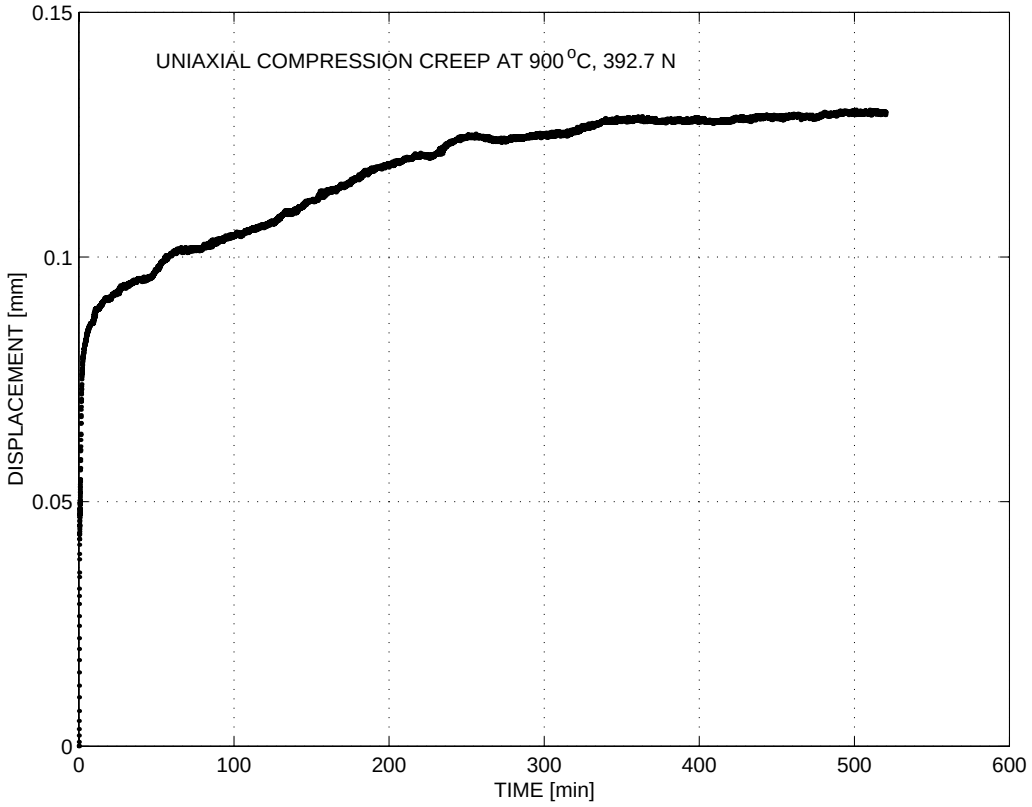
UNIAXIAL COMPRESSION CREEP AT 900 °C, 392.7 N
DISPLACEMENT [mm]
TIME [min]
0
0.05
0.1
0.15
0
100
200
300
400
500
600

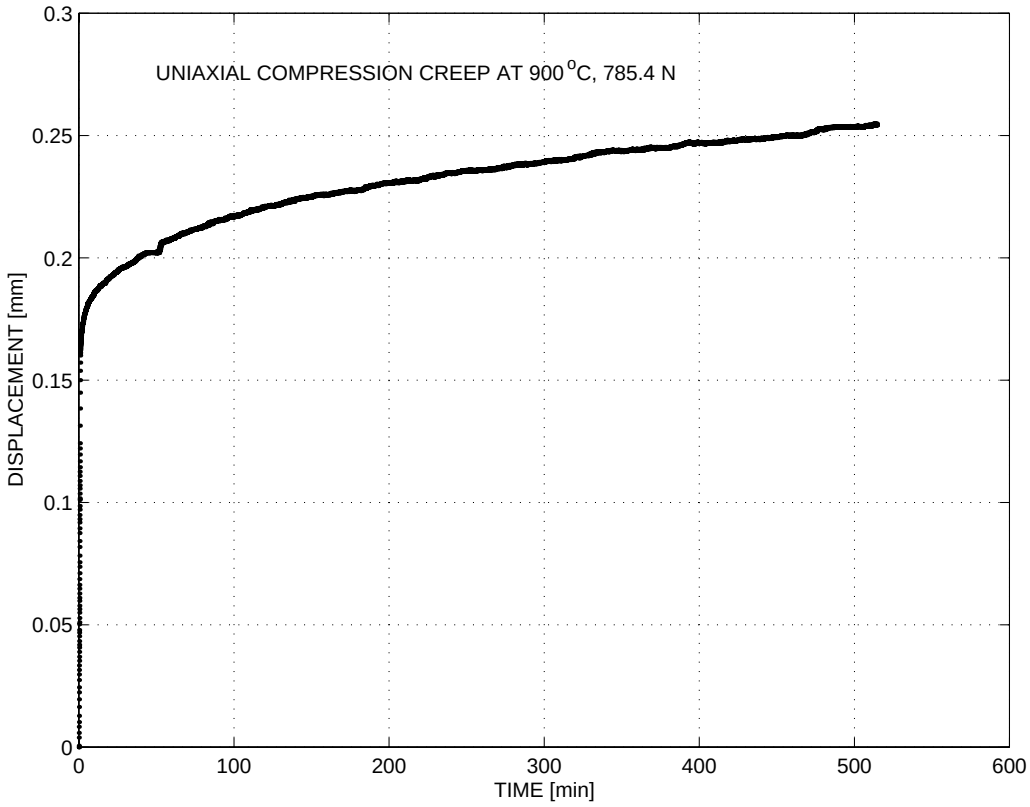
UNIAXIAL COMPRESSION CREEP AT 900 °C, 785.4 N
DISPLACEMENT [mm]
TIME [min]
0
0.05
0.1
0.15
0.2
0.25
0.3
0
100
200
300
400
500
600

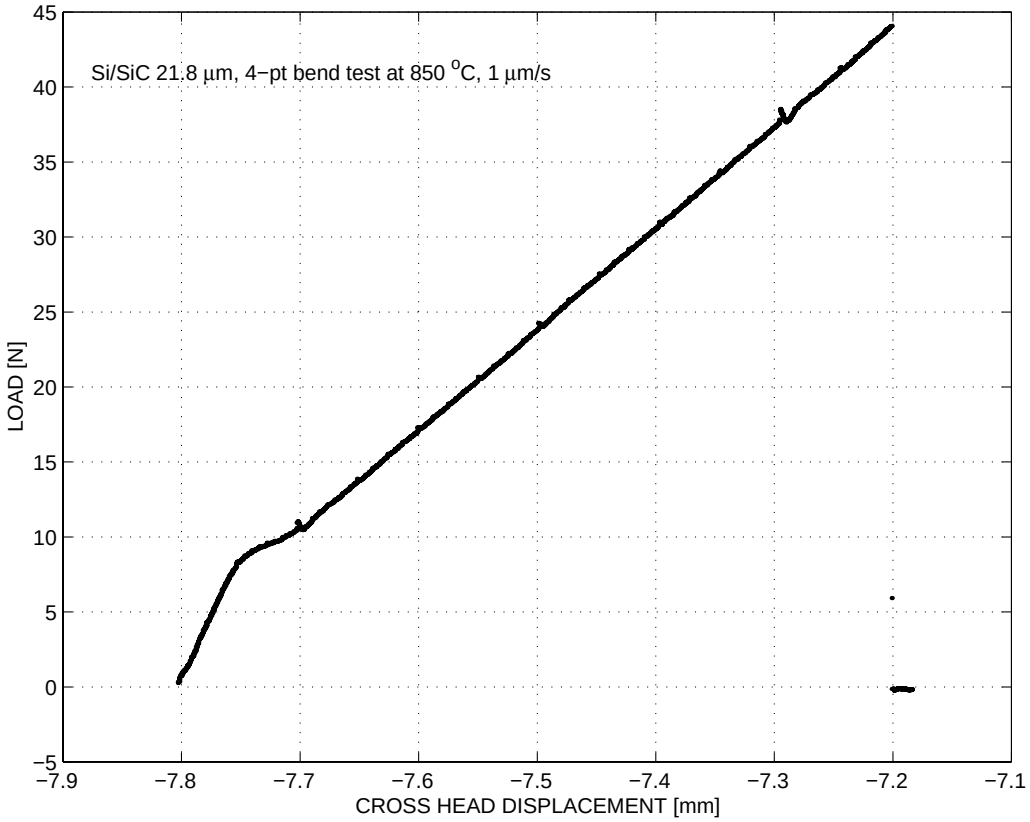
Si/SiC 21.8 µm, 4−pt bend test at 850 °C, 1 µm/s
LOAD [N]
CROSS HEAD DISPLACEMENT [mm]
45
40
35
30
25
20
15
10
5
0
−5
−7.9
−7.8
−7.7
−7.6
−7.5
−7.4
−7.3
−7.2
−7.1

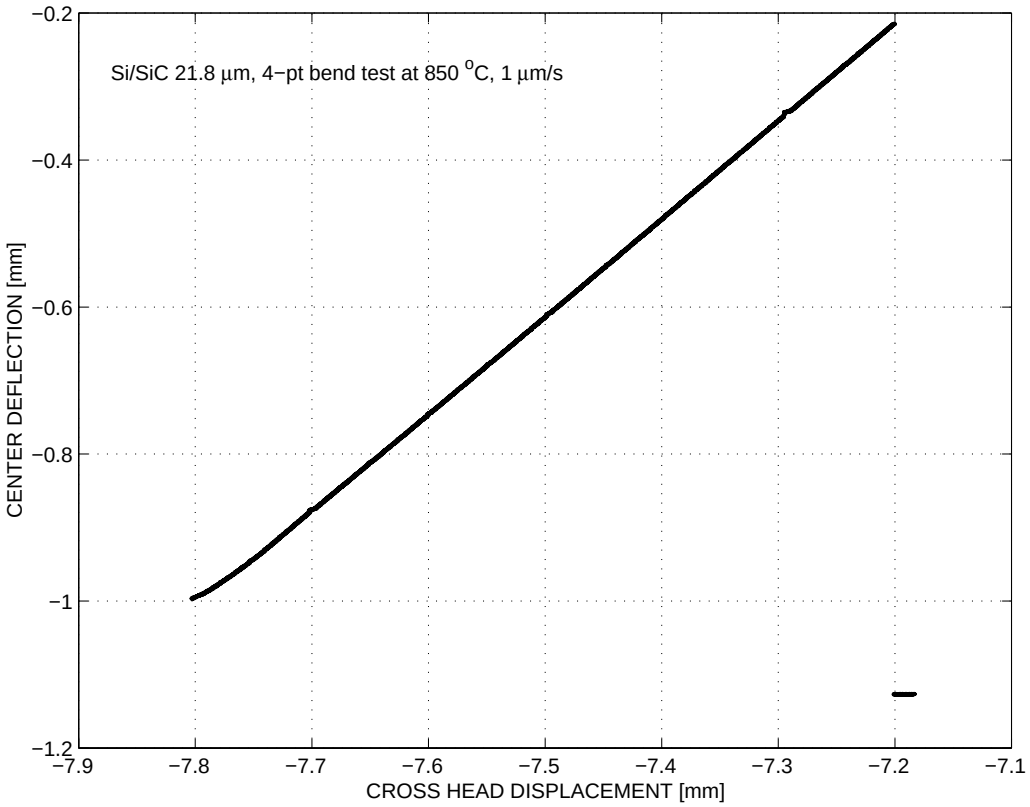
Si/SiC 21.8 µm, 4−pt bend test at 850 °C, 1 µm/s
CENTER DEFLECTION [mm]
CROSS HEAD DISPLACEMENT [mm]
−0.2
−0.4
−0.6
−0.8
−1
−1.2
−7.9
−7.8
−7.7
−7.6
−7.5
−7.4
−7.3
−7.2
−7.1

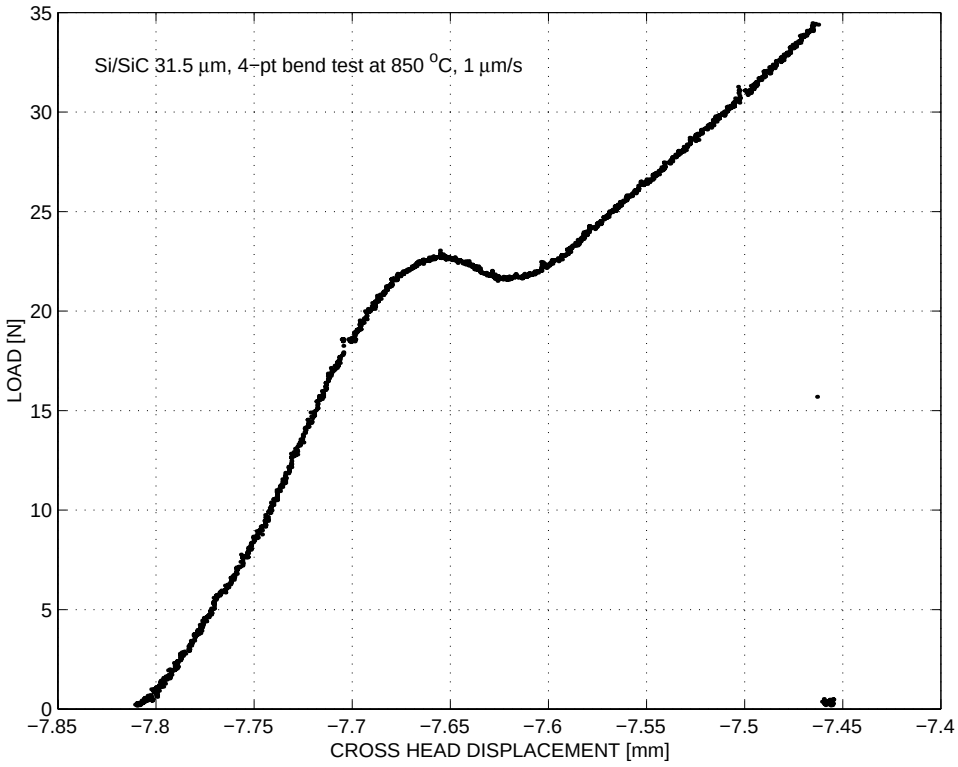
Si/SiC 31.5 µm, 4−pt bend test at 850 °C, 1 µm/s
LOAD [N]
CROSS HEAD DISPLACEMENT [mm]
35
30
25
20
15
10
5
0
−7.85
−7.8
−7.75
−7.7
−7.65
−7.6
−7.55
−7.5
−7.45
−7.4

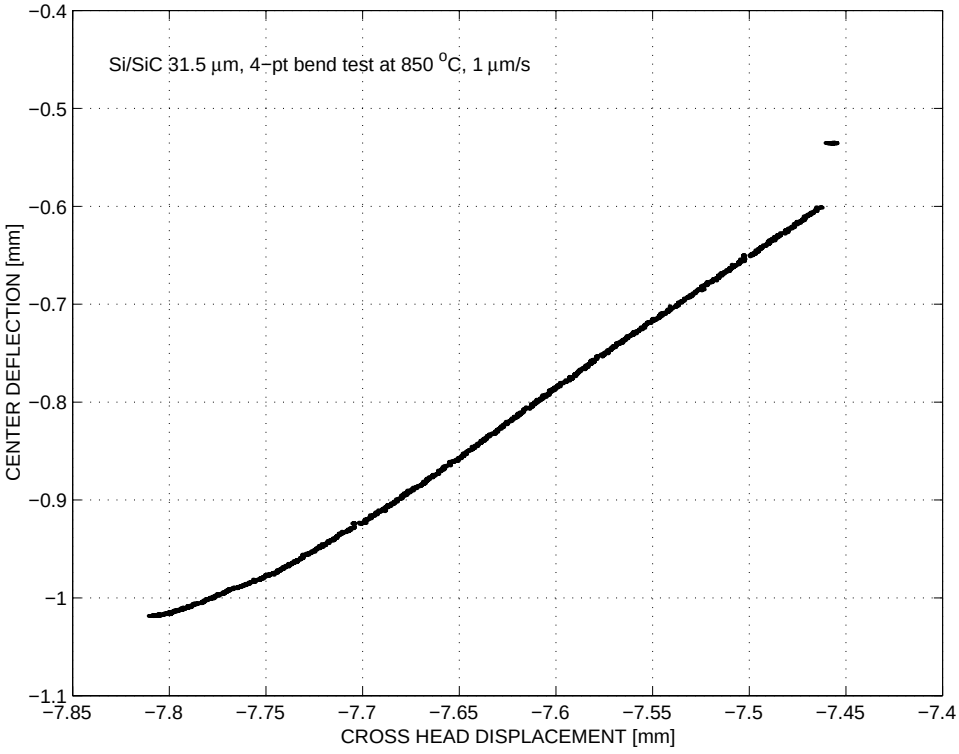
Si/SiC 31.5 µm, 4−pt bend test at 850 °C, 1 µm/s
CENTER DEFLECTION [mm]
CROSS HEAD DISPLACEMENT [mm]
−0.4
−0.5
−0.6
−0.7
−0.8
−0.9
−1
−1.1
−7.85
−7.8
−7.75
−7.7
−7.65
−7.6
−7.55
−7.5
−7.45
−7.4

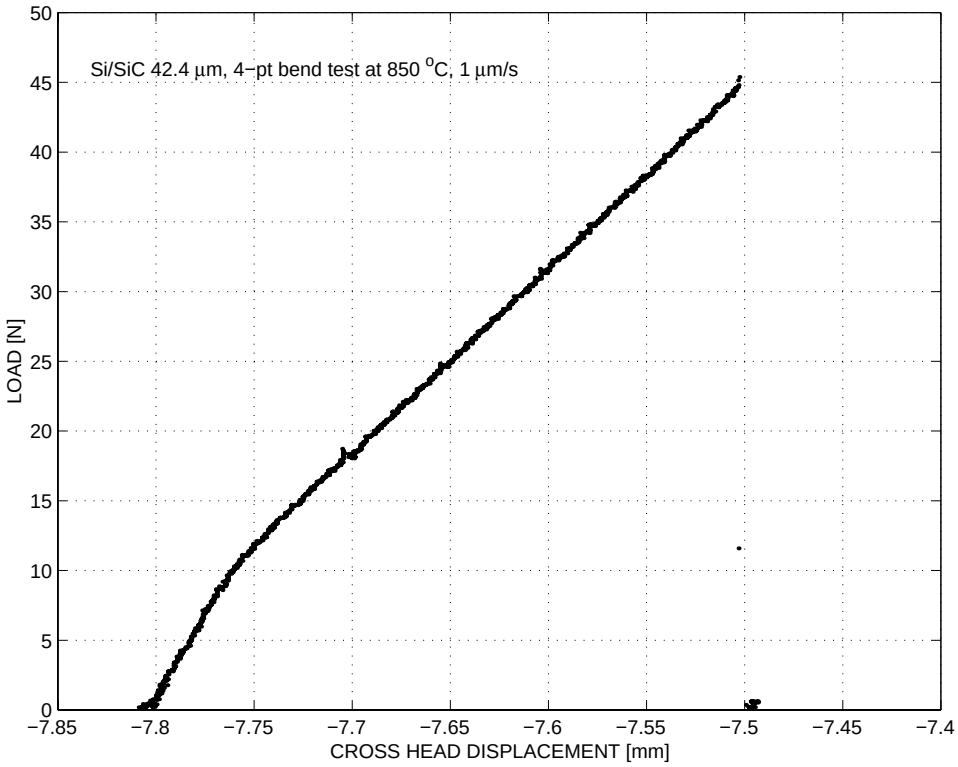
Si/SiC 42.4 μm, 4−pt bend test at 850 °C, 1 μm/s
LOAD [N]
CROSS HEAD DISPLACEMENT [mm]
50
45
40
35
30
25
20
15
10
5
0
−7.85
−7.8
−7.75
−7.7
−7.65
−7.6
−7.55
−7.5
−7.45
−7.4

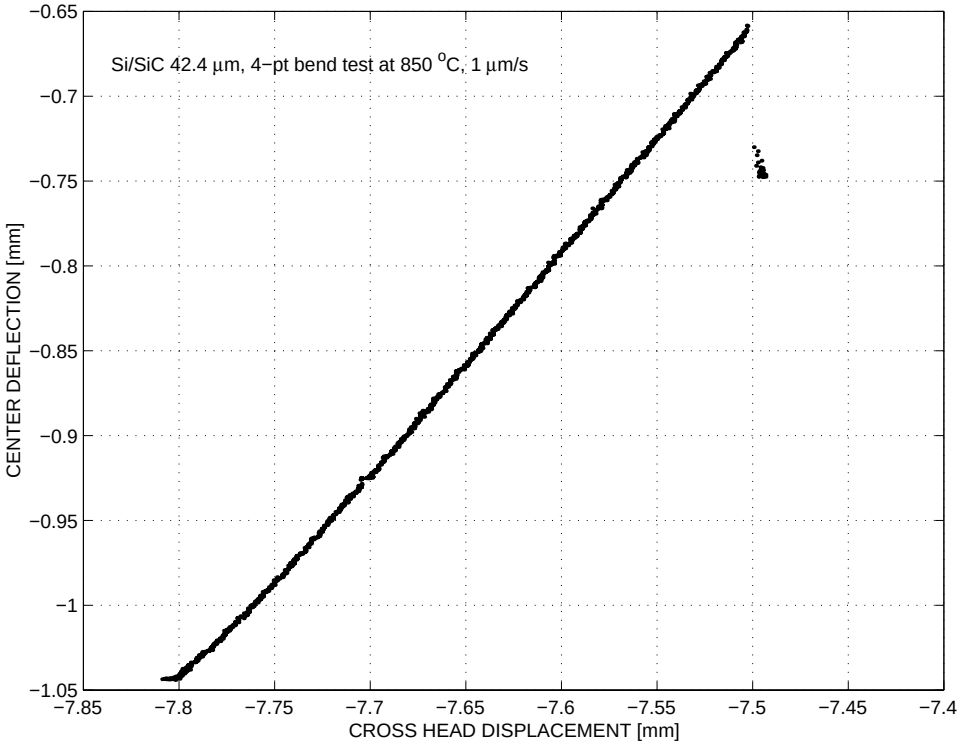
Si/SiC 42.4 μm, 4−pt bend test at 850 °C, 1 μm/s
CENTER DEFLECTION [mm]
CROSS HEAD DISPLACEMENT [mm]
−0.65
−0.7
−0.75
−0.8
−0.85
−0.9
−0.95
−1
−1.05
−7.85
−7.8
−7.75
−7.7
−7.65
−7.6
−7.55
−7.5
−7.45
−7.4

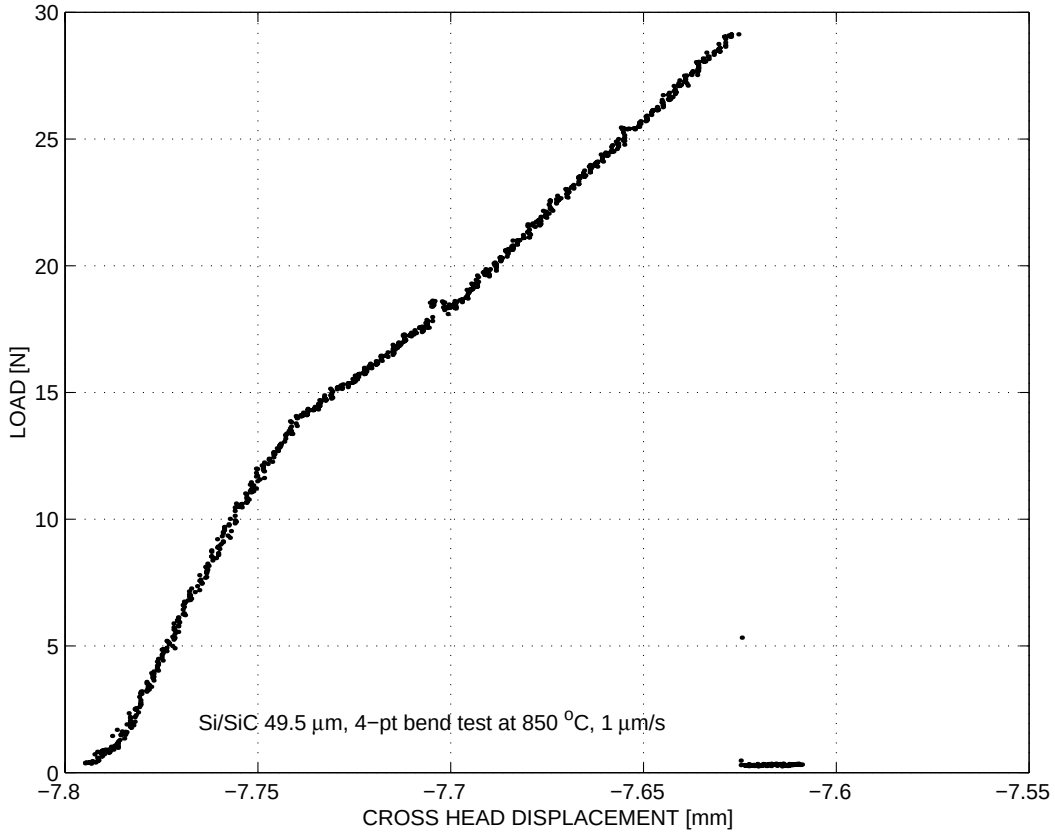
LOAD [N]
CROSS HEAD DISPLACEMENT [mm]
Si/SiC 49.5 µm, 4−pt bend test at 850 °C, 1 µm/s
30
25
20
15
10
5
0
−7.8
−7.75
−7.7
−7.65
−7.6
−7.55

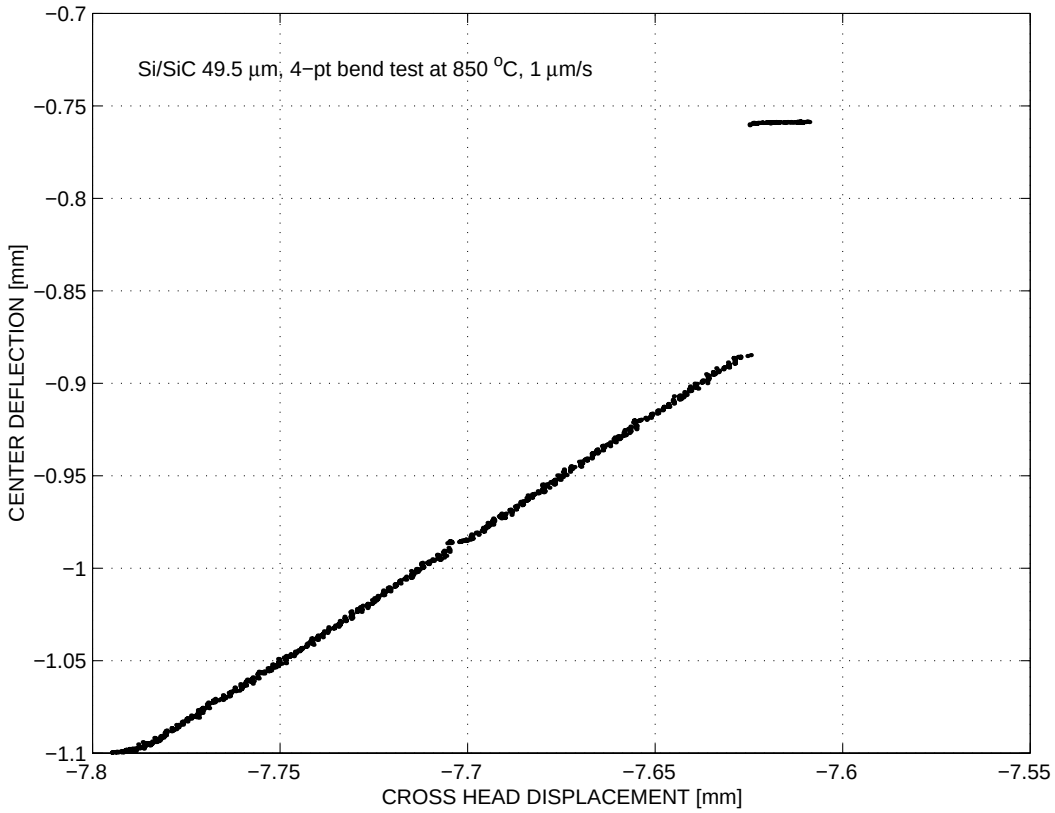
CENTER DEFLECTION [mm]
CROSS HEAD DISPLACEMENT [mm]
Si/SiC 49.5 µm, 4−pt bend test at 850 °C, 1 µm/s
−0.7
−0.75
−0.8
−0.85
−0.9
−0.95
−1
−1.05
−1.1
−7.8
−7.75
−7.7
−7.65
−7.6
−7.55

APPENDIX H

Experimental Error Analysis

As discussed in Chapter 5, the experimental error was estimated to be approximately 15 % from the comparison of the Si compression creep data for multi-slip system <100> and <111> orientations. Here, the experimental errors associated with the Si uniaxial compression creep testing are investigated in detail. The sources for the experimental errors include the creep temperature, load, strain measurement (LVDT), friction between the load pad and the specimen, seating of the load-train, and any misalignment in the load-train. The experimental error boundaries can be conceived as:

$$e_{total} \cong e_{temperature} + e_{load} + e_{LVDT} + e_{alignment} + e_{friction} + e_{seating}\ (\%) \qquad (G.1)$$

Effect of uncertainty in creep temperature and load

First, the effect of creep temperature and load change on Si creep strain in compression was considered. Chen[1] discussed the uncertainty in creep temperature of ±7 °C pertaining to the thermocouples installed in the furnace. He also identified the noise level in load of approximately 5 N. This corresponds to the stress level of 0.25 MPa for the compression specimen dimensions. The machining tolerance of the compression specimen also adds more variations in the creep load of approximately 0.5 MPa. Figure G.1 shows the model prediction on the effect of creep temperature and load change on Si creep in compression. From this result, the sensitivity of the temperature to creep strain, S_T^e, can be obtained to be approximately 0.2 %/°C, and the sensitivity of the load to creep strain, S_P^e, approximately 2 %/MPa. Thus, the errors in creep strain due to the creep temperature and load, $e_{temperature}$ and e_{load}, are approximately 1.5 % and 1.5 %, respectively.

[1] K.-S. Chen, Materials characterization and structural design of ceramic micro-turbomachinery, Ph.D., Dept. of Mechanical Engineering, MIT, 1999.

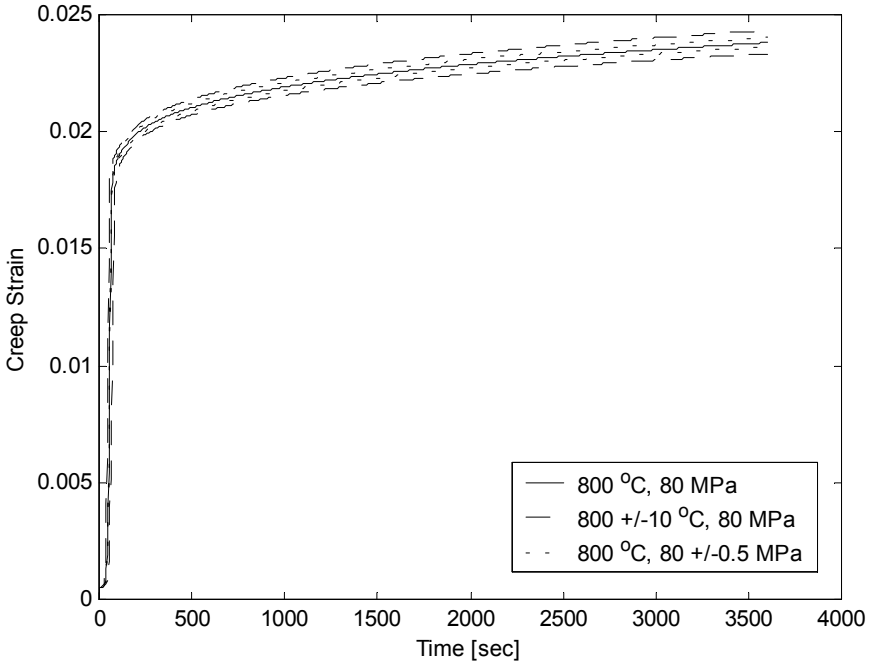

Figure H.1 Effect of creep temperature and load change on Si creep in compression

Effect of accuracy in strain measurement (LVDT)

From the specification of the machine, the accuracy of the Linear Variable Differential Transducer (LVDT) installed in the testing machine is ±1 μm. This results in an error of 0.5 % in strain measurements.

Effect of misalignment of the load train

Misalignments in the load train including the specimen and fixture might cause elastic/plastic buckling and undesirable stress gradients in the specimen. Figure G.2 shows the configuration of the Si compression creep testing with a finite misalignment of 0.5 mm. The model prediction for the deformation under a nominal creep load of 80 MPa at 800 °C is also presented. As described in the test procedure in Appendix B, specimens and fixtures are centered by eye-inspection, which may lead to a misalignment of 0.5 mm with ease. In the analysis, the friction coefficient of 0.1 was used for the contact interface that consists of a pair of SiC load pads, a Si specimen, and BN solid lubricant. The lateral movement of the node at the center of the top load pad was fixed in

order to simulate the rolling contact of the hemispherical top load pad in the experiments. This boundary condition was verified by the fact that experimentally relative lateral movements of the specimen to the load pads were seldom observed. Figure G.3 shows the normal stress distribution within the specimen due to the misalignment with non-uniform stress gradients. As shown in Figure G.4, the misalignment of the load train yields a change in creep strain of approximately 10 %. It appears that the areas of low stresses yielding low creep rates tend to reduce the overall creep rate due to the geometric constraints of the top load pad block.

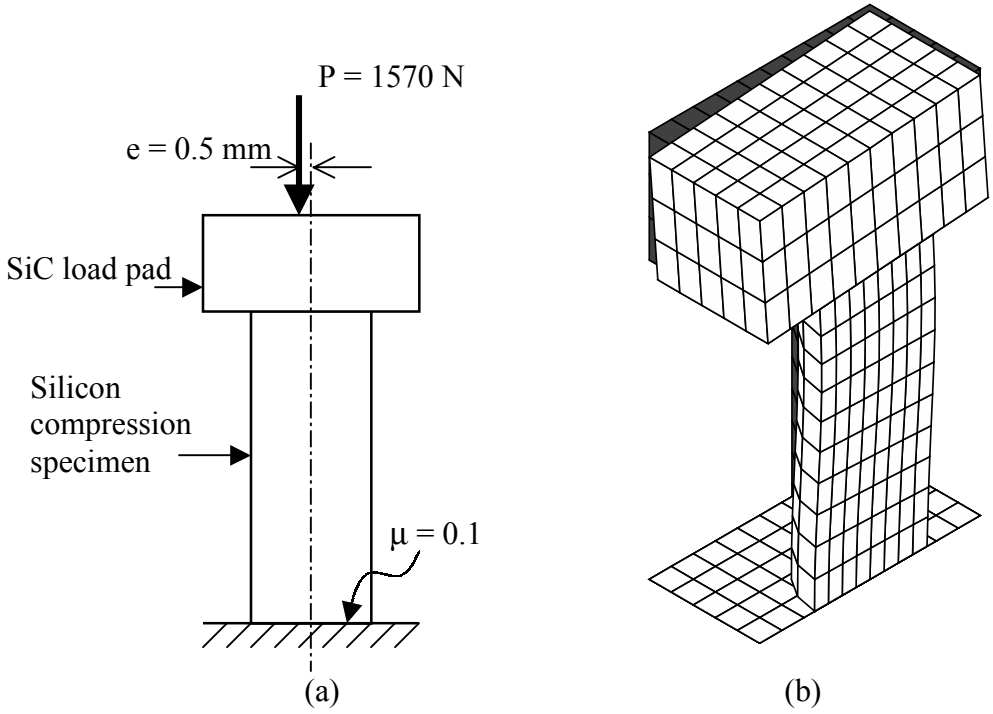

Figure G.2 (a) Configuration of the Si compression creep testing considering a finite misalignment of 0.5 mm, (b) deformed FE mesh under a nominal creep load of 80 MPa at 800 °C.

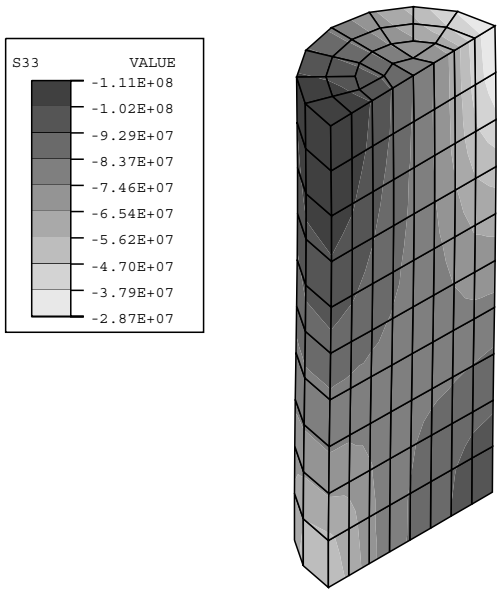

Figure G.3 Non-uniform stress gradients within the specimen due to the misalignment of 0.5 mm under a nominal creep load of 80 MPa at 800 °C.

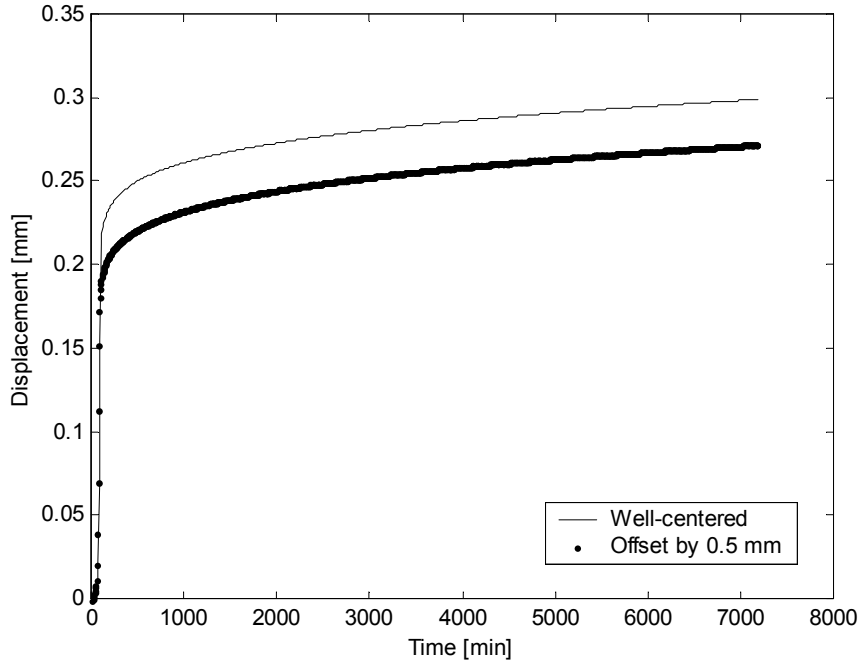

Figure G.4 Comparison of the model predictions for Si creep in compression for cases of well-centered and misaligned by 0.5 mm at the creep temperature of 800 °C and nominal creep load of 80 MPa.

Effect of seating of the load train

The initial displacement during the load ramp is composed of contributions from the elastic/plastic deformation of the specimen, machine compliance, seating of the load train, namely:

$$\delta^{ramp} = \delta^{E} + \delta^{in} + \delta^{seating} + O(e) = \delta^{E,\,Si} + \delta^{E,\,machine} + \delta^{in,\,Si} + \delta^{seating} + O(e) \quad (G.2)$$

As shown in Figure G.5, the overall displacement during the ramp, δ^{ramp}, was measured to be approximately 150 μm for the test at the creep temperature of 800 °C and the nominal creep load of 80 MPa. First, the elastic deformation of the Si specimen is:

$$\delta^{E,\,Si} = PL/EA = 6.2\ \mu m. \quad (G.3)$$

The machine stiffness, $K^{machine}$, was measured to be approximately 16000 N/mm. From this, the contribution of the testing machine can be obtained as:

$$\delta^{E,\,machine} = P/K^{machine} \cong 100\ \mu m. \quad (G.4)$$

From the model prediction, the inelastic deformation of the specimen during the load ramp was found to be negligible. Substituting the obtained values into Equation G.2, the contribution of the seating of the load train during the load ramp is obtained as:

$$\delta^{seating} \cong 45\ \mu m. \quad (G.5)$$

It is still unclear whether or not the seating of the load train is completed at the start of the creep load. Considering the difference in the time constants of the viscous deformation (i. e. creep) of Si and other factors such as the BN solid lubricant and loose interfaces of the load train, the creep deformation after the load ramp, however, appears to be almost free of the seating of the load train. Thus, the effect of the seating of the load train is considered negligible during creep.

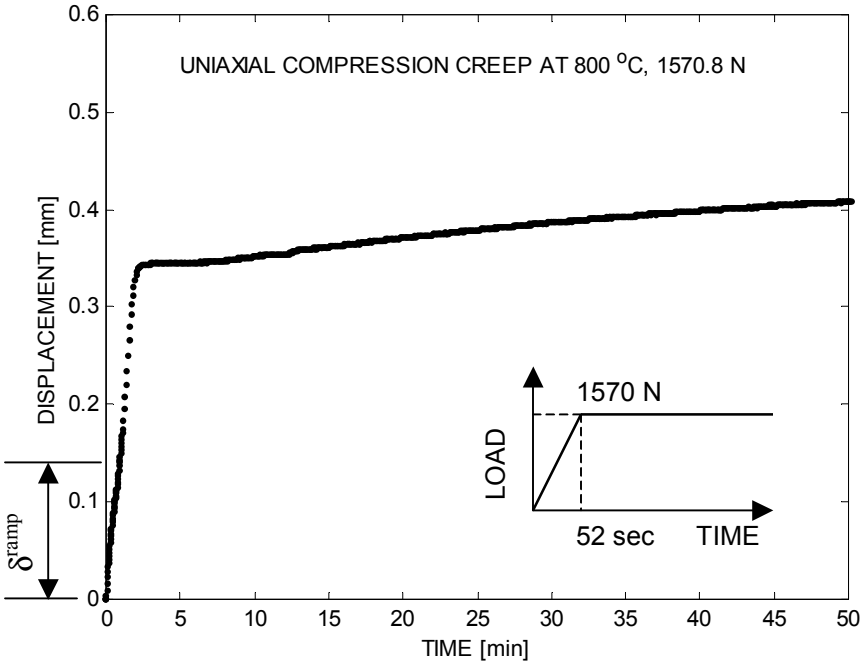

Figure G.5 Experimental creep data at 800 °C and 1570.8 N.

Effect of friction between the load pad and specimen

As discussed in Chapter 3, Debschutz[2] claimed that the additional stress required to maintain a given creep rate, ranged from 6 to 10 % of the average creep stress for an aspect ratio of specimen base, 21, to height, h, ranging from 1/3 to 1/1.5. For the dimensions of the specimen in this work, the additional creep stress is estimated to be 7 %. This was verified in Chapter 5, where the numerical prediction of the creep strain with an axisymmeric FE model is smaller than those of the model prediction using a single-element mesh.

Overall, the experimental error boundaries in the uniaxial compression creep testing are estimated to be approximately 20 %. From this error analysis, the misalignment of the load train is identified to be the most critical factor that determines the experimental error boundaries in compression creep testing, and the friction between the load pads and specimen the second most critical factor. The experimental errors can be minimized by

[2] K. Debschutz, et. al, Critical evaluation of the compression creep test, J. Am. Ceram. Soc., Vol. 76, No. 10, pp 2468-74, 1993.

adopting improved alignment methods such as using a better fixture design or a long range optical telescope. If properly designed, specifically with attention to the grip and strain measurement technique, tensile testing has the potential to provide more accurate results.

APPENDIX I

GDMS Analytical Report for Si (compression specimen)

Element	Concentration [ppmwt]
B	0.2
C	0.3
N	~ 0.9
O	7
Si	Matrix
P	980
S	< 0.01
As	0.02
Ta	< 1

Data provided by Lattice Materials Corporation